



TUS

**Technological University of the Shannon:
Midlands Midwest**

Ollscoil Teicneolaíochta na Sionainne:
Lár Tíre Iarthar Láir

**THE OPTIMISATION OF BIOMIMETIC
SCAFFOLD FABRICATION FOR THE
CONTROLLED RELEASE OF OSTEOGENIC
FACTORS FOR BONE TISSUE REGENERATION**

FARAH ALWANI BINTI AZAMAN

**Doctor of Philosophy
Polymer Engineering**

2023



TUS Midlands
Midwest

**THE OPTIMISATION OF BIOMIMETIC
SCAFFOLD FABRICATION FOR THE
CONTROLLED RELEASE OF OSTEOGENIC
FACTORS FOR BONE TISSUE REGENERATION**

A thesis submitted for the degree of

Doctor of Philosophy

by

Farah Alwani Binti Azaman, BSc., Hons.

Based on the research carried out under the supervision of

Dr. Declan M. Devine & Dr. Margaret E. Brennan Fournet

Submitted to

Technological University of the Shannon:

Midlands Midwest

PRISM Research Institute

Technological University of the Shannon: Midlands Midwest

Ireland

August 2023

**All information described in this document is
confidential and subject to Intellectual Property.**

Declaration of Authorship

I hereby certify that this material, which I now submit for assessment on the program of study leading to the degree of Doctor of Philosophy by Research program in the Polymer, Recycling, Industrial, Sustainability and Manufacturing (PRISM) Research Institute, Technological University of the Shannon: Midlands Midwest is entirely my own work and has not been taken from the work of others and to the extent that such work has been cited and acknowledged within the text of my work.

I confirm that:

- This work was carried out wholly or mainly while in candidature for a research degree at this university.
- Where any part of this thesis has previously been submitted for a degree or any other qualification at this university or any other institution, this has been clearly stated.
- Where I have consulted the published work of others, this is always clearly attributed.
- Where I have quoted from the others, the source is always given.
- With the exception of such quotations, this thesis is entirely my own work.
- I have acknowledged all primary sources of help

Signed:



Date: 15th Aug 2023

Dedication

Bismillahirrahmanirrahim.

I dedicate this work to both my parents; my late father, Azaman bin Ibrahim and my mother, Noor Asiah binti Md Noor; my brothers and family members, as well as my loving husband, Zainal Hisham bin Burhanuddin for their endless and infinity support that made this a reality. This is also a manifestation from all the love, prayers and support from all good people around me that kept me strong throughout the journey. Of course, Alhamdulillah 'ala kulli hal, for I wouldn't be able to do any of this without Him, Allah The Almighty.

Abah, I dedicate this PhD to you, for now I'll carry your name; Dr. Azaman, F.A..

Al-Fatihah.

Thank you for not clipping my wings :)

Acknowledgements

This PhD could have never been a success without the help and support of many people. I would like to express my sincere gratitude to both my dedicated supervisors, Dr Declan M. Devine and Dr Margaret E. Brennan Fournet for all the help and guidance throughout my PhD journey and growth. Special thanks to Dr Mohamed Shuaib Mohamed Saheed from Universiti Teknologi Petronas for recommending me to go for this project, although you firstly mentioned that it would just be a ‘mini project’ in the ads! My gratitude extends to the sponsors of my PhD; International Education Scholarship from the Government of Ireland, commercialization fund from Enterprise Ireland and also the President Seed Fund from TUS for the financial support to this research until its end. I am forever grateful for the privilege to have a full sponsorship throughout my studies.

Definitely a lot of thanks to my colleagues in the research hub and everyone in TUS that was there in my life as a PhD and international student here since 2018. To name some, Laura Rodriguez, Chaitra Venkatesh, Ismin Zainol, Ashima Chawla, Marina Bandeira, Ana Da Costa, Keran Zhou, Alya Karim, Eduardo Lanzagorta, and Eyman Manaf, all of you will forever be in my heart (especially the gems from the countless coffee sessions we’ve had). The brilliant proteomics and HPLC tips from Tomasz Szank, I owe you forever! The super helpful staff in the grad school, Siobhan Lee, Susan Carroll and Amanda Murray; the academic staff, Mark Lynch, Crevan O’ Donnell, Alan Murphy and CISD members, who made my research life easier with the help and knowledge shared full-heartedly. It was definitely a great pleasure working with the team.

Not to forget, to all my family friends in Ireland, kak Lina and family, kak Nadiah and family and many more, I am super grateful to be able to meet all of you. Thank you for being there during my ups and downs. It felt so safe to know that my lovely Malaysian people is around me. I will miss our gatherings, tadarus al-Quran and the trips with you guys. I learnt the best about blessings in disguise from all of you. My friends in Malaysia especially EIFJAN, Aqilah and Hannan, I owe you guys infinity thank you for the endless love and support, since before I start this journey until the submission of this thesis. Almost tearing up when I know some of you even surveyed the flight tickets to Ireland from Malaysia for the convocation!

To my field research host in Universiti Sains Malaysia, Prof Dr Suzina Sheikh and Dr Muhamad Syahrul Fitri Zawawi, as well as the staff in Tissue Bank, Animal Research and Service Centre and Craniofacial Science Lab, thank you for accepting my visit and helping me throughout the stay for the animal trial there. Thanks to Dr Jimmy Muldoon from University College Dublin for MALDI-TOF training and knowledge. Finally, a million thanks to Prof. Dr. Valdemiro Amaro da Silva Junior from the Federal Rural University of Pernambuco, Brazil for the help in the final bits of the histological work. This one couldn’t be finished without your patience and expertise.

Wishing the best to all of you ☺.

Table of Contents

Declaration of Authorship.....	ii
Table of Contents	v
List of Figures.....	x
List of Tables.....	xv
Abstract	xix
<i>Introduction</i>	20
1. Research Challenge.....	21
2. Research Gap	21
3. Proposed Solution: Design of an Ideal Chitosan Composite Scaffold for Growth Factor Release	22
4. Research Outcomes.....	27
Chapter 1: Literature Review.....	41
1.1 Long Bone Fractures	41
1.1.1 The Healing Process of Bone Fractures.....	42
1.1.2 Non-Union Fractures in Long bones	45
1.2 Traditional Bone Grafting for Long Bone Fractures.....	46
1.2.1 Autologous Bone Graft	47
1.2.2 Allogenic Bone Graft.....	48
1.3 Bone Tissue Engineering in Treating Bone Fractures	48
1.3.1 Diamond Concept in Bone Healing.....	50
1.3.2 The Ideal Properties of Bone Tissue Scaffolds.....	51
1.3.3 Conventional Scaffold Fabrication Methods	52
1.3.4 Polymer Crosslinking through UV Curing Procedures.....	53
1.4 Biodegradable Scaffold.....	55
1.5 Naturally and Synthetically Derived Biodegradable Scaffold Materials.....	55
1.5.1 Chitosan	56
1.6 Bioactive Ceramics.....	59
1.6.1 Hydroxyapatite.....	59
1.6.2 Tricalcium Phosphate	60
1.7 Promoting Signalling Molecules for Bone Healing Treatment.....	61
1.7.1 Bone Morphogenetic Protein-2	63

1.7.2	Peptides derived from Bone Morphogenetic Protein-2	64
1.8	Clinical Application of Protein and Peptide and its Related Issues	65
1.9	Research Question	67
1.10	Objectives	67
Chapter 2: Materials and Methods		70
2.1	Materials	70
2.2	Fabrication of Chitosan Composite Scaffolds	71
2.2.1	Optimisation of Chitosan Composite Scaffold through Extended UV Crosslinking	71
2.2.2	Incorporation of Hydroxyapatite (HAp) and Tri-Calcium Phosphate-α (TCP-α) into Chitosan Scaffold	71
2.2.3	Preparation of Fluorapatite into Chitosan Composite	72
2.2.4	Chitosan/Hydroxyapatite Blend using Various Amounts of Photoinitiator	73
2.2.5	Chitosan Composite Fabrication using Different Crosslinking Time in UV Curing Chamber	73
2.2.6	Osteogenic Factor Incorporation into Chitosan/Hydroxyapatite Scaffolds	73
2.2.7	Chitosan-based Scaffolds for <i>In vivo</i> Implantation	74
2.2.8	Pulse UV Sterilisation of Osteogenic Factor Incorporated Chitosan/Hydroxyapatite Scaffold	74
2.3	Crosslinking Test	75
2.4	Fourier-Transform Infrared Spectroscopy	75
2.5	Compression Test	76
2.6	Simulated Body Fluid Preparation	76
2.7	Degradation Assessment	77
2.8	Swelling Studies	78
2.9	Identification and Evaluation of Osteoinductive Factors-Release from Chitosan/Hydroxyapatite Scaffold	79
2.9.1	High-Performance Liquid Chromatography Method Development for Bone Morphogenetic Protein-2 Release Analysis	80
2.9.2	High-Performance Liquid Chromatography Method Development for P28 Peptide Release Analysis	82
2.9.3	Preliminary P28 Peptide Release Analysis Using UV Spectrometer	83
2.10	Resazurin Antimicrobial Assessment of the Scaffolds in Gram-Positive and Gram-Negative Bacteria	84
2.10.1	Liquid Bacteria Culture	84
2.10.2	Bacterial Plating	85
2.10.3	Resazurin Antimicrobial Assay	85
2.11	Cell Culture	85

2.11.1	Cell Resuscitation	86
2.11.2	Cell Passaging	87
2.12	Alkaline Phosphatase Activity	88
2.13	Evaluation of Osteogenic Differentiation of C2C12 cell line through Alizarin Red Staining	90
2.14	<i>In vivo</i> Evaluation of Bone Regeneration Scaffold in Femoral Condyle Defects of Sprague Dawley Rats	91
2.14.1	Animals' Husbandry	93
2.14.2	Surgical Interventions	93
2.14.3	Post-operative Monitoring	96
2.14.4	Fluorescent Bone Labelling for Dynamic Bone Formation	96
2.14.5	Animal Euthanasia	97
2.14.6	Macroscopic Histopathological Evaluation	97
2.14.7	Micro Computed Tomography Scanning	98
2.14.8	Histological Processing, Embedding and Cutting	98
2.14.9	Fluorescent Imaging	99
2.14.10	Histopathologic Analysis from Hematoxylin and Eosin Staining	100
2.14.11	Measurements of Mineralised and Osteoid Tissue Volume into the Defect by Von Kossa Staining	101
2.14.12	Measurements of Osteoclasts Surface into the Defect by Tartrate-Resistant Alkaline Phosphatase Staining	101
2.14.13	Measurement of the Dynamic Bone Formation Parameters through Fluorescent Labelling Analysis	102
2.14.14	Histomorphometric Parameters Calculations	102
2.15	Statistical Analysis	103
Chapter 3: Bioresorbable Chitosan-Based Bone Regeneration Scaffold Using Various Bioceramics and the Alteration of Photoinitiator Concentration in an Extended UV Photocrosslinking Reaction		105
3.1	Abstract	105
3.2	Introduction	105
3.3	Results and Discussions	112
3.3.1	Analysis of Crosslinkage Formation Following UV-Photocrosslinking Procedure	112
3.3.2	Fourier-Transform Infrared Spectroscopy	116
3.3.3	Mechanical Assessment	118
3.3.4	Biodegradation Assessment	120

3.3.5	Scanning Electron Microscopy and Energy Dispersive X-ray Spectrometry	125
3.3.6	Analysis of UV Curing Time on the Crosslinking of Chitosan/Hydroxyapatite Composite Scaffold	127
3.4	Summary.....	131
	Chapter 4: Chitosan/Hydroxyapatite Scaffolds with P28 as a Promising Osteoinductive Scaffold for Bone Healing Applications	134
4.1	Abstract.....	134
4.2	Introduction.....	134
4.3	Results and Discussion.....	137
4.3.1	Scaffold Characterisation through a Fourier-Transform Infrared Spectroscopy.....	137
4.3.2	Kinetic Release of BMP-2.....	138
4.3.3	<i>In Vitro</i> Kinetic Release of P28.....	142
4.3.4	C2C12 Mineralisation through Culture with P28 Peptide and BMP-2 Loaded Scaffolds Using Alkaline Phosphatase.....	143
4.3.5	C2C12 Mineralisation through Culture with P28 Peptide and BMP-2 Loaded Scaffolds Using Alizarin Red Staining.....	148
4.3.6	Post-Operative Evaluations of the Animals	151
4.3.7	Macroscopic Evaluation	152
4.3.8	Micro-CT Evaluation of the Femoral Defects Treated with the Scaffolds	154
4.3.9	Histopathologic Analysis	156
4.3.10	Mineralised and Osteoid Tissue Evaluation through Von Kossa Staining.....	165
4.3.11	Evaluation of the Presence of Osteoclast through Tartrate-Resistant Acid Phosphatase Staining.....	169
4.3.12	Dynamic Bone Formation Analysis through Fluorescent Labelling.....	172
4.3.13	Overall Analysis	175
4.4	Summary.....	177
	Chapter 5: Enhancement of Scaffold <i>in Vivo</i> Biodegradability for Bone Regeneration using P28 peptide Formulations	180
5.1	Abstract.....	180
5.2	Introduction.....	180
5.3	Results and Discussion.....	184
5.3.1	Antimicrobial Functionality of UV-Crosslinked Chitosan Scaffolds with Fluorapatite Bioceramics	185
5.3.2	Post-operative Monitoring.....	186
5.3.3	Macroscopic Evaluation	187

5.3.4	Histological Analysis using Hematoxylin-Eosin Staining	190
5.3.5	Fluorochrome Labelling Analyses	193
5.4	Impact of Coronavirus Disease 2019 (COVID 19) Pandemic on the Studies	195
5.5	Summary.....	195
Chapter 6:	Conclusions & Recommendations.....	198
6.1	Conclusions.....	198
6.2	Future Work Recommendations.....	202
6.3	Invention Declaration	203
6.4	Commercial Feasibility Review for an Orthopaedic Scaffold.....	204
	REFERENCES.....	205
	RESEARCH PARTICIPATIONS.....	256
	TRAININGS.....	259
	APPENDICES.....	260

List of Figures

Figure 1 Medtronic Infuse™ rhBMP-2 and the collagen sponge.....	22
Figure 2 Microscaled agglomerates of hydroxyapatite particles embedded between chitosan matrix (Devine et al., 2017).	24
Figure 3 Main requirements of bone scaffolds. De Witte et al. (2018).....	25
Figure 1.1 The complex architecture of long bones. (Nair et al., 2013).....	41
Figure 1.2 Normal formation of new bone post-fracture, starting from the hematoma or the inflammatory responses until the newly remodelled bone in 35 days (Einhorn and Gerstenfeld, 2015).	44
Figure 1.3 A clinical case example of healing a humerus shaft fracture over two years (Ghiasi et al., 2017).	45
Figure 1.4 The iliac crest serves as autografts for bone grafting treatment (Jenis, 2016).	47
Figure 1.5 Biomimetic acellular approach of bone tissue engineering (Fernandez-Yague et al., 2015).	49
Figure 1.6 Procedure of scaffold fabrication and evaluation highlighting the structural, mechanical, and in vivo assessments (Zhang, Fang and Zhou, 2017).....	50
Figure 1.7 The diamond concept and the biological chamber illustration highlighted vascularisation in avoiding an impaired healing response, which is the non-union (Calori and Giannoudis, 2011).....	51
Figure 1.8 Chitosan chemical structure.....	57
Figure 1.9 Modelled complex structure of BMP-2 dimer, highlighting the wrist and knuckle epitope region of the BMPR-I and BMPR-II cognate receptors, respectively (Y. Wu et al., 2020).	64
Figure 1.10 Current methods for fabricating GF-loaded scaffolds, mainly binding the GF to the scaffolds and the physical entrapment within scaffolds. (Blackwood et al., 2012).....	66
Figure 2.1 Fluorapatite (FAp) powder prepared through chemical substitution method.	72
Figure 2.2 Pulse-UV chamber with xenon flash lamp utilised for scaffold sterilisation (Kelly, 2019).	75
Figure 2.3 The BMP2 and P28 scaffolds release sample setup.....	80
Figure 2.4 HPLC system equipped with a dual-wavelength UV detector used in the growth factor analysis.	81
Figure 2.5 The morphology of the C2C12 myoblast cell line captured using Olympus CKX41 inverted light-microscope with an IS300, 3.0MP camera attachment (Olympus Life Science, Hamburg, Germany).	86
Figure 2.6 Elongated myotubes morphology of differentiated C2C12 myoblast viewed using TSVIEW Imaging Software (Version 7.3.1.7).	87
Figure 2.7 The cleanroom setup for animal implantation procedures.	93
Figure 2.8 The 3 mm defect made on the femoral condyle of an SD rat.....	94
Figure 2.9 A summary of the conducted femoral defect induction and scaffold implantation procedures.....	95
Figure 2.10 Euthanasia using cardiac puncture method.....	97
Figure 2.11 Cutting procedure of the embedded condyles on sagittal axis.	99
Figure 2.12 The Invitrogen EVOS M7000 fluorescent microscope and M7000 software utilised in the fluorochrome-labelling assessment.	100

Figure 2.13 Example of VK staining. Mineralised tissue appears in black, osteoid tissue appears in dark pink (red arrows), bone marrow and muscle appear in orange and fibrotic tissue appears in pink.	101
Figure 2.14 Example of TRAP staining. Bone tissue appears in light blue, activated osteoclasts appear red (yellow arrows), and the nucleus appears dark blue.	101
Figure 2.15 Example of the fluorescent scans. Calcein labelling appears in green and xylenol labelling appears in orange. Single labelling (sLS) along the bone with either orange or green labelling was designated with blue arrows, and double labelling (dLS) along the bone with both green and orange labelling was designated with the yellow arrows.....	102

Figure 3.1 Chemical structure of the protonated chitosan.....	108
Figure 3.2 Postulated end-product from the chemical crosslinking of chitosan and PEGDMA600 post-curing using the original method.....	110
Figure 3.3 The proposed extended crosslinking reaction of chitosan and PEG600DMA following the method modification.	111
Figure 3.4 Photographs of CS scaffolds with various ceramics and BP content which were placed in 1% v/v acetic acid solution in the water acting as a solvent for CS. Minimal swelling or dissolution was observed for up to 24 hours indicating the success of the crosslinking reaction.	112
Figure 3.5 FTIR spectrum of individual components and different CS/ceramic scaffolds following the crosslinking reaction.	117
Figure 3.6 FTIR spectrum of CS/HAp scaffolds incorporating 50, 20, 5 and 1 μ l BP at 0.1% w/v.	118
Figure 3.7 The compressive strength of the chitosan scaffolds with different bioceramics recorded similar values achieving a strength above 12 MPa.	119
Figure 3.8 The Young's modulus values of the chitosan scaffolds with different BP contents present the lowest strength in the least BP volume.	120
Figure 3.9 The degradation profile of the chitosan scaffolds in simulated body fluid over eight weeks shows a similar degradation rate for chitosan scaffolds with HAp, TCP- α and FAp ceramics.	121
Figure 3.10 The scaffolds' physical condition following submerging in SBF for two weeks, where the swelling of chitosan was observed the most in CS/FAp.	122
Figure 3.11 The degradation profile of CS/HAp scaffolds with different benzophenone content in SBF, where CS/HAp/5 μ l BP presented a stable degradation rate for eight weeks.	122
Figure 3.12 The compressive strength profile of the scaffolds while degrading in SBF for CS/HAp and CS/TCP- α , showing a reduction in the scaffold strengths over the eight weeks (n=3).	124
Figure 3.13 The compressive strength profile of the CS/HAp scaffolds with different BP contents while degrading in SBF for eight weeks (n=3). An increase in strengths might be indicative of the remaining strong crosslinked chains following the initial disintegration of the weaker chains.	125
Figure 3.14 SEM-EDX analysis for the scaffolds showing the highest Ca/P values in CS/HAp followed by CS/TCP- α and CS/FAp.	126
Figure 3.15 SEM-EDX analysis for the degraded CS/HAp 5 μ l BP scaffolds in weeks 1 to 8, showing a low Ca/P value in week 1 before increasing in week 2 and decreasing gradually to week 8.....	127
Figure 3.16 The crosslinking test of 5 mm diameter scaffolds in acetic acid for 5 minutes, 1.5 hours, 3 hours and 24 hours to assess the linkage formed.....	128
Figure 3.17 The crosslinking test of 20 mm diameter scaffolds in acetic acid for 5 minutes, 1.5 hours and 24 hours to assess the linkage formed.	129

Figure 3.18 The FTIR spectrum of scaffolds with 20 mm diameter under different curing times in the UV chamber.130

Figure 3.19 The FTIR spectrum of scaffolds with 5 mm diameter under different curing times in the UV chamber.131

Figure 4.1 FTIR responses of the scaffolds, BMP-2 and P28, presenting the success of the covalent bonding through the increase in the peak height at 1650 cm^{-1}138

Figure 4.2 The HPLC chromatogram of 30 ng/ml BMP-2 standard shows a more consistent response in the SST. a) represents the complete chromatogram while b) shows the zoomed peak region.139

Figure 4.3 The graph shows the BMP-2 released concentration from the CS/HAp scaffold over 14 days.141

Figure 4.4 P28 release profile showing an initial burst release in the first 48 h, followed by a sustained release until 335 h (14 days). Blue line indicates the extrapolated graph to estimate the release in 672 h (4 weeks) and 1008 h (6 weeks).143

Figure 4.5 Alkaline phosphatase response of C2C12-treated with various concentrations of (a) BMP-2 and (b) P28 controls and (c) the CS/HAp scaffolds. An increased ALP response was observed in the culture with $1\text{ }\mu\text{g/ml}$ BMP-2 after 14 days, despite the high background control.144

Figure 4.6 Morphological changes in C2C12 following cultured with the various scaffold formulations in differentiation media (magnification: $10\times$) and growth media (magnification: $4\times$). Cuboidal morphology can be observed in the culture with CS/HAp/BMP-2 and CS/HAp/P28 compared to the controls.147

Figure 4.7 Alizarin red stained images and the destaining by CPC quantitation. (a) ARS of C2C12 treated with various concentrations of BMP-2. (b) CPC quantitation of the destained ARS of C2C12 treated with various concentrations of BMP-2. (c) ARS of C2C12 treated with various concentrations of P28. (d) CPC quantitation of the destained ARS of C2C12 treated with various concentrations of P28. (e) ARS of C2C12 treated with various CS/HAp scaffolds. (f) CPC quantitation of the destained ARS of C2C12 treated with various CS/HAp scaffolds. Positive ARS was observed in week 4 following the treatments with BMP-2 and P28 as well as CS/HAp/BMP-2, CS/HAp/P28 compared to the controls. (* $p < 0.05$).150

Figure 4.8 Mean body weight curve for each group.152

Figure 4.9 Defects visibility on the condyles after eight weeks (red circle). Traces of defects were still visible and appeared as small irregular bumps, especially in condyles with the implanted CS/HAp scaffolds.153

Figure 4.10 Representative images of twisted condyles comparisons between the implanted and physiological femoral condyle after eight weeks, showing that all groups experienced twisted condyle formation that might be caused by rotational instability from the defect induction and implantation. Annotations: Yellow broken lines=condyle axis; Red broken lines= femoral diaphysis axis.153

Figure 4.11 Representative coronal view images of the femoral condyle in CT scan per sample group after eight weeks of implantation. The condyle implanted with collagen sponge/rhBMP-2 is observed to reach the terminal healing process while traces of scaffolds were still present in CS/HAp scaffolds. However, CS/HAp/P28 gave better defect closure compared to CS/HAp and CS/HAp/rhBMP-2. (Annotation: Yellow circle= Implantation site).155

Figure 4.12 (a) Graph of mean volume fraction for each sample group in the entire defect and its margin after eight weeks (ROI 4 mm) (CS/HAp: $39 \pm 9.3\%$; CS/HAp/BMP-2: $45.7 \pm 6.6\%$; CS/HAp/P28: $34.1 \pm 6.1\%$; Collagen sponge: $26.2 \pm 2.3\%$; Collagen sponge/BMP-2: $23.2 \pm 3.3\%$). (b) Graph of mean bone mineral density per sample group in the entire defect and margin

after eight weeks (ROI 4 mm) (CS/HAp: $449.06 \pm 66.69 \text{ mg/cm}^3$; CS/HAp/BMP-2: $497.03 \pm 57.45 \text{ mg/cm}^3$; CS/HAp/P28: $438.37 \pm 38.94 \text{ mg/cm}^3$; Collagen sponge: $402.6 \pm 28.45 \text{ mg/cm}^3$; Collagen sponge/BMP-2: $360.83 \pm 22.93 \text{ mg/cm}^3$. Significant difference was achieved in CS/HAp/rhBMP-2 treatments compared to the others. However, the values might be due to traces of HAp, which is a type of ceramic. (* $p < 0.05$).155

Figure 4.13 Representative images of condyles per sample group on H&E stained slides (x1 magnification).....157

Figure 4.14 Representative images of the defect behaviour in scaffold and collagen sponge in H&E stained slides (x1.25 magnification). Annotations: A=CS/HAp; B=Collagen sponge; Yellow line=Defect boundaries; X=remaining material inside the defect;*= defect entry; arrow=bone tissue at the defect margin.158

Figure 4.15 Remaining materials in scaffold-implanted condyles in the defect (A) leaked outside the defect (B&C) on H&E stained slides (x10 magnification for A and x1.25 magnification for B and C. Annotations: A= CS/HAp/BMP-2; B= CS/HAp; C= CS/HAp/BMP-2; x=mineralised acellular fragments; *=homogenous to lamellar eosinophilic fragment; X=leakage of materials.158

Figure 4.16 Graph of mean score of biomaterial residues per sample group.159

Figure 4.17 Representative images of inflammatory process and fibroplasia inside the defects in scaffold conditions in HES stained slides (x20 magnification on the left panel and x40 magnification on the right panel). Annotations: *=homogenous to lamellar eosinophilic fragments; X=mineralised acellular fragments; Arrows=immune cells; Arrow heads=deposition of collagen fibres.160

Figure 4.18 Graph of mean score of inflammation (a) and fibroplasia (b) per sample group ...160

Figure 4.19 Representative images of necrotic areas in scaffold conditions on H&E stained slides (x5 magnification). Annotations: A=CS/HAp/rhBMP-2; B=CS/HAp *= homogenous to lamellar eosinophilic fragments; X= mineralised acellular fragments; •= necrotic areas161

Figure 4.20 Graph of mean score of necrosis per sample group.162

Figure 4.21 Representative images of newly formed bone at the defect margin (A&D) and inside the defect (B&C) on HES stained slides (x10 magnification for A-C, x2.5 magnification for D). Annotations: A&B= CS/HAp; C= CS/HAp/P28; D= Collagen sponge; Blue stars= woven bone; black star= small lamellae, disseminated not anastomosed; yellow star= mature lamellar bone; arrow heads= osteoblast lining.....163

Figure 4.22 Graph of mean score of new trabecular bone quality (a), trabecular bone quantity (b) and osteoblast activity (c) per sample group.....165

Figure 4.23 Overview of the implanted defects stained using Von Kossa staining (x1 magnification).....166

Figure 4.24 The representative images of mineralised tissue in the defect and margin in scaffold conditions (A&B) or sponge conditions (C&D). Von Kossa stained slides (x1.25 magnification on left panels, x5 magnification on right panels). Annotations: A= CS/HAp; B= CS/HAp/P28; C= Collagen sponge; D= Collagen sponge/rhBMP-2. Yellow arrows = bone tissue at defect margin; Red arrows = osteoid tissue; Yellow star = defect entrance; Black star = homogenous material fragments; Yellow cross = mineralised fragments.167

Figure 4.25 Graph of mean mineralised volume fraction (a), osteoid volume fraction (b) and mean osteoid volume to mineralised volume (c) per sample group.....168

Figure 4.26 Overview of the implanted defects stained using TRAP staining (x1 magnification).170

Figure 4.27 Representative images of TRAP-positive osteoclasts at defect level in scaffold conditions (A to D) and sponge conditions (E & F) on TRAP stained slides (x10 magnification). Annotations: A= CS/HAp; B&C= CS/HAp/P28; D= CS/HAp/rhBMP-2; E= Collagen sponge/rhBMP-2; F= Collagen sponge; Yellow arrow = TRAP positive osteoclasts; White cross

= mineralised fragments; Blue stars = homogenous material fragments; White star = woven bone; Black stars = lamellar bone.....	171
Figure 4.28 Graph of mean osteoclast surface to the bone surface per material.	172
Figure 4.29 Representative images of the fluorochromes-labelled condyles viewed under a fluorescent microscope (x1.25 magnification). Annotations: Blue arrowheads = double labelling; Yellow arrowheads = single calcein green labelling, Red arrowheads = single xylenol orange labelling.	173
Figure 4.30 Graph of mean mineral apposition rate (a), mean mineralised surface to bone surface (b) and mean bone formation rate to bone surface (c) per sample group.	174
Figure 4.31 An overview of the HE, VK and TRAP staining as well as the calcein and xylenol fluorescent labelling on the femoral condyles after eight weeks of healing. Observing the defect closure, the CS/HAp/P28 scaffolds presented better bone healing compared to CS/HAp and CS/HAp/rhBMP-2. (Annotation: Yellow circle= Implantation site).....	176
Figure 5.1 Summary of the second animal trial experiments.	184
Figure 5.2 a) The resazurin blue dye reduction to pink colour was observed in the tests after 24 hours of incubation. Left panel= Treatments in Staphylococcus aureus (S.aureus). Right panel= Treatments in Escherichia coli (E.coli). b) The antimicrobial activity of the scaffold treatments in both S.aureus and E.coli strains, showing the highest bacterial inhibition in the CS/FAp treatments.	186
Figure 5.3 Post-operative weight monitoring of nine implanted Sprague Dawley rats.	187
Figure 5.4 The macroscopic monitoring for the harvested condyles. Note: R1-R9 means Rat 1-9. R means right condyle and L means left condyle. The Kruskal-Wallis test showed $p > 0.05$ for the investigated criteria, possibly due to the small sample size used in this preliminary study.	187
Figure 5.5 Macroscopic observations of the harvested condyles implanted with the developed bone regeneration scaffolds.	190
Figure 5.6 HE stained slides of the implanted condyle defects. Yellow circles highlight the site of implanted defects. Blue arrows represent the newly formed bone structure where the composite was implanted. Red coloured A,B shows the two different densities of the compact bone tissue.	191
Figure 5.7 Fluorescent labelling imaging, observing the calcein green and xylenol orange labelling formed on the newly formed bone.	194

List of Tables

Table 2.1 Chitosan scaffold formulations with bioactive ceramics.....	71
Table 2.2 Scaffold compositions with various benzophenone concentrations.	73
Table 2.3 Scaffold compositions for the second in vivo implantation.	74
Table 2.4 The chemical components used in preparing the simulated body fluid.....	77
Table 2.5 The scaffold composition utilised for degradation test.	78
Table 2.6 Gradient-mobile phase for BMP-2 analysis with A: 0.1% trifluoroacetic acid (TFA) in 100% water (H ₂ O) and B: 0.1% TFA in 100% acetonitrile (ACN).	82
Table 2.7 Gradient-mobile phase for P28 analysis with A: 0.1% trifluoroacetic acid (TFA) in 100% water (H ₂ O) and B: 0.1% TFA in 100% acetonitrile (ACN).	83
Table 2.8 Scouting gradient to identify the retention time of the analyte.	83
Table 2.9 The routine culture vessels used throughout this work and their associated components.	88
Table 2.10 ρ NPP standard curve dilution preparation. Each dilution was enough to set up duplicate readings (2 x 120 μ l).	89
Table 2.11 Test samples used in the initial animal implantation procedures.	92
Table 2.12 List of the scaffold formulations used in the optimised animal trial.	92
Table 2.13 Modified histopathological evaluation scoring (Rudert et al., 2005).	98
Table 2.14 MicroCT measurement parameters.	98
Table 2.15 Evaluation criteria for Hematoxylin-Eosin slide, focusing on the material integration and the bone reconstruction.	100
Table 2.16 Parameters for histomorphometric calculations.	103
Table 3.1 Gel fraction values for scaffolds with varied ceramics and BP content in acidic conditions. The higher gel fraction values indicate a better linkage formed.....	113
Table 3.2 Swelling studies of chitosan scaffolds with different ceramics (HAp, TCP- α and FAp) and benzophenone contents (20, 10 and 5 μ l), comprising the EWC, WU, percentage of swelling and gel fraction in PBS.	114
Table 4.1 The table shows the system suitability test calculations to determine the best wavelength for the analysis of BMP-2.....	139
Table 4.2 The quantification of BMP-2 released samples at different time points by HPLC. ..	140

Abbreviations

% RSD	Percentage Relative Standard Deviation
μCT	Micro-Computed Tomography
AA	Acetic Acid
ALP	Alkaline Phosphatase
ARS	Alizarin Red Staining
BMD	Bone Mineralised Density
BMP-2	Bone Morphogenetic Protein-2
BP	Benzophenone
BS	Bone Surface
BTE	Bone Tissue Engineering
BV	Bone Volume
CG	Calcein Green
Conc	Concentration
CS	Chitosan
dLS	Double Labelling
DM	Differentiation Media
DMEM	Dulbecco's Modified Eagle Media
ECM	Extracellular Matrix
FAp	Fluorapatite
FBS	Foetal Bovine Serum
FDA	Food and Drug Administration
FTIR	Fourier-Transform Infrared Spectroscopy
GF	Growth Factor

GM	Growth Media
HAp	Hydroxyapatite
HE	Hematoxylin-Eosin
HPLC	High-Performance Liquid Chromatography
MAR	Mineral Apposition Rate
MdV	Mineralised Volume
MPa	Megapascal
MS	Mineralised Surface
OcS	Osteoclast Surface
OV	Osteoid Volume
P28	P28 Peptide
PBS	Phosphate Buffered Saline
PEG600DMA	Poly(Ethylene Glycol) (600) Dimethacrylate
rcf	Relative Centrifugal Field
ROI	Region of Interest
ROS	Reactive Oxygen Species
SBF	Simulated Body Fluid
SD	Sprague Dawley
SEM	Scanning Electron Microscopy
sLS	Single Labelling
Std	Standard
Std Dev	Standard Deviation
TCP- α	Tri Calcium Phosphate- α
TRAP	Tartrate-Resistant Alkaline Phosphatase

TV	Total Volume
UV	Ultraviolet
VK	Von Kossa
XO	Xylenol Orange
pNPP	para-nitrophenyl phosphate

Abstract

The Optimisation of Biomimetic Scaffold Fabrication for the Controlled Release of Osteogenic Factors for Bone Tissue Regeneration Farah Alwani Binti Azaman

Bone tissue defect is a rising global concern and is one of the leading causes of morbidity and disability in patients. Bone regeneration treatments that demonstrate all key characteristics for successful bone healing: osteoinductivity, osteoconductivity, osteogenicity and mechanical stability, are not yet available. Also, mitigation against bacterial infections, an increasing complication associated with impeded bone tissue repair, is urgently required. This report presents the development of a biomimetic antimicrobial scaffold that capable of inducing bone tissue-specific regeneration. The tunable biodegradability feature for a sustained bio-agent release was facilitated using a tailored crosslinking formulation that maintained the scaffolds' mechanical performance.

In this work, biodegradable chitosan (CS) scaffolds were prepared with combinations of bioactive ceramics, namely hydroxyapatite (HAp), tricalcium phosphate- α (TCP- α), and fluorapatite (FAp), crosslinked using a UV curing system. The efficacy of the crosslinking reaction was assessed using swelling and compression testing, SEM and FTIR analysis, and biodegradation studies in simulated body fluid. Consequently, various benzophenone concentrations were added to CS/HAp formulations to determine their effect on the degradation rate. The results presented indicate that incorporating bioceramics with a suitable photoinitiator concentration can tailor the biodegradability and load-bearing capacity of the scaffolds.

Subsequently, a combination of CS/HAp scaffold was UV crosslinked with either bone morphogenetic protein-2 (BMP-2) or its related peptide P28. Alkaline phosphatase (ALP) activity and alizarin red staining (ARS) were conducted to validate that the photo-crosslinking fabrication method did not interfere with the functionality of the growth factors. The C2C12 cultured with CS/HAp/BMP-2 and CS/HAp/P28 scaffolds showed an increased ALP activity compared to the negative control. The *in vivo* osteoconductive of the treatment was then investigated through a rat femoral condyle defect model. The *ex vivo* histological assessment showed a favourable bone regeneration efficacy of the CS/HAp/P28 compared to the CS/HAp/BMP-2 treatment, thus showing the use of P28 as a promising osteoinductive treatment.

Further work was carried out to improve the degradation rate *in vivo*, utilising CS, HAp and FAp at different ratios. Various P28 concentrations were incorporated into the CS/HAp/FAp scaffolds for implantation *in vivo*. H&E staining shows minimal scaffold traces in most of the defects induced after eight weeks, showing that the combination of HAp and FAp in the chitosan-based delivery system has enhanced the biodegradability of the scaffolds *in vivo*. Histological assessments indicated ongoing bone formation throughout the *in vivo* duration of the study. These results show the ability of this tailored formulation to improve the scaffold degradation for bone regeneration and presenting a cost-effective alternative to BMP-2.

In conclusion, the CS/ceramic scaffold with the presence of P28 peptide appears to have potential in bone defect healing due to its potent osteogenicity, biocompatibility and non-toxicity features.

Introduction

Introduction

1. Research Challenge

The critical-sized defect treatment is currently considered the focal attention for the clinicians and researchers, mainly in orthopaedic and plastic surgery. This is due to the risk of delayed unions or non-unions of the critical-sized bone fractures. Normal fractures typically heal within 6-8 weeks in healthy adults. However, in 5-13% of cases, the bone does not heal properly, while the defects occurring on the load-bearing bones such as the femur might lead to a delayed union or non-union (Lu et al., 2016; Nandra et al., 2016; J. D. Thomas & Kehoe, 2022). Although orthopaedic surgeons routinely use the traditional treatments known as autograft and allograft, these options are associated with several underlying issues such as the additional surgery requirement to harvest the autograft and also, the lack of supply as well as the high risk of disease transmission of the allograft (Bai et al., 2018; T.-M. De Witte et al., 2018; Lavanya et al., 2020; Y. Zhang et al., 2020). In addition, these existing treatments are also time-consuming and commonly result in reduced optimal efficacy (Jahan et al., 2020; Lu et al., 2016; W. Wang & Yeung, 2017) and thus leading to the explorations in the bone tissue engineering (BTE) field.

2. Research Gap

A growth factor (GF) delivery system incorporating bone morphogenetic protein-2 or BMP-2 is available commercially under the trade name INFUSE[®] with an absorbable collagen sponge carrier (Figure 1). INFUSE[®] is the market leader in bone grafts approved by Food and Drug Administration (FDA) to be used as a bone graft substitute in treating open tibial fractures, in line with another FDA-approved AUGMENT[®] by Wright Medical and i-Factor by Cerapedics (Arnold et al., 2021; Biswas et al., 2019; Govoni et al., 2021; James et al., 2016). However, this INFUSE[®] treatment is claimed to bring no significant non-union healing (Bullock et al., 2021), and this product is unfortunately associated with several documented complications, such as ectopic bone formation, which is the off-target reaction (Durham et al., 2018; James et al., 2016). INFUSE[®] has also faced an FDA warning following the severe dysphagia from the inflammation, as well as the increased loss of life (Govoni et al., 2021). Furthermore, a scaffold degradation profile that outlines the scaffold's capability to release the growth factors in the time frame was still not successfully altered. The high cost factor together with the initial burst

release of the growth factor are also remain as concerns to be addressed (Blackwood et al., 2012; Oliveira et al., 2021).

The aforementioned issues are indeed showing the gap for the development of a new highly potent BTE treatment that has the ability to control the release of the active agents and thereby avoiding complications, at a lower cost and in an off-the-shelf manner.

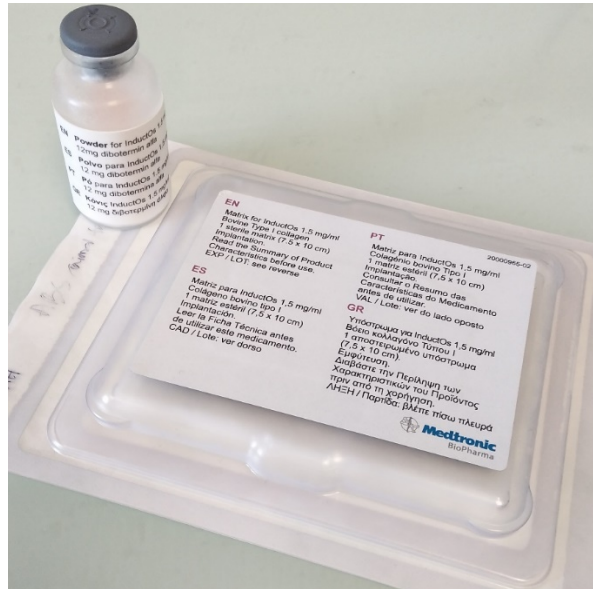


Figure 1 Medtronic Infuse™ rhBMP-2 and the collagen sponge.

3. Proposed Solution: Design of an Ideal Chitosan Composite Scaffold for Growth Factor Release

To date, substantial investigations have been carried out by tissue engineering researchers in collaboration with orthopaedics and plastic surgeons to come out with off-the-shelf treatment alternatives for treating bone defects (Henkel, 2017; S. Jiang et al., 2021; Kargozar et al., 2019). Researchers are investigating the use of available biomaterials to produce biodegradable bone substitutes that have been the current go-to alternatives since it is a critical factor in the success of new tissue turnover (Burke et al., 2019). This biodegradable biomaterial comprises synthetic biodegradable polymers such as poly lactic-co-glycolic acid (PLGA) and naturally occurring polymers such as chitosan, silk fibroin and collagen, as well as inorganics such as hydroxyapatite, tri-calcium phosphate and antimicrobial fluorapatite (Burke et al., 2019; L. Chen et al., 2020).

Chitosan has been utilised in numerous research articles as a bone substitute for materials due to its biocompatible and biodegradable properties, the ability to promote cell attachment and proliferation, and it has a lower cost compared to the other materials (Brun

et al., 2021; Maji et al., 2016; Sukpaita et al., 2019). It has also been approved by the Food and Drug Administration (FDA) to be used for biomedical applications (Chang et al., 2016). Bone regeneration research nowadays has directed a significant application of chitosan composite in the formulation since it gives minimal foreign-body inflammatory responses, has intrinsic antibacterial feature, and can also be constructed into various geometries and forms for tuning the porosity, osteoinduction and osteoconduction properties (Y. Liao et al., 2020; Sanchez-Salvador et al., 2021; Venkatesan & Kim, 2010). Chitosan can also mimic the extracellular matrix (ECM) due to its similar structure to proteoglycans, which has led researchers to utilise it for tissue engineering (Barroso et al., 2022; F. Zhang & King, 2020). However, owing to its low solubility in natural pH condition, chitosan is often combined with other biomaterials such as hydroxyapatite to improve its solubility as well as enhance the mechanical properties and provide bioactive features to the scaffold (B. Li, Wang, et al., 2019; Maachou et al., 2008).

The nature of biodegradability and biocompatibility features has made chitosan and hydroxyapatite the go-to choices among researchers to be used in BTE research. For instance, Devine *et al.* (2017) have incorporated various hydroxyapatite ratios in chitosan to investigate the protein release rate in scaffolds fabricated for bone regeneration. The structure of the chitosan/hydroxyapatite (CS/HAp) scaffold was observed through a scanning electron microscope (SEM), revealing the microscaled particles of the scaffold (Figure 2). However, despite their known osteoconductive properties, these two materials are incapable of causing the osteodifferentiation of the stem cells into osteoblasts without growth factors association, thus expanding the studies in the incorporation of osteoinductive agents in the scaffolds (Reves et al., 2011; Sukpaita et al., 2019).

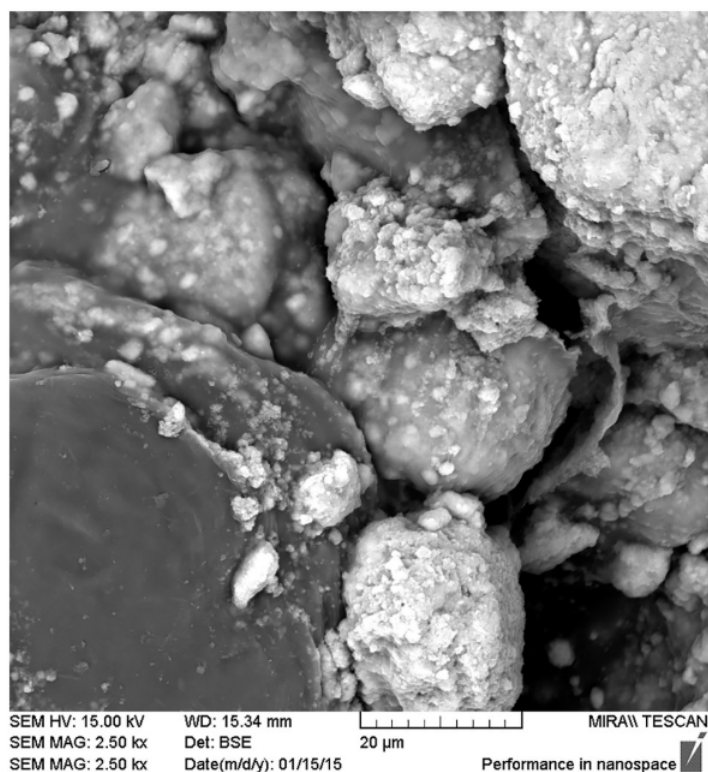


Figure 2 Micro-scaled agglomerates of hydroxyapatite particles embedded between chitosan matrix (Devine et al., 2017).

Furthermore, the diamond concept of the fracture healing treatments has outlined four demands in bone healing treatments: potential osteogenic cells, osteoconductive extracellular matrix, osteoinductive growth factors and a mechanically supportive environment (Brydone et al., 2010; Foster et al., 2021; T. Kim et al., 2020; Wildemann et al., 2021). These features will fulfil the main objective of designing a bone scaffold that mimics the extracellular matrix (ECM) and provides adequate mechanical support and other properties, including biocompatible, biodegradable and porous structure (Figure 3). In addition, based on the fourth requisite for bone scaffold composites, the formulations should be altered to make them mechanically stable and have the full weight-bearing feature to be an ideal scaffold for the bone regeneration process. Mechanical stability is essential to avoid the complications like stress-shielding, implant-related diseases such as osteopenia and subsequent re-fracture after implanting the bone scaffold (T.-M. De Witte et al., 2018; Glatt et al., 2021; Haubruck et al., 2016; Prasad & Wong, 2018).

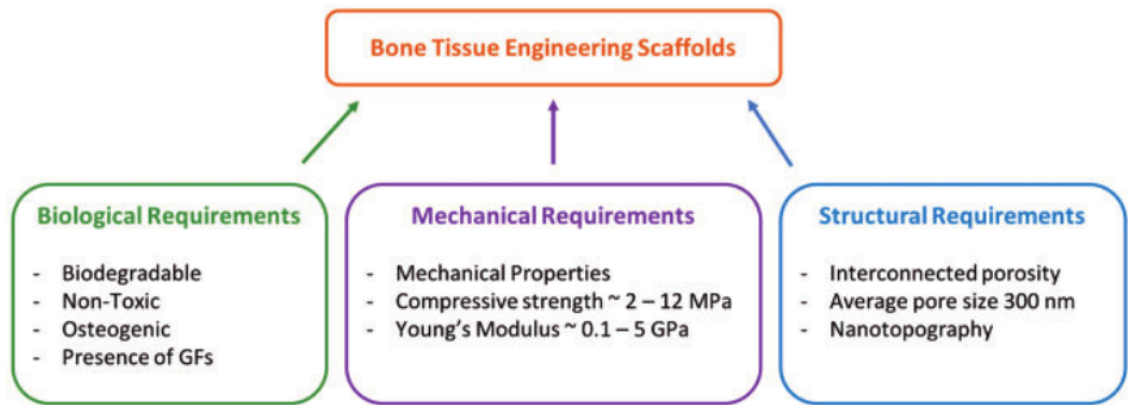


Figure 3 Main requirements of bone scaffolds. De Witte et al. (2018)

While the human bones recorded the compressive strength of 100-500 MPa, the designed scaffold's strength should be in the range of cancellous bone, which is generally about 0.1-16 MPa, (Lan Levengood & Zhang, 2015; Roohani-Esfahani et al., 2016; Ryan & Yin, 2022; Y. Zhang et al., 2020). In addition, the tensile strength of the scaffold should be tailored to achieve between 1-5 MPa to match the human cancellous bone (Nga et al., 2020; Osuchukwu et al., 2021). It is challenging to adjust the mechanical properties to be suitable to the porosity of the scaffold, which will aid in cell proliferation and provide a pathway for excellent nutrient diffusions during the tissue culture since the high porosity of the bone scaffold will consequently reduce the mechanical strength (Abbasi et al., 2020; Jiao et al., 2022; Polo-Corrales, L. ; Latorre-Esteves, M. ; Ramirez-Vick, 2013). Therefore, considerable research has been carried out and is in progress to optimise the bone scaffold formulations and fabrication methods in controlling the mechanical properties without compromising the porosity of the composite. This work will be manoeuvred towards filling the gaps in relating the scaffold structure and material properties to the load-bearing capacity, as suggested previously, to achieve the native mechanical properties (Hernandez et al., 2016; Homayoni et al., 2009; Venkatesan & Kim, 2010; F. Zhang & King, 2020).

Consequently, a promising acellular strategy centres on developing scaffolds incorporating osteogenic factors is employed. This plan combines biology and engineering principles to develop viable substitutes to restore and maintain the function of human bone tissue. Therefore, this project aims to enhance the mechanical and biodegradable properties of bone scaffolds by modifying the crosslinking reaction to avoid the burst release of the growth factors. These objectives can be achieved by fabricating a biodegradable scaffold that will release growth factors while degrading and

then be secreted from the body naturally after it completes its function. Therefore, an ideal scaffold should be able to degrade in a gradational way for an expected period to be replaced by a newly formed bone tissue from the bonded cells, known as the osteotransduction process (Alves et al., 2020). This degradation will result in the breakdown of the scaffold and the resorption of the osteogenic factor such as bone morphogenetic protein-2 (BMP-2) incorporated in the scaffold to the targeted location.

In addition, many studies have been carried out on developing biomaterials that possess antibacterial properties for various applications, including bone regeneration research. It has been reported that the antimicrobial properties present in several chitosan derivatives with the application and the mode of performance regarding the antibacterial feature caught the attention of researchers as a go-to biomaterial for tissue engineering (Fourie et al., 2022; Mututuvari et al., 2013; Tsiklin et al., 2022). Consequently, antimicrobial fluorapatite was also implemented in our scaffold formulation to improve infection-related concerns highlighted by industry and clinicians during dissemination, including infections and inflammation following implantation in a patient's body. Indeed, the antimicrobial feature is crucial in preventing dangerous bacterial growth subsequent scaffold implantation, thus preventing diseases, extending the shelf-life of contents, reducing odours, and, most importantly, preventing moulds (Kus-Liskiewicz et al., 2019; Muñoz-Bonilla & Fernández-García, 2012; Seyedmajidi & Seyedmajidi, 2022; M. V. Thomas & Puleo, 2011).

Furthermore, other than using a clinically relevant bone morphogenetic protein-2 as the growth factor for osteogenesis, the research has examined P28 peptides derived from the knuckle epitope of BMP-2. This peptide is postulated to present a comparable osteoinductive performance to its protein of origin since it was previously found to be a potential substitute for the full-length rhBMP-2 in inducing new bone-cell formation due to its high performance with greater control over cellular interactions and a cost-effective alternative to BMP-2 (Bain et al., 2015; Bullock et al., 2021).

4. Research Outcomes

Book chapter

A book chapter entitled “*Orthopaedic 3D Printing in Orthopaedic Medicine*” was written in collaboration with the supervisors and several other researchers in PRISM TUS. This chapter was published as Chapter 6 in a book entitled *Polymer-Based Additive Manufacturing* by Springer-Nature. ISBN 978-3-030-24531.

Chapter 6 Orthopaedic 3D Printing in Orthopaedic Medicine



Margaret E. Brennan Fournet, Farah Alwani Azaman, Suzan Gunbay,
Yuan Yuan Chen, and Declan M. Devine

Abstract Orthopaedic surgeries are commonly extremely challenging, and innovations are required to overcome a series of recognised difficulties and improve patient outcomes. Complications, in particular, the high occurrence of infections, often leads to prolonged patient pain, implant failure and loss of functions. 3D printing technology provides an ideal opportunity to integrate cutting edge technologies to address the major identified clinical problems directly. 3D-printed orthopaedic implants, designed to fit anatomical defects or malformations precisely, can resolve the current limited availability of appropriate well-fitting patient-specific implant parts. Integrated technologies can be included to target postoperative infections, which is an increasingly important concern, particularly considering population demographic and health profile changes. Improved osteointegration technologies can be incorporated to overcome inadequate tissue adherence to implants and bone on-growth. With increasing numbers of patients now outliving their implants, loosening difficulties and premature implant failure rates using conventional technologies are projected to increase dramatically. With these projections, the emergence of 3D printing is a welcome reprieve for patients and surgeons alike. 3D printing technologies hold the promise of significantly advancing current orthopaedic implant capabilities, delivering bespoke customised site-specific implants, which resolve fundamental clinical problems and achieve better results for patients.

This chapter explores the unprecedented solution offered by 3D-printed technologies for orthopaedic surgeries. The use of 3D printing for orthopaedic applications and advances, which may lead to future large-scale 3D-printed polymeric orthopaedic implant production, is discussed.

Keywords PEEK · Patient-specific implants · 3D printing · Surgical jigs

Margaret E. Brennan Fournet and Farah Alwani Azaman contributed equally to this work.

M. E. Brennan Fournet (✉) · F. A. Azaman · S. Gunbay · Y. Y. Chen · D. M. Devine
Athlone Institute of Technology, Co. Westmeath, Ireland
e-mail: mfournet@ait.ie

© Springer Nature Switzerland AG 2019
D. M. Devine (ed.), *Polymer-Based Additive Manufacturing*,
https://doi.org/10.1007/978-3-030-24532-0_6

121

i) The first part of this research in terms of the development of chitosan-based bone regeneration scaffold was published in Gels MDPI, entitled “*Bioresorbable Chitosan-Based Bone Regeneration Scaffold Using Various Bioceramics and the Alteration of Photoinitiator Concentration in an Extended UV Photocrosslinking Reaction*”. This article was published on 28th October 2022. DOI: <https://doi.org/10.3390/gels8110696>



Article

Bioresorbable Chitosan-Based Bone Regeneration Scaffold Using Various Bioceramics and the Alteration of Photoinitiator Concentration in an Extended UV Photocrosslinking Reaction

Farah Alwani Azaman ¹, Keran Zhou ¹, María del Mar Blanes-Martínez ^{1,2}, Margaret Brennan Fournet ¹ and Declan M. Devine ^{1,*}

¹ PRISM Research Institute, Technological University of the Shannon, Midlands Midwest, Athlone Main Campus, N37 HD68 Athlone, Ireland

² Department of Chemical and Nuclear Engineering, Universitat Politècnica de València, 46022 Valencia, Spain

* Correspondence: ddevine@ait.ie

Abstract: Bone tissue engineering (BTE) is an ongoing field of research based on clinical needs to treat delayed and non-union long bone fractures. An ideal tissue engineering scaffold should have a biodegradability property matching the rate of new bone turnover, be non-toxic, have good mechanical properties, and mimic the natural extracellular matrix to induce bone regeneration. In this study, biodegradable chitosan (CS) scaffolds were prepared with combinations of bioactive ceramics, namely hydroxyapatite (HAp), tricalcium phosphate- α (TCP- α), and fluorapatite (FAP), with a fixed concentration of benzophenone photoinitiator (50 μ L of 0.1% (*w/v*)) and crosslinked using a UV curing system. The efficacy of the one-step crosslinking reaction was assessed using swelling and compression testing, SEM and FTIR analysis, and biodegradation studies in simulated body fluid. Results indicate that the scaffolds had comparable mechanical properties, which were: 13.69 ± 1.06 (CS/HAp), 12.82 ± 4.10 (CS/TCP- α), 13.87 ± 2.9 (CS/HAp/TCP- α), and 15.55 ± 0.56 (CS/FAP). Consequently, various benzophenone concentrations were added to CS/HAp formulations to determine their effect on the degradation rate. Based on the mechanical properties and degradation profile of CS/HAp, it was found that 5 μ L of 0.1% (*w/v*) benzophenone resulted in the highest degradation rate at eight weeks (54.48% degraded), while maintaining compressive strength between $(4.04 \pm 1.49$ to 10.17 ± 4.78 MPa) during degradation testing. These results indicate that incorporating bioceramics with a suitable photoinitiator concentration can tailor the biodegradability and load-bearing capacity of the scaffolds.

Keywords: chitosan; hydroxyapatite; biodegradation; photoinitiator; photopolymerisation; crosslinking



Citation: Azaman, F.A.; Zhou, K.; Blanes-Martínez, M.d.M.; Brennan Fournet, M.; Devine, D.M. Bioresorbable Chitosan-Based Bone Regeneration Scaffold Using Various Bioceramics and the Alteration of Photoinitiator Concentration in an Extended UV Photocrosslinking Reaction. *Gels* **2022**, *8*, 696. <https://doi.org/10.3390/gels8110696>

Academic Editors: Chengtao Yu, Jian Hu, Yong Zheng and Xiaohua Chang

ii) The second part of this work, discussing the *in vitro* and *in vivo* osteogenic assessments of the BMP-2 and P28 incorporated CS/HAp scaffolds was published in Micro MDPI, entitled “Chitosan/Hydroxyapatite Scaffolds with P28 as a Promising Osteoinductive Scaffold for Bone Healing Applications”. This article was published on 31st January 2023.

DOI: <https://doi.org/10.3390/micro3010010>



Article

Chitosan/Hydroxyapatite Scaffolds with P28 as a Promising Osteoinductive Scaffold for Bone Healing Applications

Farah Alwani Azaman ¹, Florence Daubin  ², Am lie Lebatard ², Margaret E. Brennan Fournet ¹ and Declan M. Devine ^{1,*}

¹ PRISM Research Institute, Technological University of the Shannon, Midlands Midwest, Athlone Main Campus, N37 HD68 Athlone, Ireland

² Atlantic Bone Screen, 44800 Saint-Herblain, France

* Correspondence: ddevine@ait.ie

Abstract: Despite bone’s inherent ability to heal, large bone defects remain a major clinical concern. This study proposes an off-the-shelf treatment combining chitosan/hydroxyapatite (CS/HAp) scaffolds, covalently linked with either bone morphogenetic protein-2 (BMP-2) or its related peptide P28 via a UV crosslinking process. Although covalently binding the growth factors was reported as a great alternative to the conventionally physical adsorption and encapsulation methods, this method presents the risk of altering the molecular activity and interaction of the growth factors. Therefore, alkaline phosphatase (ALP) activity and alizarin red staining (ARS) with a quantitative cetylpyridinium chloride (CPC) assay were conducted to validate that our photo-crosslinking fabrication method did not interfere with the functionality of the growth factors. The ALP activity of C2C12 with 100 µg/mL P28 was found to be comparable to 0.5 µg/mL BMP-2 after two weeks, where 0.001 U/mL was recorded for both treatments. The C2C12 cultured with CS/HAp/BMP-2 and CS/HAp/P28 scaffolds also showed an increased ALP activity compared to the negative control. ARS-CPC assay presented the highest optical density in 0.3 µg/mL BMP-2 and 50 µg/mL P28, while the highest intensity of ARS was observed in C2C12 cultured with CS/HAp/BMP-2 and CS/HAp/P28 scaffolds compared to the negative controls. The osteoconductive capability of this delivery system was then investigated through a rat femoral condyle defect model, where the new bone mineral density and the bone volume increased for all CS/HAp scaffolds compared to the collagen sponge control treatment. The histological assessment showed a favourable bone regeneration efficacy of the CS/HAp/P28 compared to the CS/HAp/BMP-2 treatment, thus showing the use of CS/HAp scaffolds with P28 as a promising osteoinductive scaffold for bone healing applications.

Keywords: bone healing; scaffold; protein; peptide; osteoinduction; calcification; femoral condyle defects model



Citation: Azaman, F.A.; Daubin , F.; Lebatard, A.; Brennan Fournet, M.E.; Devine, D.M. Chitosan/Hydroxyapatite Scaffolds with P28 as a Promising Osteoinductive Scaffold for Bone Healing Applications. *Micro* **2023**, *3*, 118–142. <https://doi.org/10.3390/micro3010010>

iii) The third part of this work, discussing the animal trial applying the optimised scaffold formulations in altering the *in vivo* biodegradation was submitted to Pharmaceuticals MDPI, entitled “Enhancement of Scaffold *in Vivo* Biodegradability for Bone Regeneration using P28 peptide Formulations”. This article was published on the 13th June 2023. DOI: <https://doi.org/10.3390/ph16060876>



Article

Enhancement of Scaffold In Vivo Biodegradability for Bone Regeneration Using P28 Peptide Formulations

Farah Alwani Azaman ^{1,2}, Margaret E. Brennan Fournet ², Suzina Sheikh Ab Hamid ², Muhamad Syahrul Fitri Zawawi ², Valdemiro Amaro da Silva Junior ³ and Declan M. Devine ^{1,*}

¹ PRISM Research Institute, Technological University of the Shannon (TUS), N37 HD68 Athlone, Ireland; f.alwani@research.ait.ie

² Pusat Pengajian Sains Perubatan, Kampus Kesihatan, Universiti Sains Malaysia (USM), Kota Bharu 16150, Malaysia

³ Departamento de Medicina Veterinária, Universidade Federal Rural de Pernambuco, Recife 52171-900, Brazil

* Correspondence: ddevine@ait.ie

Abstract: The field of bone tissue engineering has shown a great variety of bone graft substitute materials under development to date, with the aim to reconstruct new bone tissue while maintaining characteristics close to the native bone. Currently, insufficient scaffold degradation remains the critical limitation for the success of tailoring the bone formation turnover rate. This study examines novel scaffold formulations to improve the degradation rate *in vivo*, utilising chitosan (CS), hydroxyapatite (HAp) and fluorapatite (FAp) at different ratios. Previously, the P28 peptide was reported to present similar, if not better performance in new bone production to its native protein, bone morphogenetic protein-2 (BMP-2), in promoting osteogenesis *in vivo*. Therefore, various P28 concentrations were incorporated into the CS/HAp/FAp scaffolds for implantation *in vivo*. H&E staining shows minimal scaffold traces in most of the defects induced after eight weeks, showing the enhanced biodegradability of the scaffolds *in vivo*. The HE stain highlighted the thickened periosteum indicating a new bone formation in the scaffolds, where CS/HAp/FAp/P28 75 µg and CS/HAp/FAp/P28 150 µg showed the cortical and trabecular thickening. CS/HAp/FAp 1:1 P28 150 µg scaffolds showed a higher intensity of calcein green label with the absence of xylenol orange label, which indicates that mineralisation and remodelling was not ongoing four days prior to sacrifice. Conversely, double labelling was observed in the CS/HAp/FAp 1:1 P28 25 µg and CS/HAp/FAp/P28 75 µg, which indicates continued mineralisation at days ten and four prior to sacrifice. Based on the HE and fluorochrome label, CS/HAp/FAp 1:1 with P28 peptides presented a consistent positive osteoinduction following the implantation in the femoral condyle defects. These results show the ability of this tailored formulation to improve the scaffold degradation for bone regeneration and present a cost-effective alternative to BMP-2.



Citation: Azaman, F.A.; Brennan Fournet, M.E.; Sheikh Ab Hamid, S.; Zawawi, M.S.F.; da Silva Junior, V.A.; Devine, D.M. Enhancement of Scaffold In Vivo Biodegradability for Bone Regeneration Using P28 Peptide Formulations. *Pharmaceuticals* **2023**, *16*, 876. <https://doi.org/10.3390/ph16060876>

Academic Editors: Yayoi Kawano and Takehisa Hanawa

Keywords: bone tissue engineering; scaffold degradation; chitosan; osteogenesis; bone regeneration

Collaborative publications

i) A collaborative research applying the developed CS/HAp scaffold to serve as the biomimetic extracellular matrix in a gold-edge-coated triangular silver nanoparticles research was published in *Nanomaterials* MDPI, entitled “Monitoring Extracellular Matrix Protein Conformations in the Presence of Biomimetic Bone-Regeneration Scaffolds Using Functionalized Gold-Edge-Coated Triangular Silver Nanoparticles”. This article was published on 23rd December 2022. DOI: <https://doi.org/10.3390/nano13010057>



nanomaterials



Article

Monitoring In Vitro Extracellular Matrix Protein Conformations in the Presence of Biomimetic Bone-Regeneration Scaffolds Using Functionalized Gold-Edge-Coated Triangular Silver Nanoparticles

Laura G. Rodriguez Barroso ¹, Farah Alwani Azaman ¹, Robert Pogue ^{1,2}, Declan Devine ¹ and Margaret Brennan Fournet ^{1,*}

¹ Technological University of the Shannon: Midlands Midwest, Dublin Rd., N37 HD68 Athlone, Co. Westmeath, Ireland

² Universidade Católica de Brasília, Campus Asa Norte. SGAN Módulo B 916 Avenida W5—Asa Norte, Brasília 70790-160-DF, Brazil

* Correspondence: mfournet@ait.ie

Abstract: In the cellular environment, high noise levels, such as fluctuations in biochemical reactions, protein variability, molecular diffusion, cell-to-cell contact, and pH, can both mediate and interfere with cellular functions. In this work, gold edge-coated triangular silver nanoparticles (AuTSNP) were validated as a promising new tool to indicate protein conformational transitions in cultured cells and to monitor essential protein activity in the presence of an optimized bone biomimetic chitosan-based scaffold whose rational design mimics the ECM as a natural scaffold. A chitosan-based scaffold formulation with hydroxyapatite (CS/HAp) was selected due to its promising features for orthopedic applications, including combined high mechanical strength biocompatibility and biodegradability. Functionalized AuTSNP-based tests with the model ECM protein, fibronectin (Fn), illustrate that the protein interactions can be clearly sensed over time through the local surface plasmon resonance (LSPR) technique. This demonstrates that AuTSNP are a powerful tool to detect protein conformational activity in the presence of biomimetic bone tissue regeneration scaffolds within a cellular environment that comprises a diversity of molecular cues.

Keywords: triangular silver nanoparticles; fibronectin; LSPR; extracellular matrix; regeneration scaffold






Citation: Rodriguez Barroso, L.G.; Azaman, F.A.; Pogue, R.; Devine, D.; Fournet, M.B. Monitoring In Vitro Extracellular Matrix Protein Conformations in the Presence of Biomimetic Bone-Regeneration Scaffolds Using Functionalized Gold-Edge-Coated Triangular Silver Nanoparticles. *Nanomaterials* **2023**, *13*,

ii) Another collaborative work discussing the alteration of CS/ceramics composition in the bone tissue regeneration application was published in Micromol MDPI, entitled “Bone Tissue Engineering Scaffold Optimisation through Modification of Chitosan/Ceramic Composition”. This article was published on the 1st June 2023. DOI: <https://doi.org/10.3390/macromol3020021>



Article

Bone Tissue Engineering Scaffold Optimisation through Modification of Chitosan/Ceramic Composition

Keran Zhou , Farah Alwani Azaman , Zhi Cao, Margaret Brennan Fournet and Declan M. Devine * 

PRISM Research Institute, Technological University of the Shannon, Midlands Midwest, Athlone Main Campus, N37 HD68 Athlone, Ireland; a00258808@student.ait.ie (K.Z.)

* Correspondence: ddevine@tus.ie

Abstract: A large bone defect is defined as a defect that exceeds the regenerative capacity of the bone. Nowadays, autologous bone grafting is still the gold standard treatment. In this study, a hybrid bone tissue engineering scaffold (BTE) was designed with biocompatibility, biodegradability and adequate mechanical strength as the primary objectives. Chitosan (CS) is a biocompatible and biodegradable polymer that can be used in a wide range of applications in bone tissue engineering. Hydroxyapatite (HAp) and fluorapatite (FAP) have the potential to improve the mechanical properties of CS. In the present work, different volumes of acetic acid (AA) and different ratios of HAp and FAP scaffolds were prepared and UV cross-linked to form a 3D structure. The properties of the scaffolds were characterised by scanning electron microscopy (SEM), Fourier transform infrared (FTIR) spectroscopy, swelling studies and compression testing. The cytotoxicity result was obtained by the MTT assay. The degradation rate was tested by weight loss after the scaffold was immersed in SBF. The results showed that a crosslinked structure was formed and that bonding occurred between different materials within the scaffold. Additionally, the scaffolds not only provided sufficient mechanical strength but were also cytocompatible, depending on their composition. The scaffolds were degraded gradually within a 6-to-8-week testing period, which closely matches bone regeneration rates, indicating their potential in the BTE field.



Citation: Zhou, K.; Azaman, F.A.; Cao, Z.; Brennan Fournet, M.; Devine,

Keywords: bone tissue engineering; ceramic; chitosan; scaffold

Conference paper and posters

i) A collaborative conference paper was written entitled “*Monitoring of Extracellular Matrix Protein Conformations in the Presence of Biomimetic Bone Tissue Regeneration Scaffolds*” for the 6th International Conference on Materials Science and Smart Materials on July 24-26, 2019 in Birmingham, United Kingdom. This paper was published on 30th September 2020. DOI: <https://doi.org/10.4028/www.scientific.net/KEM.865.43>

Key Engineering Materials
ISSN: 1662-9795, Vol. 865, pp 43-47
doi:10.4028/www.scientific.net/KEM.865.43
© 2020 Trans Tech Publications Ltd, Switzerland

Submitted: 2019-06-10
Revised: 2019-11-13
Accepted: 2020-01-12
Online: 2020-09-30

Monitoring of Extracellular Matrix Protein Conformations in the Presence of Biomimetic Bone Tissue Regeneration Scaffolds

Rodriguez Barroso, L.^{1a}, Lanzagorta Garcia, E.^{1b}, Azaman, F.A.^{1c}, Devine, D.M.^{1d}, Lynch M.^{1e}, Huerta, M.^{2f}, Fournet, M.B.^{1g}

¹Materials Research Institute, Athlone Institute of Technology, Athlone, Ireland

²Department of Science and Technology, Linköping University, Norrköping, Sweden

^al.rodriguez@research.ait.ie, ^be.lgarcia@research.ait.ie, ^cf.alwani@research.ait.ie,

^dddevine@ait.ie, ^emarklynch@ait.ie, ^fmiriam.huerta@liu.se, ^gmfournet@ait.ie

Keywords: Tissue scaffolds, extracellular matrix, fibronectin, triangular silver nanoplates, local surface plasmon resonance.

Abstract. Tissue scaffolds can be designed to mimic the native extracellular matrix (ECM), making them attractive for the development for a range of regenerative medicine applications. The macromolecules present in the ECM are critical for the provision of structural support to surrounding cells and signalling cues for the modulation of diverse processes including cell migration, proliferation and healing activation. Here, conformational and transitional behaviour of the ubiquitous ECM protein, fibronectin (Fn), in the presence of bone tissue regeneration scaffolds and living C2C12 myoblast cells is reported. Spectral monitoring of Fn functionalised high plasmonic resonance responsive gold-edge-coated triangular silver nanoplates (AuTSNP) is used to distinguish between compact and extended fibronectin conformations. Large spectral red shifts of ~20 to ~57 nm indicate Fn unfolding and fibril formation on incubation with C2C12 cells. The label-free nature, excellent sensitivity and straightforward application of the AuTSNP within cellular environments presents them as a powerful new tool to signature protein conformational activity in living cells and monitor essential protein activity for the assisted development of improved tissue scaffolds promoting enhanced tissue repair.

Introduction

Chitosan is a promising crustacean derivative biomaterial prepared by the deacetylation of chitin and is abundant in nature. Chitosan has excellent biodegradability, biomimetic and biocompatibility properties for tissue engineering applications and the simulation of self-healing matrices and mimetic tissue repair scaffolds [1]. Here chitosan (CS) is combined with the bone ceramic hydroxyapatite (HAp) and photocrosslinked to form an osteoconductive and osteointegrative CS-HAp bone tissue regeneration scaffold as previously reported [2].

Tissue scaffolds mimic the native extracellular matrix (ECM), this critical component controls fundamental cellular processes and provides structural support to surrounding cells. The three-dimensional structure of the macromolecules present in the ECM is essential for the delivery of signalling cues for the modulation of diverse cell behaviours including cell-cell communication and promoting tissue repair [3].

ECM proteins are implicated in cancer and have active participation in tumor progression [3]. In particular, fibronectin (Fn), a critical ECM protein whose functions are governed by its conformational activity, is receiving increasing attention due to its participation in various phases of tumor proliferation. Fn can exhibit a compact soluble formation while circulating within the bloodstream [3]. Under conditions where Fn expression is altered, it can

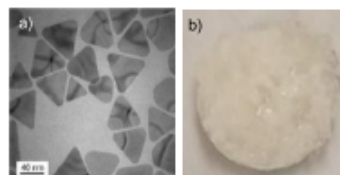


Fig. 1. (a) Transmission electron microscopy (TEM) of AuTSNP, b) CS-HAp bone tissue regeneration scaffold sample,

ii) In the first year of this project, a poster presentation was attended at World Congress on Advanced Biomaterials and Tissue Engineering on October 17-18, 2018, in Rome, Italy. The same poster entitled “Development of Biomimetic Scaffold for Controlled Release of Osteogenic Factors” was presented again in AIT Research Seminar on May 2, 2019, with a 1-minute pitch, where this poster was then recorded in AIT Repository.

THE TIMES
THE SUNDAY TIMES
GOOD UNIVERSITY GUIDE 2018
INSTITUTE OF TECHNOLOGY OF THE YEAR

AIT Research

DEVELOPMENT OF BIOMIMETIC SCAFFOLDS FOR CONTROLLED RELEASE OF BIOACTIVE AGENT

Farah Alwani Azaman^a, Margaret E. Brennan Fournet^a, Maria del Mar Blanes Martinez^a, Declan M. Devine^a
^aMaterials Research Institute, Athlone Institute of Technology, Athlone, Ireland

OBJECTIVES

Optimizing the bone scaffold fabrication to enhance mechanical and biodegradable properties.

i) Chitosan scaffold incorporating bone based bioactive ceramics : Hydroxyapatite, Tricalcium phosphate

ii) Extended crosslinking via chemical protocol modifications

METHODS

RESULTS

Compression test

It was expected that the modification of crosslinking will increase the Young's modulus of the scaffolds compared to the original method due to the higher strength of the linkage formed.

Biodegradation test

After 8 weeks in simulated body fluid, the samples showed significant biodegradation as indicated by the slope on the plot.

Crosslinking test

It showed that the chitosan composite scaffolds were well-crosslinked when they did not dissolve after being submerged in acetic acid solution for 24 hours.

CONCLUSIONS

- * Chitosan with hydroxyapatite composite has better degradation ratio compared to the other combination of bioceramics.
- * The mechanical properties were enhanced with the modification of crosslinking stage in the scaffold fabrication.

REFERENCE

Devine, D.M., Hctor, E., Hayes, J.S., Sheehan, E. and Evans C.H. Material Science & Engineering C. (2017), <https://doi.org/10.1016/j.msec.2017.11.001>

CONTACT INFORMATION

Dr. Declan Devine, ddevine@ait.ie Materials Research Institute, Athlone Institute and Technology, Dublin Rd., Athlone, Co. Westmeath, Ireland
Farah Alwani Azaman, falwani@research.ait.ie, Materials Research Institute, Athlone Institute of Technology, Dublin Rd., Athlone, Co. Westmeath, Ireland

ACKNOWLEDGEMENTS

Funding for this project was provided by Government of Ireland scholarship and Enterprise Ireland.

iii) On January 19, 2019, Bioengineering in Ireland 2019 conference (BinI'19) was joined for an oral presentation entitled “*Optimization of Biomimetic Scaffold Fabrication for Controlled Release of Osteogenic Factors in Bone Tissue Regeneration*” in Limerick, Ireland. This presentation covered the modification of the scaffold fabrication method and the effect on degradation profile and strength.

Early Stage Researcher (PhD Year 1)	<input type="checkbox"/>	Post-Doctoral Researcher/Senior Researcher/PI	<input type="checkbox"/>
Entry for the Engineers Ireland Biomedical Research Medal	<input type="checkbox"/>	Corresponding author has completed PhD and would like to review BinI abstract submissions	<input type="checkbox"/>

Please place an X in any appropriate categories

OPTIMIZATION OF BIOMIMETIC SCAFFOLD FABRICATION FOR THE CONTROLLED RELEASE OF OSTEOGENIC FACTORS

Azaman, F.A.¹, Fournet, M.B.¹, Devine, D.¹

¹ Materials Research Institute, Athlone Institute of Technology
email: ddevine@ait.ie

INTRODUCTION

Non-union fractures, the incomplete healing when bone fragment cortices fail to reconnect, are commonly associated with long bone fractures and can result in persistent pain, swelling and instability (Pountos et al., 2016).

In the world of bone tissue engineering, significant research has been directed towards the creation of novel porous 3D bone scaffolds to overcome the limitations of traditional bone grafting techniques (Turnbull, 2018).

The bone scaffolds are designed to be biocompatible, have high porosity, interconnected pores and adjustable degradation, Polo-Corrales et al., (2014), enabling them to mimic the natural bone regeneration environment. Here we present chitosan and hydroxyapatite composite 3D bone scaffolds with excellent biocompatibility, antimicrobial properties and biodegradability for the delivery of osteogenic factors.

MATERIALS AND METHODS

High MW chitosan and hydroxyapatite powder were obtained from Sigma Aldrich, USA.

Chitosan powder was dissolved with acetic acid before neutralized with sodium bicarbonate solution. The scaffolds were then crosslinked in the presence of bioceramics.

The mechanical properties, linkage formed and biodegradation profile of the scaffolds were assessed for 3 batches as follows:

- 1) Varying the bioceramics composition.
- 2) Varying the crosslinking reaction.
- 3) Adding the antimicrobial properties.

RESULTS

The mechanical properties of each batches were augmented through modification of the crosslinking process. Tailoring of the bone scaffold composition has been demonstrated to enable tuning of the degradation profile.

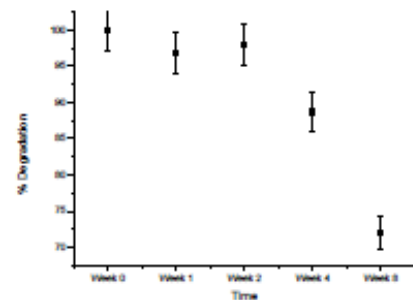


Figure 1 The degradation profile of 3D chitosan composite bone scaffolds for up to 8 weeks duration in simulated body fluid.

DISCUSSION

The overall results showed that the scaffolds degraded in less than 8 weeks indicating that the optimization of the bone regeneration scaffold fabrication leads to improved degradation profile.


REFERENCES

- Journals:
- Pountos, I., Panteli, M., Lampropoulos, A., Jones, E., Calori, G. M., & Giannoudis, P. V. (2016). The role of peptides in bone healing and regeneration: A systematic review. *BMC Medicine*, 14(1), 1–15.
- Turnbull, G., Clarke, J., Picard, F., Riches, P., Jia, L., Han, F., Shu, W. (2017). 3D bioactive composite scaffolds for bone tissue engineering. *Bioactive Materials*, 3, 278–314.
- Polo-Corrales, L.; Latorre-Estevés, M.; Ramirez-Vick, J. (2013). Scaffold Design for Bone Regeneration. *Journal of Nanoscience and Nanotechnology*, 31(9), 1713–1723.
- Devine, D. M., Hctor, E., Hayes, J. S., Sheehan, E., & Evans, C. H. (2017). Extended release of proteins following encapsulation in hydroxyapatite/chitosan composite scaffolds for bone tissue engineering applications. *Materials Science and Engineering C*, (November), 1-9.

iv) On November 22, 2019, another poster entitled “ *Evaluation on Osteogenic and Antimicrobial Properties of Bioactive Bone Regeneration Scaffolds*” was presented in Athlone Institute of Technology Research Seminar 2019 on November 22, 2019, in Athlone, Ireland. This poster focused on the bioactivity assessment of the chitosan/hydroxyapatite scaffolds and also the antimicrobial functionality in the presence of gram-positive and gram-negative bacteria.

THE SUNDAY TIMES
GOOD UNIVERSITY GUIDE
2018
INSTITUTE OF TECHNOLOGY OF THE YEAR

AIT Research



In Vitro Evaluation on Osteogenic and Antimicrobial Properties of Bioactive Bone Regeneration Scaffolds

Farah Alwani Azaman¹, Margaret E. Brennan Fournet¹, Declan M. Devine¹
¹Materials Research Institute, Athlone Institute of Technology, Ireland

Introduction

Here we present the development of an anti-infective biomimetic scaffold capable of inducing bone tissue specific regeneration. Multiple intricate factors are integrated in this orthopaedic implant that is easy to fabricate and adopt in the surgical setting.

This microporous bio-active scaffold designed for sustained bio-agent release comprises an osteoconductive composite of natural polymers and bioceramics combined with growth factors providing osteogenic properties to the scaffold. The ability of the scaffolds to mitigate against bacterial infections is an additional goal of this project.

Evidential proof that the growth factors remain active and the antimicrobial functionality of the bone regeneration scaffolds are presented.

Research Stages

Fabrication of bone regeneration scaffold

Characterization Mechanical properties Degradation profile

Bioactivity assessment of scaffold

Growth factors release profile In vitro osteogenic activity evaluation

Bone regeneration assessment

In vivo scaffold implantation

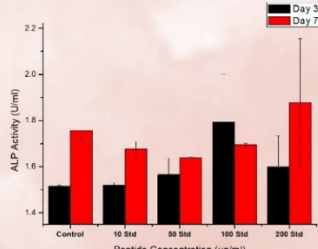
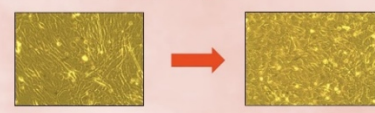
Antimicrobial functionality

*In vitro antimicrobial assessment **In vivo antimicrobial assessment

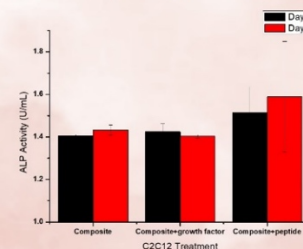
Indications:
* Ongoing work
** Future work

Results

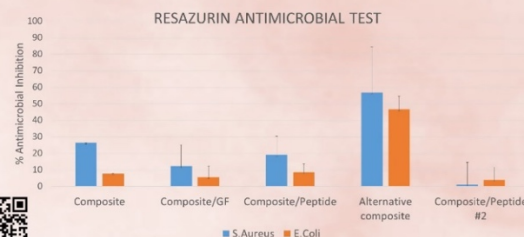
(1) In vitro bioactivity evaluation of growth factor incorporated chitosan/hydroxyapatite scaffolds

Morphological changes of C2C12 myoblast cell line after treatment with osteogenic factors in differentiation media.





(2) In vitro antimicrobial assessment of bone regeneration scaffolds




Conclusion

Both bioactivity testing and antimicrobial testing have validated the effective osteogenicity and antimicrobial functionality of these bone regeneration scaffolds.





v) A virtual AIT Postgraduate Research Seminar & Poster Event through Microsoft Teams was attended on June 19, 2020, with a poster entitled “*Preclinical Assessment of Biomimetic and Bioactive Bone Regeneration Scaffold in Femoral Condyle Defect of Sprague Dawley Rats*”. It was great to be able to join this virtual event from Malaysia since we got connected without any boundary even during the Covid’19 pandemic. The certificate of participation is attached in Appendix 1.




**THE TIMES
GOOD UNIVERSITY
GUIDE
2020**
INSTITUTE OF
TECHNOLOGY
OF THE YEAR

AIT Research



PRECLINICAL ASSESSMENT OF BIOMIMETIC AND BIOACTIVE BONE REGENERATION SCAFFOLD IN FEMORAL CONDYLE DEFECT OF SPRAGUE DAWLEY RATS

Farah Alwani Azaman¹, Margaret E. Brennan Fournet¹, Declan M. Devine¹
¹ Materials Research Institute, Athlone Institute of Technology, Athlone, Ireland



INTRODUCTION: A fabricated biomimetic bone scaffold, incorporating osteogenic factors, presents a promising alternative to traditional autologous and allogeneic bone fracture treatments. Here, the principles of biology and engineering are combined in the development of viable tissue regeneration scaffolds designed to restore and maintain the function of human (bone) tissue. Our aim is to produce a cost effective bone healing biodegradable scaffold that overcomes current technology limitations and provides better safety than current mainstay market products. To date, the initial development phase of this project has been completed and in vitro studies have been performed providing positive outcomes. A preclinical assessment, where the scaffolds was implanted in Sprague Dawley rat defective femoral condyles has been carried out to investigate the efficiency of the scaffold in promoting bone healing. Histological analysis of the osteogenic and bioactive properties of the scaffolds has been conducted validating the efficacy of controlled low dose growth factor release compared with equivalent commercially available bone healing products.

METHODS:

Surgical Implantation

Implantation of scaffold composite into femoral condyle defects in Sprague Dawley rats

Post-operative Assessment

Clinical follow up for 8 weeks before euthanasia

Tissue Harvesting and Fixation

Harvesting the femoral condyles and fixed in 10% neutral buffered formalin


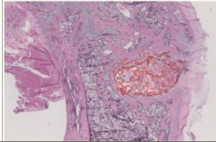

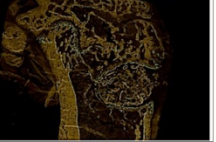

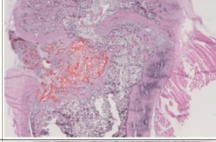

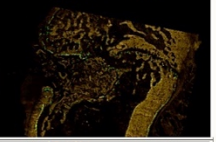

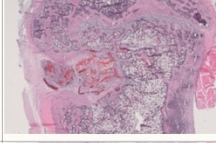
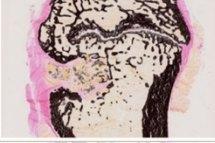
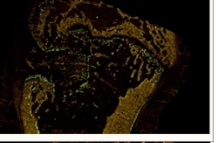



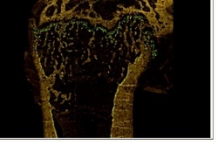
Micro CT Scan

- Bone volume, BV (mm³)
- Bone volume fraction, BV/TV (%)
- Bone mineral density, BMD (g/cm³)

Histological Staining

- Hematoxylin & Eosin (H&E)
- Von Kossa
- Tartrate-Resistant Acid Phosphatase
- Fluorescent Labelling

RESULTS:

	MicroCT Scan	H&E Staining	Von Kossa Staining	Fluorescent Labelling
Chitosan Composite				
Chitosan Composite + Protein				
★ Chitosan Composite + Peptide				
Commercial Delivery System + Protein				


★ Scaffold was observed in the defect, but reduced in size compared to other chitosan composite groups. Islands of bone formation were observed in the defect, highlighting the peptide as an alternative to protein.

CONCLUSION: The fabricated scaffold composite with growth factors showed promising bioactive functionality in the femoral condyle defects healing comparable to the commercial protein delivery system. The chitosan composite with peptide out performed the protein incorporated chitosan composite, addressing industry requirement to have a clean supply chain.

REFERENCES:


- Yang, L. et al. (2017) 'Evaluation of Osteogenic Inductivity of a Novel BMP2-mimicking Peptide P28 and P28-containing Bone Composite', Journal of Biomedical Materials Research Part A, 106(1), pp. 210–220. doi: 10.1002/jbm.a.36228.
- Suliman, S. et al. (2015) 'Release and Bioactivity of Bone Morphogenetic Protein-2 are Affected by Scaffold Binding Techniques In Vitro and In Vivo', Journal of Controlled Release. Elsevier B.V., 197, pp. 148–157. doi: 10.1016/j.jconrel.2014.11.003.

Funded by:



where innovation means business

Co-funded by:



European Union
European Regional
Development Fund CF-2016-0600-P

vi) Materials Info 2021 conference was participated as an oral presenter held via Zoom Meeting in GMT times, presenting the work entitled “*Preclinical Assessment of Biomimetic and Bioactive Bone Regeneration Scaffold in Femoral Condyle Defect of Sprague Dawley Rats*”. It was an excellent experience to learn about the current research carried out by the experts in their representative fields. The certificate of participation is attached in Appendix 2.



Preclinical Assessment of Biomimetic and Bioactive Bone Regeneration Scaffold in Femoral Condyle Defect of Sprague Dawley Rats

Farah Alwani Azaman, Margaret E. Brennan Fournet and Declan M. Devine

Materials Research Institute, Athlone Institute of Technology, Ireland

A fabricated biomimetic bone scaffold, incorporating osteogenic factors, presents a promising alternative to traditional autologous and allogeneic bone fracture treatments. Here, the principles of biology and engineering are combined in the development of viable tissue regeneration scaffolds designed to restore and maintain the function of human (bone) tissue. Our aim is to produce a cost effective bone healing biodegradable scaffold that overcomes current technology limitations and provides better safety than current mainstay market products. To date, the initial development phase of this project has been completed and *in vitro* studies have been performed providing positive outcomes. A preclinical assessment, where the scaffolds were implanted in Sprague Dawley rat defective femoral condyles has been carried out to investigate the efficiency of the scaffold in promoting bone healing. Histological analysis of the osteogenic and bioactive properties of the scaffolds has been conducted validating the efficacy of controlled low dose growth factor release compared with equivalent commercially available bone healing products.


Keywords: bone scaffold, osteogenic factor, bone healing, femoral condyle defect, *in vivo* .

Biography

Farah Alwani binti Azaman is a PhD candidate in Athlone Institute of Technology (AIT), Ireland and currently conducting research focusing on developing biodegradable biomimetic and bioactive bone regeneration scaffolds by using biomaterials and osteogenic factors since 2018, funded by Enterprise Ireland and co-funded by European Regional Development Fund. To date, Farah has published a few collaborative research papers and attended several conferences throughout her postgraduate journey to present her research. Recently, Farah has published a book chapter in collaboration with the experts of Materials Research Institute (MRI AIT) entitled Orthopaedic 3D Printing in Orthopaedic Medicine in Polymer-Based Additive Manufacturing book published by Springer in 2019. Farah sets her hopes high that this research will benefit the world, specifically in leading towards better quality of life.


f.alwani@research.ait.ie

vii) A postgraduate poster festival was organized by TUS graduate school research on January 27th 2022, via Zoom. The participants were divided into four categories: ‘Early Stage’, ‘Mid-Stage’, ‘Getting There’ and ‘Almost There’. A poster entitled “Osteoinduction of C2C12 Myoblast Cell-line treated with Growth Factor-incorporated Biocomposites” was submitted and won the best poster under the ‘Almost There’ category.



TUS
Technological University of the Shannon:
Midlands Midwest
Ollscoil Technolaíochta na Sionainne:
Lár Tíre Iarthar Láir

TUS Research



TITLE: OSTEOINDUCTION OF C2C12 MYOBLAST CELL-LINE TREATED WITH GROWTH FACTOR-INCORPORATED BIOCOMPOSITES

Farah Alwani Azaman¹, Margaret Brennan-Fournet¹, Declan Devine¹
¹Materials Research Institute, Technological University of the Shannon, Ireland

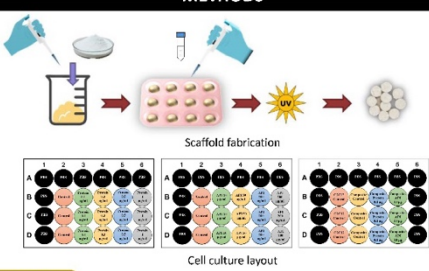
INTRODUCTION

Bone regeneration scaffold serves as an alternative treatment to critical bone defects, substituting the traditional gold standard autologous bone grafting. A number of biomaterials and osteogenic growth factors are of the scientists' interest in developing this bone scaffolds, to satisfy the required characteristics including having the osteoconductive and osteoinductive features.

FDA-approved treatments are known as Medtronic Infuse™ rhBMP-2 and Stryker Osigraft™ rhBMP-7, where both are osteogenic proteins. However, Infuse™ was shown to induce ectopic bone growth, while Osigraft™ was unable to prove its effectiveness in treating non-unions, thus being discontinued from the market.

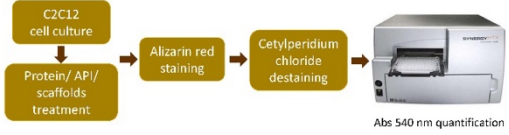
This research is interested in comparing the use of an alternative active pharmaceutical ingredients (API) to have a comparable osteogenic performance to the protein, since it is advantageous in terms of greater conformational control, giving higher stability over cellular interactions.

METHODS



Scaffold fabrication

Cell culture layout

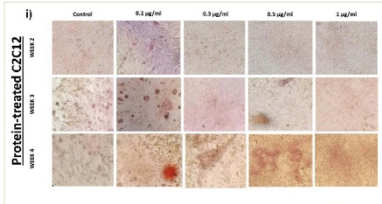


OBJECTIVES

- Investigating the ability of an API acting as an osteoinductive growth factor in changing the C2C12 differentiation pathway from myoblast to an osteoblastic phenotype comparable to the osteogenic protein performance.
- Evaluating the *in vitro* bioactivity of the covalently-bonded protein/API to biomimetic scaffold composite in UV crosslinking procedures, through Alizarin red staining and followed by quantitative cetylperidium chloride destaining.

RESULTS & DISCUSSION

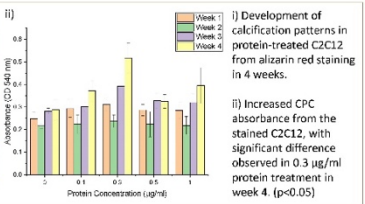
ALIZARIN RED STAINING



i) Development of calcification patterns in protein-treated C2C12 from alizarin red staining in 4 weeks.

ii) Increased CPC absorbance from the stained C2C12, with significant difference observed in 0.3 µg/ml protein treatment in week 4. (*p*<0.05)

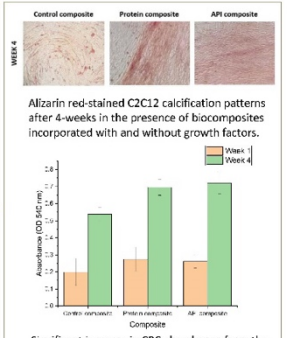
CETYLPERIDIUM CHLORIDE DESTAINING



iii) Comparable intensity of calcification patterns in API-treated C2C12 from alizarin red staining in 4 weeks.

iv) CPC absorbance from the stained API-treated C2C12 almost on par to the protein, with significant difference observed in 50 µg/ml in week 4. (*p*<0.05)

SCAFFOLDS



i) Alizarin red-stained C2C12 calcification patterns after 4-weeks in the presence of biocomposites incorporated with and without growth factors.

ii) Significant increase in CPC absorbance from the stained C2C12 after 4-weeks of incubation in the presence of biocomposites, where no significant difference was observed between protein and API biocomposite. (*p*<0.05)

CONCLUSION

- API shows comparable osteoinductivity to the protein of origin.
- Protein and API retained their osteogenicity following the covalent bonding through UV crosslinking to the biomimetic scaffold composite.

ACKNOWLEDGEMENTS



European Union
European Regional Development Fund
CF-2016-0600-P

REFERENCES

- Bullock, G. et al. (2021) doi:10.3390/fb1202022
- Hidaka, Y. et al. (2020) doi:10.3390/pharmaceutics12030218.
- Fu, C. et al. (2017) doi:10.1038/s41598-017-12935-x
- Chen, Y. et al. (2017) doi:10.7150/thno.18193



TUS
Technological University of the Shannon:
Midlands Midwest
Ollscoil Technolaíochta na Sionainne:
Lár Tíre Iarthar Láir

TUS Research



Chapter 1

Chapter 1: Literature Review

1.1 Long Bone Fractures

Long bones are crucial for most load-bearing functions during daily activities and thus assist skeletal mobility (Manolagas et al., 2018). The bone has an extraordinary hierarchical architecture consisting of soft collagen protein and stronger apatite mineral, as shown in Figure 1.1 (Nair et al., 2013). Long bone fractures, a global and clinical challenge, can be induced by several factors such as a sudden trauma or extreme impact, either directly or indirectly and given the excessive mechanical force applied (X. Zhang et al., 2019). It can also happen due to pre-existing microdamage and repetitive stress to the point of mechanical fatigue or from everyday stresses acting on the abnormally weakened bone, such as osteoporotic bone, Paget's disease or bone tumours that are known as Pathologic fracture (Dittmer & Firth, 2017; Solomon et al., 2005).

Furthermore, it was reported in Surgeon's General Report in 2004 that about 1.5 million fracture cases due to osteoporosis occurred in Americans per year, and 300,000 hospitalised cases from this number were hip fractures, thus making it a deleterious cause for bone fractures. Subsequently, a research report has updated the annual fracture treatments in the United States alone to increase to 18.3 million cases in 2018 (Chitnis et al., 2020; Khalifeh et al., 2018). In addition, 20% of these cases were reported as mortality, and 20% were confined in a nursing home within a year of the fracture. The patients' quality of life was also affected since many patients were reported to be afraid to step out of home due to fear of falling (J. Li & Stocum, 2014).

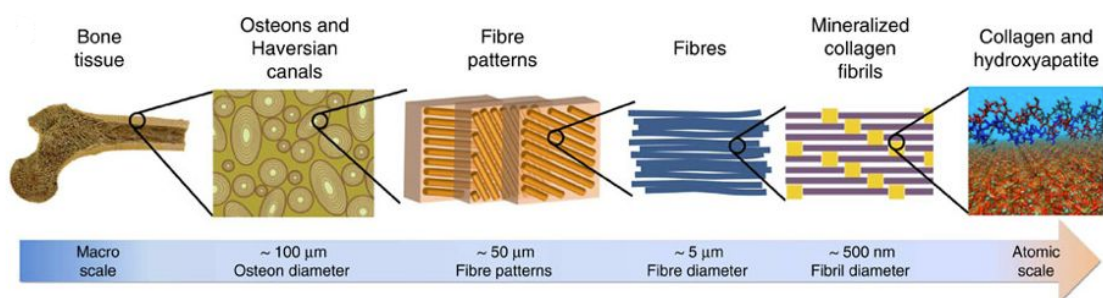


Figure 1.1 The complex architecture of long bones. (Nair et al., 2013)

The femur is the longest, strongest and heaviest tubular bone in the human body and the foremost load-bearing bone in the lower extremity. High energy forces such as impacts occurring in motor vehicle collisions can cause fractures of the femoral shaft (Asplund,

2018b; Fields, 2018; Tucker et al., 2021). The Swedish Fracture Register had reported that fractures are most commonly occurred in five locations: distal radius (16.4%), the proximal femur (14.7%), the ankle (10.3%), the proximal humerus (8.2%), and the metacarpal bones (7.2%) in a 4-years study involving 23,917 individuals, where the proximal femur fracture being the second highest incidence after distal radius (Bergh et al., 2021). Additionally, IBM MarketScan® Research Commercial and Medicare Databases had reported 14,961 femoral, 14,101 tibial, and 7,059 humeral fracture patients between January 2016-July 2019 (Chitnis et al., 2020). A global burden of disease study 2019 had also reported that 14.6 millions of femur fractures had occurred over the 29 years (1990-2019) in 204 countries, showing the significant yearly fracture incidence involving the long bones (A. M. Wu et al., 2021).

Fractures of the tibia, the prominent weight-bearing bone of the lower leg, often occur not only in both high energy trauma such as a motor vehicle, winter sports and cycling accidents but also in low energy trauma such as falls, contact sports, distance running and other persistence or repetitive activities (Fields, 2018; Marongiu et al., 2020). These extremity fractures caused by trauma require repeated hospitalisations, therapies and treatments, as well as the possible complications that a study reported these cases demanded a massive cost of near to \$2 billion (Blanchette & Wenke, 2018). The most frequent long-bone fractures in children and adults are closed tibial fractures, with more than 70,000 hospitalisations, 800,000 clinician appointments and 500,000 hospital days per year only in the United States (US) alone. The National Center for Health Statistics also records 492,000 tibial fractures per year in the US (Fields, 2018).

1.1.1 The Healing Process of Bone Fractures

The healing process for fractures is time-consuming and depends on the skeletal sites. The new bone regeneration and remodelling process require typically extra time due to the reduced blood supply to the broken bone area and the insufficient supply of minerals like calcium and phosphorus that aid in strengthening and hardening the *de novo* bone formed (Asplund, 2018a; Y. Li et al., 2015; Ng et al., 2017). The expected time for fracture healing for the upper limb is typically 4-6 weeks and 8-12 weeks for lower limb fractures, while almost all fractures will achieve the complete union before six months (Andrzejowski & Giannoudis, 2019; Solomon et al., 2005). Fracture repair can be classified into primary healing and secondary healing. Primary healing can occur through the direct reestablishment of the cortex in joining the fracture fragments that lead to the

precise fracture reduction. Rigid internal fixation with dynamic compression plates and screws was used to achieve absolute stability and reduce the interfragmentary movement during this treatment (Brydone et al., 2010; Chitnis et al., 2020; Dittmer & Firth, 2017; J. Li & Stocum, 2014; Walsh et al., 2021).

On the other hand, secondary or spontaneous healing is the usual fracture repair that implies the surrounding soft tissue and periosteum response as the prime bone injury reaction. The mechanism involves several stages, including blood clotting, inflammatory response mechanisms, fibro-cartilage formation, callus formation, intramembranous and endochondral ossification, and bone remodelling (Figure 1.2) (Einhorn & Gerstenfeld, 2015; Glatt et al., 2021). This secondary healing is further elevated through splinting, casting, intramedullary pins, external skeletal fixators and other fixation tools that will reduce the fragment motion while permitting controlled macro motion at the fracture site to stimulate the callus formation (Brydone et al., 2010; Dittmer & Firth, 2017).

The bone healing mechanism covers three phases: reactive, reparative, and remodelling. The reactive phase starts after fracturing with inflammation that results from the disturbance of the blood vessels due to the injury by increasing the local granulation tissue volume. This initial anabolic phase is crucial since it will determine the outcome of the healing process. Formation of hematoma or blood clotting through the extravascular blood cells will occur at the fracture site as a temporary scaffold allowing the stem cell to differentiate into fibrous tissue, cartilage and bone (AffshanaM. & Saveethna, 2015; Ghiasi et al., 2017). In addition, this hematoma formation reduces mechanical stability, lacks oxygen and nutrients at the fracture site, and causes the release of various growth factors from platelets. Besides, inflammatory cells such as macrophages and leukocytes will also spread around the injury site (J. Li & Stocum, 2014).

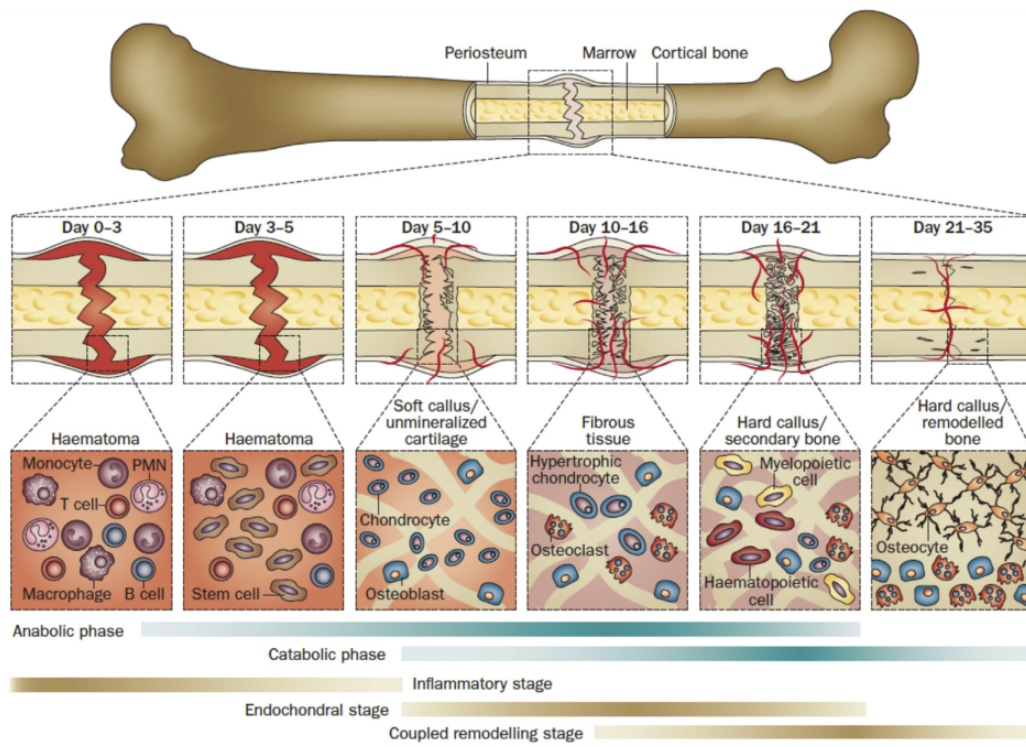


Figure 1.2 Normal formation of new bone post-fracture, starting from the hematoma or the inflammatory responses until the newly remodelled bone in 35 days (Einhorn and Gerstenfeld, 2015).

The soft callus (cartilage) formation will proceed following inflammation, and the skeletal stem cells will proliferate and differentiate into chondrocytes. New vessels, fibroblasts, intracellular material and supporting cells will replace the damaged ones, where a fibrin-rich granulation tissue forms. The endochondral formation between the fracture will end within this tissue, and fibrocartilage will then stabilise the bone ends (Augat et al., 2021; Glatt et al., 2021; Marsell & Einhorn, 2012). Subsequently, hard callus (endochondral ossification) will be formed, where the occurrence of fibrovascular tissue will replace the cartilage through vessel invasion and endochondral ossification, which will be followed by the formation of periosteal bone apposition that also contributes to the primary bone development (J. Li & Stocum, 2014). Osteoclasts will then resorb this primary bone and first mineralised cartilage in a process known as bone remodelling. This callus resorption by osteoclasts and lamellar bone formation by osteoblast will be coordinated over several months. Figure 1.3 below shows an example of a clinical case of this process on a comminuted (bone-breaking to more than two fragments) spiral humerus shaft fracture over two years (Ghiasi et al., 2017).



Figure 1.3 A clinical case example of healing a humerus shaft fracture over two years (Ghiasi et al., 2017).

1.1.2 Non-Union Fractures in Long bones

Non-union fracture is the incomplete healing of a critical-sized fracture when the cortices of the bone fragments fail to reconnect without any intervention (Spicer et al., 2012; Wildemann et al., 2021). These fractures are commonly associated with long bone fractures resulting in persistent pain, swelling or instability beyond the time of normal healing. If a bone has not successfully healed within nine months following fracture with no signs of healing, it is classified as a non-union (Howe, 2018; Nandra et al., 2016; Rupp et al., 2018), while the absence of radiological healing signs after three to six months is considered a delayed union (Higgins et al., 2014; J. D. Thomas & Kehoe, 2022). This definition was in line with the one published by the US Federal Drug Administration council as “a failure to achieve union by nine months since the injury, and for which there have been no signs of healing for three months” (Andrzejowski & Giannoudis, 2019).

Generally, the non-union rate in the United Kingdom (UK) is 5-10% out new fracture cases identified, which is estimated at 20 per 100,000 cases, leading to the need for high-cost treatments (Mills & Simpson, 2013; Nicholson et al., 2021). Apart from that, European Union (EU) citizens recorded about 3.5 million new bone fractures in 2010, including hip fractures, vertebral fractures, forearm fractures and other fractures (Svedbom et al., 2013). Pountos *et al.* (2016) also reported that 5 to 10% of the diagnosis

from the traumatic accidents to the bones are associated with impaired healing, resulting in delayed or non-unions. Subsequently, a study from Australia reported that 8% of 853 patients with fractures had been admitted for their healing complications. In comparison, about 1.9% of the pelvis and femur fracture cases in Scotland was reported to be non-union in patients between 25-44 years old and costs about £ 21,183 to £ 33,752 per patient recently (Andrzejowski & Giannoudis, 2019). Furthermore, these fragility fracture cases have led into the high economic burden and thus resulted to the loss of over 1 million quality of life adjusted years from the previous fractures. This is subsequently expected to increase the fracture treatment costs up until €46 billion by 2025 (Costa-Pinto et al., 2021; Svedbom et al., 2013; Walsh et al., 2021).

1.2 Traditional Bone Grafting for Long Bone Fractures

The most common surgical treatment used to enhance bone regeneration in orthopaedic procedures is bone grafting, making it the second most frequent tissue transplantation after blood transfusion (Fourie et al., 2022; Predoi et al., 2019; Sommer et al., 2020; W. Wang & Yeung, 2017). It is used as a therapeutic strategy in clinical bone surgery to fill the bone defects and promote new bone formation for skeletal fractures or diseased bone healing. The bone graft will substitute and rebuild large bone segments lost due to trauma, enhancing the bone healing response and reconstructing bone tissue following the insertion of any implants surgically (Junka & Yu, 2020; Y. Li et al., 2015; Polo-Corrales, L. ; Latorre-Esteves, M. ; Ramirez-Vick, 2013; Zhong et al., 2020).

Initially, the orthopaedic surgeons will identify the function of the lost bone to decide on a suitable bone graft since the options available have variations in their strength, osteoconductivity, osteoinductivity and osteogenicity. The osteoconductivity of the bone graft, where gradual replacement of the biomaterial with the viable bone tissue occurs, is also crucial for osseointegration, which is the fusion of the surface of the material to the living bone (Alves et al., 2020; Brydone et al., 2010; Burger, 2004; Goharian, 2019). This bone grafting success will depend on the complex biological interactions happening at the graft-host interfaces, together with the action of the native bone marrow and periosteum in providing osteogenicity and vascularity to the site that will then result in the new bone formation (Ghiacci et al., 2016; Y. Zhang et al., 2020).

1.2.1 Autologous Bone Graft

Usually, autologous bone grafting presents as the go-to treatment for non-union fractures by harvesting a bone segment from another part of the patient for use in their own body (AffshanaM. & Saveethna, 2015; Schmidt, 2021). The iliac crest (Figure 1.4) is the most commonly used donor site and is harvested as free vascularised osteocutaneous flaps (Jenis, 2016; L. Li, Lu, et al., 2019). Autografting is considered the gold standard treatment since it exhibits a superior therapeutic effect in bone fusion. It also meets all the required properties, such as osteoconduction, which stimulates the growth of bone cells, osteoinduction, which is the activation of mesenchymal stem cells (MSC) to divide into preosteoblasts before the bone-forming process starts and also osteogenesis, which is the formation of the bone. In addition, autograft also accommodates both osteogenic cells and osteoconductive mineralised extracellular matrix that can further grow and proliferate (Hao et al., 2022; Jahan et al., 2020; Mohiuddin et al., 2019; Polo-Corrales, L. ; Latorre-Esteves, M. ; Ramirez-Vick, 2013; X. Zhang et al., 2019).

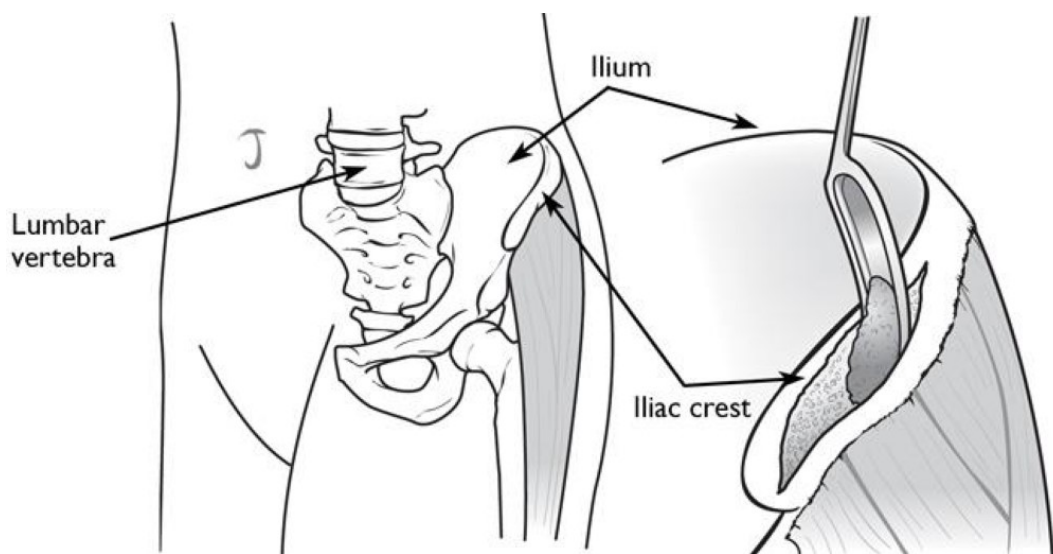


Figure 1.4 The iliac crest serves as autografts for bone grafting treatment (Jenis, 2016).

Nevertheless, autografts are restricted by the graft size that can be harvested due to the limited supply and requires a second surgery. It can also carry a risk of donor-site morbidity from infection and ongoing pain following surgery, leading to unguaranteed clinical benefits, thus limiting its wide application (AffshanaM. & Saveethna, 2015; Junka & Yu, 2020; Turnbull et al., 2017; X. Zhang et al., 2019). In addition, it was reported that this technique could also lead to haemorrhage formation (Y. Li et al., 2015).

The researchers then came up with another option to autograft, known as an allograft for treating bone defects.

1.2.2 Allogenic Bone Graft

The autograft alternative, allografts harvested from cadaveric or living sources, is favoured to eliminate donor-site morbidity. They are also available in various shapes and sizes, such as granules and blocks, distributed through regional tissue banks and most orthopaedic and spinal companies (Fournet et al., 2019; Greenwald et al., 2010). This good, natural, and bone-like structure type of bone graft will be processed to remove the living cellular components of the bone to avoid the host-graft immune response (Bai et al., 2018; Brydone et al., 2010; Lu et al., 2016). However, the potential risk of infectious disease transmission and immune rejection whilst lacking a cellular component to aid tissue regeneration has limited the use of the allograft. Indeed, it has been reported that up to 25% of bone grafts resorb within a 5-year time frame (Fernandez-Yague et al., 2015; Polo-Corrales, L. ; Latorre-Esteves, M. ; Ramirez-Vick, 2013; Turnbull et al., 2017). Considering that an estimated 2.2 million bone-grafting is performed annually, this would equate to over 500,000 allograft failures. The current availability of this bone graft type does not meet the clinical needs, which is crucial for the advances in bone healing treatments (W. Wang & Yeung, 2017).

There is an urgent clinical need due to these drawbacks and non-satisfactory results of these available bone grafts. Thus, extensive research has been carried out to find possible alternatives to treat bone fractures using reliable artificial bone grafts that can be used off-shelf in the bone tissue engineering field. Therefore, the researchers are focusing on mimicking the extracellular matrix architecture and properties of a native bone to formulate a synthetic bone graft to achieve the optimum efficacy in bone regeneration treatment (Patel et al., 2019).

1.3 Bone Tissue Engineering in Treating Bone Fractures

In the world of bone tissue engineering (BTE), significant research creating novel alternatives to overcome the limitations of current treatment options in treating bone fractures has been performed, such as the porous 3D scaffolds with controlled material characteristics including the morphology, dissolution kinetics, swelling profile and mechanical strength (Davidenko et al., 2016; Sahu & Modi, 2021). Three main components were combined, including engineering bone tissue scaffolds, incorporating

biological strategies, and physicommechanical strategies, leading to feasible bone substitutes (Figure 1.5). As the bone healing goes without the presence of connective tissue scars and it deposits similar tissue, the re-establishment of pre-fracture properties of the bones will be achieved through the aid of a well-developed bone scaffold (Fernandez-Yague et al., 2015; F. Zhang & King, 2020).

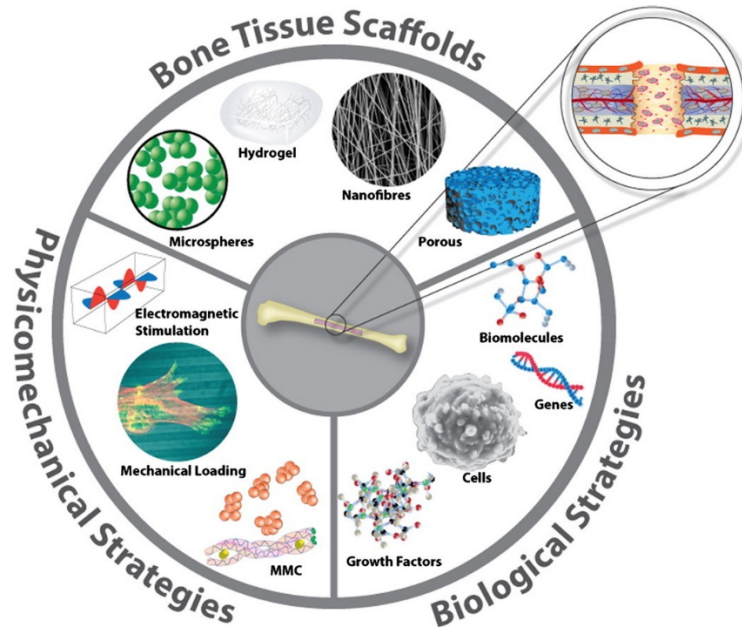


Figure 1.5 Biomimetic cellular approach of bone tissue engineering (Fernandez-Yague et al., 2015).

The scientists focus on fabricating bone scaffolds that have characteristics close enough to autologous bone grafts. Therefore, bone-mimicking scaffolds are designed to have the ability to induce specific cellular responses at the molecular level by using various natural or synthetic biomaterials and also combinations of these (Barroso et al., 2022; López-Lacomba et al., 2006; X. Zhang et al., 2014; Zustiak et al., 2013). There are two categories of bone graft substitutes: osteoconductive materials, which are bioresorbable bone void fillers that allow the bone to regenerate, such as collagen composites, sea coral and various ceramics, and also osteoinductive materials that contain biological factors such as growth factors, which can initiate progenitor cells and differentiate them into osteoblasts (bone-forming cells) and form *de novo* bone including in the non-osseous region (Albulescu et al., 2019; H. Lin et al., 2019; Sheikh et al., 2015).

In addition, Zhang, Fang and Zhou (2017) had outlined the general process of BTE (Figure 1.6). It started from designing the scaffold structure according to an atomic structure of the bone at the site of injury, which comprises the set of geometrical features and a personalised external shape. Subsequently, the process proceeds to select the best

material and fabrication method suited to develop the scaffold. The scaffolds will then be tested *in vitro* and *in vivo* for further analysis.

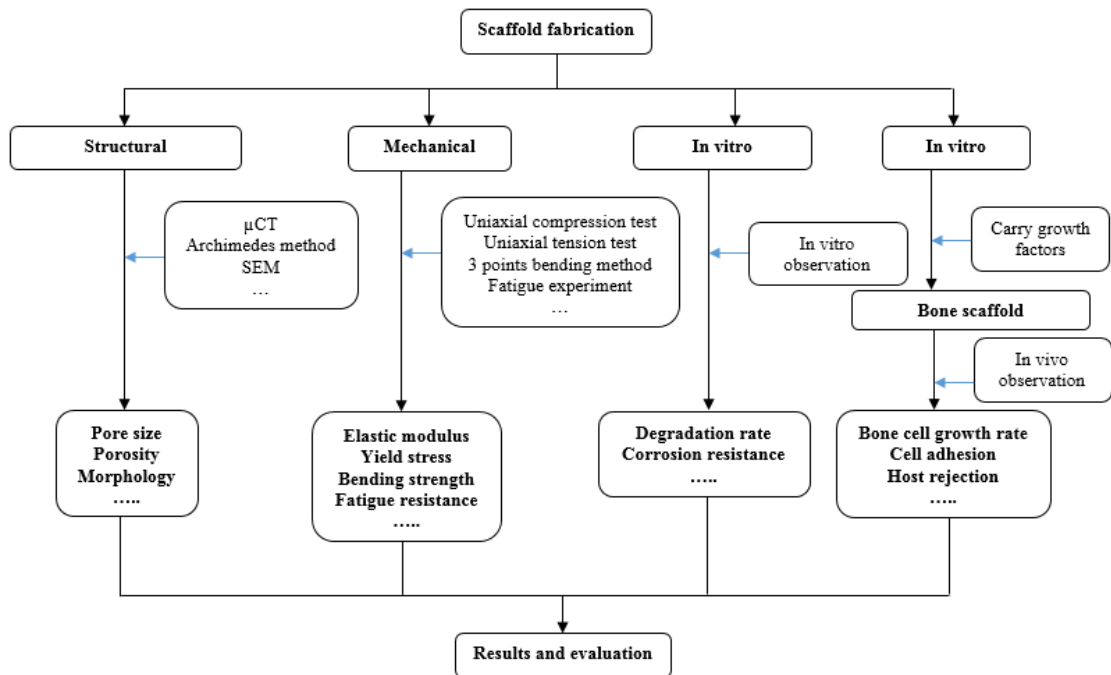


Figure 1.6 Procedure of scaffold fabrication and evaluation highlighting the structural, mechanical, and *in vivo* assessments (Zhang, Fang and Zhou, 2017).

1.3.1 Diamond Concept in Bone Healing

Calori and Giannoudis (2011) reported a theory called the ‘diamond concept’ (Figure 1.7) for bone healing strategies to understand the minimal requirements for fracture healing. This concept gives equal importance to mechanical stability and biological environment, where a deficit in either one or the failure to recognize the associated diseases of the host and a lack of vascularity will lead to the risk of necrosis formation, thus leading to impaired healing (Andrzejowski & Giannoudis, 2019; Rademakers et al., 2019).

**DIAMOND CONCEPT
For Enhancement of Bone Healing**

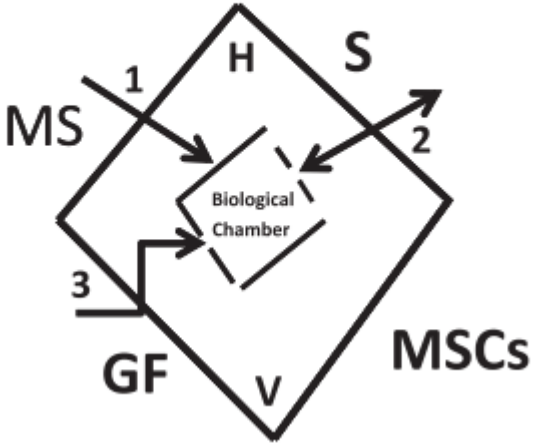


Figure 1.7 The diamond concept and the biological chamber illustration highlighted vascularisation in avoiding an impaired healing response, which is the non-union (Calori and Giannoudis, 2011).

V = vascularity, H = host, MS = mechanical stability, MSC = osteoprogenitor cells, S = scaffold, GF = growth factor.
1. Closed chamber; 2. Open chamber; 3. Partially open chamber

This diamond concept emphasises the mechanical stability properties of the scaffold in conjunction with the other three essential scaffold features, which are the presence of osteoprogenitor cells, growth factors incorporation and also the osteoconductive extracellular matrix for a successful bone healing response (Andrzejowski & Giannoudis, 2019; Glatt et al., 2021; Marongiu et al., 2020). The promoting signalling molecules hold the osteoinductive properties crucial for cell proliferation and differentiation towards the desired cell lineage, such as the osteoblastic phenotype. In contrast, the recruitment of bone progenitor cells often requires an appropriate vascularisation-inducing environment to promote the healing and an excellent scaffold as a transport for the growth factors, thus acting as the extracellular matrix for the cell recruitments (Barroso et al., 2022; Svystonyuk et al., 2018; C. Wang et al., 2020). Moreover, this diamond concept highlights the mechanical property of the scaffold for its importance in providing load-bearing support to the fracture sites during the healing process (Augat et al., 2021; Calori & Giannoudis, 2011).

1.3.2 The Ideal Properties of Bone Tissue Scaffolds

The bone scaffolds are also designed to effectively carry the essential properties in aiding the new bone tissue formation in the bone regeneration process, such as biocompatibility, so it does not induce any local or systemic response. In addition, highly interconnected

porous architecture and customizable shape are great features to allow proper nutrient delivery and remove metabolic waste while upgrading the diffusion rates and accelerating vascularisation (Cai et al., 2018; Donnalaja et al., 2020; P. Feng et al., 2014; Xu et al., 2021).

Moreover, osteoconductivity is also required with micro and nanoscale structures that allow migration, adherence, proliferation and differentiation of osteoprogenitor cells to form bone. Most importantly, the degradation rate must be adjusted to provide the necessary support and not leave traces of material behind and give no side effects to the body. Mechanical strength should also be adequate to withstand cellular contractile forces and possess growth factor delivery properties (Polo-Corrales, L. ; Latorre-Esteves, M. ; Ramirez-Vick, 2013; Sukpaita et al., 2019; X. Y. Zhang et al., 2017).

1.3.3 Conventional Scaffold Fabrication Methods

Five fabrication methods are commonly utilised to manufacture conventional scaffolds, including the solvent casting-particle leaching process, gas foaming, freeze-drying/emulsification, phase separation and electrospinning process. However, although these methods can produce porous scaffolds, these techniques have disadvantages in controlling the porosity and pore size, shapes and pore interconnectivity (Bhushan et al., 2022; Cai et al., 2018; Dehghani & Annabi, 2011; C. Liao et al., 2001). There are also negative impacts that influence cell growth, including compact soft structures that could lead to poor cell attachment, remnants of organic solvent residues and porogens that might deprive cell growth and death, as well as rapid degradation that will reduce the mechanical strength of the scaffolds. These drawbacks will usually form irregular growth in the bone tissues (C. G. Liu et al., 2018).

In addition, there is an in-trend method in fabricating bone scaffolds via additive manufacturing to create 3D scaffolds, using 3D-printing technology to overcome the drawbacks of the traditional methods since it disregards the use of porogens and organic solvents in generating pores in the scaffold (C. G. Liu et al., 2018). Indeed, orthopaedics is among the pioneer fields that integrate 3D printing technology to produce artificial prosthetics for treating or replacing bone defects. Customizable bone implants are also achievable according to desired shapes and sizes, known as patient-specific implants (Fournet et al., 2019). For instance, biomaterial-based 3D-printed grafts were previously developed using polyetheretherketone (PEEK), a high-performance thermoplastic and

coated with titanium dioxide (TiO₂) for orthopaedic applications, including spinal fusion implants, where 3D-printed PEEK possess high durability, lightweight as well as elastic modulus close to the human native cortical bone (Kizuki et al., 2015; Suamte et al., 2023; Wong, 2016).

Subsequently, Devine *et al.* (2017) reported a scaffold fabrication method via a novel photo-crosslinking reaction through a hydrogen-abstracting free radical photo-initiation process using ultraviolet (UV) curing. This method can instantly crosslink the chitosan composite, including the potential to induce the covalent bond of osteogenic factors within the composite. Previously, an evaluation was carried out on a range of UV light intensities to crosslink collagen and gelatine-based scaffolds and modify their material characteristics while maintaining biological functionality. The UV light was concluded not to affect the cell attachment, spreading and proliferation on the collagen materials (Davidenko et al., 2016). Therefore, this method is utilised in this current study as a promising approach to creating biomimetic and bioactive bone regeneration implants.

1.3.4 Polymer Crosslinking through UV Curing Procedures

Crosslinking polymers using UV curing technology for fabricating 3D scaffolds are vastly used due to its rapid processing and high energy efficiency. It is one of a go-to method to crosslink materials for the application of dental clinical, drug delivery systems, tissue engineering scaffolds, coatings, adhesive and also food packaging (Chiyindiko & Conradie, 2021; H. J. Kim et al., 2022; Sanchez-Salvador et al., 2021). Crosslinking enables customisable physical properties of polymers, especially the mechanical properties through the covalent or ionic bond formation between adjacent chains of a polymer during the procedures (Y.-H. Jiang et al., 2022; Sanchez-Salvador et al., 2021). There are two covalent bonding formation during crosslinking, known as irreversible and reversible covalent bonding. The linkages would maintain their structure under stresses and changes in the environment through the irreversible bonding, while reversible bonds can be broken and reformed, providing flexibility to the 3D structure (J. Chen et al., 2020).

The crosslinking process is normally started by the application of a photoinitiator, an organic molecule which absorbs light and forms reactive initiating species e.g., radicals. Then, the initiation and propagation of the monomer is occurred for photopolymerisation (Huang et al., 2020). There are a lot of commercially available photoinitiators with ideal

properties including non-complex synthesis, economical and low or absence of toxicity. The photoinitiator should also be stable to avoid unwanted effects such as yellowing and odour of the product material. Some examples of the commercial photoinitiators known as benzophenone, α -ketoesters, camphorquinone and Irgacure 2959 are commonly used in photocrosslinking the materials (Devine & Higginbotham, 2006; Kowalska et al., 2021; Taschner et al., 2019).

There are two classes of photoinitiator, namely Type I and Type II photoinitiators. Type I photoinitiator such as Irgacure 2959 involves direct cleavage under UV light to produce two initiating radicals, while Type II photoinitiator such as benzophenone is a hydrogen abstracting photoinitiator, where the excited benzophenone generates radicals and transferring these radicals to hydrogen donor co-initiator to initiate polymerisation (Allushi et al., 2017; Huang et al., 2020; Qin et al., 2014).

The type II photoinitiator, mainly benzophenone (BP) is commonly used as the hydrogen abstracting molecules for its efficient photoreactivity to induce grafting and low in cost. The photochemical reduction of BP started with the absorption of UV light by the BP (excitation wavelength: 350-360 nm), causing the intersystem crossing to occur and producing a diradical, a molecule with two unpaired electrons. The BP will then abstract a hydrogen atom of the neighbouring molecules, forming an -OH bond. In the absence of a suitable reaction molecules, the diradical will return to the ground state, and the excitation can be repeated until the favourable reaction is obtained. This reversible excitation properties of BP is promising in the alteration of the crosslinking that will further influence the physicochemical properties of the product material including the mechanical strength (Bagheri et al., 2021; Chiyindiko & Conradie, 2021; Kowalska et al., 2021; Riga et al., 2017; Verma, 2017).

According to the diamond concept, a mechanically stable crosslinked biodegradable scaffold is a favourable feature in creating a bone regeneration scaffold to support the healing process. In addition, Wolff's law also stated that bones that bear a lot of weight remodels at a higher rate (Dittmer & Firth, 2017; Foster et al., 2021; Marongiu et al., 2020). Therefore, the photoinitiator indeed plays a huge role in producing biodegradable scaffolds with the desired mechanical properties, through the alteration of crosslinking network.

1.4 Biodegradable Scaffold

A bone scaffold is vital in supporting and promoting bone tissue regeneration by having all the essential properties including biocompatible, biodegradable as well as adequate mechanical stability (Becerra et al., 2022; Gleeson et al., 2010; Predoi et al., 2019). Various natural and synthetic biomaterials are suitable for formulating scaffolds that can integrate into the surrounding tissue without being rejected and keeping the host and implant reaction risks at a minimal level, known as biodegradable polymers (Dorati et al., 2017; Suamte et al., 2023).

Biodegradation is a process initiated by enzyme activities or the degeneration of the living organisms through the shredding of the compounds into the lower molecular mass by biotic or abiotic reactions, followed by the conformation of the polymer pieces by the microorganisms (Mohanani et al., 2020; Vroman & Tighzert, 2009). On the other hand, The American Society for Testing of Materials (ASTM) and the International Standards Organization (ISO) defined degradable polymers as the polymers that undergo a significant change in chemical structure and properties, including the tensile strength, colour and shape under specific environmental conditions such as heat, light or chemicals. These conditions will then lead to the loss of mechanical and physical properties (Y. Chen, 2018).

Other than the biodegradable scaffolds' well-established performance *in vivo*, researchers are choosing the biodegradable polymers to be applied in the scaffold fabrications because of the tuneable mechanical properties offered, together with the controlled degradation, which enables the scaffolds to reduce the mechanical strength consistently during the tissue regeneration process. In addition, the ability of this technology to prevent the need for a second surgery after the complete degradation of the scaffold is also a significant advantage. (Dai et al., 2016; Ghassemi et al., 2018).

1.5 Naturally and Synthetically Derived Biodegradable Scaffold Materials

Some natural biocompatible and biodegradable materials are natural polymers such as collagen, chitosan, silk, alginate, hyaluronic acid and peptide hydrogels. These natural polymers possess excellent biocompatibility and biodegradability features with good porosity, charge, and mechanical strength control. These features can be achieved by manipulating the polymer concentration and polymerisation conditions or introducing functional groups to the reaction. The bioactivity of these materials can also be controlled

by adding several chemicals, proteins, peptides and cells to improve the osteogenic properties of bone (Dehghani & Annabi, 2011; Wei et al., 2020).

Biodegradable materials such as polyesters, copolymers, calcium phosphate and coral are also available for use, where their degradation products can be secreted naturally through the human metabolic pathways. In addition, bone scaffolds can also be formulated using composite materials such as the combination of polymer/ceramics, metal/ceramics and metal/polymers. They can be manipulated depending on the needs and to achieve different capabilities, especially in the surface reactivity, bioactivity, mechanical strength, and functionality in the drug or growth factor delivery application (Polo-Corrales, L. ; Latorre-Esteves, M. ; Ramirez-Vick, 2013; Wei et al., 2020; F. Zhang & King, 2020).

According to Devine *et al.* (2017), the development of biodegradable scaffolds infiltrated with osteogenic factors released in an extended period is a promising cell-free strategy promoting bone formation through endogenous osteoprogenitor cells. Furthermore, the scaffold biodegradation profile plays a vital role in releasing a loaded drug, where the disintegration rate of this material can be controlled to obtain a suitable drug release mechanism. In addition, these biomaterials are proven to accelerate tissue healing (Chao et al., 2021; M. Wu et al., 2020). Most importantly, there is no need for further surgical procedures after implanting polymeric scaffolds as they can deteriorate naturally or be wholly integrated with the newly formed tissue (Dorati et al., 2017).

1.5.1 Chitosan

Chitosan is an abundant linear polyamine copolymer of β -(1,4)-D-glucosamine and acetyl- β -(1,4)-D-glucosamine. It is obtained from the alkaline N-deacetylation of chitin, the second most abundant polysaccharide on Earth (Costa-Pinto et al., 2021; Donnalaja et al., 2020; Sultankulov et al., 2019; F. Zhang & King, 2020). Chitin is exploited from two primary sources of marine crustaceans, shrimp and crabs. Extraction of chitin from crustaceans is carried out by dissolving calcium carbonate in acid treatment followed by alkaline extraction to make the protein soluble. Following that, a decolourisation step is usually carried out to remove the excess pigments and thus obtain a colourless product. In addition, chitosan produced by mushrooms is also available on the market (Dorati et al., 2017; Nga et al., 2020; Rinaudo, 2006).

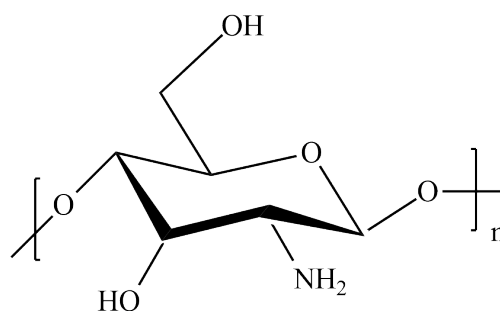


Figure 1.8 Chitosan chemical structure.

Chitosan is insoluble in pure water or organic solvents, but it can become soluble in aqueous acidic media. The deacetylation degree (DD) of chitin will reach about 50% by the protonation of the $-NH_2$ function to $-NH_3^+$ on the C-2 position of the D -glucosamine repeating unit (Figure 1.8), with the conversion of polysaccharide to a polyelectrolytic and chelating chitosan in acidic media (Rinaudo, 2006; Ross et al., 2022). The deacetylation degree of chitosan is closely related to its reactivity and properties and represents the ratio of glucosamine to N-acetyl-glucosamine, which usually falls between 50-95% (Lan Levengood & Zhang, 2015; Yadav et al., 2021). Although chitosan is generally insoluble in neutral pH water, its hydrophilicity and positive charge enable the polymer to interact with negatively charged polymers, macromolecules, and some polyanions in the aqueous environment, specifically in forming thermosensitive hydrogels. Furthermore, the positively charged properties of this material can also improve its adhesion to the mucosal surfaces of humans and animals, which will then draw attention to using chitosan in mucosal drug delivery (Abidin et al., 2020; Dorati et al., 2017). It was also mentioned that a low DD chitosan (55-70%) is insoluble in water compared to the high DD chitosan (85-95%) that has a good solubility in water. The better solubility can also be tailored by reducing the molecular weight of chitosan (Aranaz et al., 2021; Kapadnis et al., 2019; Lv, 2016; W. Wang et al., 2020).

In addition, the formation of viscous solutions after being solubilised in organic acid solutions makes chitosan very versatile in various applications such as solutions, hydrogels, films or fibres. Previously, the mechanical and barrier properties of non-plasticized chitosan films by using various chitosan molecular weights and different organic acids was investigated. It was found that the suitable chitosan molecular weight and the solvent system can regulate the chitosan films' mechanical and barrier properties,

which are helpful for food and medical packaging and applications (Brun et al., 2021; Marques et al., 2020; Park et al., 2002). Chitosan has also been formulated as an injectable *in situ* forming gels for cartilage repair and filling material in repairing bones (Fourie et al., 2022; Jahan et al., 2020; Raftery et al., 2013). Moreover, chitosan is widely used to mimic the natural tissue regeneration process due to its similar structural properties to glycosaminoglycan (GAG) found in the native ECM (Chang et al., 2016; Islam et al., 2020).

In bone tissue engineering, the biodegradable, biocompatible, antibacterial, wound healing, and bioadhesive properties of chitosan have made it an excellent natural polymer material in fabricating 3D bone scaffolds (Chatzipetros et al., 2018; Polo-Corrales, L. ; Latorre-Esteves, M. ; Ramirez-Vick, 2013; Turnbull et al., 2017). A plethora of studies have been carried out in developing biomaterials that possess antibacterial properties for various applications, including bone regeneration research. It has been reported that the antimicrobial properties are present in several chitosan derivatives, and it caught the attention of researchers as a go-to biomaterial to date (Alhazmi et al., 2022; De Mori et al., 2019; Mututuvvari et al., 2013; Tsiklin et al., 2022).

Another outstanding characteristic of chitosan is that it will undergo enzymatic degradation *in vivo*, and the degradation products can be digested naturally after entering the metabolic cycle of a body (Lavanya et al., 2020). Nevertheless, the *in vivo* performances of chitosan may be different depending on the chitosan's deacetylation degree, molecular weight and also functionalisation with the other chemical groups, such as trimethylated chitosan, which can be tailored based on the specific necessities (Dorati et al., 2017; Sultankulov et al., 2019). Raftery, O'Brien and Cryan (2013) have reported that high deacetylated chitosan will degrade slowly *in vivo* and may reach several months before completely degraded, while rapid degradation can be achieved by using a low deacetylated chitosan.

To date, the low stability of chitosan due to its outstanding hydrophilic character and also the pH and temperature dependency has led the researchers to various chemical modification techniques at the active sites of chitosan structure, including $-NH_2$ or $-OH$ groups (Harugade et al., 2023; A. Kumar & Kumar, 2017; Sanchez-Salvador et al., 2021). Appropriate groups can be introduced at these active sites to modify the polymers for specific applications as well as to control their mechanical and chemical properties (Park

et al., 2002; Rinaudo, 2006; Yun et al., 2013). In addition, several other materials were used together with chitosan for various applications. Therefore, the versatility of chitosan as a biopolymer, especially in terms of its considerable biodegradability properties, has guided this research to employ chitosan in bone scaffold fabrication for bone healing treatments.

1.6 Bioactive Ceramics

Different classes of materials are utilised in fabricating scaffolds, including bioactive calcium phosphate ceramics. The similar chemical structures of the synthetic calcium phosphate-based ceramics such as biphasic calcium phosphate, β -tricalcium phosphate and hydroxyapatite have made them more popular to be used as scaffolding materials in tissue regeneration (Ercal & Pekozer, 2020; Qiu, 2008; Ryan & Yin, 2022). These bioceramics can enhance the crucial properties of a scaffold in terms of osteoconductivity, osteoinductivity and bioactivity, which is the bonding ability between bones (Canillas et al., 2016; Redondo et al., 2022; Y. Zhang et al., 2020).

1.6.1 Hydroxyapatite

In humans, about 60 to 65% of the bone is made up of inorganic material known as hydroxyapatite [$\text{Ca}_{10}(\text{PO}_4)_6(\text{OH})_2$], which is one of the most stable forms of calcium phosphate (Ma, 2019). The modification of hydroxyapatite structure at the hydroxyl (OH^-) group can also yield other bioceramics known as fluorapatite and chlorapatite by using either fluoride, chloride or carbonate (Malysheva et al., 2021; Rey et al., 2008), making HAp a versatile bioceramic. This material is often used in nanocomposite technology to mimic the fine structure of the natural bone while enhancing the load-bearing capacity of the composite to act as a promising bone scaffold (Devine et al., 2017; Venkatesan & Kim, 2010). Therefore, hydroxyapatite (HAp) is incorporated in the formulation for organ transplants, surgical reconstructive materials, and artificial prostheses to regenerate bone or treat organ failures (Cui et al., 2016; Rameshbabu et al., 2006; Venkatesan & Kim, 2010). Interestingly, HAp can also be utilised as orbital implants or ophthalmological prosthetics, percutaneous implants, and artificial blood vessels (Costa-Pinto et al., 2021).

Furthermore, the nanocrystalline form of hydroxyapatite is validated to have a better effect on promoting osteoblast adhesion, proliferation and apatite formation, which can be synthesised through several methods, including co-precipitation process,

mechanochemical reaction, emulsion precipitation, microwave synthesis and sol-gel approach (Galindo et al., 2019; N. Li, Wu, et al., 2019; Rameshbabu et al., 2006). However, the main drawback of HAp is the low solubility leading to a slower degradation rate up until more than a year (Pajor et al., 2019; N. Yang et al., 2016; Q. Zhang et al., 2021). Therefore, HAp is often paired with higher bioresorption materials to compensate for the slow degradation rate, thus leading to an ideal biodegradability *in vitro* and *in vivo*, followed by the placement in the body.

1.6.2 Tricalcium Phosphate

Tricalcium phosphate, $\text{Ca}_3(\text{PO}_4)_2$, is used in orthopaedic and dentistry applications for its similar inorganic chemical components of human bone tissues. It is commonly used as an alternative to hydroxyapatite for several reasons, where it is more soluble *in vivo* and has rapid bio-resorption without leaving traces behind (Canillas et al., 2016; Moreno et al., 2020; Szurkowska et al., 2020). There are two commonly used tricalcium phosphate (TCP) known as α -TCP and β -TCP. α -TCP is more soluble compared to β -TCP and mainly used as the injectable artificial bone repair materials since it possess an excellent self-setting property (T. Feng et al., 2020). It was previously shown that highly purified β -TCP imposed greater stability, osteoinductivity and osseointegration properties. In addition, β -TCP also has good biocompatibility both *in vitro* and *in vivo*, where it can directly bond (osseointegration) with the native bone (Choy et al., 2021; Y. Zhang et al., 2020).

Nevertheless, the low flexibility of tricalcium phosphate has led the researchers to modify this material by using other components leading it to more flexible features (Canillas et al., 2016; Ogose et al., 2005). To overcome this limitation, Taktak *et al.* (2018) then incorporated fluorapatite into β -TCP to maximise the mechanical properties of this biphasic ceramic to study the bioactivity response of this composite *in vivo* for use in bone graft substitute research. In addition, 3D poly (lactic-co-glycolic acid)/ β -tricalcium phosphate (3D-PLGA/ β -TCP) was also fabricated by Cao et al. (2020), while polylactic acid was chosen to be combined with the β -TCP by Salamanca et al. (2021), both to improve the flexibility if the ceramics.

1.6.3 Fluorapatite

Fluorapatite with the chemical formula $\text{Ca}_5(\text{PO}_4)_3\text{F}$ is another common phosphate mineral and is a highly insoluble calcium phosphate phase. Fluorapatite can be produced

synthetically from hydroxyapatite by complete substitution of hydroxide ions (OH^-) with fluoride ions (F^-), where it has the role of developing the skeletal and dental naturally while enhancing the acid resistance and hydroxyapatite stability. It is often accompanied by hydroxyapatite and forms solid solutions naturally in our bodies, such as bone and teeth (Nordquist et al., 2011; Pajor et al., 2019; Rameshbabu et al., 2006; Rey et al., 2008).

This bioceramic is widely used in the dental field due to the fluoride ions (F^-) present in fluorapatite and hydroxyl-fluorapatite that has a cariostatic effect with the ability to reduce demineralisation, thus promoting remineralisation of enamel through the restorative material (Beyth et al., 2014; Borkowski et al., 2020). This benefit is supported by a statement by the World Health Organization (WHO) stating that fluoride ions (F^-) are a vital substance, especially towards the enamel, in preventing the formation of dental cavities and promoting healthy bone growth. FAp was also shown to be well-integrated with the adjacent tissues (K. Zhou et al., 2023). In addition, fluoride ions in fluorapatite can also reduce the adhesion of the biofilm and bacteria cells and increase the sensitivity to acidic medium in the presence of these ions. However, excess F^- is detrimental on human osteoblast-like cells such as a reduced osteoconductivity and mechanical properties, thus requiring a proper control of the amount of F^- in the bone regeneration scaffolds (Anastasiou et al., 2019; Borkowski et al., 2020; Kulshrestha et al., 2016).

Furthermore, the documented antimicrobial properties of fluorapatite have led to an increased interest in developing novel biomaterials to mitigate bacterial infection and colonisation around implants and scaffolds, which is a deleterious clinical problem in both regenerative orthopaedics and dentistry (Anastasiou et al., 2019; Malysheva et al., 2021). FAp is commonly combined with other materials to enhance the desired properties of developed composite. Previously, it was used together with a poly-ether ether ketone (PEEK) in dental implants to support the lack of bacterial activity, and the binding ability of PEEK to the natural bone tissue in research carried out by Wang *et al.* (2014). In addition, FAp was reported to reduce the fragility and the weak rupture resistance of the β -TCP ceramics upon incorporation (Taktak et al., 2018).

1.7 Promoting Signalling Molecules for Bone Healing Treatment

Bone signalling molecules, mainly known as growth factors (GF), are the proteins secreted from cells that function as the communication network in the cellular environments by giving signals for specific actions to a targeted cell, including cell

proliferation and differentiation. The growth factors are in the interest of many researchers due to their expression during bone fracture healing, and making them an essential component in bone tissue engineering (Y. Liao et al., 2020; Oliveira et al., 2021).

Growth factors loaded into a scaffold play a significant role in bone regeneration since they will aid the osteoprogenitor cells to migrate and proliferate before differentiating to regenerate the bone. There are several popular bioactive agents among the researchers, such as bone morphogenetic proteins (BMP), wingless/integrated (Wnt), vascular endothelial growth factors (VEGF) and fibroblast growth factors (FGF), as well as recombinant human platelet-derived growth factor (rhPDGF). These GF are mainly responsible for enhancing the proliferation and differentiation of cells, as well as their involvement in angiogenesis and osteogenesis (Glatt et al., 2021; Z. Wang et al., 2017; Yi et al., 2016).

Wnt signalling pathway is responsible for cell function regulation like osteogenesis and differentiation of the cells. However, Wnt can interfere with the chondrocytes and adipocytes formation (T. Feng et al., 2020; Guler et al., 2021; Yi et al., 2016). It was also reported that it failed in repairing the bone when the mesenchymal stem cells (MSC) did not differentiate into osteoblast, although its proliferation in the mice model increased when they incorporated Wnt with β -catenin (Y. Chen et al., 2007).

Generally, VEGF, FGF and also placental growth factors were utilised to repair most tissue types, while the most extensively used growth factors for the new bone induction in repairing bone tissues were transforming growth factor-beta (TGF- β) and BMPs, commonly BMP-2, BMP-4 and BMP-7. These various types of BMPs have different organs of expression, as well as the individual functions (Borok et al., 2020; Sheikh et al., 2015). However, BMP-2 and BMP-7 had raised the attention of the researchers due to the fact of being among the BMPs that had acquired FDA approval (Z. Wang et al., 2017; Wei et al., 2020). Furthermore, another two bone grafts incorporated with growth factors that have acquired FDA approval are known as AUGMENT[®] (β -TCP granules and a collagen matrix with rhPDGF) for the fusion procedures of the ankle and hindfoot, and also i-Factor (P15 infused hydroxyapatite particles suspended in a hydrogel vehicle) (Arnold et al., 2021; Govoni et al., 2021).

1.7.1 Bone Morphogenetic Protein-2

A commonly used bone-forming factor among researchers is a bone morphogenetic protein (BMP), a member of the β -transforming growth factor (β -TGF). It was approved by the FDA in 2002 for use in bone-regenerative scaffolds (Bessa, P.C., Casal, M. and Reis, 2008; Govoni et al., 2021; James et al., 2016). Its sequence was first identified by Wozney *et al.* in 1989 and validated to have the ability to induce the mice endochondral cells' ossification process (Gimble et al., 1995). There are over 40 types of BMPs available since it was found, such as BMP-2, BMP-3, BMP-4, BMP-5, BMP-6 and BMP-7, but in the bone regeneration process, BMP-2 and BMP-4 will have higher expression in the early stages (Dimitriou et al., 2005). This information is vital for bone tissue regeneration engineers to investigate the proliferation and differentiation process of the cells in demineralised bone. Besides the pleiotropic nature of the BMP-2, which can intensify fracture healing, it gathers the stem cells to the site of injury before differentiating them into osteoblast, together with the angiogenesis stimulation towards better vascularisation (Reves et al., 2011).

In addition, BMPs play a significant task in regulating cell proliferation, osteoblast differentiation, embryonic development and further bone development, as well as in organogenesis and apoptosis (Borok et al., 2020; Chao et al., 2021; Saito et al., 2003). Nevertheless, their molecular pathway regarding osteoblast differentiation remains the need for further exploration. Subsequently, the adverse effects associated with BMP-2 including abnormal osteoclast differentiation that causes increased bone resorption is also a concern regarding its use (Lee et al., 2021; Xiong et al., 2020).

Although the effectiveness of BMP-2 in speeding up bone healing has been validated, the studies on its performance on critical-sized defects and non-unions are still ongoing (Hettiaratchi et al., 2020; Lee et al., 2021; Rosenberg et al., 2019; Tsiklin et al., 2022). This growth factor has been utilised in a collagen sponge carrier; however, its main limitation was the burst release, where it was recorded that approximately 50% of BMP-2 was released in the first 2.5 days and a complete release after two weeks, leading to limited bioavailability in situ (Busch et al., 2021; Huber et al., 2017; Wigmosta et al., 2021).

1.7.2 Peptides derived from Bone Morphogenetic Protein-2

Researchers have also derived osteogenic peptides from BMP group proteins due to their small relative molecular weight, known physiological effect, flexibility to use, as well as lower cost demands (Meng et al., 2021; Xiong et al., 2020; J. Zhou et al., 2020). There are two sites of interest in the complex structure of BMP-2 dimer, known as wrist and knuckle epitope regions (Figure 1.9). Extensive reports were proposing the ability of peptides derived from this knuckle region to induce osteogenesis, thus enabling it to substitute the full-length of rhBMP-2 (Bain et al., 2015; Cui et al., 2016; Saito et al., 2003; Y. Wu et al., 2020).

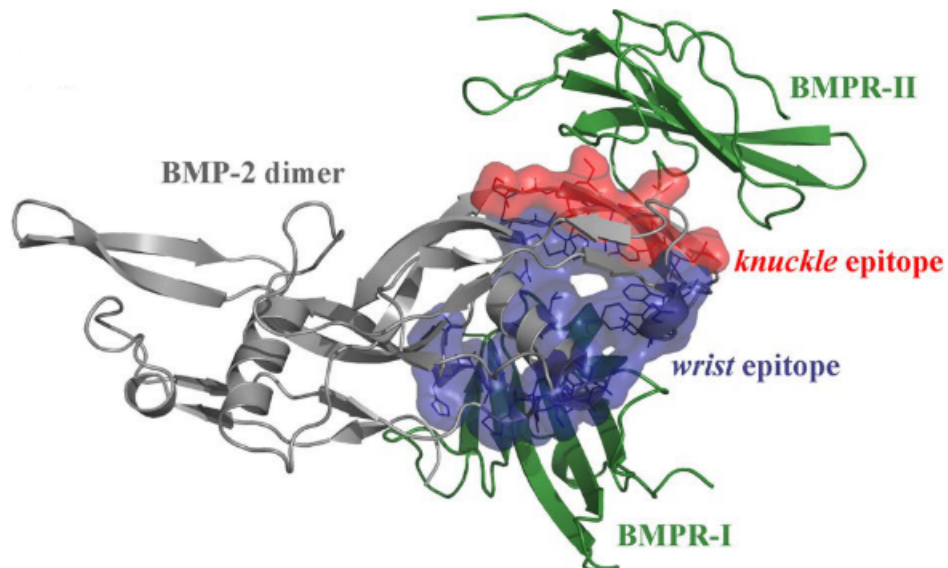


Figure 1.9 Modelled complex structure of BMP-2 dimer, highlighting the wrist and knuckle epitope region of the BMPR-I and BMPR-II cognate receptors, respectively (Y. Wu et al., 2020).

Initially, a synthetic peptide, P4, synthesised from the knuckle epitope of BMP-2 (73-92), was reported to increase the alkaline phosphatase (ALP) and osteocalcin activity to the highest levels in the murine multipotent mesenchymal cell line, C3H10T1/2, compared to the other BMP-2 derived peptides, P1, P2, P3, P4sp, P5 and P6 (68-87, 68-92, 78-97 and 44-58) (Ahn & Je, 2019; Saito et al., 2003). This BMP-2 knuckle epitope derived peptide (P4) has also shown to increase the osteopontin and mineral deposition in clonally derived murine mesenchymal stem cells (7F2) (Madl et al., 2014). Subsequently, another short BMP-2 related peptide called P24 with a molecular weight of 2630.88 g/mol was then synthesised, that can regulate bone-repairing responses similar to P17 and P20. This peptide consists of chemically stable small molecules and a linear structure as a biological

active site, and is believed to promote bone marrow stromal cell adhesion, enhance ectopic osteogenesis, and repair critical-sized rabbit bone defects (Y. Chen et al., 2017; Niu et al., 2009; C. Wang et al., 2017).

Following the P24 synthesis, Cui *et al.* (2016) had improved the work mentioned above by synthesising a longer BMP-2 dimer-knuckle epitope derived peptide chain called P28. This P28 peptide was incorporated in silicon-doped HAp scaffold and shown to induce a similar osteoinductive function as rhBMP-2 itself (Cui et al., 2016, 2018). P28 indeed possess several significant properties compared to BMP-2 in terms of its smaller relative molecular weight and better chemical stability that can improve its biological effects (Meng et al., 2021). The most impressive feature of P28 in this bone tissue engineering field is its repetitive amino acid sequences with high bonding ability towards calcium phosphate materials. This feature can lead to an extended release with higher delivery specificity to the intended site, thus giving a promising outcome to be discovered in future bone substitutes research (Meng et al., 2021; Xiong et al., 2020). Furthermore, the biomimetic feature of peptides in retaining the osteogenic features of the larger proteins offers greater control over cellular interactions. The shorter chains of peptides are advantageous in overcoming the steric effects, folding, immunogenicity and susceptibility to degradation problems of the larger proteins, thus leading to better signalling and binding domains availability for the required cellular interactions (Bullock et al., 2021).

1.8 Clinical Application of Protein and Peptide and its Related Issues

Other than the challenges faced in using BMP-2 such as the off-target complications, including ectopic calcification, transient bioactivity, and short half-life *in vivo*, researchers also need to overcome the insufficient mechanical strength of scaffold and lack of BMP-2 bioactivity (Huber et al., 2017; Sheikh et al., 2015; Xiong et al., 2020). Therefore, despite the great osteogenic features possessed by P28 as mentioned in the previous section, there is a need to design a fully-functional carrier, which is the scaffolds. The performance of bone substitute scaffolds can be improved by tuning the scaffold composition and its fabrication method, as well as incorporating the osteoinductive therapeutic ingredients. Several methods can be considered in fabricating the best binding or incorporation method of the osteogenic factors to the bone scaffolds (Blackwood et al., 2012), visualised in Figure 1.10.

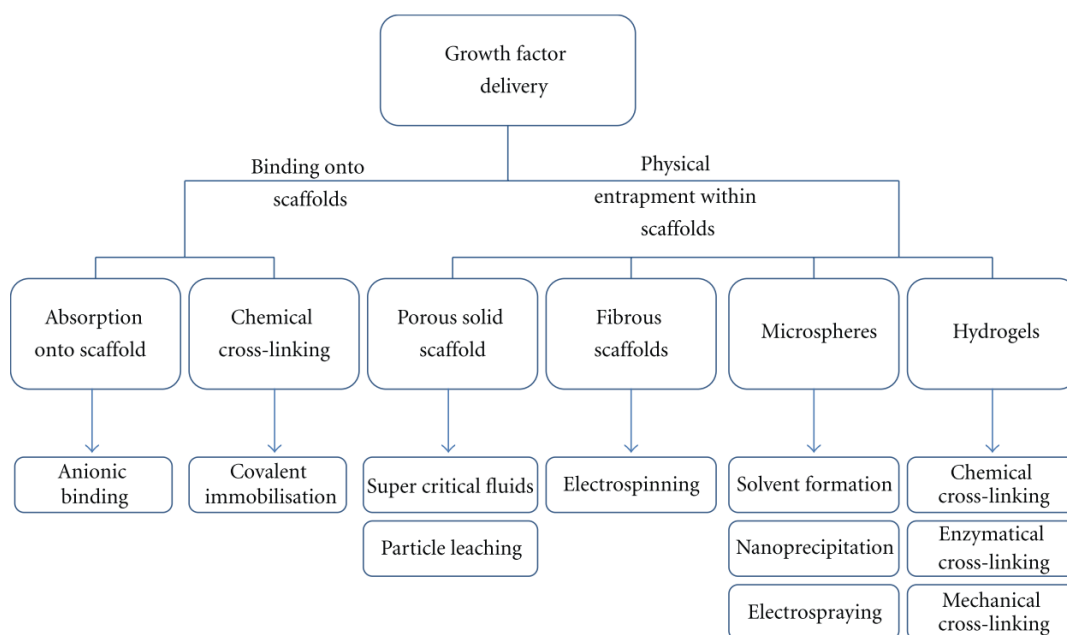


Figure 1.10 Current methods for fabricating GF-loaded scaffolds, mainly binding the GF to the scaffolds and the physical entrapment within scaffolds. (Blackwood et al., 2012)

The researchers used two approaches in incorporating growth factor to the vehicles: binding the growth factors directly onto the scaffolds or entrapping the growth factors within the porous scaffolds. The most commonly used method is just by soaking the pre-fabricated scaffolds in a solution containing a high concentration of growth factors with or without buffers, such as BMP-2 due to its high binding capacity (Amariei et al., 2018; Durham et al., 2018; Gherasim et al., 2021; Suliman et al., 2015; Yun et al., 2013). However, this physical immobilisation method requires a very high loading concentration of growth factors, resulting in less binding efficiency, thus increasing the cost needed. These physical methods can also lead to the burst release phenomenon without a stable combination (Meng et al., 2021; Paxton et al., 2020; H. Zhang et al., 2010).

In order to ensure better growth factor release control while maintaining its therapeutic effects, more advanced technologies were considered in loading the growth factors into the scaffolds, including encapsulating the growth factor in microspheres before embedding them into the scaffolds, as well as covalently crosslinking the growth factors through the enzymatical reaction between the materials (Blackwood et al., 2012; He et al., 2018; Mumcuoglu et al., 2018; Suliman et al., 2015). Furthermore, a one-step photocrosslinking of the osteogenic agents into the scaffolds under UV light has also caught the interest of the tissue engineering researchers, where this method eliminates the step of functionalising photoreactive materials to the growth factors before incorporating

them into the scaffolds (T. M. De Witte et al., 2020; Devine et al., 2017; Julia E. Samorezov & Alsberg, 2016; Masters, 2011). Previously, it was reported that the UV treatment on bovine serum albumin (BSA) in the presence of riboflavin photosensitiser did not induce protein denaturation, shown by the unchanged Amide I and Amide II bands of this BSA hydrogel in FTIR spectra (Rusu et al., 2019). However, the functionality of the UV-crosslinked growth factors on scaffolds such as the osteogenicity following the procedures is still insufficient, requiring a more detailed investigations.

Based on the extensive information outlined in this section, our proposed body of work has covered the modification of chitosan scaffold fabrication in terms of crosslinking reaction, with several types of bioactive ceramics incorporation, different amount of photoinitiator application and the tests for equivalent crosslinking time for the scaffolds. The studies on the mechanical properties and biodegradation behaviour, as well as the release profile, were also outlined in this document, while the incorporation of several bone-inducing factors was addressed in terms of their bioactivity. Finally, the bone regenerative capacity of the growth factors-crosslinked scaffolds was described through the implantation of the scaffolds in the femoral condyle defects of Sprague Dawley rats, with several modifications in the scaffold formulations for the subsequent animal testing.

1.9 Research Question

Can the controlled release of low doses of osteoinductive agents covalently-linked to biodegradable scaffolds result in equivalent bone healing to commercially available products?

1.10 Objectives

- 1) To optimise the fabrication method of bone regeneration scaffolds to enhance the mechanical properties that will lead to a higher load-bearing capacity of the scaffolds.
- 2) To tune the biodegradation profile of the scaffolds while reducing the burst release response and extending the release of the osteoinductive agents from the scaffolds.
- 3) To investigate the osteogenicity of P28 peptide as an alternative osteoinductive agent to the existing FDA-approved BMP-2 treatment for bone healing.
- 4) To validate the osteoinductivity of the osteogenic agents following the covalent bonding to the scaffold under UV-crosslinking procedures.

- 5) To investigate the ability of the osteoinductive agent-loaded scaffolds in forming new bone following implantation in the rat femoral condyle defect model.
- 6) To introduce antimicrobial functionality by developing fluorapatite from hydroxyapatite prior to incorporating it into scaffolds and thus leading to antimicrobial, osteoconductive scaffold composite formulation.

Chapter 2

Chapter 2: Materials and Methods

2.1 Materials

Chitosan, high molecular weight (MW) (419419-50G), Hydroxyapatite (04238-1KG), Ethanol $\geq 99.8\%$ (51976-500ML-F), Water for HPLC (270733-2.5L), Phosphoric acid ≥ 85 (438081-500ML), Sodium fluoride $\geq 99\%$ (S7920-100G), Trifluoroacetic acid 99% (T6508-100ML), Phosphate buffered saline (P4417-50TAB), Hydrochloric acid, ACS reagent (258148-500ML), C2C12 Mouse C3H Muscle Myoblast (91031101-1VL), Dulbecco's Modified Eagle's Medium-high glucose (D1145-500ML), Trypsin-EDTA Solution 1X (59428C-500ML), Fetal Bovine Serum (F7524-500ML), Penicillin-Streptomycin (P4333-20ML) and L-Glutamine solution (G7513-20ML) were obtained from Sigma Aldrich. Human/Murine/Rat BMP-2 (E.coli) (120-02) were purchased from Peprotech (Peprotech House, London, United Kingdom), while P28 Peptide sequence $>98\%$ purity was synthesised by Pepmic (Pepmic Co. Ltd., Suzhou, China). Sodium bicarbonate 99.5% was purchased from Acros Organics (Fisher Scientific UK Ltd, Loughborough, United Kingdom), Poly(ethylene glycol) (600) dimethacrylate (02364-100) was obtained from Polysciences Inc. (Polysciences Europe GmbH, Germany) and Benzophenone, 99% (A10739.30) was purchased from Alfa Aesar (Thermo Fisher (Kandel) GmbH). Water HPLC Gradient for HPLC 2.5L (CC34877-2.5L-F) and Acetonitrile Hplc Chromasolv Gradient Grade 99.9% 2.5L (CC34851-2.5L-F) were purchased from Lennox. PLRP-S 300A 3uM 150X4.6MM (AGIPL1512-3301) and InfinityLab Deactivator Additive (25mL) (AGI5191-3940) were obtained from APEX Scientific (APEX Scientific Ltd., Maynooth, Kildare. Powder for Induct Os 1.5mg/ml 12 mg Dibotermis Alfa and Collagen Sponge Matrix for InductOs Bovine Type I Collagen were generously provided by Medtronic (Medtronic BioPharma, Watford, United Kingdom). Ketamine, 90 mg/kg (Narketan[®]-10, Vetoquinol UK Ltd.), Xylazine, 5 mg/kg (Xylaxin[®], Med Vet Biolinks Pvt. Ltd., India), Lidocaine hydrochloride injection 2%, 4 mg/kg (Anacaine, USA) and Isoflurane gas (Abbot Laboratory Ltd., England) were used for general anaesthesia. Ethanol, povidone-iodine (Betadine[®], USA), chlorhexidine (Hibiscrub[®], UK), Opsite spray (Smith and Nephew, England) and normal saline (RinsCap[®], Ain Medicare, Malaysia) were also used. Double-fluorochrome injections: Calcein and xylenol orange tetrasodium salt were purchased from Sigma Aldrich, UK.

2.2 Fabrication of Chitosan Composite Scaffolds

2.2.1 Optimisation of Chitosan Composite Scaffold through Extended UV Crosslinking

A chitosan-based scaffold was prepared by dissolving 1.5 g of high MW chitosan powder in 12.5 ml of 1% (v/v) acetic acid, yielding a 12% (w/v) paste. The paste was left on the bench for an hour, allowing a protonation reaction to occur before being neutralised in 0.1 M sodium bicarbonate solution for 10 min. It was then pressed between filter papers to remove excess sodium bicarbonate solution. Subsequently, 100 μ l of PEGDMA600 and 50 μ l of 0.1% (w/v) benzophenone in ethanol were consecutively added to the paste and mixed well. The chitosan paste was then transferred into silicone moulds to make 20 mm circular tablets and subjected to an ultraviolet (UV) crosslinking process using a UV curing system (Dr. Gröbel UV-Electronik GmbH, Opsytec Dr. Gröbel, Ettlingen, Germany) under 20 UV lamps with a spectral range between 315–400 nm and at the average intensity of 10–13.5 mW cm² for 40 min. All the samples were flipped over mid-process. This crosslinking time was determined experimentally in the previous investigations to be sufficient to cure the composites (Devine et al., 2017; Killion et al., 2011, 2014).

2.2.2 Incorporation of Hydroxyapatite (HAp) and Tri-Calcium Phosphate- α (TCP- α) into Chitosan Scaffold

Table 2.1 Chitosan scaffold formulations with bioactive ceramics.

	Weight (g)			Volume (μ l)		Volume (ml)	
	CS	HAp	TCP- α	BP	PEG600DMA	Acetic acid	
CS+HAp +TCP-α	1:0:0	1.5	0	0	50	100	12.5
	1:1:0	1.5	0	0	50	100	12.5
	2:1:0	1.5	0	0	50	100	12.5
	1:0:1	1.5	1.5	1.5	50	100	12.5
	2:0:1	1.5	0.75	0.75	50	100	12.5
	2:1:1	1.5	0.75	0.75	50	100	12.5

Annotations: CS: chitosan; HAp: hydroxyapatite; TCP- α : tri calcium phosphate- α ; BP: benzophenone; PEG600DMA: polyethylene glycol dimethacrylate 600

Chitosan paste was prepared as per section 2.2.1. Following the addition of benzophenone, various ratios and combinations of scaffold formulations were made by

adding HAp and/or TCP- α into chitosan paste with ratios as shown in Table 2.1. After mixing, the sample pastes were placed in the silicon moulds and cured as outlined in Section 2.2.1.

2.2.3 Preparation of Fluorapatite into Chitosan Composite

Fluorapatite (FAp) was prepared from hydroxyapatite and sodium fluoride through the chemical substitution method (Campillo et al., 2010; Nordquist et al., 2011) before incorporating this material into chitosan-based scaffolds. A solution of 10 mol/litre phosphoric acid (H_3PO_4) was prepared by making up 6.85 ml H_3PO_4 with water in a 10 ml volumetric flask. The high acid concentration was made to dissolve sodium fluoride (NaF). Subsequently, 3.2 ml of the acid solution prepared in a beaker was added to 4.6 g of NaF. The mixture was subjected to magnetic stirring until all the NaF was dissolved. Once all the NaF was dissolved, the solution was added gradually into 5 g of hydroxyapatite powder until mixed thoroughly. The fluorapatite powder was finally obtained at the end of the process (Figure 2.1). This FAp powder was sent to scanning electron microscopy (SEM) to analyse the elements present. This FAp powder was then incorporated into chitosan paste similar to the HAp and TCP- α mixing method in section 2.2.2, making CS/FAp composite (1:1).



Figure 2.1 Fluorapatite (FAp) powder prepared through chemical substitution method.

2.2.4 Chitosan/Hydroxyapatite Blend using Various Amounts of Photoinitiator

Four beakers of chitosan paste with hydroxyapatite were made as outlined in section 2.2.2. However, different amounts of 0.1% (w/v) benzophenone (50, 20, 5 and 1 μ l) were added into CS/HAp paste to investigate the effect of the photoinitiator concentrations on the scaffold degradation profile and followed by UV curing as mentioned in section 2.2.1.

Table 2.2 Scaffold compositions with various benzophenone concentrations.

	Weight (g)		Volume (μ l)	Volume (ml)	
	CS	HAp	BP	PEGDMA 600	Acetic acid
CS/HAp	1.5	1.5	20	100	12.5
1:1	1.5	1.5	5	100	12.5
	1.5	1.5	1	100	12.5

Annotations: CS: chitosan; HAp: hydroxyapatite; BP: benzophenone; PEGDMA600: polyethylene glycol dimethacrylate 600

2.2.5 Chitosan Composite Fabrication using Different Crosslinking Time in UV Curing Chamber

In order to test the effect of different UV curing times on different scaffold sizes, two sets of chitosan/hydroxyapatite (CS/HAp) scaffolds of two different sizes, 2.1 and 0.5 cm in diameter, were made as outlined in section 2.2.4 with 5 μ l 0.1% (w/v) benzophenone. The scaffolds in both sizes were UV-cured for 10, 20, 30 and 40 minutes. All of the samples were flipped mid-curing.

2.2.6 Osteogenic Factor Incorporation into Chitosan/Hydroxyapatite Scaffolds

CS/HAp scaffold with 5 μ l 0.1% (w/v) benzophenone (0.5 cm diameter) was prepared prior to the growth factor and peptide incorporation. Briefly, 1.5 g of high molecular weight chitosan was dissolved in 12.5 ml 1% v/v acetic acid and left on the bench for an hour. The chitosan paste was then neutralised in 0.1 M sodium bicarbonate solution for 10 min before being pat-dried with filter paper. Subsequently, 100 μ l of PEGDMA600 and 5 μ l of 0.1% w/v benzophenone in ethanol were consecutively added and thoroughly mixed. HAp powder of a similar ratio to chitosan was then added to the paste and mixed thoroughly. The BMP-2 and P28 peptide powder were reconstituted in ultrapure water to provide 20 μ g/ml and 5000 mg/ml solutions, respectively. Then, either 5 μ l of the BMP-2 solution or P28 was injected into each scaffold, making CS/HAp/100 ng BMP-2 and CS/HAp/25 μ g P28 scaffolds. Samples were then UV-cured for 10 min and flipped over

mid-curing. Following the UV curing, all scaffolds were kept in a sterile container and frozen at $-20\text{ }^{\circ}\text{C}$ until they were ready to use. CS/HAp control scaffolds without osteogenic factors were made in the same manner.

2.2.7 Chitosan-based Scaffolds for *In vivo* Implantation

For the initial *in vivo* test, CS/HAp scaffolds were made as outlined in section 2.2.6. However, 2 mg/ml rhBMP-2 and 5 mg/ml P28 were prepared before injecting 5 μl of the solutions into scaffolds prior to UV crosslinking to make CS/HAp/10 μg rhBMP-2 and CS/HAp/25 μg P28, respectively.

Subsequently, another animal trial utilised six different formulations with varied chitosan molecular weights, bioceramics ratio and P28 peptide concentrations: 12% LW CS/HAp/FAp 1:1, 12% HW CS/HAp/FAp 1:1, 12% HW CS/HAp/FAp 1:0.75, 12% HW CS/HAp/FAp 1:1/P28 25 μg , 12% HW CS/HAp/FAp 1:1/P28 75 μg and 12% HW CS/HAp/FAp 1:1/P28 150 μg . The compositions of these scaffolds are outlined in (Table 2.3) and UV-cured similar to the steps detailed in section 2.2.6.

Table 2.3 Scaffold compositions for the second *in vivo* implantation.

Ratio	Weight (g)				Volume (μl)		Volume (ml)	
	HAp:FAp	CS (MW)	HAp	FAp	BP	PEGDMA 600	5 mg/ml P28	Acetic acid
1:1	(LW)	1.5	0.75	0.75	5	100	0	12.5
1:1	(HW)	1.5	0.75	0.75	5	100	0	12.5
1:0.75	(HW)	1.5	1	0.75	5	100	0	12.5
1:1	(HW)	1.5	0.75	0.75	5	100	5	12.5
1:1	(HW)	1.5	0.75	0.75	5	100	15	12.5
1:1	(HW)	1.5	0.75	0.75	5	100	30	12.5

2.2.8 Pulse UV Sterilisation of Osteogenic Factor Incorporated Chitosan/Hydroxyapatite Scaffold

All chitosan/hydroxyapatite (CS/HAp) scaffolds were sterilised using a bench-scale Pulsed-UV chamber (Samtech Pulsed UV system, Samtech Ltd., Glasgow, Scotland) (Figure 2.2). A low pressure (60 kPa) flash lamp containing xenon gas (Heraeus Noblelight XAP type NL4006 series encased in a clear UV transparent quartz tube) was

connected to this chamber. This flash lamp generated a high-intensity broad spectrum polychromatic pulsed light beam between 200-1100 nm (Kelly, 2019). This method was preferred over liquid sterilisation due to the concern that liquid such as isopropyl alcohol (IPA) might wash out the osteogenic factors from the scaffolds before the treatment in the cells.

Before starting the sterilisation procedures, scaffold discs were placed in three different petri dishes and labelled according to the formulations. The voltage was set to 800 V. The setting button and the pulse control were set to be 'auto' and one pulse/second, respectively, shooting 90 UV pulses of 800 V onto the scaffolds.

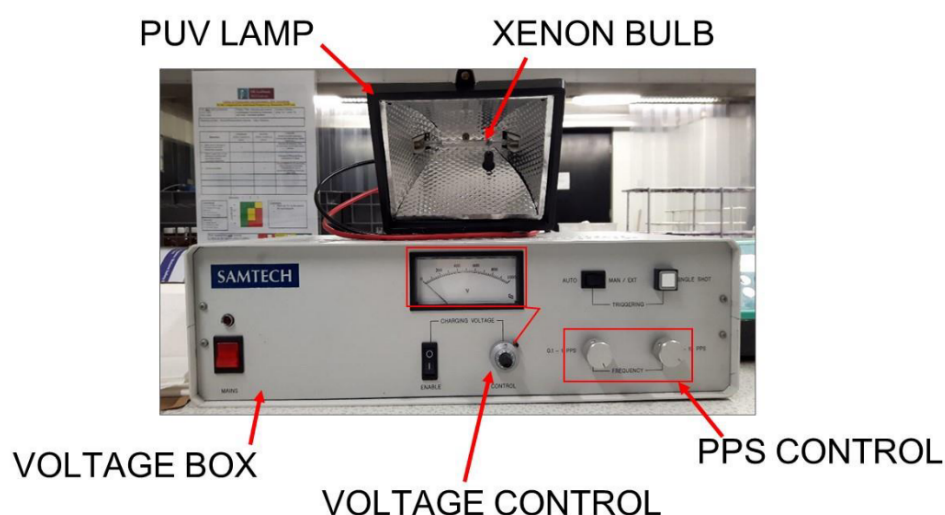


Figure 2.2 Pulse-UV chamber with xenon flash lamp utilised for scaffold sterilisation (Kelly, 2019).

2.3 Crosslinking Test

Crosslinking testing was carried out by submerging all types of the scaffold in 1% (v/v) acetic acid for 5 minutes, 1.5 hours and 24 hours to qualitatively assess the linkage formed between the materials post-UV curing process.

2.4 Fourier-Transform Infrared Spectroscopy

An attenuated total reflectance (ATR) Fourier-transform infrared (FTIR) spectroscopy was utilised to study the linkage and structural properties of the scaffolds using a Perkin-Elmer Spectrum One FTIR spectrometer fitted with a universal ATR sampling accessory. A spectral range of 4000-650 cm^{-1} and four scans per sample cycle were carried out, with a resolution of 0.5 cm^{-1} at room temperature.

All samples were dried in a vacuum oven at 37 °C and 70 mbar prior to the tests to avoid the broad water peak from shadowing the significant signature peaks of the materials. All spectra obtained were analysed following the tests to observe the linkage formed within all the formulations.

2.5 Compression Test

Compression testing was carried out to assess the strength of the scaffold fabricated using a Lloyd LRX tensometer (Lloyd Instruments Ltd., Hampshire, England) with a 2.5 KN load cell in compression mode, and the results were analysed in NEXYGEN™ software. The samples were dried using a vacuum oven (Salvis Lab Vacucenter VC50, Rotkreuz, Schweiz) at 37°C and 70 mbar for 24 hours prior to testing. Then, they were submerged in phosphate-buffered saline (PBS) for an hour prior to testing. The PBS solution was made by dissolving a PBS tablet in 200 ml of deionised water, yielding a pH of 7.4. Their weight was recorded using an analytical balance (Denver Instrument M-310, Bohemia, New York) and denoted as w_0 .

Subsequently, the compression test was carried out at a rate of 0.5 mm/min and set to stop at 60% strain. The Young's modulus values of all the samples obtained from the software were analysed.

2.6 Simulated Body Fluid Preparation

Simulated body fluid (SBF) was prepared as outlined by Kokubo and Takadama (2006). First, 1500 ml ultra-pure water was poured into a 2L beaker and covered with a watch glass, and it was subjected to magnetic stirring at 36.5 °C. Eight reagents were added consecutively following the dissolution of the previous reagent (Table 2.4). After reagent eight (Sodium sulphate, Na_2SO_4) was added to the mixture, the volume of the solution was made to be 1800 ml by adding water. A pH meter was used to monitor the pH value, which was found to be a pH 2 due to the presence of the acidic reagents before adding reagent nine. This reagent (tris-hydroxymethyl aminomethane) in Table 2.4 was added gradually to avoid an excessive increase in the pH of the solution. The addition of reagent nine was stopped when the pH reached 7.45. A few drops of 1M HCl were added to bring the pH value to 7.42. This process was repeated until the whole amount of reagent nine was added to the SBF solution.

The temperature was kept to be 36.5 °C throughout the experiment. The SBF solution was then transferred into the 2L volumetric flask, and ultra-pure water was added to adjust the

volume of the solution to two litres. It was then allowed to cool for an hour at room temperature, and the volume of the solution was expected to decrease upon cooling and so the volume of solution was adjusted again by adding ultra-pure water until it reached the graduation mark. The flask was then closed and lightly shaken. The solution was transferred to a 2L polypropylene bottle and stored in the refrigerator at 4 °C. The stability of the solution was tested by transferring 50 ml of the solution into a bottle and left in an incubator at 36.5 °C. After 2-3 days, it was examined to determine any precipitate formation. If precipitation was present, the solution was discarded and remade.

Table 2.4 The chemical components used in preparing the simulated body fluid.

Order	Reagent	Amount
1	Sodium chloride, NaCl	16.7 g
2	Sodium bicarbonate, NaHCO ₃	0.71 g
3	Potassium chloride, KCl	0.45 g
4	Dipotassium hydrogen phosphate trihydrate, K ₂ HPO ₄	0.462 g
5	Magnesium chloride, MgCl	0.291 g
6	Hydrochloric acid, HCl (1M)	78 ml
7	Calcium chloride, CaCl	0.584 g
8	Sodium sulphate, Na ₂ SO ₄	0.144 g
9	Tris-hydroxymethyl aminomethane (CH ₂ OH) ₃ CNH ₂	12.236 g
10	Hydrochloric acid, HCl (1M)	X ml (For adjusting pH)

2.7 Degradation Assessment

Three batches of samples were subjected to degradation assessment in the previously made simulated body fluid (SBF). The first batch applied different bioactive ceramics incorporated in the scaffold formulations. In contrast, the second batch consisted of varying amounts of benzophenone (BP) in the CS/HAp scaffold, and fluorapatite was added as the third batch of the degradation profile assessment. All the formulations were prepared as described earlier, and the compositions are listed (Table 2.5).

Table 2.5 The scaffold composition utilised for degradation test.

Batch No.	Composition	Number of samples (n)
1	CS/HAp (1:1) with 50 µl BP	5
	CS/TCP-α (1:1) with 50 µl BP	5
	CS/HAp/TCP-α (2:1:1) with 50 µl BP	5
2	CS/HAp with 20 µl BP	3
	CS/HAp with 5 µl BP	3
	CS/HAp with 1 µl BP	3
3	CS/FAp with 20 µl BP	3

Annotations: CS: chitosan; HAp: hydroxyapatite; TCP-α: tri calcium phosphate-α, FAp: fluorapatite; BP: benzophenone

The samples were dried in a vacuum oven at 37°C and 70 mbar for 24 hours. The dried weight of each of the samples was measured and noted as the dried weight before degradation, w_0 . The samples were then placed into small petri dishes with lids, and 5 ml of SBF were added to each of the petri dishes. The dishes containing the scaffold samples were wrapped with parafilm and kept in the oven (Gallenkamp Hotbox Oven with Fan Size 1, Sanyo, Weiss) at 37°C under static conditions. The SBF solution for all samples was refreshed twice a week.

All samples were collected at weeks 0, 1, 2, 4, 8, and 16 or until the samples were disintegrated during handling. Their integrity was assessed during handling before being subjected to compression testing to evaluate their degradation profile and strength while degrading. The scaffolds' dry weight before and after the test were recorded, and the percentage weight of the materials washed off the scaffolds over eight weeks was calculated (n=3) by using the formula below (Y. Chen, 2018; X. Liu et al., 2014; Saravanan et al., 2011).

$$\text{Degradation weight} = (w_0 - w_1) / w_0 \times 100$$

w_0 represents the initial dry weight, and w_1 represents the final dry weight.

2.8 Swelling Studies

Swelling studies were conducted on the crosslinked scaffolds (n=3) with different bioceramic formulations (CS/HAp, CS/TCP-α and CS/FAp) and also the varied photoinitiator amount (CS/HAp with 20, 10 and 5 µl of 0.1% w/w benzophenone) to quantitatively assess the cross-linkage formed within the biomaterials.

The scaffolds with an average mass of 2.45 g each were dried in the vacuum oven at 37 °C and 70 mbar for 72 hours before recording the dry weight, w_d . The scaffolds were then submerged in 1% acetic acid for 48 hours before drying them again in the vacuum oven for 72 hours to assess the effectiveness of the crosslinking reaction. The final equilibrium dry weight was recorded and denoted as w_{ef} before calculating the gel fraction in acetic acid (GF_{AA}) by using the following formula:

$$GF_{AA} = \frac{w_{ef}}{w_d} \times 100$$

Subsequently, a new set of scaffolds as detailed above were further submerged in pH 7.4 PBS at ambient temperature for 48 hours until the samples had reached swelling equilibrium. The samples were pat dried using filter papers, and the weight was recorded as w_s . Subsequently, the scaffolds were dried again in the vacuum oven for 72 hours until they reached equilibrium dry weight, w_e . The swelling percentage, equilibrium water content (EWC), water uptake (WU) and gel fraction in PBS (GF_{PBS}) of the scaffolds was calculated by using the formulas:

$$\% \text{ Swelling} = \frac{w_s}{w_d} \times 100$$

$$EWC = \frac{(w_s - w_d)}{w_s} \times 100$$

$$WU = \frac{(w_s - w_d)}{w_d} \times 100$$

$$GF_{PBS} = \frac{w_e}{w_d} \times 100$$

2.9 Identification and Evaluation of Osteoinductive Factors-Release from Chitosan/Hydroxyapatite Scaffold

BMP-2 and P28 incorporated scaffolds, and the empty control scaffolds (CS/HAp/BMP-2, CS/HAp/P28 and CS/HAp) were defrosted to room temperature on the bench for ca. five minutes prior to use. All scaffold samples used in this study had a thickness of 3 mm and 5 mm in diameter. The samples were separately placed in 2 ml Eppendorf tubes and filled with 200 μ l of ultrapure water. Three scaffolds were used per formulation. (Figure 2.3). The scaffolds were then incubated at 37 °C in a 120 rpm incubator shaker (Innova 4000, New Brunswick Scientific) for the following time points: 1, 6, 24, 48, 72, 192, 264 and 336 h to release the covalently-bonded growth factors over these 14 days. Aliquots of 150 μ l were collected from each scaffold formulation at each time point and stored in

200 μ l tubes. Aliquots were frozen at -20 $^{\circ}$ C until testing ($n = 3$). The tubes were then refreshed with the same 150 μ l of ultrapure water.



Figure 2.3 The BMP2 and P28 scaffolds release sample setup.

2.9.1 High-Performance Liquid Chromatography Method Development for Bone Morphogenetic Protein-2 Release Analysis

The growth factor-release samples were analysed using high-performance liquid chromatography (HPLC) (Waters Alliance 2965 Separations Module, Waters Ges.m.b.H., Vienna, Austria) fitted with Waters 2487 Dual Wavelength Absorbance Detector (Figure 2.4). A BMP-2 standard was prepared to 30 ng/ml solutions and transferred into HPLC vials following the filtration using centrifugal concentrators at 12,000 rcf for ten minutes.

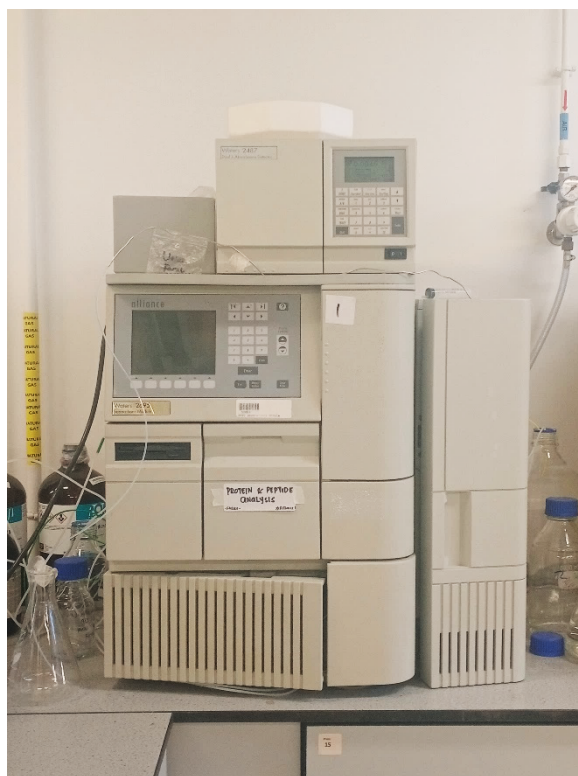


Figure 2.4 HPLC system equipped with a dual-wavelength UV detector used in the growth factor analysis.

In the beginning, a system suitability testing of two wavelengths (220 and 240 nm) was carried out by running six injections of each standard before calculating the mean, standard deviation (Std Dev) and percentage relative standard deviation (%RSD) following the run. This method was purposed to find the suitable wavelength and to ensure that the system set has a good reproducibility indicated by lower values of %RSD.

Subsequently, the HPLC system was set up to run the prepared protein standard. A PLRP-S column (Agilent Technologies, USA) with 3 μ m particle size, 300Å pore size and 4.6 x 150 mm dimensions was used with 220 nm wavelength set on the detector, while the flow rate was set to be 1 ml/min with an injection volume of 10 μ l. The runtime was set for 35 minutes to observe the elution of these standards at the retention time outlined at 28 minutes. The gradient-mobile phase was fixed with two compositions, A: 0.1% trifluoroacetic acid (TFA) in 100% water (H₂O) and B: 0.1% TFA in 100% acetonitrile (ACN) (Table 2.6).

Table 2.6 Gradient-mobile phase for BMP-2 analysis with A: 0.1% trifluoroacetic acid (TFA) in 100% water (H₂O) and B: 0.1% TFA in 100% acetonitrile (ACN).

Gradient/Time	A	B
0.1 min	74%	26%
25 min	49%	51%
25.1 min	0%	100%
30.0 min	stop	

The needle-wash solution of 90% of ACN: 10% H₂O and a maximum volume of this solution were utilised to rinse the needle to ensure the needle was thoroughly rinsed before the subsequent injections.

The release samples were prepared for the HPLC run from the earlier 150 µl frozen aliquots. The samples were thawed to room temperature for ten minutes, and 350 µl of ultrapure water was added to make up 500 µl total solution. Following that, all the samples were filtered by using centrifugal concentrators at 12 000 rcf for ten minutes to remove any particulate from the scaffolds that might be present. Then, they were transferred into HPLC vials and labelled.

Subsequently, the protein release samples and control were run in the same system set up as the standards before calculating the concentration of the release samples from the peak areas of the chromatogram by using the following formulas:

$$(i) \quad \begin{aligned} \text{Adjusted area} &= \text{Area of standard} - \text{Area of water (for standards)} \\ &= \text{Area of sample} - \text{Area of control (for samples)} \end{aligned}$$

$$(ii) \quad \begin{aligned} \text{Concentration of Sample} &= \text{Area of Sample} / \text{Area of Standard} \times \\ &\text{Concentration of Standard} \end{aligned}$$

2.9.2 High-Performance Liquid Chromatography Method Development for P28 Peptide Release Analysis

The HPLC system was set up using the mobile phase gradient outlined by the peptide supplier. A bioZen 2.6 µm WidePore C4 column (Phenomenex, USA) with 150 mm x 2.1 mm dimension was utilised to analyse the P28 peptide. The wavelength was set to 220 nm, and the flow rate was set to 0.3 ml/min with an injection volume of 10 µl. A column oven was set up to 30°C to reduce peptide viscosity in the mobile phase

throughout the system. A gradient mobile phase was utilised, with A: 0.1% TFA in 100% H₂O and B: 0.1% TFA in ACN (Table 2.7).

Table 2.7 Gradient-mobile phase for P28 analysis with A: 0.1% trifluoroacetic acid (TFA) in 100% water (H₂O) and B: 0.1% TFA in 100% acetonitrile (ACN).

Gradient/Time	A	B
0.1 min	85%	15%
25 min	45%	55%
30.0 min	0%	100%
31.0 min	stop	

Subsequently, a scouting gradient was applied since there was no peak was observed using the outlined gradient using the same mobile phase A and B (Table 2.8):

Table 2.8 Scouting gradient to identify the retention time of the analyte.

Gradient/Time	A	B
0 min	95%	5%
20 min	5%	95%
	stop	

Upon no analyte peak present, an isocratic mobile phase was used in a 5% A and 95% B mixture.

2.9.3 Preliminary P28 Peptide Release Analysis Using UV Spectrometer

Initially, both BMP-2 and P28-released samples were detected and analysed using the HPLC system. However, issues related to the high affinity of the osteoinductive agents towards the stainless-steel system were encountered, despite a number of troubleshooting executed to overcome these biocompatibility issues. The troubleshooting included increasing the needle wash volume and organic content of the wash, as well as conducting column cleaning procedures as enclosed by the supplier to ensure that the column was cleared from any protein contaminants to eliminate the pre-sampling peaks before the new sample run but to no avail.

Therefore, the amount of P28 released was quantified by using a UV-1280 UV Spectrometer (Shimadzu, Torrance, CA, USA) at 220 nm. The serial standards of P28 peptide were prepared at dilution factors of 1:20, 1:40, 1:80, 1:160, 1:320 and 1:640. The

percentage of the released P28 peptide from the scaffolds was calculated using the equation from the standard curve.

(i) Analyte concentration ($\mu\text{g/ml}$) = Concentration from equation \times dilution factor.

(ii) Mass of analyte (μg) = Analyte concentration \times volume of samples.

(iii) Percentage of analyte (%) = Mass of analyte \div Initial mass of P28 \times 100.

However, BMP-2 samples were unable to be analysed using this system since the concentrations of the initial concentration used fell below the detection limit of the UV spectrometer.

2.10 Resazurin Antimicrobial Assessment of the Scaffolds in Gram-Positive and Gram-Negative Bacteria

Resazurin, also known as Alamar blue, was utilised to investigate the antimicrobial capacity of the four developed scaffold formulations, CS/HAp, CS/HAp/BMP-2, CS/HAp/P28 and CS/FAp through the reduction of blue resazurin to pink fluorescent resorufin in the presence of metabolically active *Staphylococcus aureus* (*S.aureus*) and *Escherichia coli* (*E.coli*) bacteria (Van den Driessche et al., 2014). The colour changes in the resazurin or Alamar blue test would indicate the cell viability, where the aerobic respiration from the cell growth chemically reduces the blue resazurin dye to pink resorufin, while the minimum inhibitory concentration is achieved upon no dye reduction occurring (Bandeira et al., 2021; Garcia et al., 2021).

2.10.1 Liquid Bacteria Culture

Tryptic soy broth (TSB) was prepared by dissolving 15 g of TSB powder in 500 ml distilled water and sterilised using an autoclave. Subsequently, 55 ml TSB was poured into two separate conical flasks before adding a colony of *S.aureus* (ATCC 25923) and *E.coli* (ATCC 25922) bacteria in the flasks, respectively, using aseptic techniques. The flasks were incubated at 37 °C overnight.

The incubated bacteria strains were diluted in sterile universals by adding 1 ml of the bacteria in 4 ml TSB, and 3 ml of each of the diluted bacteria was transferred into three separate cuvettes, while TSB without bacteria was set as blank. The absorbance was read using a spectrometer at 600 nm, where the TSB blank was calibrated to '0'. The bacteria were then diluted to 1:10, and the absorbance was measured to be 0.01, leading to 10^6 CFU/ml, before further dilution to a final concentration of 10^4 CFU/ml.

2.10.2 Bacterial Plating

The bacteria were plated in two sets of 24-well plates for *S.aureus* and *E.coli*, respectively, by pipetting 25 µl of the bacteria solution into 500 µl TSB in each well. The bacteria were then treated using different scaffold formulations: CS/HAp, CS/HAp/BMP-2 and CS/HAp/P28. Wells without any treatments were set as the negative control. Subsequently, the plates were incubated at 75 rpm and 37 °C for 24 hours.

2.10.3 Resazurin Antimicrobial Assay

Resazurin stock solution (15 mg/ml) was diluted into 0.15 mg/ml before adding 75 µl of the solution into each well containing the samples and mixing by pipetting up and down. The plates were incubated at 37°C for two hours. The colour changes were observed, where the bacteria present will reduce the blue resazurin to pink prior to reading the absorbance at 600 nm with ten seconds of pre-shake using Biotek® Synergy HT Microplate Reader with Gen5 Microplate Reader Software (Version 2.01.14) (Biotek® Instruments GmbH, Germany). The percentage of bacterial inhibition was calculated and plotted, presenting the antimicrobial activity using the following formula:

$$\text{Cell viability (\%)} = \frac{\text{Abs (sample)}}{\text{Abs (control)}}$$

$$\text{Bacterial inhibition (\%)} = 100 - \text{Cell viability}$$

2.11 Cell Culture

C2C12 mouse C3H muscle myoblast (91031101-1VL) cell line (Figure 2.5) was received from The European Collection of Authenticated Cell Cultures (ECACC) in Passage 3 (P3). All cell culture testing was conducted using cells from P6-P10. On the normal pathway, the myoblast cells will differentiate into myotubes upon reaching a confluence rate of 90%. Note that growth factors such as bone morphogenetic protein-2 (BMP-2) can induce the osteogenic differentiation into osteoblastic lineage (Akiyama et al., 1997; Hidaka et al., 2020; Katagiri et al., 1994; Song et al., 2017).

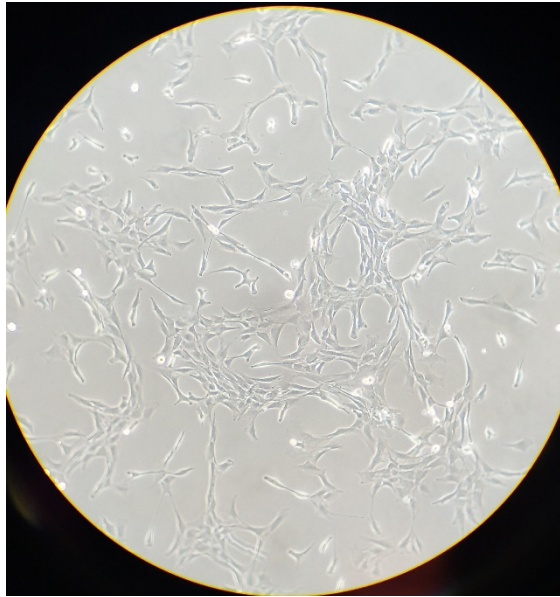


Figure 2.5 The morphology of the C2C12 myoblast cell line captured using Olympus CKX41 inverted light-microscope with an IS300, 3.0MP camera attachment (Olympus Life Science, Hamburg, Germany).

The cell culture growth medium was composed of Dulbecco's Modified Eagle's Medium (DMEM) + 1% 2Mm L-Glutamine + 1% penicillin/streptomycin + 10-15% fetal bovine serum (FBS). A differentiation culture media was prepared using the same composition, with a reduced percentage of FBS to 2%. This differentiation medium was used to compare the alkaline phosphatase activity of different media in the presence of osteogenic factors incorporated CS/HAp scaffold.

2.11.1 Cell Resuscitation

An Eppendorf tube containing C2C12 cells was collected from the nitrogen tank and thawed in a 37 °C water bath for two minutes. The thawed cells were then poured into a 15 ml Falcon tube containing 9 ml of the prepared supplemented media and centrifuged at 150 rcf for five minutes. The cells were then resuspended using 1 ml of the complete media and poured into a T25 flask with 4 ml of culture media. The flask was labelled with the type of cells, date and initials, as well as Passage 3 (P3) as noted by the supplier. The T25 flask was placed into an incubator with 5% carbon dioxide (CO₂) flow at 37°C for three days. Cells were relatively slow-growing upon resuscitation from frozen, taking four to five days to reach 50% confluence, according to the European Collection of Cell Cultures (ECACC) General Cell Collection Detail for C2C12 cell type (European Collection of Authenticated Cell Cultures, 2019).

2.11.2 Cell Passaging

Trypsin, phosphate-buffered saline (PBS) and supplemented media were thawed and warmed in a hot water bath prior to use. Cell passaging procedures were started by washing off the excess media that would deactivate the trypsin using PBS. Then, the cells were detached from the surface of the flask using 1 ml of trypsin. A further detachment of the cells was carried out by tapping the flask gently several times.

Furthermore, 5 ml of growth media was added to the flask containing the cells in the trypsin solution to deactivate the trypsin prior to the following procedure. The cells were then centrifuged at 150 rcf ($\times g$) for five minutes to obtain a cell pellet. The cell pellet was then resuspended using 1 ml media before transferring the cell suspension into a T175 flask and adding 19 ml of the culture media. The flask was closed tightly and was labelled with the cell type, date, initials and passage number. The flask was incubated in 5% carbon dioxide (CO₂) at 37°C, and cell growth was observed daily. The cells were passaged again upon reaching 80% confluence to avoid the differentiation of the myoblasts into myotubes (Figure 2.6). Table 2.9 summarises the other cell culture routine vessels used in this work and their associated components.

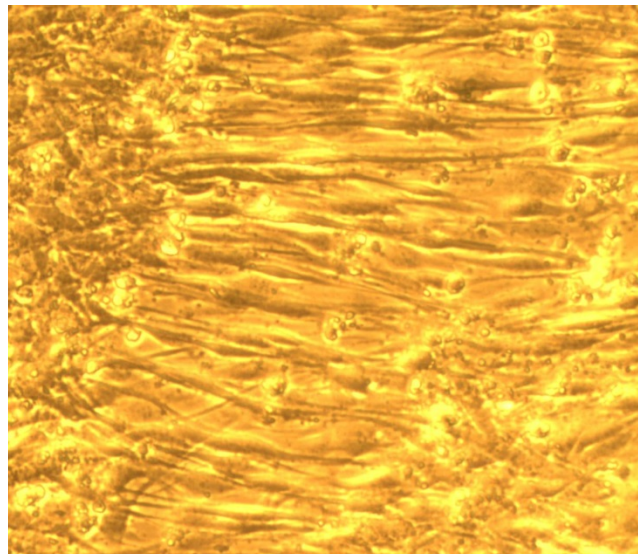


Figure 2.6 Elongated myotubes morphology of differentiated C2C12 myoblast viewed using TSVIEW Imaging Software (Version 7.3.1.7).

Table 2.9 The routine culture vessels used throughout this work and their associated components.

Culture vessels	Approx. surface area (cm ²)	Medium volume (ml)	Trypsin-EDTA volume (ml)
24-well plate	2 cm ² /well	0.5-1	0.2
96-well plate	0.3 cm ² /well	0.1-0.2	0.1
T-25 flask	25 cm ² /flask	5	1
T-75 flask	75 cm ² /flask	12	2
T-175 flask	175 cm ² /flask	15	4

The C2C12 myoblast cells were counted and frozen as stock cells when they reached 70-80% confluency. The cells were harvested and stained with 0.4% Trypan blue solution before counting using a haemocytometer. Subsequently, a cell pellet obtained by centrifugation was then resuspended with 1 ml freezing media composed of 90% FBS and 10% dimethyl sulfoxide (DMSO). Approximately $\pm 3 \times 10^6$ C2C12 cells were allocated per cryotube to freeze. The cryotubes were then transferred into a Mr Frosty™ cryo-safe freezing container containing ethanol and were then frozen in the -80°C freezer before transferring into the nitrogen tank for extended storage.

2.12 Alkaline Phosphatase Activity

An alkaline phosphatase (ALP) assay in the presence of C2C12 myoblast cell lines was conducted to assess the efficacy of the protein and peptide incorporated in CS/HAp scaffolds. An ALP test kit was purchased from Abcam (Abcam Plc., Cambridge, United Kingdom). ALP assay buffer was stored at -20°C and was ready to use as supplied. ALP enzyme was reconstituted with 1 ml assay buffer and kept on ice. The aliquots were stored at 4°C. A 5 mM ρ -nitrophenyl phosphate (ρ NPP) solution was prepared by reconstituting one ρ NPP tablet in a 2.7 ml assay buffer. The stop solution was ready to use as supplied. The standard dilution for the standard curve was prepared (Table 2.10) by diluting 40 μ l of 5 mM ρ NPP standard in 160 μ l of assay buffer, making 1 mM ρ NPP standard.

Table 2.10 ρ NPP standard curve dilution preparation. Each dilution was enough to set up duplicate readings (2 x 120 μ l).

Standard #	1 mM ρNPP standard (μl)	Assay Buffer (μl)	Final volume standard in well (μl)	End amount ρNPP in well (nmol/well)
1	0	300	120	0
2	10	290	120	4
3	20	280	120	8
4	30	270	120	12
5	40	260	120	16
6	50	250	120	20

C2C12 was seeded in a 24-well plate at a density of 5×10^4 cells per well and incubated for six hours before treating with BMP-2 (30, 300, 500 and 1000 ng/ml), P28 peptides (10, 50, 100 and 200 μ g/ml) and the osteogenic factor-infused CS/HAp scaffolds. Untreated cells and cells with the nude CS/HAp were set as the negative control. These growth factors and scaffolds were sterilised under UV lamps in the biosafety cabinet for five minutes before use to avoid any contaminations in the treatments.

All cells proliferated from each treatment were harvested and lysed at days four, seven and 14. The cells were placed into a microtube with 50 μ l of assay buffer and lysed using a vortex for 20 s. After which they were kept on ice for ten minutes to break the cell membrane. Subsequently, the cell lysates were centrifuged at 4 °C and 10,000 rpm for 15 min in a cold microcentrifuge to remove any insoluble material. The supernatant was collected and kept in 0.2 ml PCR tubes.

ALP assay was conducted using C2C12 lysates from days four, seven, and 14 of all treatments and ρ NPP standards prepared earlier. The samples were adjusted to 80 μ l/well with the assay buffer. Subsequently, 50 μ l of 5 mM ρ NPP solution was added to each well containing the sample. Then, 10 μ l ALP enzyme was added to each ρ NPP standard well and mixed by pipetting up and down. The plate was incubated at 25 °C for 60 minutes, and protected from light by wrapping the well plate with aluminium foil. The enzyme will convert the ρ NPP substrate to an equal amount of coloured ρ -nitrophenol (ρ NP). After 60 minutes of incubation, the reaction in the sample and standard wells were deactivated by adding a 20 μ l stop solution provided into each well. Finally, the 96-well

plate was pre-shaken for ten seconds, and the output was measured at an optical density of 405 nm on a microplate reader (n=3).

The ALP activity was calculated with respect to the ρ NPP standard curve using the following formula:

$$\text{ALP activity } \left(\frac{\text{Unit}}{\text{ml}} \right) = \left(\frac{\text{B}}{\Delta T \times V} \right) \times D$$

Where:

B = ρ NP concentration from the equation (μmol)

ΔT = reaction time (min)

V = Original sample volume added into the reaction well (ml)

D = Sample dilution factor

Following the completion of this ALP assay in evaluating the best scaffold bioactivity performance, the work progressed to the alizarin red staining to further validate the osteogenic capacity of the developed scaffolds.

2.13 Evaluation of Osteogenic Differentiation of C2C12 cell line through Alizarin Red Staining

Alizarin red staining was utilised to stain calcium deposits or mineralised nodules due to osteogenic differentiation of C2C12. The induction from BMP-2 and P28 will shift the differentiation pathway of the myoblasts towards an osteoblastic phenotype instead of the normal myotube pathway (Akiyama et al., 1997; D. P. L. Lin et al., 2017; Rauch et al., 2002).

C2C12 myoblasts were seeded in 24-well plates at a density of 5×10^4 in 500 μl growth media per well and left to reach 80-90% confluency (approximately two days). The cells were refreshed with new growth media and treated with BMP-2 and P28 peptide standards as well as the scaffolds similar to the steps outlined in section 3.13 for four different time points; days 7, 14, 21 and 28. ThinCertTM transwells with a 0.4 μm pore diameter, compatible with 24-well plates were utilised in the test using scaffolds.

Alizarin red staining procedures were conducted at each specified time point. All wells containing the cells were rinsed with PBS twice before the fixation using 300 μl of 10% formalin for 20 minutes. The wells were washed with PBS thrice after the fixation to remove the excess formalin solution. The wells were then stained with 300 μl of 2% ARS

solution in water for another 20 minutes. The ARS solution was freshly prepared before each assay, with the pH of the ARS solution adjusted to 4.2 using 0.5% ammonium hydroxide. After 20 minutes, all wells were washed with 1 ml distilled water approximately five times or until no unbound ARS staining solution was left in each well. The stained C2C12 cells were left to air dry before capturing the images using Olympus CKX41 inverted microscope.

Subsequently, the cells were then de-stained with 10% cetylpyridinium chloride (CPC) (Gleeson et al., 2010) to quantify the mineralisation that was exposed to the ARS stain, where 1 ml of CPC was added into each of the wells with dried ARS stain and incubated in 37 °C for 1 hour. The dissolved stain was then spectrometrically analysed using the plate reader at 540 nm, pre-shake for ten seconds.

Afterwards, the work progressed to the verification step of the bioactive functionality of the scaffold *in vivo* through the implantation in femoral condyle defects of Sprague Dawley rats.

2.14 *In vivo* Evaluation of Bone Regeneration Scaffold in Femoral Condyle Defects of Sprague Dawley Rats

In vivo analysis of scaffolds was assessed using a femoral defect model in Sprague Dawley (*Rattus norvegicus*) rats aged three months upon receipt. This model was authorised by the local Ethical Committee and the French Ministry for Education and Research (agreement number: APAFIS#1437). The bilateral model applied for this study was according to the European Directive 2010/63/UE.

Three formulations of scaffolds were fabricated for the initial *in vivo* implantation procedures, with two additional samples as the positive control (Table 2.11). The scaffolds fabricated off-the-shelves were CS/HAp, CS/HAp/10 µg Medtronic Infuse® rhBMP-2 (Medtronic BioPharma, Watford, UK) and CS/HAp/25 µg P28 and prepared similar as outlined in section 2.2.7. Two additional samples were freshly prepared on the day of the implantation before the surgery: i.e., nude collagen sponges and collagen sponges infused with 10 µg of rhBMP-2 (Infuse®). Twelve SD rats were involved in this work (24 implantation sites).

Table 2.11 Test samples used in the initial animal implantation procedures.

Label	Test samples	Quantity (n)
A	Chitosan/hydroxyapatite scaffold (nude)	5
B	Chitosan/hydroxyapatite scaffold + rhBMP2	5
C	Chitosan/hydroxyapatite scaffold + P28 peptide	5
D	Collagen sponge	5
E	Collagen sponge + rhBMP-2	4
Total of implant sites		24

Subsequently, a second animal study was conducted in the Animal Research and Service Centre, Universiti Sains Malaysia (ARASC USM), following the ethics approval (USM/IACUC/2020/(122)(1048)), where nine Sprague Dawley rats aged 11 weeks and initial weights ranging from 300 g to 400 g were received. This animal trial employed the revised P28 delivery systems with a faster degradation than previous formulations by incorporating the combinations of hydroxyapatite and fluorapatite in the current formulations. In addition, the osteogenicity of different P28 concentrations was tested since the initial animal trial utilising 25 µg P28 showed a promising osteoinductivity. Therefore, an increased P28 content (75 and 150 µg) was also included in CS/HAp/FAp scaffolds and prepared as outlined in section 2.2.7. The six groups of different types of scaffolds are presented (Table 2.12).

Table 2.12 List of the scaffold formulations used in the optimised animal trial.

Label	Test samples	Notes	Quantity (n)
A	12% LW CS/HAp/FAp 1:1	Varying the chitosan molecular weight	3
B	12% HW CS/HAp/FAp 1:1		3
C	12% HW CS/HAp/FAp 1:0.75	Varying FAp ratio	3
D	12% HW CS/HAp/FAp 1:1/P28 25µg	Varying P28 peptide concentrations	3
E	12% HW CS/HAp/FAp 1:1/P28 75µg		3
F	12% HW CS/HAp/FAp 1:1/P28 150µg		3
Total of implant sites			18

2.14.1 Animals' Husbandry

All rats were ear-tagged individually on the arrival date. The animals were acclimatised for a minimum of seven days and housed in adapted installations (air-conditioned rooms with a temperature of 22 ± 3 °C and a 50–60% humidity level). The artificial day/night light cycle was set to 12 h of light and 12 h of darkness. All animals had free access to water and were fed *ad libitum* with commercial chow daily. Cages were cleaned and changed weekly to prevent any unwanted infections at the surgical wound of the rats and their health generally. The general state of the animals was monitored daily.

2.14.2 Surgical Interventions

The scaffold implantation was conducted using an aseptic technique. The implantation comprised 3 mm round defects on both right and left femoral condyles of animal models, which were adapted and modified from work carried out by Klein *et al.* (2019) and Mohiuddin *et al.* (2019). All instruments and apparatus were set up in a cleanroom (Figure 2.7).



Figure 2.7 The cleanroom setup for animal implantation procedures.

The procedure started with anaesthesia induction with an intraperitoneal injection of ketamine and xylazine. The doses of all drugs were calculated based on animal weight which was measured just before the surgery using the formula below:

$$\text{Dosage (ml)} = \frac{\text{weight (kg)} \times \text{dose} \left(\frac{\text{mg}}{\text{kg}}\right)}{\text{concentration} \left(\frac{\text{mg}}{\text{ml}}\right)}$$

Mixtures of oxygen/isoflurane (oxygen (0.4 L/min)/Isoflurane (1.5-2%)) were given as anaesthesia maintenance throughout the surgery. The flanks of the animals were shaved

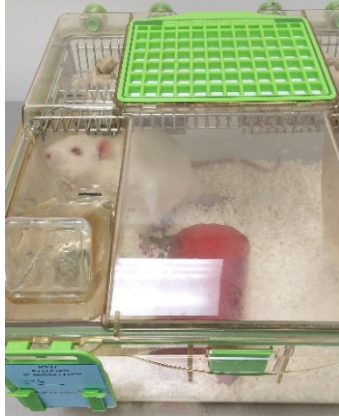
by using an electronic hair shaver. Chlorhexidine was applied to the exposed skin, followed by povidone-iodine in an outward circular motion. A scalpel blade was used to make a firm incision on the skin into the muscle. The muscle mass was then dissected, exposing the bone surface of the femoral condyle. A 3 mm size defect was induced with a commercial micro drill equipped with a 3 mm bur (Figure 2.8). Saline irrigation was applied while drilling.



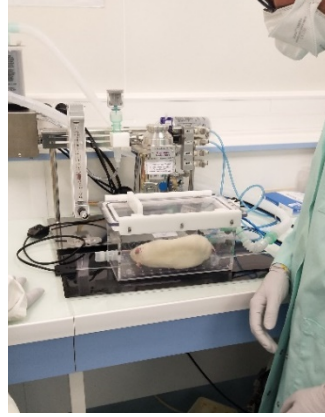
Figure 2.8 The 3 mm defect made on the femoral condyle of an SD rat.

The chitosan-based scaffold was quickly inserted into the defect in a randomised manner. Subsequently, the muscle was sutured with an absorbable suture, followed by suturing of the skin with the same absorbable suture. Iodine was reapplied and a transparent film dressing spray, Opsite spray (Smith&Nephew, UK), was applied as a final layer to protect the wounds. The procedures were repeated on the contralateral condyle. Dexamethasone, an anti-inflammatory drug (Dexavet 0.5%, Range Pharma, Malaysia), was injected intramuscularly before returning to the cage. The post-operative health condition, weights, wound healing and behaviour of the animals were monitored twice daily for the first week, daily on the second week and every two or three days for the rest of the eight weeks' study until the euthanasia procedure.

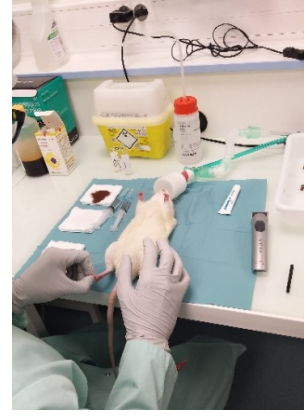
A summary of the surgical procedures is outlined (Figure 2.9).



1. Before the procedure



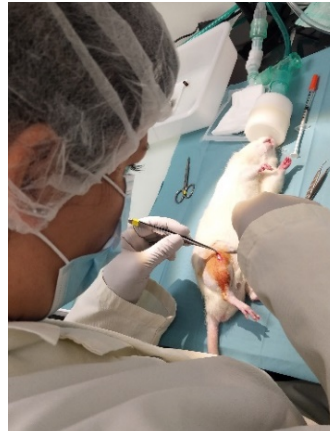
2. Isoflurane anaesthesia



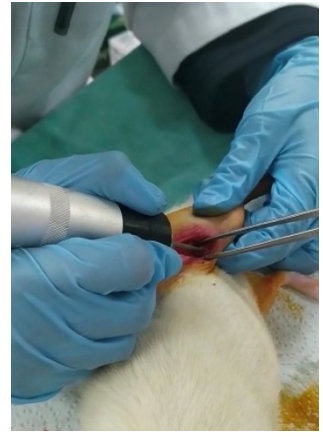
3. Eye gel & saline injection



4. Shaving



5. Femoral incision & local anaesthesia



6. Femoral condyle defect induction



7. Scaffold insertion



8. Muscle and skin suture



9. Back in the cage

Figure 2.9 A summary of the conducted femoral defect induction and scaffold implantation procedures

2.14.3 Post-operative Monitoring

The general post-operative conditions of the animals were monitored daily, and deeper monitoring in terms of the body weight was recorded every two days in the early weeks post-implantation and every four days towards the end of the experiment. These monitoring procedures were carried out to observe whether the animals had reached the endpoints below, where removal from the study would be recommended:

- Weight loss > 20% of the mean weight of rats
- Severe lameness
- Diarrhoea/blood in faecal material
- Circling phenomenon
- Severe necrosis at the implantation site
- Persistent self-induced trauma five days after analgesic treatment as well as local and general treatment
- Abnormal behaviour even in the presence of appropriate treatment (e.g. sign of pain even under analgesic)

2.14.4 Fluorescent Bone Labelling for Dynamic Bone Formation

All rats were subcutaneously injected with double-fluorochrome labelling; calcein green (CG) and xylenol orange (XO) (ten and four days, respectively) prior to sacrifice in order to highlight the calcification formed (van Gaalen et al., 2010).

Calcein injection (10 mg/kg) was prepared by dissolving 0.1 g of calcein powder in a 2% sodium bicarbonate solution under sterile conditions (McGregor et al., 2020; Porter et al., 2017; Ruvinov et al., 2019). The solvent was first prepared by dissolving 0.05 g sodium bicarbonate powder in 10 ml of 0.9% sterile saline solution, making the concentration 10 mg/ml. Xylenol injection (90 mg/kg) was prepared by weighing 0.2 g sodium bicarbonate and dissolved in 10 ml of 0.9% sterile saline solution under sterile conditions. The solvent was poured into 1 g of xylenol orange tetrasodium salt and shaken until dissolved. The dosage for these double-fluorochrome injections was calculated based on the formula below and injected subcutaneously four days (calcein) and ten days (xylenol) prior to sacrifice:

$$Dosage (ml) = \frac{weight (kg) \times dose \left(\frac{mg}{kg}\right)}{concentration \left(\frac{mg}{ml}\right)}$$

2.14.5 Animal Euthanasia

Rats were sacrificed humanely via cardiac puncture (Figure 2.10) under anaesthesia after eight weeks of being implanted with six groups of chitosan-based bone regeneration scaffolds on both sides of femoral condyles. The rat was anaesthetised using Dorminal 20% (200 mg/ml pentobarbital sodium) purchased from Alfasan International, Woerden, Netherlands, intraperitoneally (200 mg/kg) prior to cardiac puncture, which was carried out immediately after anaesthesia was induced.



Figure 2.10 Euthanasia using cardiac puncture method.

Following euthanasia, the femurs of the rats were collected by incising the muscle until reaching the femoral head, and the ligaments holding the femoral head and the condyles were cut. The surrounding muscle was removed as much as possible. The femurs were then fixed in 10% neutral buffered formalin and cut using a hard tissue cutter, obtaining the implanted femoral condyles.

2.14.6 Macroscopic Histopathological Evaluation

A local macroscopic evaluation was carried out by observing the exposed femoral condyle implant sites. The observation focused on the defects' visibility, colour, and texture through a macroscopic scoring system adapted and modified from Rudert *et al.* (2005). This scoring system (Table 2.13) was also applied in several other studies involving *in vivo* osteochondral experiments (Abdallah *et al.*, 2016; Betsch *et al.*, 2013; Tosun *et al.*, 2017) and reviewed by (Radzak *et al.*, 2021).

Table 2.13 Modified histopathological evaluation scoring (Rudert et al., 2005).

Criterion	Score	Macroscopic characteristics
Defect visibility	1	Appeared as small irregular bumps
	2	Regular hole closed by a transparent tissue
	3	Completely closed
Colour	1	Yellowish paste observed
	2	White bony appearance
Surface	1	Rough and bumpy
	2	Smooth

2.14.7 Micro Computed Tomography Scanning

Following the fixation step, femoral condyles were washed in 0.9% physiological saline solution, rolled up in cellophane to keep them wet and scanned at room temperature with the following parameters (Table 2.14):

Table 2.14 MicroCT measurement parameters.

Parameters	Set values
Voltage	70 kV
Filter	Aluminium 0.5 mm
Resolution	9 μm
Tomographic rotation	180°
Rotation degree	0.6°
Number of scans per position	1

Calibration phantom scans for bone mineral density (BMD) measurements were run using calcium hydroxyapatite samples of known BMD by utilising the same conditions as the test samples. The images were analysed using SkyScan Image Analyses Software and Bruker CTAn Micro-CT Software (CTAn software v.1.18) to assess two bone morphology parameters: bone mineral density (BMD) ($\text{g}\cdot\text{cm}^{-3}$) and bone volume fraction (BV/TV) (%), where BV is the bone volume, and TV is the total volume.

2.14.8 Histological Processing, Embedding and Cutting

Tissue samples were fixed in 10% neutral buffered formalin for two weeks prior to the histological processing. Histological processing involved dehydration in ascending series of ethanol (70-100%), clearance in chloroform and infiltration with PMMA Technovit®

7200 (Kulzer, Germany) in ascending concentration (10-100% PMMA in ethanol), prior to embedding in Technovit® 7200 hard resin with 1% benzoyl peroxide using blue light polymerisation, kept cool throughout the curing process.

Serial longitudinal sections of 100-300 µm thickness were made at the defect level to obtain the sagittal view of the defect using an EXAKT diamond embedded saw equipment and polished using an EXAKT grinder machine to obtain 3-7µm sections (EXAKT Advanced Technologies GmbH, German) (Figure 2.11).

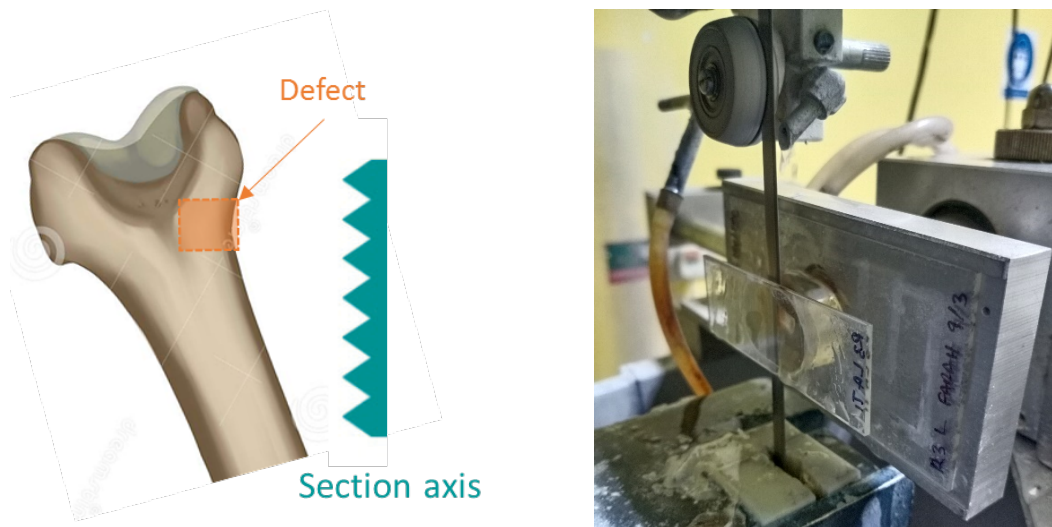


Figure 2.11 Cutting procedure of the embedded condyles on sagittal axis.

The bone sections were laid on slides immersed in an alcohol solution and covered with polyethylene films. After the slides were dried, sections were deplasticised, and the staining procedures were performed: Hematoxylin-Eosin (HE), Von Kossa (VK) and Tartrate-resistant acid phosphatase (TRAP). The optimised animal trial utilised HE stain. Each stained slide was scanned to have a global view of the samples (x20 objective), where brightfield was used. In addition, unstained sections from both animal studies were directly observed under the fluorescent microscope to analyse the fluorochrome labels administered prior to the sacrifice.

2.14.9 Fluorescent Imaging

Fluorochrome labels were assessed on non-stained sections using an Invitrogen EVOS M7000 fluorescent microscope with M7000 software (Life Technologies Corporation, USA) (Figure 2.12). The labels were used to mark the bone formation on the injection days (Pautke et al., 2005). The fluorochrome labels were analysed using three light

sources; GFP, RFP and transmitted light (brightfield). The GFP emission filter permits fluorescent signals with wavelengths of 510 nm to 540 nm to pass through (CG), while the RFP emission filter allows signals with 575 nm to 590 nm to pass through (XO), thus producing clean signals and images.

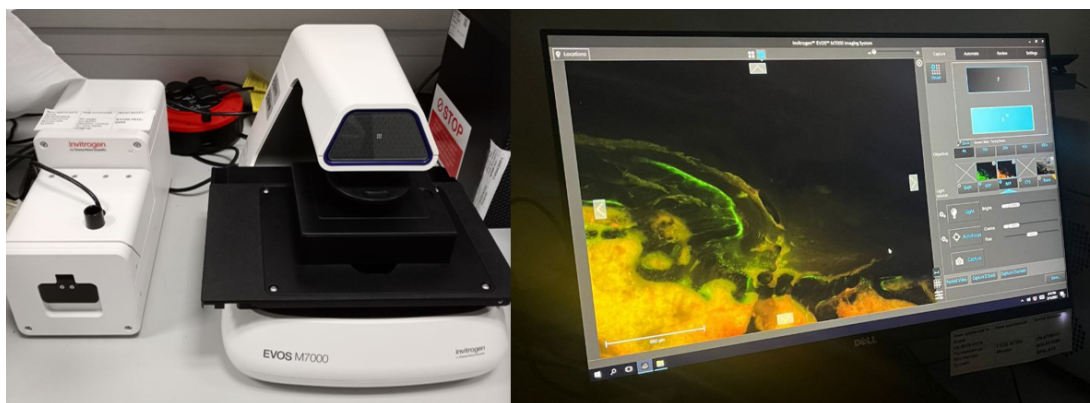


Figure 2.12 The Invitrogen EVOS M7000 fluorescent microscope and M7000 software utilised in the fluorochrome-labelling assessment.

2.14.10 Histopathologic Analysis from Hematoxylin and Eosin Staining

A pathologist blinded to the treatment evaluated HE slides to screen for any microscopical abnormalities. Findings were reported, scored for intensity (Table 2.15) on a scale of 0 (no lesion) to 4 (severe lesion) and interpreted in terms of relation to the presence of scaffold/sponge (scaffold/sponge-associated with growth factors-related effect versus background findings with scaffold/sponge alone):

Table 2.15 Evaluation criteria for Hematoxylin-Eosin slide, focusing on the material integration and the bone reconstruction.

Criteria	Scores
Material integration	
Inflammation (intensity, nature and distribution)	0 (absence) to 4 (severe)
Fibrosis (intensity, maturity and distribution)	0 (absence) to 4 (severe)
Hemorrhages / Edema (intensity and distribution)	0 (absence) to 4 (severe)
Necrosis (intensity and distribution)	0 (absence) to 4 (extent)
Biomaterial residues (quantity and distribution)	0 (absence) to 4 (a lot)
Bone reconstruction	
Reconstructed bone maturity	0 (woven bone) to 4 (mature bone tissue)
Quantity of reconstructed bone	0 (absent) to 4 (large amount)
Osteoblast activity / osteoid tissue	0 (absence) to 4 (large amount)

2.14.11 Measurements of Mineralised and Osteoid Tissue Volume into the Defect by Von Kossa Staining

The mineralised and osteoid tissue volume in the defect was measured on VK scanned images since the staining allows the visualisation of mineralised tissue in black while osteoid tissue in dark pink (Figure 2.13).

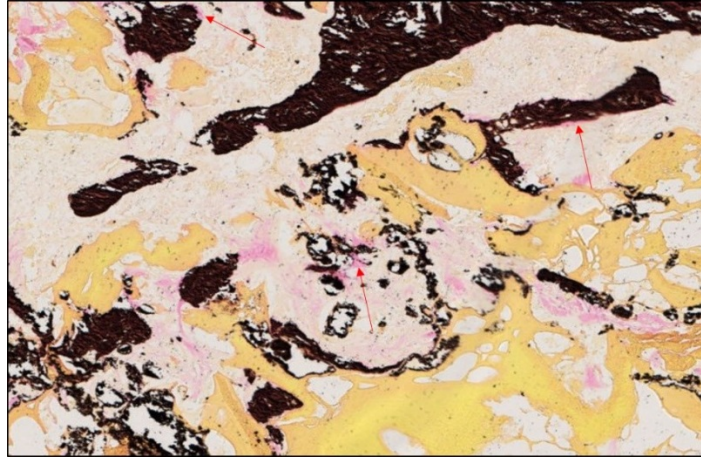


Figure 2.13 Example of VK staining. Mineralised tissue appears in black, osteoid tissue appears in dark pink (red arrows), bone marrow and muscle appear in orange and fibrotic tissue appears in pink.

2.14.12 Measurements of Osteoclasts Surface into the Defect by Tartrate-Resistant Alkaline Phosphatase Staining

The osteoclast surface in the defect was measured on TRAP stained slides since the staining permits highlighting the activated osteoclast in red colour (Figure 2.14).

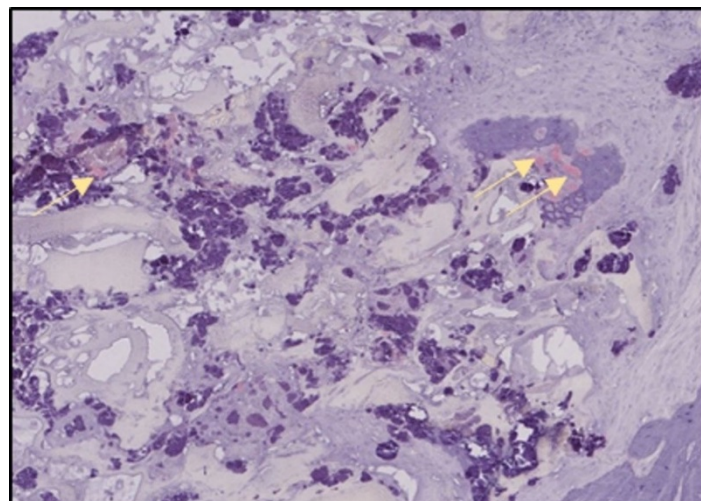


Figure 2.14 Example of TRAP staining. Bone tissue appears in light blue, activated osteoclasts appear red (yellow arrows), and the nucleus appears dark blue.

2.14.13 Measurement of the Dynamic Bone Formation Parameters through Fluorescent Labelling Analysis

The dynamic bone formation parameters in the defect were measured using fluorescent scanned images (from the unstained slides), highlighting the calcein and xylenol fluorochromes injected *in vivo* (Figure 2.15). The measurements were carried out manually by using Osteoquant Bioquant® software. All the single labelling (sLS - either orange or green labelling alone: blue arrows on the image above) and the double labelling (dLS - orange and green: yellow arrows on the image above) were drawn manually in the defect and its margin. The Osteoquant Bioquant® software automatically calculates the mineralised surface ($MS = dLS + sLS/2$) and the length between both labellings (IrLth).

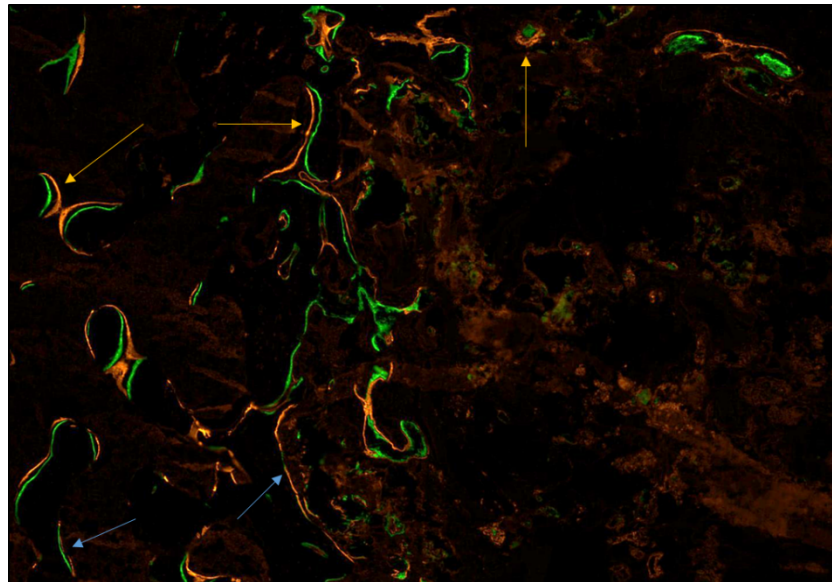


Figure 2.15 Example of the fluorescent scans. Calcein labelling appears in green and xylenol labelling appears in orange. Single labelling (sLS) along the bone with either orange or green labelling was designated with blue arrows, and double labelling (dLS) along the bone with both green and orange labelling was designated with the yellow arrows.

2.14.14 Histomorphometric Parameters Calculations

The following parameters were measured on the slides (Table 2.16). Therefore, for each sample, the following histomorphometric parameters were calculated:

- Mineralised volume / total volume (Mdv/TV)
- Osteoid volume / total volume (OV/TV)
- Osteoid volume / mineralised volume (OV/Mdv)
- Osteoclast surface / bone surface (OcS/BS)
- Mineral apposition rate (MAR) = Length between both labelling (IrLth) / delay between injections

- Mineralised surface / bone surface (MS/BS)
- Bone formation rate / bone surface = MAR x MS/BS

Table 2.16 Parameters for histomorphometric calculations.

Staining	Measured parameters
VK	<ul style="list-style-type: none"> • Mineralised volume (Mdv) • Osteoid volume (OV) • Total volume (TV) • Bone surface (BS)
TRAP	<ul style="list-style-type: none"> • Osteoclast surface (OcS)
Fluorescent	<ul style="list-style-type: none"> • Mineralised surface (MS) • Length between labelling (IrLTh)

2.15 Statistical Analysis

All statistical analysis in this document was performed using the Minitab software. Firstly, a descriptive statistic was performed to evaluate the mean and standard deviation between the samples. The significance between the two data groups was then tested using the student t-test. Subsequently, a one-way ANOVA was utilised to compare three or more parametric data groups, followed by a Tukey's test to assess the significant changes in the data. Kruskal-Wallis test was conducted for non-parametric tests. Significance was achieved with data exhibiting a p-value less than 0.05 ($p < 0.05$).

Chapter 3

Chapter 3: Bioresorbable Chitosan-Based Bone Regeneration Scaffold Using Various Bioceramics and the Alteration of Photoinitiator Concentration in an Extended UV Photocrosslinking Reaction

3.1 Abstract

Bone tissue engineering (BTE) is an ongoing field of research based on clinical needs to treat delayed and non-union long bone fractures. An ideal tissue engineering scaffold should have a biodegradability property matching the rate of new bone turnover, be non-toxic, have good mechanical properties, and mimic the natural extracellular matrix to induce bone regeneration. In this study, biodegradable chitosan (CS) scaffolds were prepared with combinations of bioactive ceramics, namely hydroxyapatite (HAp), tricalcium phosphate- α (TCP- α), and fluorapatite (FAp), with a fixed concentration of benzophenone photoinitiator (50 μ l of 0.1% (w/v)) and crosslinked using a UV curing system. The efficacy of the one-step crosslinking reaction was assessed using swelling and compression testing, SEM and FTIR analysis, and biodegradation studies in simulated body fluid. Results indicate that the scaffolds had comparable mechanical properties, which were: 13.69 ± 1.06 (CS/HAp), 12.82 ± 4.10 (CS/TCP- α), 13.87 ± 2.9 (CS/HAp/TCP- α), and 15.55 ± 0.56 (CS/FAp). Consequently, various benzophenone concentrations were added to CS/HAp formulations to determine their effect on the degradation rate. Based on the mechanical properties and degradation profile of CS/HAp, it was found that 5 μ l of 0.1% (w/v) benzophenone resulted in the highest degradation rate at eight weeks (54.48% degraded), while maintaining compressive strength between (4.04 ± 1.49 to 10.17 ± 4.78 MPa) during degradation testing. These results indicate that incorporating bioceramics with a suitable photoinitiator concentration can tailor the biodegradability and load-bearing capacity of the scaffolds.

3.2 Introduction

Bone tissue defects are a rising global concern and are one of the leading causes of morbidity and disability, especially in elderly patients. Normal fractures typically heal within 6-8 weeks in healthy adults, but in 5-13% of cases, the bone does not heal properly and can lead to delayed or non-union, which is classified as the absence of bone healing signs three months post-trauma (Andrzejowski & Giannoudis, 2019; Devine et al., 2017; Pountos et al., 2016; Rupp et al., 2018; Solomon et al., 2005; Tian et al., 2020). A critical-sized bone defect is a defect that exceeds the natural capacity of bone healing, and these are the major cause of the non-unions, which necessitate a planned reconstruction and

secondary surgery to implement and add to the patient's burden and overall cost of the treatment (Donnalaja et al., 2020; Ercal & Pekozer, 2020). Fracture repair is a global challenge, with about 3.5 million new bone fractures recorded in European Union citizens, involving hip fractures, vertebral fractures, forearm fractures, and other fractures (Svedbom et al., 2013). The non-union rates in the United States is 1.9-10%, while in the United Kingdom (UK), 5-10% out of approximately 850,000 new fracture cases identified or 0.02% in 100,000 population (Nicholson et al., 2021; J. D. Thomas & Kehoe, 2022).

Autografts harvested from the patient's own non-essential bone stock are considered the gold standard in treating fractures. Autografts account for 2.2 million transplantations in orthopaedic and dentistry repair worldwide due to their high success rate of 80-90% (Ansari, 2019; Cui et al., 2018; Elakkiya et al., 2017; Fernandez-Yague et al., 2015; Fourie et al., 2022; Jin et al., 2019). While bone grafts can be donated (allograft) to support and supplement the limited supply of autografts, these treatments require using a considerable amount of the bone grafts with a higher potential risk of disease transmission or even being rejected by the recipient's body (Donnalaja et al., 2020; Polo-Corrales, L. ; Latorre-Esteves, M. ; Ramirez-Vick, 2013; Y. Zhang et al., 2020). Therefore, an engineered bone scaffold is an attractive alternative treatment for bone fractures replacing these conventional autologous and allogenic treatment options. Scientists are now focusing on fabricating bone scaffolds that can mimic specific cellular responses at the molecular level by using various natural or synthetic biomaterials and also combinations of these, such as collagen, gelatin, silk fibroin, chitosan, alginate, polycaprolactone (PCL), polylactic acid (PLA) and poly(lactic-co-glycolic acid) (PLGA) (S. M. Choi et al., 2018; Dixon & Gomillion, 2022; Donnalaja et al., 2020; Fernandez-Yague et al., 2015; López-Lacomba et al., 2006; Wei et al., 2020; X. Zhang et al., 2014; Zustiak et al., 2013).

Additionally, the bone scaffolds are tailored to have compulsory characteristics in line with the diamond concept of bone graft substitutes through the combination of osteoconductive materials, osteoinductive growth factor, osteogenic cells, and adequate mechanical stability (Calori & Giannoudis, 2011; Henkel, 2017; T. Kim et al., 2020). The development of scaffolds infiltrated with osteogenic factors released in an extended period is a promising acellular strategy to promote bone formation. The first commercially available and FDA-approved growth factor delivery system for bone healing treatment is known as Medtronic Infuse[®], which incorporates recombinant bone

morphogenetic protein-2 (rhBMP-2) in a collagen sponge carrier (Govoni et al., 2021). However, this system requires intra-operative preparation and is associated with high burst release that can lead to unwanted adverse effects, including higher rates of implant displacement, subsidence, infection, ectopic bone formation, osteolysis, and thus may result in ineffective treatment of non-unions (Bullock et al., 2021; Durham et al., 2020; James et al., 2016; Raftery et al., 2013).

The scaffold biodegradation profile plays an essential role in releasing a loaded drug through customising these scaffolds to degrade at a similar rate to the bone ingrowth, where the newly formed bone gradually replaces the scaffolds in an osteoconductive manner, thus obtaining a suitable drug release mechanism (Alves et al., 2020; Devine et al., 2017; Fournet et al., 2019). Since chitosan (CS) can undergo enzymatic degradation *in vivo* due to its degradable glycosidic chains and the degradation products can be digested naturally after entering the bodies' metabolic cycle, a plethora of studies have been carried out in fabricating bone scaffolds involving this biopolymer (Fourie et al., 2022; Khouri et al., 2019; Lan Levengood & Zhang, 2015; Lavanya et al., 2020; Maji et al., 2016). CS is also popular since it is derived from natural sources (typically the exoskeleton of crustaceans and insects), it is biocompatible, has antimicrobial properties, and is non-toxic as well as osteoconductive, making it a versatile biomaterial (Fourie et al., 2022; Lavanya et al., 2020; Yadav et al., 2021).

The *in vivo* performances of CS may be different depending on its deacetylation degree, molecular weight and also functionalisation with the other chemical groups, such as trimethylated chitosan, which can be tailored based on the specific necessities (Dorati et al., 2017). It was reported that high deacetylated CS will degrade slowly *in vivo* and may reach several months before being completely degraded, while rapid degradation can be achieved by using a low deacetylated CS (Raftery et al., 2013). Moreover, the performance of CS in BTE is restricted by its being insoluble in neutral pH and its insufficient mechanical stability, where De Witte et al. (2018) proposed that a bone scaffold should possess a compressive strength between 2-12 MPa and an elastic modulus of 0.5-1 GPa (T.-M. De Witte et al., 2018). However, chemical modifications utilising the crosslinking of CS to another material allow the possibility to introduce different functional groups to the CS chain and thus altering the properties of the composite in achieving the desired scaffold features (Sanchez-Salvador et al., 2021). Previously, it was reported that a CS/HAp scaffold fabricated using novel ultraviolet (UV)-crosslinking

procedures failed to degrade after ten weeks in the simulated body fluid, which might disturb the bone turnover process *in vivo* (Devine et al., 2017).

Hence, researchers have examined the effect of combining CS with osteoinductive bioceramics, including hydroxyapatite, tricalcium phosphate and bioactive glass, to overcome these limitations (Kaliva et al., 2020; Wei et al., 2020). These osteoconductive ceramics have biologically similar inorganic components to the natural bone and bone-bonding properties, enabling the regenerated bone tissue to form a chemical bond with the scaffold surfaces (Maji et al., 2016; Y. Zhang et al., 2007). Furthermore, the addition of these bioceramics into scaffold formulations was previously investigated to increase the tensile and compressive strength. These biomaterials are also proven to accelerate tissue healing without requiring further surgical procedures after implanting polymeric scaffolds, as they can deteriorate naturally or be wholly integrated with the newly formed tissue once implanted (Dorati et al., 2017).

Based on these findings, it is hypothesised that it will be possible to create a CS-ceramic scaffold with suitable mechanical and swelling properties using one-step hydrogen abstracting free radical initiation process to crosslink the CS matrix. This approach will address the extended crosslinking reaction of CS scaffolds with several types of bioactive ceramics incorporation and different concentrations of photoinitiator application that was not yet investigated. It is hypothesised that this will lead to tuneable bioresorption rates while maintaining strong crosslinking and high load-bearing capacity.

Initially, chitosan was first mixed with 1% (v/v) acetic acid to make it soluble through a protonation reaction (Figure 3.1).

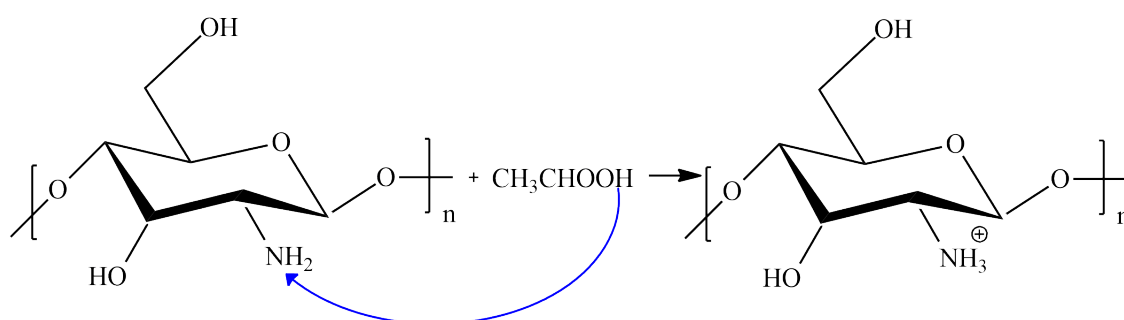


Figure 3.1 Chemical structure of the protonated chitosan.

The scaffold fabrication was then modified based on the method described by (Devine et al., 2017) (Figure 3.2) by altering the chemical protocol to enhance and extend the linkage within the chitosan molecule. The scaffold samples were assessed using crosslinking

testing in 1% acetic acid, FTIR analysis and compression testing to compare the properties of scaffolds produced from this modified method. Improved mechanical strength and ability of the scaffolds to remain intact in acidic environments were achieved using the modified scaffold preparation method, where the neutralisation process was carried forward after the protonation reaction before adding PEG600DMA and benzophenone solution for the crosslinking reaction.

It was previously reported that the incorporation of PEG, which is among the limited biocompatible synthetic polymer that has the approval by the FDA to be used in biomedical applications, has the capability to tune chitosan non-covalent/hydrophobic interactions and PEG hydrophilic interactions that presented the properties of hydrogel (Chang et al., 2016). It was postulated that PEG600DMA and benzophenone were added to attain chitosan's neutral structure again after being protonated by acetic acid. This structure will have fewer hydrogen atoms at the active sites for modification, thus enabling further free-radical polymerisation reactions yielding two radicals at hydroxyl and amino groups. These radicals will then crosslink with PEG600DMA after the initiation by benzophenone solution. The efficacy of this method is proposed through the chemical reaction mechanism (Figure 3.3), proposing the linkage formed. This mechanism was previously detailed in the section 1.3.4.

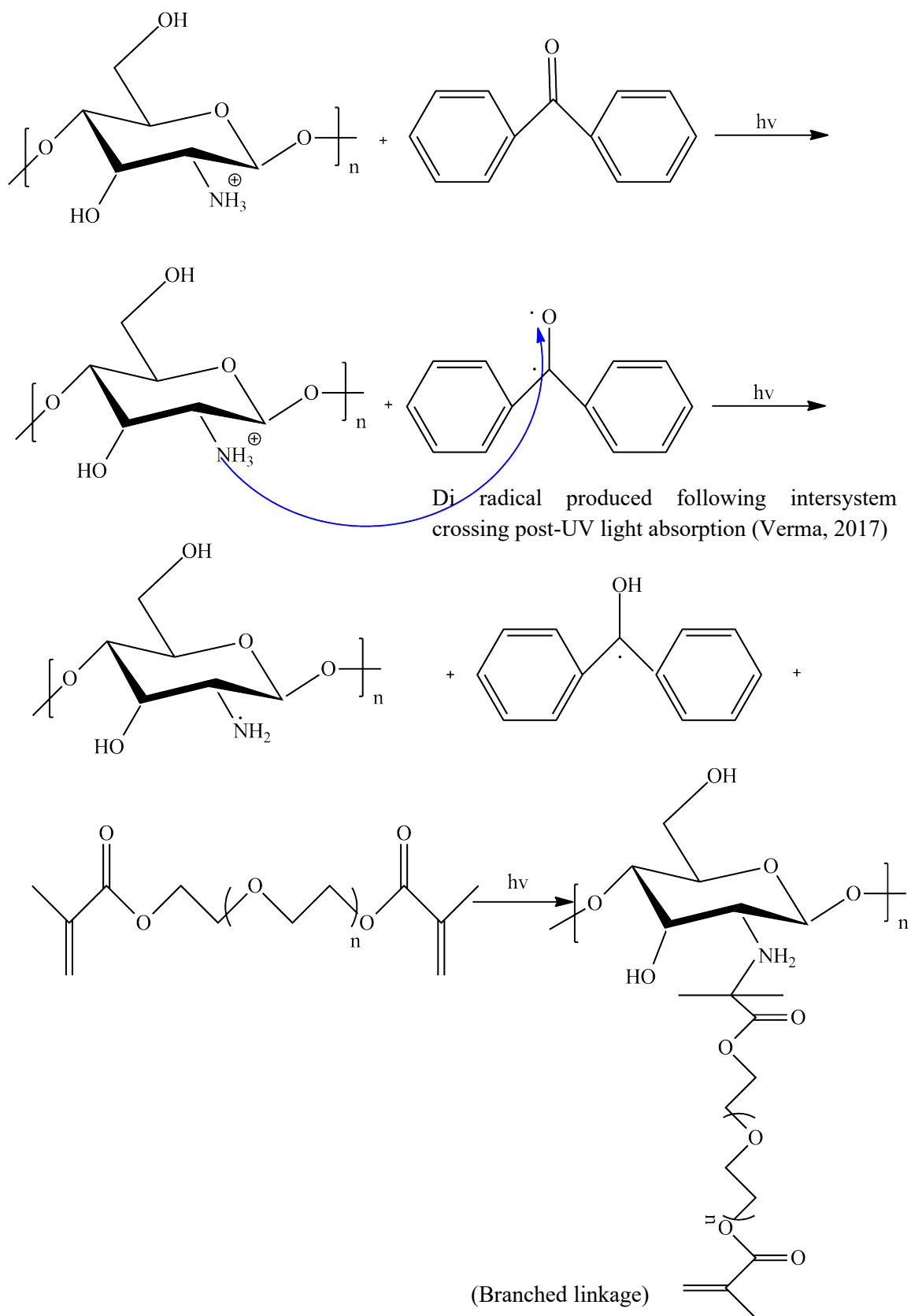


Figure 3.2 Postulated end-product from the chemical crosslinking of chitosan and PEGDMA600 post-curing using the original method.

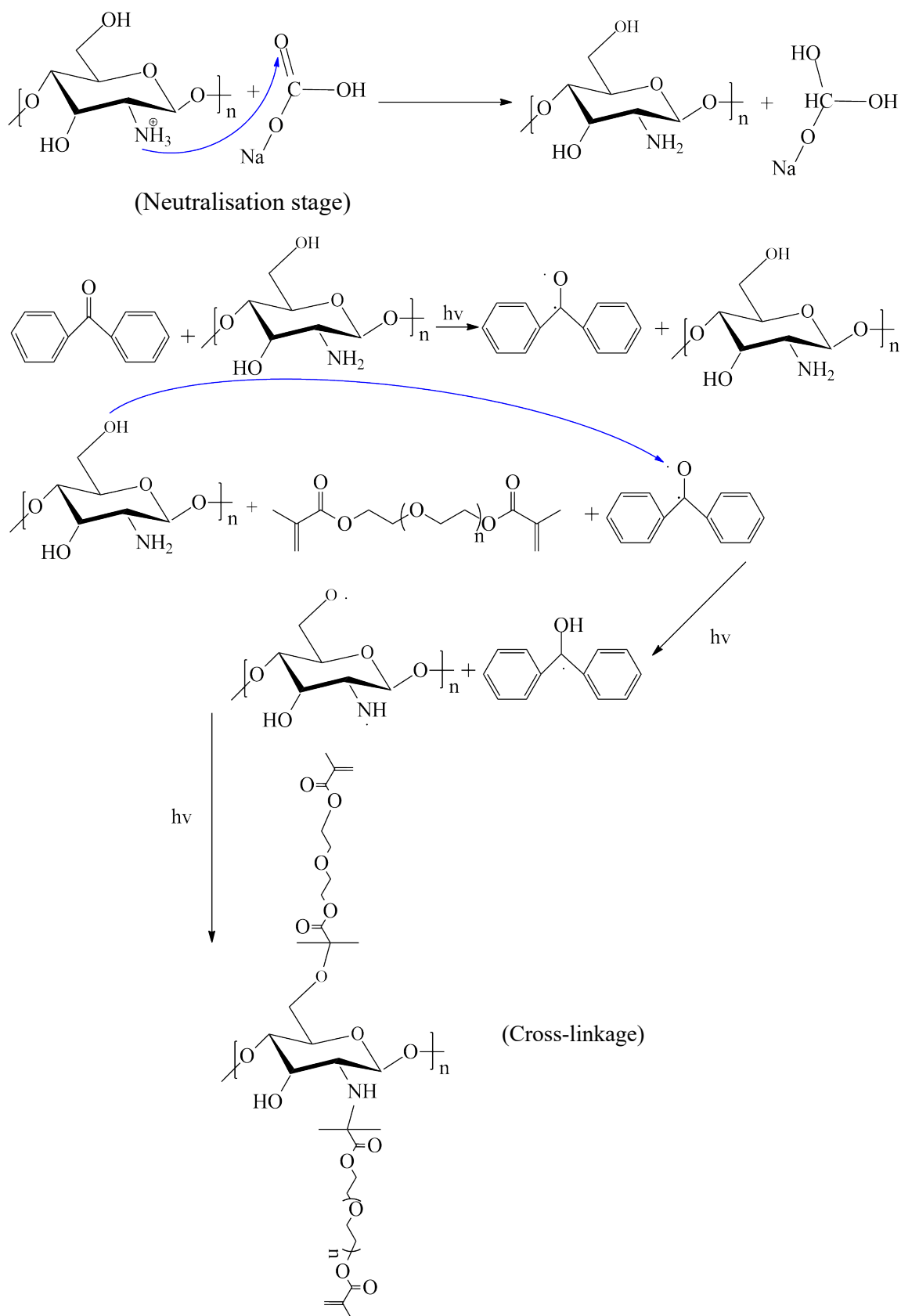


Figure 3.3 The proposed extended crosslinking reaction of chitosan and PEG600DMA following the method modification.

3.3 Results and Discussions

3.3.1 Analysis of Crosslinkage Formation Following UV-Photocrosslinking Procedure

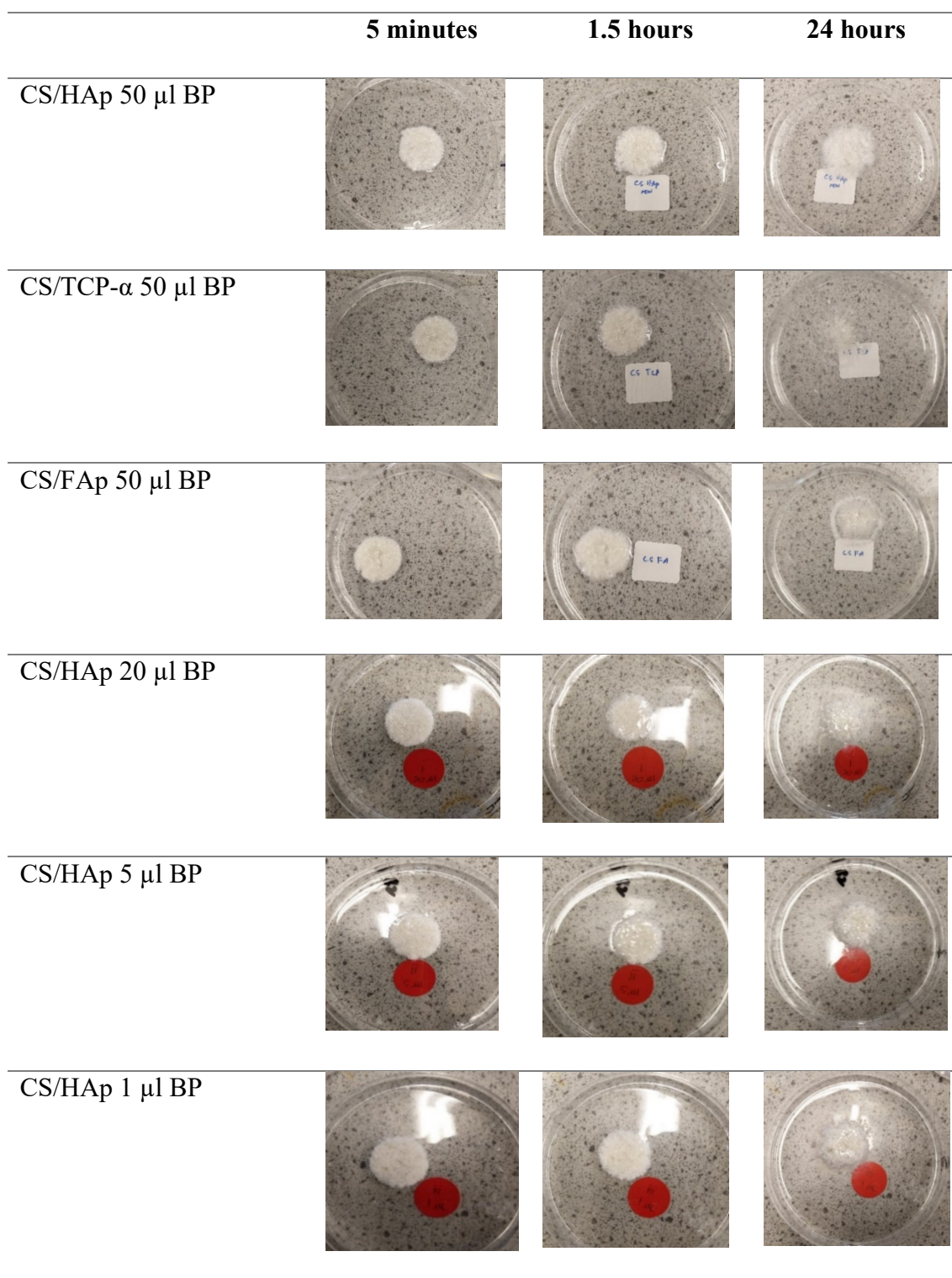


Figure 3.4 Photographs of CS scaffolds with various ceramics and BP content which were placed in 1% v/v acetic acid solution in the water acting as a solvent for CS. Minimal swelling or dissolution was observed for up to 24 hours indicating the success of the crosslinking reaction.

Swelling studies were conducted in 1% (v/v) acetic acid solution due to chitosan's insolubility in water. As such, the swollen samples in 1% (v/v) acetic acid would dissolve if not crosslinked.

The scaffolds were visually inspected following the submerging in 1% (v/v) acetic acid at 5 minutes, 1.5 and 24 hours (Figure 3.4). Among the various ceramic compositions, it was found that CS/TCP- α and CS/FAp swelled the most in the acetic acid in 24 hours, leading to difficulty during handling. Upon varying the BP content, CS/HAp scaffolds with 5 μ l of benzophenone were observed to remain intact during handling compared to CS/HAp/20 μ l BP and CS/HAp/1 μ l BP.

Table 3.1 Gel fraction values for scaffolds with varied ceramics and BP content in acidic conditions. The higher gel fraction values indicate a better linkage formed.

Sample	Various Ceramic Compositions			Various BP content		
	CS/HAp /50 μ l BP	CS/TCP- α / 50 μ l BP	CS/FAp/ 50 μ l BP	CS/HAp /20 μ l BP	CS/HAp /10 μ l BP	CS/HAp /5 μ l BP
Gel fraction in 1% v/v acetic acid \pm SD	55.437 \pm 6.37	67.1465 \pm 7.93	49.0943 \pm 4.01	53.4653 \pm 4.79	56.5475 \pm 2.46	51.1598 \pm 4.16

The gel fraction (GF) is a measure of the percentage of unreacted polymer components which had leached from the scaffold during testing (Meeremans et al., 2021; Nokoarani et al., 2021). GF in acidic conditions (Table 3.1) indicates partial crosslinking of the scaffold (Dorati et al., 2017; Grabska-Zielińska et al., 2020; Kurniati et al., 2021). CS/TCP- α exhibited the highest value among the various ceramics scaffolds with a value of 67.1465 ± 7.93 followed by CS/HAp (55.437 ± 6.37) and CS/FAp (49.0943 ± 4.01). Evaluating the scaffolds with different BP contents, the CS/HAp/BP 5 μ l recorded the lowest gel fractions in acetic acid of 51.1598 ± 4.16 compared to 56.5475 ± 2.46 for CS/HAp/10 μ l BP and 53.4653 ± 4.79 for CS/HAp/20 μ l BP. The lowest gel fraction value of CS/HAp/5 μ l BP subsequent to the submerging in acetic acid is accepted as an adequately crosslinked scaffold considering the least photoinitiator used since samples did not dissolve after 24 hours in the acetic acid solution, indicating that crosslinking had occurred (Abbasi et al., 2020; Bachtiar et al., 2016; Oustadi et al., 2020; Wei et al., 2020).

On top of that, this low BP usage is more desirable to avoid any hazard of unreacted BP to the human body (Oustadi et al., 2020; Qiu, 2008; Taschner et al., 2019).

Recently, Nokoorani et al. (2021) investigated the effect of different concentrations of allantoin in chitosan/gelatin scaffolds for wound healing application and recorded gel fraction in double distilled water with values of 86-89% upon utilising 1-Ethyl-3-[3-dimethylaminopropyl] carbodiimide hydrochloride (EDC) as their crosslinker (Nokoorani et al., 2021). As chitosan is insoluble in water, these values are not comparable to results in the acetic acid and as such tests were repeated in PBS to determine comparable data and to replicate the human *in vivo* environment (Table 3.2). GF in PBS indicated that CS/FAp had the lowest gel fraction in PBS (94.55 ± 1.03), while similar values were obtained for CS/HAp and CS/TCP- α scaffolds at 99.28 ± 0.59 and 99.72 ± 0.88 , respectively. In addition, no significant differences were shown in GF in PBS for scaffolds with various BP content, exhibiting the values of 97.40 ± 1.86 , 96.83 ± 0.27 and 96.34 ± 0.18 for CS/HAp/5 μ l BP, CS/HAp/10 μ l BP and CS/HAp/20 μ l BP, respectively. These results demonstrated the highest GF in PBS for CS/HAp/5 μ l BP with only $\pm 3\%$ unreacted materials being washed away compared to the other two BP concentrations. These results were $>10\%$ higher than previously reported data from swelling CS scaffolds in ddH₂O.

Table 3.2 Swelling studies of chitosan scaffolds with different ceramics (HAp, TCP- α and FAp) and benzophenone contents (20, 10 and 5 μ l), comprising the EWC, WU, percentage of swelling and gel fraction in PBS.

Sample	Equilibrium water content, EWC \pm SD	Water uptake, WU \pm SD	% Swelling \pm SD	Gel Fraction PBS \pm SD
CS/HAp/50 μ l BP	65.74 ± 0.79	191.97 ± 6.84	291.97 ± 6.84	99.28 ± 0.59
CS/TCP- α /50 μ l BP	59.29 ± 0.95	145.74 ± 5.68	245.74 ± 5.68	99.72 ± 0.88
CS/FAp/50 μ l BP	87.71 ± 1.92	726.65 ± 127.2	826.65 ± 127.22	94.55 ± 1.03
CS/HAp/20 μ l BP	64.47 ± 0.08	181.43 ± 0.63	281.43 ± 0.63	96.34 ± 0.18
CS/HAp/10 μ l BP	64.60 ± 0.5	182.51 ± 4.04	282.51 ± 4.04	96.83 ± 0.27
CS/HAp/5 μ l BP	63.61 ± 0.43	174.85 ± 3.28	274.85 ± 3.28	97.40 ± 1.86

Moreover, it was evident that the CS/FAp-containing scaffolds recorded the highest values in EWC, WU, and swelling percentage showing the weak crosslinking degree of the scaffolds. EWC of the scaffolds were shown to be 59.29 ± 0.95 for CS/TCP- α , 65.74 ± 0.79 for CS/HAp and 87.71 ± 1.92 for CS/FAp scaffolds. Meanwhile, the EWC for the scaffolds with different BP contents were 63.61 ± 0.43 (CS/HAp/5 μ l BP), 64.60 ± 0.5 (CS/HAp/10 μ l BP) and 64.47 ± 0.08 (CS/HAp/20 μ l BP), indicating that their swelling ability was around a similar level despite the varied photoinitiator amount. While the EWC of human bone is about 15-25%, this shows the importance of water in bones since it is the main factor affecting the mechanical behaviour of the bones (Granke et al., 2015; Surowiec et al., 2022). As such, a lower EWC would be desirable.

In addition, the swelling test recorded the water uptake (WU) capacity of 145.74 ± 5.68 , 191.97 ± 6.84 , and 726.65 ± 127.2 for CS/TCP- α CS/HAp and CS/FAp scaffolds, respectively, while CS/HAp/5 μ l BP, CS/HAp/10 μ l BP and CS/HAp/20 μ l BP recorded WU values of 174.85 ± 3.28 , 182.51 ± 4.04 and 181.43 ± 0.63 , respectively, showing a reduced WU for CS/HAp/5 μ l BP. Although water uptake is essential for nutrient transport and gas interchange, swelling under physiological conditions should be controlled to avoid excessive degradation from the diffusion of water into weakly crosslinked scaffolds and thus further causing the loss of mechanical integrity and compressive stresses to the cellular environment (Kamoun et al., 2018; Maji et al., 2016; Nga et al., 2020; Tao et al., 2017). A similar trend was also shown in the percentage of swelling, with values of 826.65 ± 127.22 (CS/FAp), 291.97 ± 6.84 (CS/HAp), 245.74 ± 5.68 (CS/TCP- α), while different BP content-scaffolds presented the swelling percentage of 274.85 ± 3.28 (CS/HAp/5 μ l BP), 282.51 ± 4.04 (CS/HAp/10 μ l BP) and 281.43 ± 0.63 (CS/HAp/20 μ l BP). Higher and faster swelling behaviour in PBS of pH 7.4 corresponding to blood pH indicates the scaffolds' hydrophilicity and porosity (Grabska-Zielińska et al., 2020; X. Zhang et al., 2019). Based on the swelling data, it appears that the relative porosity of scaffolds were: CS/FAp > CS/HAp > CS/TCP- α and CS/HAp/20 μ l BP > CS/HAp/10 μ l BP > CS/HAp/5 μ l BP. It has been previously reported that crosslinking reactions are normally influenced by the type of crosslinker and its concentration as well as the reaction time (Hasirci et al., 2017; Oustadi et al., 2020; Sanchez-Salvador et al., 2021). These results validated that a high crosslinking density can be achieved even with a low BP content due to the reversible BP excitation, enabling the diradicals to revert to the ground state and continue to react with the favourable CH-

group, thus ensuring an efficient covalent bonding (Riga et al., 2017). However, since the cross conjugation took place using UV light, free radicals may be present in the scaffold. As such a radical reactive oxygen species (ROS) test should be conducted to ensure radicals are not present in the final construct.

3.3.2 Fourier-Transform Infrared Spectroscopy

The chemical compositions of the fabricated scaffolds were analysed using FTIR. In this work, chitosan exhibited peaks corresponding to N-H stretching and OH- peaks at 3336-3358 cm^{-1} , asymmetrical C-H stretch of $-\text{CH}_2$ at 2869-2921 cm^{-1} , C=O stretching of amide I at 1638-1657 cm^{-1} , the N-H deformation of amide II at 1540-1559 cm^{-1} , C- CH_3 band at 1372 cm^{-1} and the saccharide C-O-C stretching at 1149-1153 and 1024-1027 cm^{-1} , which correspond to reported values in the literature (Figure 3.5) (Becerra et al., 2022; Y. Liao et al., 2020; Nikonenko et al., 2000; Queiroz et al., 2015).

HAp powder presented characteristic peaks corresponding to PO_4^{3-} at 1026 and 1092 cm^{-1} , while scaffolds containing HAp exhibited PO_4^{3-} peaks at 1027 and 1149 cm^{-1} , with phosphate symmetrical stretching vibration at 962 cm^{-1} and CO_3^{2-} groups at 1411-1657 cm^{-1} . Referring to the literatures, hydroxyapatite is commonly identified through the presence of symmetrical phosphate stretching (950-962 cm^{-1}), orthophosphate asymmetrical stretching (1029, 1089, 980-1100 cm^{-1}), carbonate groups (1670-1420, 1418, 1471 cm^{-1}) as well as hydroxyl group stretching bands (3372-3348, 3570, 3575 cm^{-1}) (Becerra et al., 2022; Fern & Salimi, 2021; Nazeer et al., 2017; Predoi et al., 2019).

TCP- α presented phosphate peak at 1009 cm^{-1} and the presence of TCP- α scaffolds was indicated by PO_4^{3-} peaks at 944, 1024, 1063 and 1149 cm^{-1} and CO_3^{2-} -region at 895 cm^{-1} , validating the structural characteristics of the calcium phosphate ceramics. TCP- α is characterised by its main PO_4^{3-} bands of ν_3 anti-symmetric P-O stretching at 1107, 1058, 1039, 1013, 1022 and 984 cm^{-1} , as well as ν_1 symmetric P-O stretching at 935-938, 954-959 cm^{-1} (Canillas et al., 2016; Moreno et al., 2020; Sinusaite et al., 2021; Szurkowska et al., 2020; Thaitalay et al., 2018). FAp is characterised by its ν_3 phosphate ions at 960, 1020-1026, and 562 cm^{-1} , where scaffolds produced in this work which contained FAp demonstrated the presence of PO_4^{3-} peak at 1024 cm^{-1} , which is in agreement with the values reported in the literature (Anastasiou et al., 2019; Borkowski et al., 2020; Vidal et al., 2022).

PEG600DMA contains two different unsaturated bonds at both ends of its repeated unit. These peaks are represented on FTIR spectra at 1637-1650 cm^{-1} for C=C and 1720-1760 cm^{-1} for C=O (Burke et al., 2019; Della Sala et al., 2020; Kasgoz & Heydarova, 2011; Maciejewska et al., 2021). In this work, corresponding peaks were observed at 1637 cm^{-1} for C=C and 1717 cm^{-1} for C=O. Following the UV reaction, these peaks were observed at 1638-1657 cm^{-1} for C=C and 1715 cm^{-1} for C=O with reduced intensity.

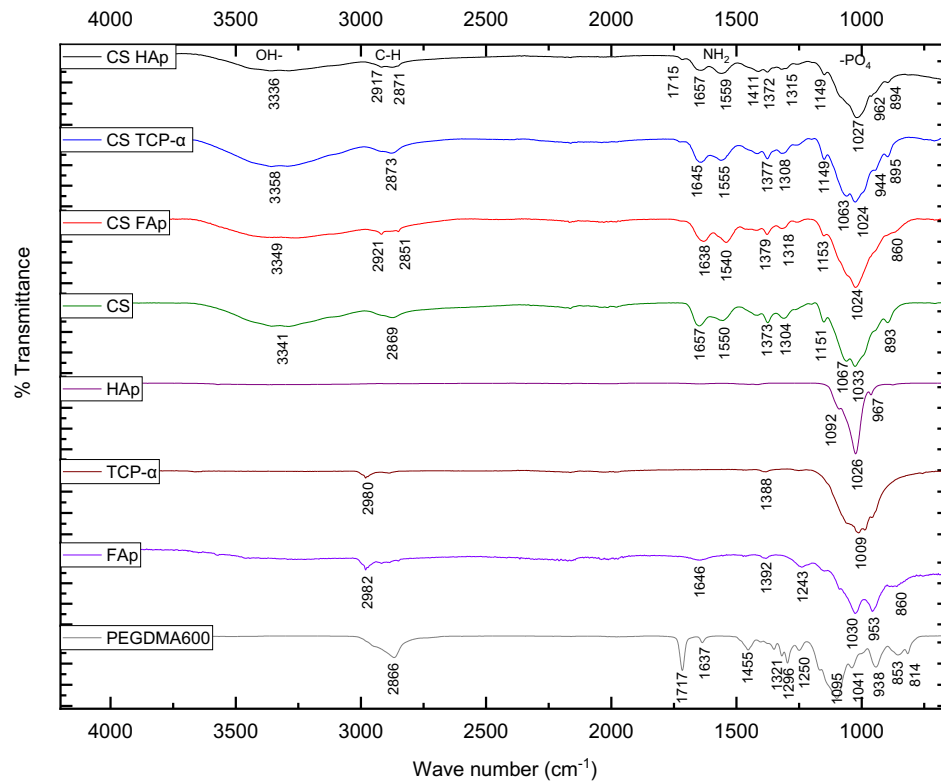


Figure 3.5 FTIR spectrum of individual components and different CS/ceramic scaffolds following the crosslinking reaction.

The FTIR spectrum of the CS/HAp scaffolds with different BP contents (50, 20, 5 and 1 μl of 0.1% w/v benzophenone) in Figure 3.6 shows that the CS/HAp scaffolds retained the structural properties with no major peaks shifting following the crosslinking reaction as outlined earlier in this section. However, with varying concentrations of BP, it was observed that the (C=C) peaks appeared to reduce with decreases in BP concentration. This peak reduction indicates breakage of the bond during crosslinking, which may have resulted in crosslinking of the chitosan structure as supported by swelling studies. This crosslinking is promising for a balance between the mechanical strength and the material degradation that will be further discussed in the next section.

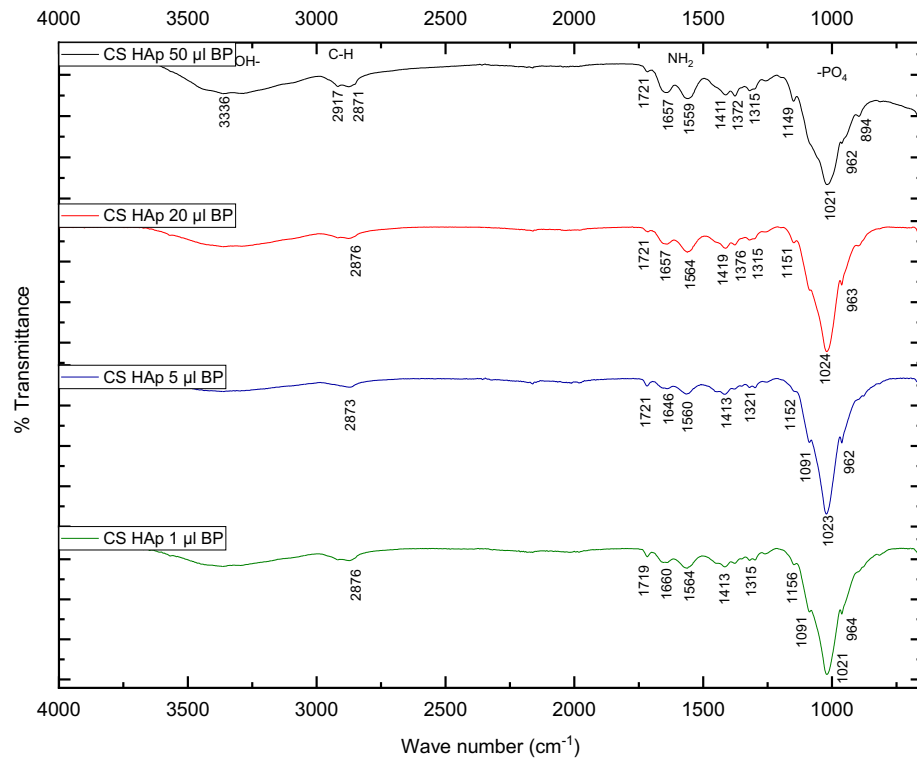


Figure 3.6 FTIR spectrum of CS/HAp scaffolds incorporating 50, 20, 5 and 1 µl BP at 0.1% w/v.

3.3.3 Mechanical Assessment

Compression testing was performed to assess the mechanical performance of the tissue engineering scaffolds. Healthy cortical bone has a strength of 100-150 MPa. However, most autografts consist of cancellous bone, which has a strength of 1.5-38 MPa (Bahraminasab, 2020; Patel et al., 2019; Roohani-Esfahani et al., 2016; Wei et al., 2020). It was found that the currently formulated scaffolds had Young's modulus values of 13.69 ± 1.06 MPa (CS/HAp), 12.82 ± 4.10 MPa (CS/TCP- α), and 15.55 ± 0.56 MPa (CS/FAp) at 60% strain (Figure 3.7), which falls into the range of cancellous bone (C. Y. Lin & Kang, 2021). Similarly, Borkowski et al. (2021) reported that their FAp/ β -1,3-glucan scaffolds achieved a compressive strength of 11.55 MPa, which is higher than their HAp/ β -1,3-glucan scaffolds of 6.57 MPa. Since β -1,3-glucan is also a polysaccharide equivalent to chitosan, their compressive strength values are relevant to the scaffolds produced in this work (Borkowski et al., 2021). These results also validated that the crosslinking of chitosan polysaccharides does enhance the mechanical properties of the scaffold products (Hasirci et al., 2017).

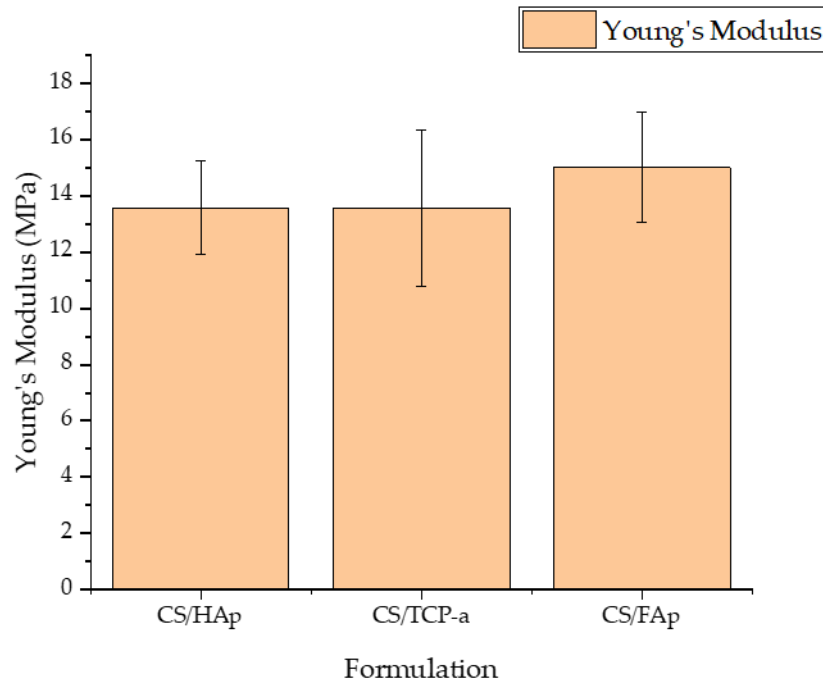


Figure 3.7 The compressive strength of the chitosan scaffolds with different bioceramics recorded similar values achieving a strength above 12 MPa.

Alterations in the photoinitiator concentration in the scaffold formulations did not have a significant effect on the compressive strength of the CS/HAp scaffolds (Figure 3.8), where values of 12.03 ± 0.98 (CS/HAp/20 μl BP), 13.62 ± 1.93 (CS/HAp/5 μl BP) and 10.75 ± 3.93 MPa (CS/HAp/1 μl BP) were recorded ($p > 0.05$, for all comparisons). A large standard deviation range in the CS/HAp scaffolds with only 1 μl BP might be caused by the least crosslinking occurred, giving unstable mechanical strength to the scaffolds. These values are higher than values reported in the literature for bone tissue engineering scaffolds, where the compressive modulus of chitosan/HAp-based composites and also aneroïn/HAp-3D complex construct were between 4-6 MPa at 60% strain and 6.42 MPa at 40% strain, respectively (G. Choi & Cha, 2019; Devine et al., 2017). Additionally, the recorded compressive strength values are also higher than the values reported by Zhang et al. (2019) from the silk fibroin (SF), carboxymethyl chitosan (CMCS), cellulose nanocrystals (CNCs) and strontium substituted hydroxyapatite (Sr-HAp) scaffold combinations, ranging from 22.91 ± 3.24 KPa to 78.55 ± 5.04 KPa (X. Zhang et al., 2019).

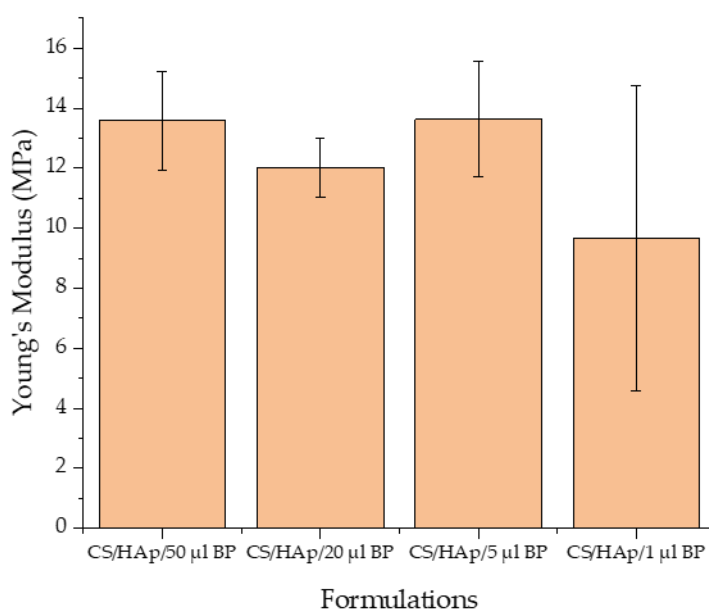


Figure 3.8 The Young's modulus values of the chitosan scaffolds with different BP contents present the lowest strength in the least BP volume.

The mechanical strength of the scaffolds is important for the recovery of two primary factors in bone healing; the load-bearing capacity and bone strength. Mechanical stimulation on the cellular level in the healing area will contribute to normal bone repair and regeneration in three stages of healing; mesenchymal stem cells proliferation in the early inflammatory phase, soft callus/non-mineralised cartilage in the reparative phase and the hard callus reconstitution in the remodelling phase (Ansari, 2019; Augat et al., 2021; T.-M. De Witte et al., 2018; X. Li et al., 2018; Y. Liao et al., 2020; Maruyama et al., 2020). Among these stages, it was found by Fu et al. (2022) that changes in mechanical stimulus can more easily manipulate the early healing process than the later ones due to the micro-motion following the initial flexible fixation (Barcik et al., 2021; Foster et al., 2021; R. Fu et al., 2022; Glatt et al., 2021; Perren, 2002; Thompson et al., 2020).

3.3.4 Biodegradation Assessment

The biodegradability of a scaffold is another vital characteristic of an engineered bone scaffold. The ideal scaffold is postulated to be able to have a degradation rate similar to the rate of the new bone formation to promote ideal bone healing (Abbasi et al., 2020; Bahraminasab, 2020; Burke et al., 2019; Grabska-Zielińska et al., 2020; Jin et al., 2019; Ligon et al., 2017; Prasad & Wong, 2018). In this work, biodegradability in the presence

of simulated body fluid (SBF) was monitored to achieve the desired degradation rate of eight weeks, which is equivalent to the bone healing time frame for healthy bone (Blackwood et al., 2012; Y. Chen et al., 2019; T. Kim et al., 2020; Mahmood et al., 2017).

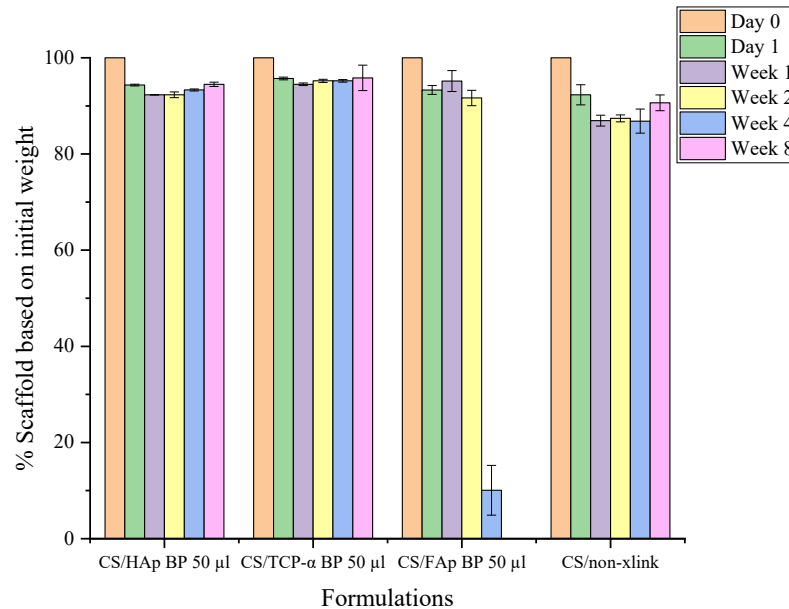


Figure 3.9 The degradation profile of the chitosan scaffolds in simulated body fluid over eight weeks shows a similar degradation rate for chitosan scaffolds with HAp, TCP- α and FAp ceramics.

After one week in the SBF, it was shown that the non-crosslinked chitosan scaffolds had lost 7.69%, which was higher than the other scaffolds tested (Figure 3.9). This weight loss is postulated to result from the absence of UV-photocrosslinking that failed to bind the biomaterials together or make a weak network, thus leading to earlier biodegradation (X. Zhang et al., 2019). It was observed from the weight-loss trend that there was a slight increase in weight at the end of the test on week eight for both CS/HAp and CS/TCP- α , which could be due to calcium phosphate salt deposition from SBF increasing the remaining scaffold weight (Bandyopadhyay et al., 2012; De Mori et al., 2019; El-fiqi et al., 2013). However, a major 81.58% weight loss was recorded for CS/FAP scaffolds between weeks 2 and 4. This high degradation rate is unlikely for fluorapatite since it was reported that FAp possesses higher resistance towards degradation in physiological conditions compared to HAp upon the insertion of F⁻ ions into OH⁻ groups (Borkowski et al., 2020; Nordquist et al., 2011; Seyedmajidi et al., 2018; Seyedmajidi & Seyedmajidi, 2022). Nevertheless, this phenomenon might be due to the higher polarity of HAp compared to FAp. As such, HAp binds more easily to the polar groups of chitosan, thereby binding the structure together and preventing high levels of swelling and

degradation. Conversely, the chitosan can swell more easily in CS/FAp (Figure 3.10) due to the electrostatic repulsion, allowing fluid ingress, which leads to an increase in hydrolytic degradation (Canillas et al., 2016).

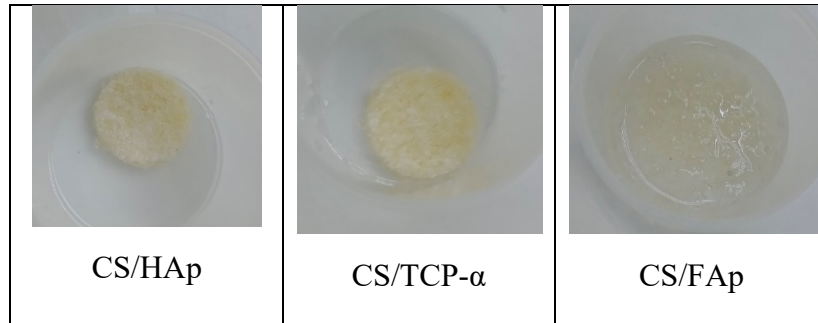


Figure 3.10 The scaffolds' physical condition following submerging in SBF for two weeks, where the swelling of chitosan was observed the most in CS/FAp.

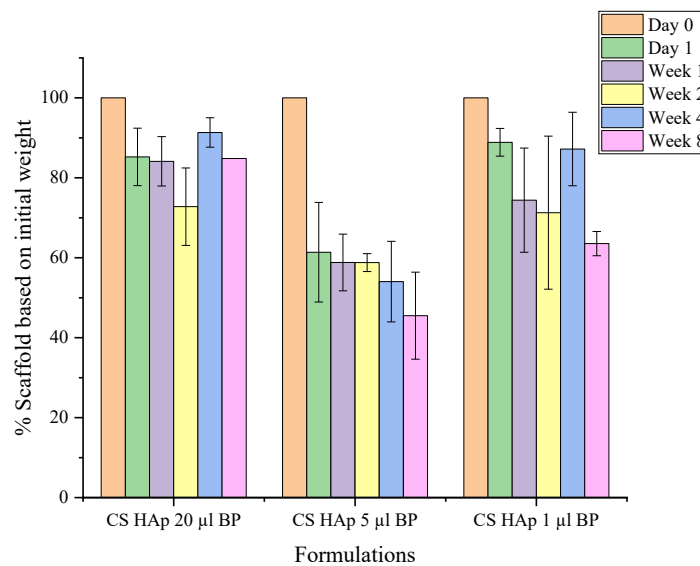


Figure 3.11 The degradation profile of CS/HAp scaffolds with different benzophenone content in SBF, where CS/HAp/5 μl BP presented a stable degradation rate for eight weeks.

Additionally, BP loading also affected the degradation rate of the scaffold (Figure 3.11). Degradation data indicated that an increased degradation was observed in CS/HAp scaffolds with reduced BP contents. Gradual and stable degradation can be observed in the CS/HAp/5 μl 0.1% w/v BP scaffold profile, where 54.48(±10.89) % weight degraded after eight weeks in SBF. The scaffolds were then left to continue degrading until week 12 and were observed to lose their integrity during handling. As such no measurement was possible at this stage, thus establishing that this representative high-strength scaffold can induce osteotransduction within the desired timeframe (Alves et al., 2020; Lavanya et al., 2020; J. Wu et al., 2019). This degradation period corresponds to a report by Turnbull et al. (2017) documenting that a porous β-dicalcium silicate (β -Ca₂SiO₄)

scaffold was aimed at bone healing applications (Turnbull et al., 2017). The loss of the scaffold integrity within this period will enable the permeation of bone healing molecules and mechanisms within the bone defect facilitating the bone regeneration process (Hernandez et al., 2016). In general, the changes in photoinitiator concentration are indeed leading to the tuneability of the degradation rate, pore size and porosity of the scaffolds (Donnaloja et al., 2020).

3.3.4.1 Mechanical Stability during Biodegradation

Since scaffolds degraded slowly over the increasing incubation period, the scaffolds' strength was also presupposed to decrease over time (C. Wang et al., 2020). The compression test was performed on the scaffolds following the degradation time points to evaluate the strength of the scaffolds while disintegrating in the SBF solution.

The compression test result (Figure 3.12) shows that the strength of the scaffolds for both formulations decreased while degrading over eight weeks. The strength of the CS/HAp scaffold decreased from 13.69(\pm 1.06) MPa after one day to 5.46(\pm 2.47) MPa after eight weeks, while CS/TCP scaffolds had reduced the strength from 12.82(\pm 4.1) MPa on day one to 8.24(\pm 1.76) MPa on week eight of the degradation test with significant difference recorded for both formulations ($p < 0.05$, for both comparisons). The decreasing trend of Young's modulus values obtained in this degradation procedure could indicate that the bonds and linkage between the materials were broken gradually, thus validating that biodegradation of the materials had occurred (F. Yang et al., 2013).

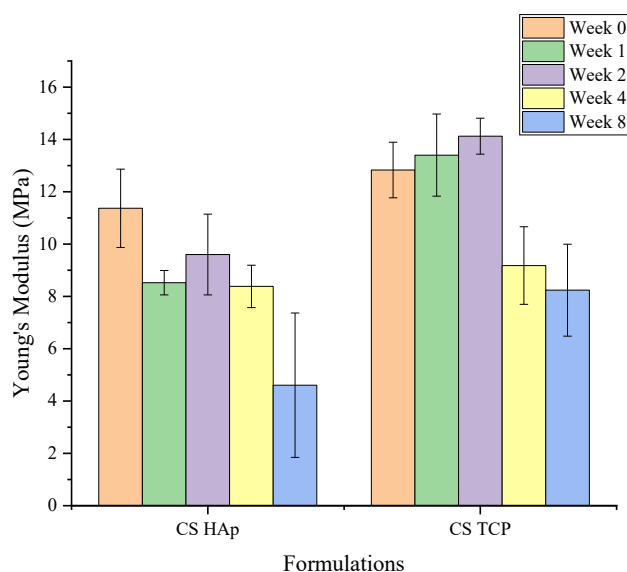


Figure 3.12 The compressive strength profile of the scaffolds while degrading in SBF for CS/HAp and CS/TCP- α , showing a reduction in the scaffold strengths over the eight weeks ($n=3$).

The compressive strength of the scaffolds fabricated with various BP content while degrading was also tested (Figure 3.13). It was found that these BP volumes which were lower than the previous 50 μl had lost their integrity during handling after four weeks in the SBF, and were thus unable to be tested after week 4. The CS/HAp scaffolds with 20 μl 0.1% w/v benzophenone showed a reduction in strength from the initial 11.20 MPa to 7.85 MPa after week 2 before increasing to 10.15 MPa in week 4. Interestingly, the compressive strength of CS/HAp/5 μl BP was observed to increase over the four weeks in the SBF. However, no significant difference was observed, illustrating that the scaffolds had maintained their strength for four weeks prior to complete disintegration in week 8 ($p>0.05$, for all comparisons). An increase in Young's modulus values after the initial reduction observed could be explained by the polymeric structural breakdown process. In the beginning, the shorter polymer chain in the scaffold composite has broken down, leaving the longer chains behind. Thus, this could result in the greater strength of the scaffold before the breaking down of the longer chain takes place. This result was highly preferable as it was aimed to maintain the strength of the scaffold following the application *in vivo* (A. Kumar et al., 2011). However, since this result was obtained from the degradation test utilising $n=3$, it is recommended to increase the sample size to $n=6$ in future investigations for a more robust outcome.

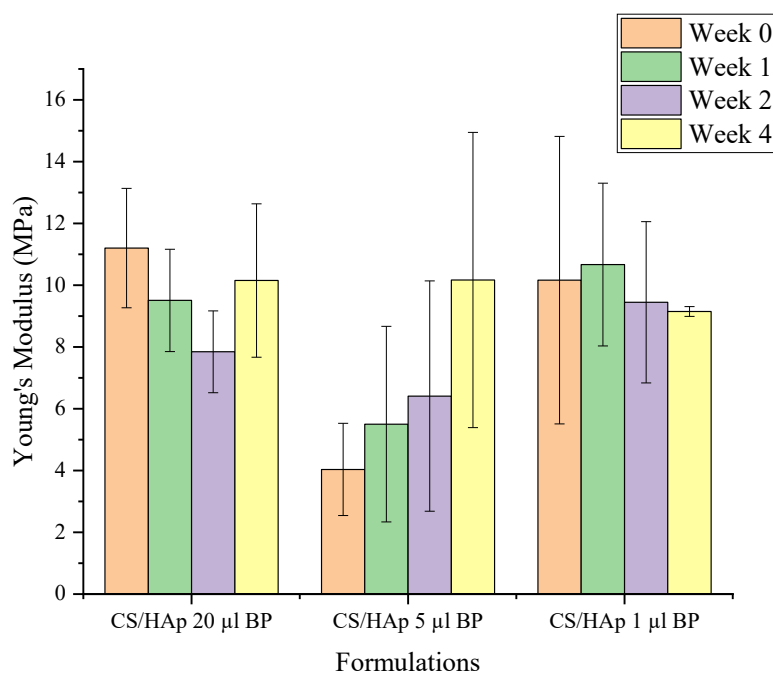


Figure 3.13 The compressive strength profile of the CS/HAp scaffolds with different BP contents while degrading in SBF for eight weeks (n=3). An increase in strengths might be indicative of the remaining strong crosslinked chains following the initial disintegration of the weaker chains.

3.3.5 Scanning Electron Microscopy and Energy Dispersive X-ray Spectrometry

Surface analysis was performed using SEM and the elemental compositions were confirmed using EDX. The main elements recorded for all scaffolds were Carbon (C), Oxygen (O) and Sodium (Na), which originated from the neutralised chitosan, while Calcium (Ca) and Phosphorus (P) represented the incorporated ceramics. In addition, the unique Fluorine (F) component present in CS/FAp scaffolds (0.9%) validated the fluorapatite prepared, although this value was less than that of the prepared FAp powder (2.5%). Chen et al. (2006) and Kimoto et al. (2011) previously validated the synthesised FAp through the presence of a fluorine peak in the EDX analysis compared to the absence of this peak in the HAp sample, thus showing the importance of fluorine in characterising FAp (H. Chen et al., 2006; Kimoto et al., 2011). CS/HAp scaffolds presented a Ca/P ratio of 2.5149 ± 0.24 , which is higher compared to the theoretical value for HAp alone and human bones of 1.66 and 2.2-1, respectively (Figure 3.14) (Alhazmi et al., 2022; Choy et al., 2021; Fernández et al., 2017; Iga et al., 2020; Mazalan et al., 2018; Miculescu et al., 2020; Nga et al., 2020; Osuchukwu et al., 2021; Redondo et al., 2022). It is hypothesised that this higher than the expected Ca/P ratio was due to the presence of unreacted calcium chloride residues in HAp (Devine et al., 2017; Ma, 2019). Also, CS/TCP- α presented a

Ca/P ratio of 1.9571 ± 0.12 which is higher than the TCP stoichiometric value (1.5) but lower than the previously reported value for TCP- β (2.02). This result might be due to the mixtures of two types of TCP, namely TCP- α and TCP- β . However, CS/FAp exhibited a Ca/P ratio of 0.986 ± 0.33 compared to its theoretical value (1.67) and previously reported Ca/P for FAp (1.4), thus showing the lesser mineralisation occurred (H. Chen et al., 2006; Choy et al., 2021; Guo et al., 2014; Ratnayake et al., 2020).

In addition, the SEM photomicrographs also revealed the porosity of the fabricated scaffold composites, which was analysed by using ImageJ software. CS/HAp presented $3.68 \pm 0.2\%$ porosity, followed by CS/FAp ($3.06 \pm 0.2\%$), and CS/TCP- α ($3.02 \pm 0.1\%$), where these values are close to the reported porosity of the cortical bone (5-30%). While it was proposed that a scaffold should possess a porosity of $>90\%$ to facilitate optimum nutrients diffusion, this will compromise the mechanical strength and thus leading to failure of load-bearing support (Donnalaja et al., 2020; Islam et al., 2020).

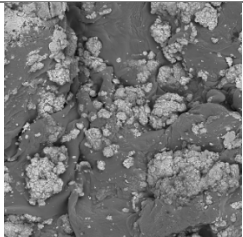
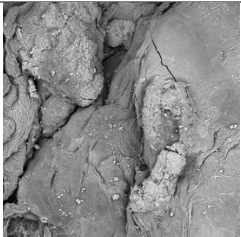
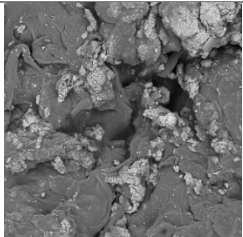
	CS/HAp/ 50 μl BP	CS/TCP-α/ 50 μl BP	CS/FAp/ 50 μl BP
SEM photomicrograph of the scaffold surface			
	1 cm: 200 μ m	1 cm: 500 μ m	1 cm: 200 μ m
Calcium	12.3 ± 3.12	17.8933 ± 5.87	7.4667 ± 3.33
Phosphate	4.925 ± 1.32	9.1467 ± 2.85	7.4 ± 0.78
Ca/P	2.5149 ± 0.24	1.9571 ± 0.12	0.986 ± 0.33

Figure 3.14 SEM-EDX analysis for the scaffolds showing the highest Ca/P values in CS/HAp followed by CS/TCP- α and CS/FAp.

The surface and elemental analyses were also conducted on the degrading CS/HAp scaffolds to observe the Ca/P ratio representing the apatite formation in SBF (Figure 3.15). The Ca/P ratio of the scaffold during the first week of degradation was observed to be the lowest (0.821 ± 0.21) compared to the later time points. This supports the theory that unreacted calcium chloride was present in the HAp. Due to its relatively high solubility, these calcium compounds dissolved leading to a reduction in the Ca/P ratio at one week. Subsequently, the Ca/P ratio increased again due to mineral deposition from

the SBF as reported by Zhang et al., (2019), Shemshad et al., (2019) and Wu et al., (2020) (Shemshad et al., 2019; M. Wu et al., 2020; X. Zhang et al., 2019). The ratio continued to decrease during the degradation study which appears to be led by an observed increase in P levels supporting the mineral deposition theory. Previously, pig bone-derived HAp was observed to reduce the Ca/P ratio after being soaked in SBF, indicating the gradual deconstruction of the ceramic in SBF as well as the elimination of organic moieties from the samples, which might as well explain the scaffolds' behaviour in this work (Lim et al., 2019).

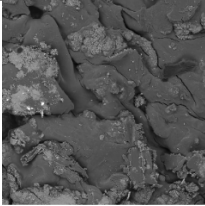
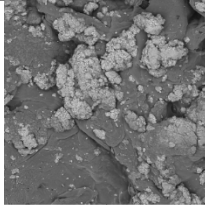
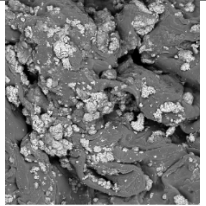
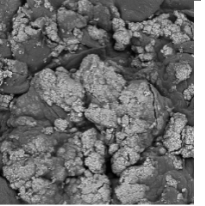
	Week 1	Week 2	Week 4	Week 8
SEM photomicrograph of the scaffold surface				
	1 cm: 200 μ m	1 cm: 200 μ m	1 cm: 200 μ m	1 cm: 200 μ m
Calcium	6.2111 \pm 2.31	13.75 \pm 3.43	10.6833 \pm 4.18	14.0833 \pm 5.44
Phosphate	7.4111 \pm 0.74	6 \pm 1.44	5.15 \pm 2.20	7.0167 \pm 2.8
Ca/P	0.821 \pm 0.21	2.2891 \pm 0.14	2.0961 \pm 0.1	2.0268 \pm 0.1

Figure 3.15 SEM-EDX analysis for the degraded CS/HAp 5 μ l BP scaffolds in weeks 1 to 8, showing a low Ca/P value in week 1 before increasing in week 2 and decreasing gradually to week 8.

3.3.6 Analysis of UV Curing Time on the Crosslinking of Chitosan/Hydroxyapatite Composite Scaffold

3.3.6.1 Crosslinking Test

A complementary test was carried out to validate the features of two different scaffold sizes (20 and 5 mm diameters), where the smaller size scaffold was intended for the upcoming tests in the cell culture. Both scaffold sizes were subjected to crosslinking testing following the UV curing process. They were submerged in 1% acetic acid for 5 minutes, 1.5 hours, 3 hours and 24 hours to assess the strength of the linkage formed.

It can be observed that the smaller 5 mm scaffolds' behaviour in the acetic acid started to dissolve in acidic conditions after 3 hours of being submerged (Figure 3.16). After 24 hours, all scaffolds were wholly dissolved in the acetic acid regardless of the curing time. If the samples were successfully crosslinked, they should remain intact in the acetic acid

(Devine & Higginbotham, 2005). It was hypothesised that the size of the scaffold might have influenced this test. Therefore, an FTIR scan was carried out for these 5 mm diameter scaffolds to confirm the linkage produced during the hydrogen abstracting free radical initiation process.

















5 minutes				
1.5 hours				
3 hours				
24 hours				
	UV 10 minutes	UV 20 minutes	UV 30 minutes	UV 40 minutes

Figure 3.16 The crosslinking test of 5 mm diameter scaffolds in acetic acid for 5 minutes, 1.5 hours, 3 hours and 24 hours to assess the linkage formed.

This crosslinking test was also carried out using the large scaffolds with 2.1 cm diameter fabricated with all four UV curing times (Figure 3.17) to compare with the small 0.5 cm diameter scaffolds. After 24 hours in contact with the acetic acid, the scaffold remained the most intact when crosslinked under UV light for 40 minutes compared to 10, 20 and 30 minutes (Figure 3.17). It was proposed that the shorter curing time had caused the samples to dissolve faster in acetic acid due to less C=C bond breaking and thus less linkage between the materials. This result was supported by a PhD dissertation stating that the amount of benzophenone will affect the crosslinking speed between the materials (Ciechacka, 2011). Subsequently, an FTIR scanning was carried out to compare the structure and bond breaking between the scaffolds of both sizes and all curing times.

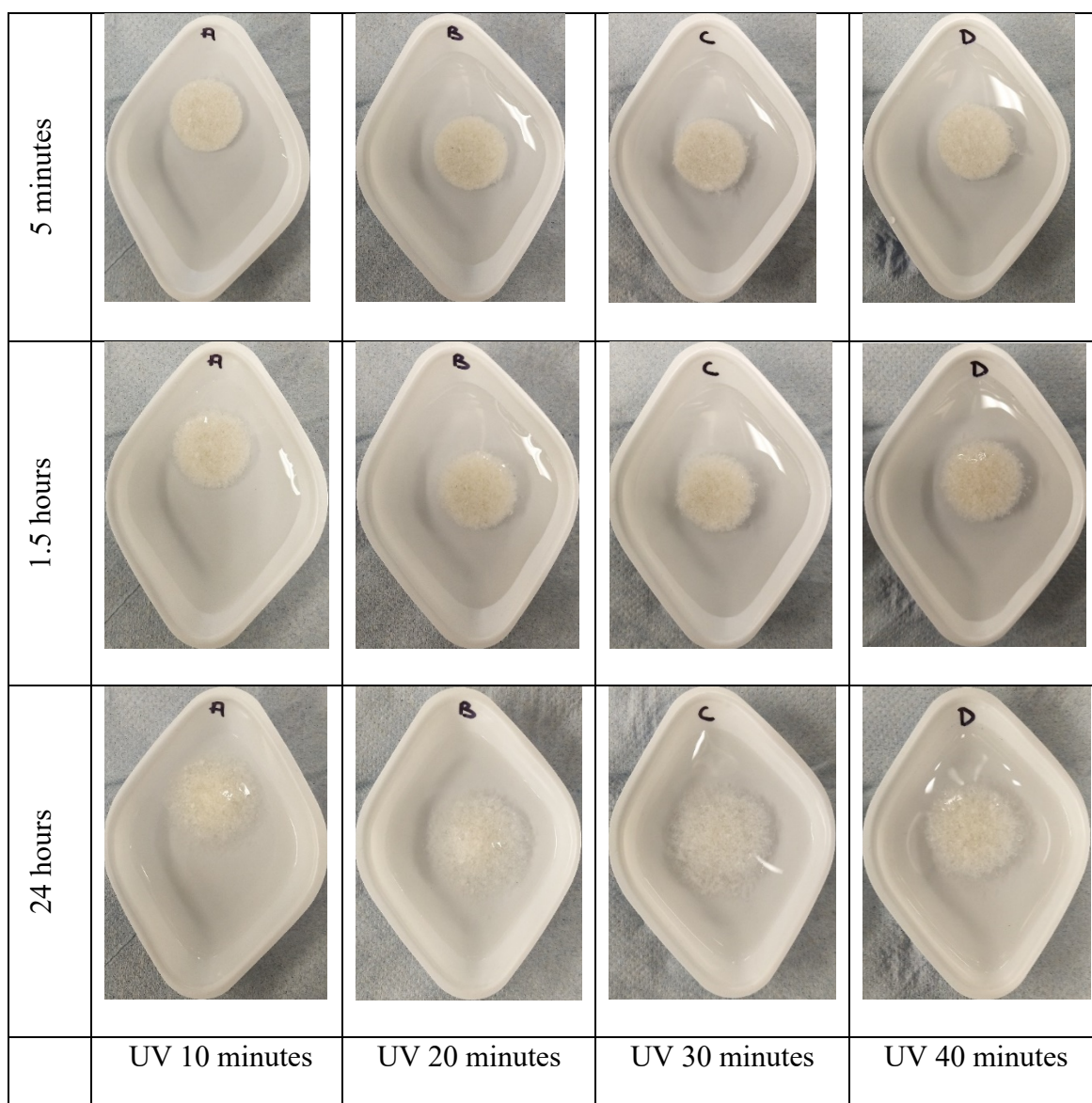


Figure 3.17 The crosslinking test of 20 mm diameter scaffolds in acetic acid for 5 minutes, 1.5 hours and 24 hours to assess the linkage formed.

3.3.6.2 Fourier-Transform Infrared Spectroscopy

The linkage formed for both scaffold sizes (20 and 5 mm diameters) was analysed using attenuated total reflectance FTIR. The spectrum for 2.0 mm scaffolds shows a shifting in samples fabricated under 40 minutes curing time at 2874 cm^{-1} peak to 2918 cm^{-1} , compared to the other curing times (Figure 3.18). This shifting could indicate the C=C bond-breaking into C-C bonds through the UV curing, which showed the sufficient curing time required for a successful crosslinking reaction. The curing time that affected the methacrylate conversion might also be the reason for this test performance (Qiu, 2008).

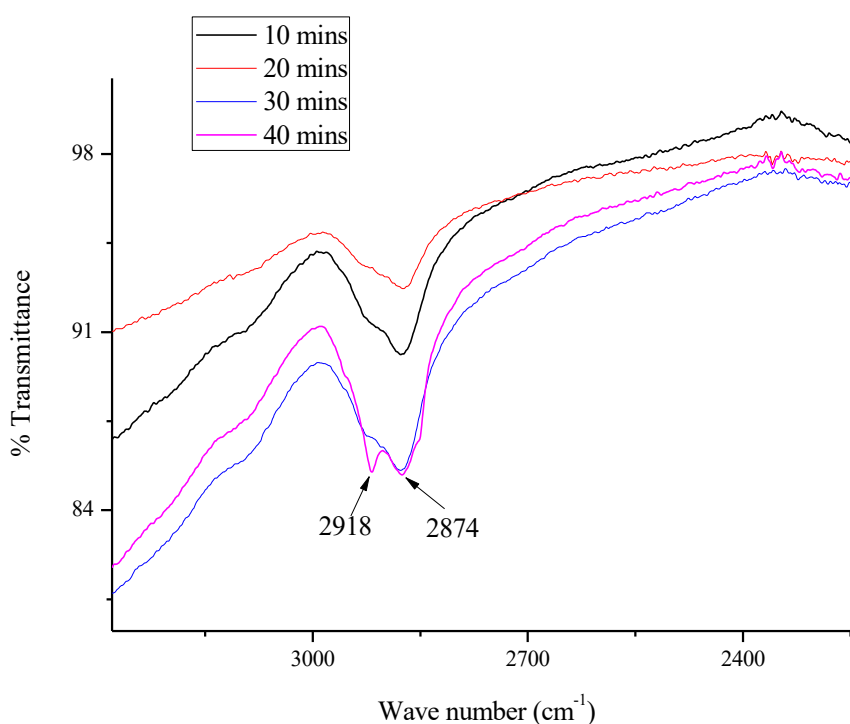


Figure 3.18 The FTIR spectrum of scaffolds with 20 mm diameter under different curing times in the UV chamber.

The previous result was then compared to the smaller scaffolds with 0.5 cm diameter (Figure 3.19), where a similar peak-shifting as found in the 20 mm diameter scaffold's spectrum was present when the smaller diameter scaffolds were UV-cured for ten minutes compared to 20, 30, and 40 minutes. This result might indicate that ten minutes of curing time under UV light was sufficient for the smaller scaffold to break the C=C bonds leading to a successful crosslinking reaction.

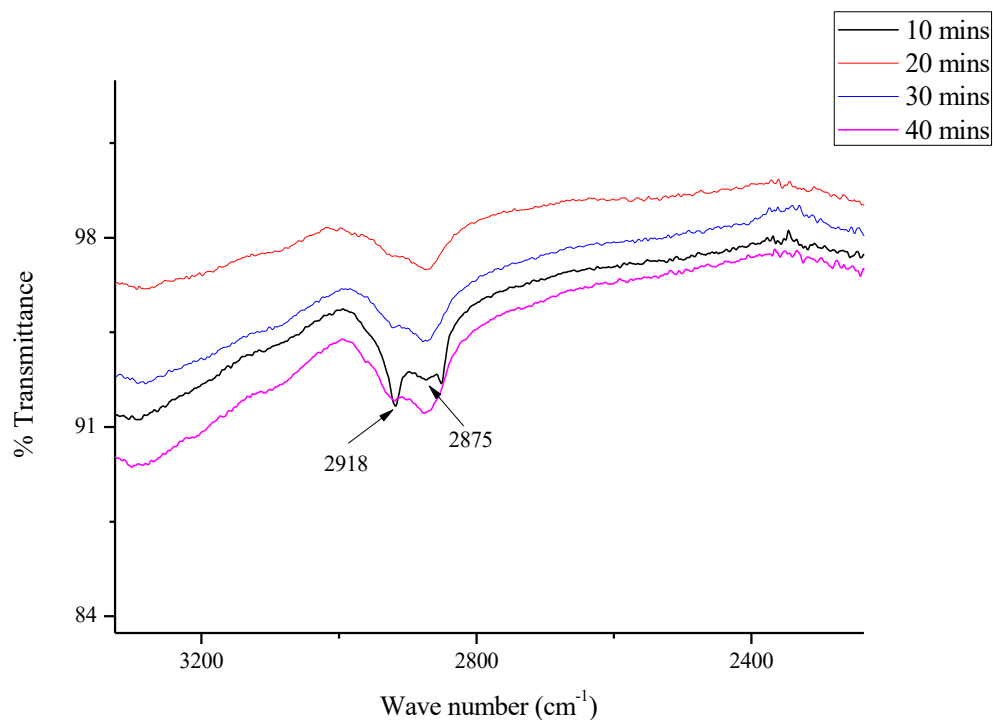


Figure 3.19 The FTIR spectrum of scaffolds with 5 mm diameter under different curing times in the UV chamber.

3.4 Summary

Developing a biodegradable bone scaffold with sufficient mechanical properties and can provide osteoconductive features is crucial in this tissue engineering field. The present study demonstrated an improved chemical crosslinking method of a chitosan-based scaffold with various bioceramics and photoinitiator alterations. The swelling test in acidic conditions presented a gel fraction of more than 50%, demonstrating crosslinking was achieved. The FTIR showed the scaffold characteristics for both chitosan and ceramics following crosslinking, where a reduction in C=C peaks were recorded with decreasing BP content. Moreover, the surface morphology was confirmed through SEM-EDX analysis. The compression testing validated the mechanical performance of the scaffolds achieving 12-15 MPa, which was sustained to at least 10 MPa during degradation recorded over eight weeks in SBF. The scaffold mineralisation in SBF was monitored semi-quantitatively using SEM-EDX, where an increase of Ca/P ratio was recorded from week 1 to week 2 before gradually reduced from week 2 to week 8.

CS/HAp with 5 μ l of 0.1% w/v benzophenone scaffold formulation is proposed for future investigation as a biomimetic bone scaffold candidate since it was found promising mechanical properties while degrading in addition to favourable swelling and gel fraction characteristics. Ultimately, the scaffold fabrication method presented is hypothesised to

provide better control of the covalent grafting of active ingredients between the scaffold structure and its release *in vitro* and later *in vivo*.

Following on from the optimisation of the scaffold fabrication in this chapter, the subsequent chapter will concentrate on the effect of loading osteogenic compounds into the scaffold and its effect on bone healing.

Chapter 4

Chapter 4: Chitosan/Hydroxyapatite Scaffolds with P28 as a Promising Osteoinductive Scaffold for Bone Healing Applications

4.1 Abstract

Despite bone's inherent ability to heal, large bone defects remain a major clinical concern. This study proposes an off-the-shelf treatment combining chitosan/hydroxyapatite (CS/HAp) scaffolds, covalently linked with either bone morphogenetic protein-2 (BMP-2) or its related peptide P28 via a UV crosslinking process. Although covalently binding the growth factors was reported as a great alternative to the conventionally physical adsorption and encapsulation methods, this method presents the risk of altering the molecular activity and interaction of the growth factors. Therefore, alkaline phosphatase (ALP) activity and alizarin red staining (ARS) with a quantitative cetylpyridinium chloride (CPC) assay were conducted to validate that our photo-crosslinking fabrication method did not interfere with the functionality of the growth factors. The ALP activity of C2C12 with 100 µg/ml P28 was found to be comparable to 0.5 µg/ml BMP-2 after two weeks, where 0.001 U/ml was recorded for both treatments. The C2C12 cultured with CS/HAp/BMP-2 and CS/HAp/P28 scaffolds also showed an increased ALP activity compared to the negative control. ARS-CPC assay presented the highest optical density in 0.3 µg/ml BMP-2 and 50 µg/ml P28, while the highest intensity of ARS was observed in C2C12 cultured with CS/HAp/BMP-2 and CS/HAp/P28 scaffolds compared to the negative controls. The osteoconductive capability of this delivery system was then investigated through a rat femoral condyle defect model, where the new bone mineral density and the bone volume increased for all CS/HAp scaffolds compared to the collagen sponge control treatment. The histological assessment showed a favourable bone regeneration efficacy of the CS/HAp/P28 compared to the CS/HAp/BMP-2 treatment, thus showing the use of CS/HAp scaffolds with P28 as a promising osteoinductive scaffold for bone healing applications.

4.2 Introduction

Critical bone defects are caused by various factors, including high-impact trauma from falling or collisions, cancer, and bone diseases, which have been a global challenge to clinical orthopaedics for centuries (Cui et al., 2018; Klein et al., 2019; Meng et al., 2021; Sparks et al., 2020; Sun et al., 2017). While autologous treatment is favoured for its gold-standard features, it requires additional surgery and its limited supply demands the need for alternatives (Jahan et al., 2020; X. Zhang et al., 2019). To date, substantial

investigations have been carried out by tissue engineering researchers collaborating with orthopaedics and plastic surgeons to come up with off-the-shelf treatment alternatives for treating bone defects (Henkel, 2017; Taraballi et al., 2017). Researchers are investigating the use of available biomaterials to produce biodegradable bone substitutes that have been the current go-to alternatives since it is a critical factor in the success of new tissue turnover (Burke et al., 2019; Fournet et al., 2019). This biodegradable biomaterial comprises synthetic biodegradable polymers, such as poly lactic-co-glycolic acid (PLGA), and naturally occurring polymers, such as chitosan, silk fibroin and collagen, as well as inorganics such as hydroxyapatite, tricalcium phosphate and antimicrobial fluorapatite (L. Chen et al., 2020; Hirenkumar & Steven, 2012).

Chitosan has been utilised in numerous research articles as a bone substitute for materials due to its biocompatible and biodegradable properties and the ability to promote cell attachment and proliferation, while it costs less compared to the other materials (Maji et al., 2016; Sukpaita et al., 2019). It has also been approved by the Food and Drug Administration (FDA) as a Generally Recognised as Safe (GRAS) biomaterial to be used for biomedical applications (Chang et al., 2016; Fourie et al., 2022; A. Kumar & Kumar, 2017; Marques et al., 2020). In addition, bone regeneration research has directed a significant application of chitosan composite in the formulation since it gives minimal foreign body reactions, has intrinsic antibacterial nature and can also be constructed into various geometries and forms for tuning the porosity, osteoinduction and osteoconduction properties (Venkatesan & Kim, 2010). Chitosan can also mimic the extracellular matrix (ECM) due to its similar structure to proteoglycans, which has led researchers to utilise it for tissue engineering (Barroso et al., 2022; Jhala et al., 2020; Nicolas et al., 2020; F. Zhang & King, 2020). However, owing to its low solubility property, chitosan is often combined with other biomaterials, such as hydroxyapatite, to improve its solubility as well as to enhance the mechanical properties and provide bioactive features to the bone scaffold (B. Li, Wang, et al., 2019; Maachou et al., 2008; Zheng et al., 2015). Moreover, despite their known osteoconductive properties, CS and HAp require the incorporation of growth factors to enhance the osteoinductive feature of the scaffolds, where osteodifferentiation of the stem cells into osteoblasts is promoted (Bjelić & Finšgar, 2021; Reves et al., 2011).

Consequently, a promising acellular strategy that centres on developing scaffolds incorporating osteogenic factors was employed. This plan combines biology and

engineering principles to create viable substitutes to restore and maintain the function of human (bone) tissue, involving covalent bonding of the growth factors to the composite vehicle through UV crosslinking. This method is one of the alternatives to overcome the limitations of surface adsorption and physical encapsulation methods, such as the unspecific affinity between the protein and carrier and the rapid uncontrolled release, respectively. This preferred alternative was reported to be efficient in yielding a thorough, stable and extended release instead (Devine et al., 2017; El Bialy et al., 2017) due to the controllable concentrations and the directed peptide conformations. In addition, covalently bound peptides were declared to have higher stability and specificity in terms of controlling the intended folding, thus allowing signalling and binding domains to be available for cellular interactions (Bullock et al., 2021).

This project was aimed at fabricating a biodegradable scaffold that will release growth factors while degrading in a gradational way for an expected period to be replaced by a newly formed bone tissue from the bonded cells (osteotransduction) and then be secreted from the body naturally after it completes its function (Alves et al., 2020). Previously, the FDA had approved a clinically relevant protein, the recombinant human bone morphogenetic protein-2 (rhBMP-2), with a collagen carrier called INFUSE[®] to induce new bone tissue following the implantation (Rosenberg et al., 2019). However, due to the ectopic bone formation resulting from the implantation, a P28 peptide derived from the knuckle epitope of BMP-2 was then examined as an alternative (Meng et al., 2021; Y. Wu et al., 2020; G. Zhao et al., 2021). This P28 peptide was postulated to present a comparable osteoinductive performance to its protein of origin since it was previously found to be a potential substitute for the full-length rhBMP-2 in inducing new bone-cell formation due to its high performance with greater control over cellular interactions and a cost-effective alternative to BMP-2 (Bain et al., 2015; Bullock et al., 2021; Cui et al., 2016).

C2C12 myoblast cell line, which has a low baseline ALP activity, normally regulates the osteoinduction process through the growth factor incorporation, typically BMP-2 (MW: 26 kDa), by altering the differentiation pathway of the myoblasts towards an osteoblastic lineage (De Gorter et al., 2010; Hidaka et al., 2020). An upregulation in ALP activity induced by BMP-2 indicates the bioactivity of these osteogenic factors (Blackwood et al., 2012; Katagiri et al., 1994). However, to our knowledge, no previous study has reported the C2C12 differentiation profile upon the osteogenic induction by P28 peptide (MW:

3091.2 Da) with the sequence of S^[PO₄] DDDDDDDKIPKASSVPTELSAISTLYL (Sun et al., 2017). Therefore, the C2C12 responses towards P28 treatments compared to BMP-2 on their own, or following the incorporation into the CS/HAp scaffolds in the cell testing, were systematically studied.

4.3 Results and Discussion

4.3.1 Scaffold Characterisation through a Fourier-Transform Infrared Spectroscopy

The chemical compositions of the fabricated scaffolds were analysed using FTIR. Chitosan characteristics could be observed through the saccharide C-O-C stretching at 1150, 1060 and 1020 cm⁻¹ and the asymmetrical C-H stretch of -CH₂ at 2921 cm⁻¹ (Becerra et al., 2022; Y. Liao et al., 2020), while HAp was commonly presented by the calcium phosphate regions at 1029, 1049, 1089, 980–1100 cm⁻¹ and carbonate regions at 1670–1420, 1418, 1471 cm⁻¹ (Fern & Salimi, 2021; Nazeer et al., 2017; Predoi et al., 2019; Shemshad et al., 2019). In this work, the CS/HAp scaffold exhibited the asymmetrical C-H stretch of -CH₂ at 2871 cm⁻¹ and the calcium phosphate regions at 1017, 1089, 1148 and 1049 cm⁻¹, corresponding to values presented in the literature.

Halloran et al. (Halloran et al., 2020) identified BMP-2 through two different amide bands of the protein at 1664 and 1393 cm⁻¹, while Rosenberg et al. (Rosenberg et al., 2019) observed the amide I at 1633 cm⁻¹ and amide II at 1533 cm⁻¹. Interestingly, the BMP-2 and P28 in this work portrayed only the amide I band at 1636 cm⁻¹ (Figure 4.1). This P28 profile was likely due to the protein of origin of the peptide, which was BMP-2, therefore it gave similar values (Cui et al., 2016; Meng et al., 2021; Sun et al., 2017).

While the concentration of BMP-2 in the mixture was low compared to the other constituents in the construct, there was an observed increase in the peak height at 1650 cm⁻¹, which could be caused by the incorporation of BMP-2. Similarly, there was a further increase in the peak height following the incorporation of P28, which was added at a higher concentration compared to BMP-2.

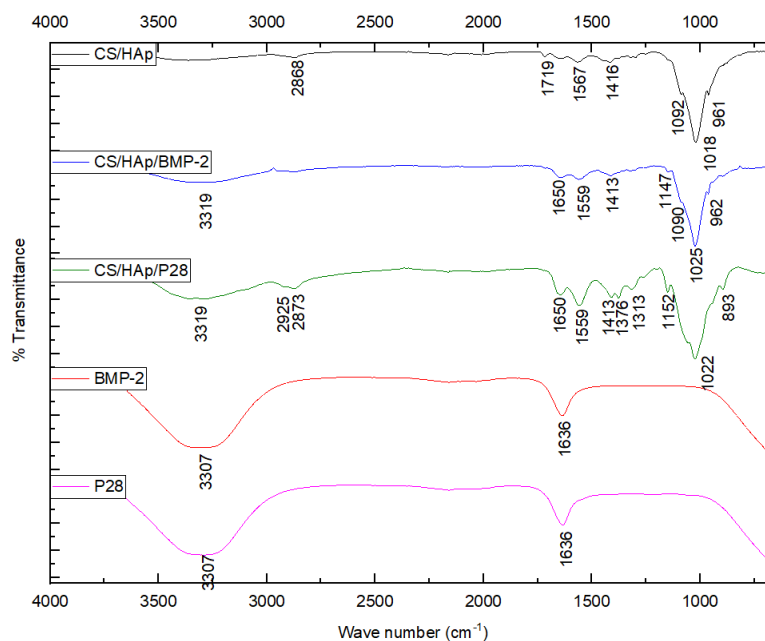


Figure 4.1 FTIR responses of the scaffolds, BMP-2 and P28, presenting the success of the covalent bonding through the increase in the peak height at 1650 cm^{-1} .

4.3.2 Kinetic Release of BMP-2

Initially, the BMP-2 and P28 release study was planned to be analysed using a high-sensitive HPLC system due to its time and cost-effective features. This technique was reported to be able to carry out a direct analysis in the analytes ranging from 2-100 $\mu\text{g/ml}$ (Biswas et al., 2019), giving a potential to detect the low GF release concentrations. Here, ultrapure water was chosen during the *in vitro* release procedure to eliminate complexity in separation.

4.3.2.1 System Suitability Test to Determine the Best Wavelength for Analysis

Initially, a system suitability test (SST) was carried out for two wavelengths (220 and 230 nm) to confirm the reproducibility of the test as an alternative to plotting the standard calibration curve. This test was performed by taking the area of each peak for each BMP-2 injection, followed by calculating the mean, standard deviation (std dev) and the percentage relative standard deviation (%RSD) (Table 4.1). It could be confirmed that the 220 nm wavelength was more suitable to be used based on its fewer variations in the peak areas of the analysis (1.40% RSD) and better reproducibility compared to 230 nm (6.64% RSD) ($p < 0.05$) (Dolan, 2008). Similarly, another study reported a 1.45% RSD from the SST for rhBMP-2 analysis, thus passing the criteria of $< 2\%$ RSD (Biswas et al., 2019).

Table 4.1 The table shows the system suitability test calculations to determine the best wavelength for the analysis of BMP-2.

	230 nm	220 nm
Injection	Total Peak Areas	
1	9346435	4524961
2	8062176	4382529
3	8115740	4390884
4	8102664	4375658
5	8153167	4429845
Mean	8356036	4420775
Std Dev	554603	61905
%RSD	6.64	1.40

Annotations: Std Dev: Standard deviation; %RSD: % Relative standard deviation

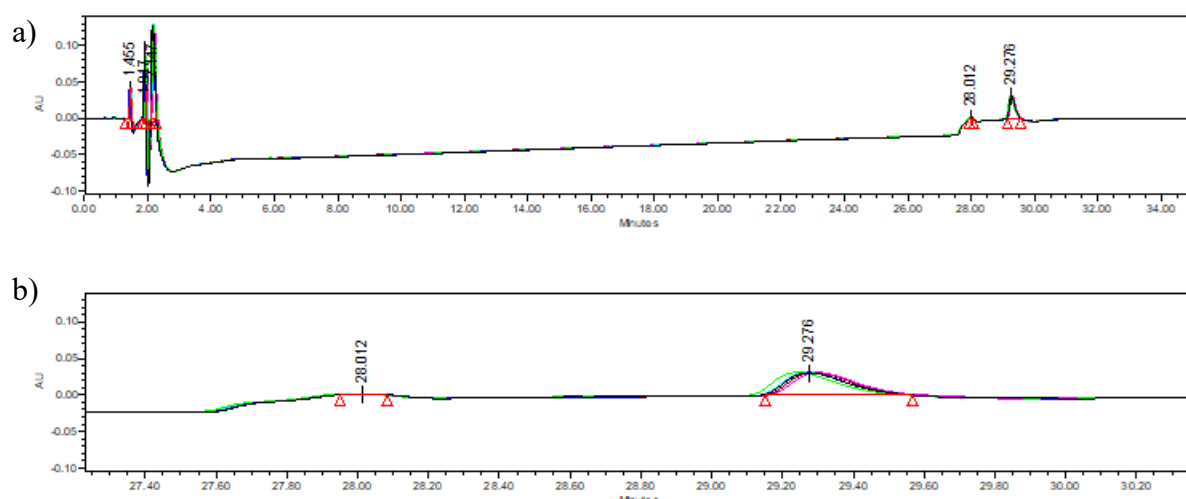


Figure 4.2 The HPLC chromatogram of 30 ng/ml BMP-2 standard shows a more consistent response in the SST. a) represents the complete chromatogram while b) shows the zoomed peak region.

4.3.2.2 The BMP-2 Release from Chitosan/Hydroxyapatite Scaffold

The HPLC was set up to run the BMP-2 release samples with wavelength set to 220 nm. Subsequently, the peak areas were calculated for the standards, negative control, and the protein released samples at different time points, starting from six hours in the water until day 14, quantifying the concentration of protein being released from the scaffold. The adjustment was made by deducting the water area from the standard and the control peak area from the samples. This procedure was carried out due to the protein's high affinity to the system, which was indicated by the pre-sampling peaks (Table 4.2), although the column and system cleaning procedures were conducted.

Table 4.2 The quantification of BMP-2 released samples at different time points by HPLC.

Sample	Peak	Adjusted Area	Released Sample Conc (ng)	BMP2 Standard Conc.
Water	443576			
BMP2 Std	539644	96068		30
Control	391161			
6h	420752	29591	9.240642	
24h	424064	32903	10.27491	
48h	433867	42706	13.33618	
72h	430149	38988	12.17513	
192h	438563	47402	14.80264	
264h	458354	67193	20.98295	
336h	453091	61930	19.33943	
Water	445874	54713	17.08571	

The values of the protein released were calculated by using this formula:

$$\text{Adjusted Area} = \text{Area of Sample} - \text{Area of Control}$$

$$\text{Adjusted Area} = \text{Area of Standard} - \text{Area of Water}$$

$$\text{Released Sample Concentration (ng)} = \frac{\text{Sample Area} \div \text{Standard Area} \times \text{Standard Concentration}}$$

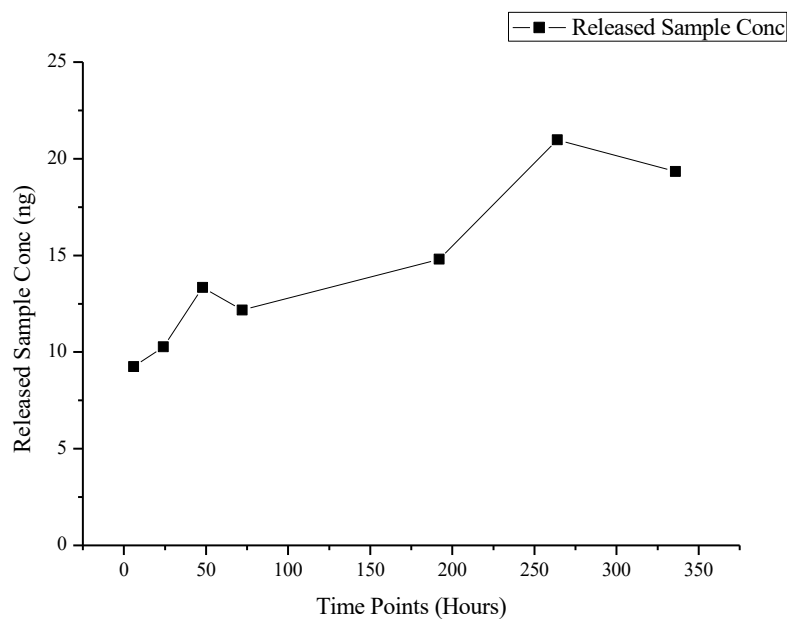


Figure 4.3 The graph shows the BMP-2 released concentration from the CS/HAp scaffold over 14 days.

It can be observed that the protein gave a slight burst release at the beginning of the test, and the scaffold continued to degrade, giving a maximum BMP-2 release after 264 hours or 11 days (20.98 ng) before decreasing at the end of the test (Figure 4.3). The trend was due to the increasing protein release from the new individual scaffold at each time point which gave the higher amount of protein released accumulated compared to the 100 ng BMP-2 incorporated into the CS/HAp scaffolds. These results concluded that the clinical-grade BMP-2 had been successfully covalently linked to the scaffold via the novel UV crosslinking procedure, and the scaffolds were able to degrade and release the protein. Therefore, this work shows an improved protein incorporation method compared to the documented previous research that utilised the adsorption method of BMP-2 onto the scaffolds. It was reported that the disadvantage of the adsorption method is the higher amount of protein needed and also the high risk of the growth factors being washed away (Y. Chen et al., 2017; C. Fu et al., 2017). For instance, collagen/hydroxyapatite composites conjugated with BMP-2 and alendronate using the physical adsorption method previously recorded a rapid release of BMP-2, where 30% of the loaded protein was washed out on the first day, and 90% of the total protein was released after seven days (Lee et al., 2021). This total release period of seven days is far too quick compared to our desired six to eight weeks of expected bone healing, thus leading us to choose another growth factor binding method instead, which is the UV photocrosslinking.

In addition, numerous research reported the quantification of the BMP-2 released from the scaffolds, but most of them had utilised the enzyme-linked immunosorbent assay (ELISA) technique instead of HPLC quantification (Draenert et al., 2013; Lee et al., 2021; Suliman et al., 2015). The HPLC method was often used to purify the peptide synthesised from protein (Cui et al., 2018; Hamilton et al., 2013; Madl et al., 2014) and quantify the peptide release instead (Cui et al., 2016). A similar approach in quantifying BMP-2 and its related peptide (P28) could be possible if an inert HPLC system is utilised in comparing the release performance following the scaffold degradation since BMP-2 has a high affinity to stainless-steel meaning the detected release rates may have been underestimated.

4.3.3 *In Vitro* Kinetic Release of P28

Due to the difficulties in terms of protein/peptide high affinity towards the stainless-steel system, the cumulative release of the P28 peptide from CS/HAp scaffolds in ultrapure water was measured using a UV spectrometer.

Within 48 h, $27.43 \pm 0.18\%$ of P28 incorporated in the scaffolds was released in a burst release manner, followed by a sustained release from 72 h until the end of the study at 14 days (2.84 ± 0.01 to $2.42 \pm 0.01\%$) (Figure 4.4). Taken together, $38.09 \pm 0.2\%$ of the total P28 was detected in 14 days. The graph was extrapolated to six weeks (1008 h) and shows a consistent P28 release rate up to this time point. This finding agreed with the bone healing timeframe, which usually takes about 6–8 weeks (Anesi et al., 2020; Fournet et al., 2019). Consequently, this release profile obtained could validate the efficiency of our CS/HAp scaffolds to retain the P28 peptide within the composite and thus serve as the delivery vehicle for the peptide, thereby promoting new bone formation (Cui et al., 2016).

These results compare favourably to previous work carried out by Sun, T. et al. (Sun et al., 2017), who incorporated P28 peptide into a nanohydroxyapatite/collagen/poly (L-lactide) (nHAp/C/PLA) scaffold and recorded a sustained release over 14 days compared to P4 peptide and BMP-2. At 14 days, $72 \pm 3\%$ of P28 had been released compared to nearly 100% for P4 and BMP-2. This profile showed the better affinity of P28 towards nHAp/C/PLA scaffolds. The affinity of P28 to HAp-containing scaffolds may also explain the slow release observed in the current study. These findings emphasise that good P28 affinity towards the scaffolds is crucial in order to extend the release profile and thus enhance osteogenesis (Xiong et al., 2020; J. Zhou et al., 2020).

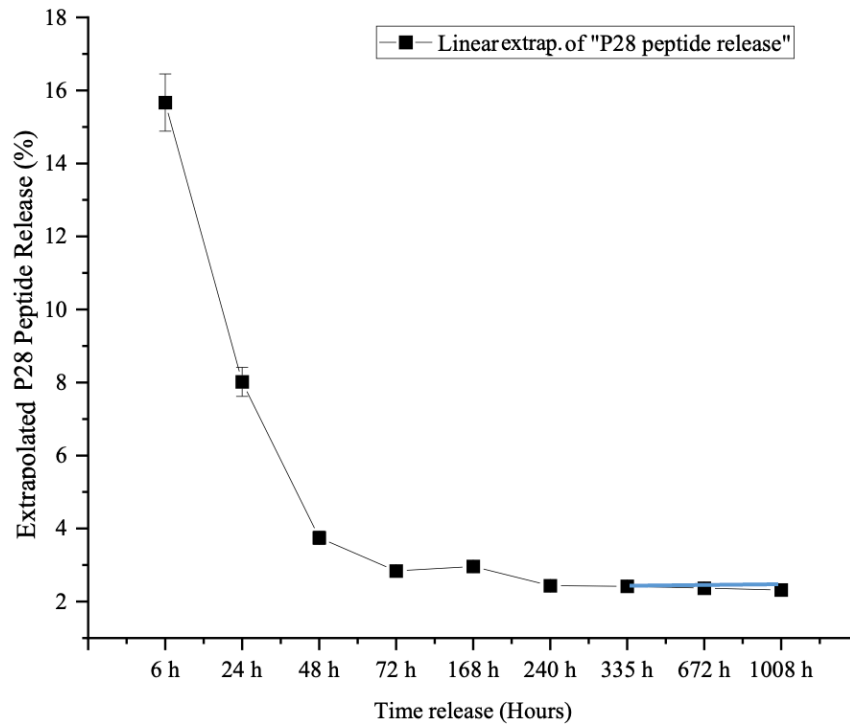


Figure 4.4 P28 release profile showing an initial burst release in the first 48 h, followed by a sustained release until 335 h (14 days). Blue line indicates the extrapolated graph to estimate the release in 672 h (4 weeks) and 1008 h (6 weeks).

Further tests with cells were carried out to verify that the released growth factor remains bioactive following the initial UV grafting step and will positively induce osteogenic differentiation .

4.3.4 C2C12 Mineralisation through Culture with P28 Peptide and BMP-2 Loaded Scaffolds Using Alkaline Phosphatase

C2C12 cells are myoblastic cells known to upregulate alkaline phosphatase (ALP) expression following exposure to BMP-2 (Honda et al., 2010). It is hypothesised that as P28 is derived from, and has a similar structure to, BMP-2, it will also upregulate ALP expression following culture with C2C12 cells. Therefore, ALP assays for C2C12 were performed in the presence of various concentrations of both BMP-2 (0.1, 0.3, 0.5 and 1 $\mu\text{g/ml}$) and P28 (10, 50, 100 and 200 $\mu\text{g/ml}$), as well as post-treatments with scaffolds (CS/HAp, CS/HAp/BMP-2 and CS/HAp/P28) in complete DMEM + 10% FBS for 4, 7 and 14 days of cell culture (Figure 4.5).

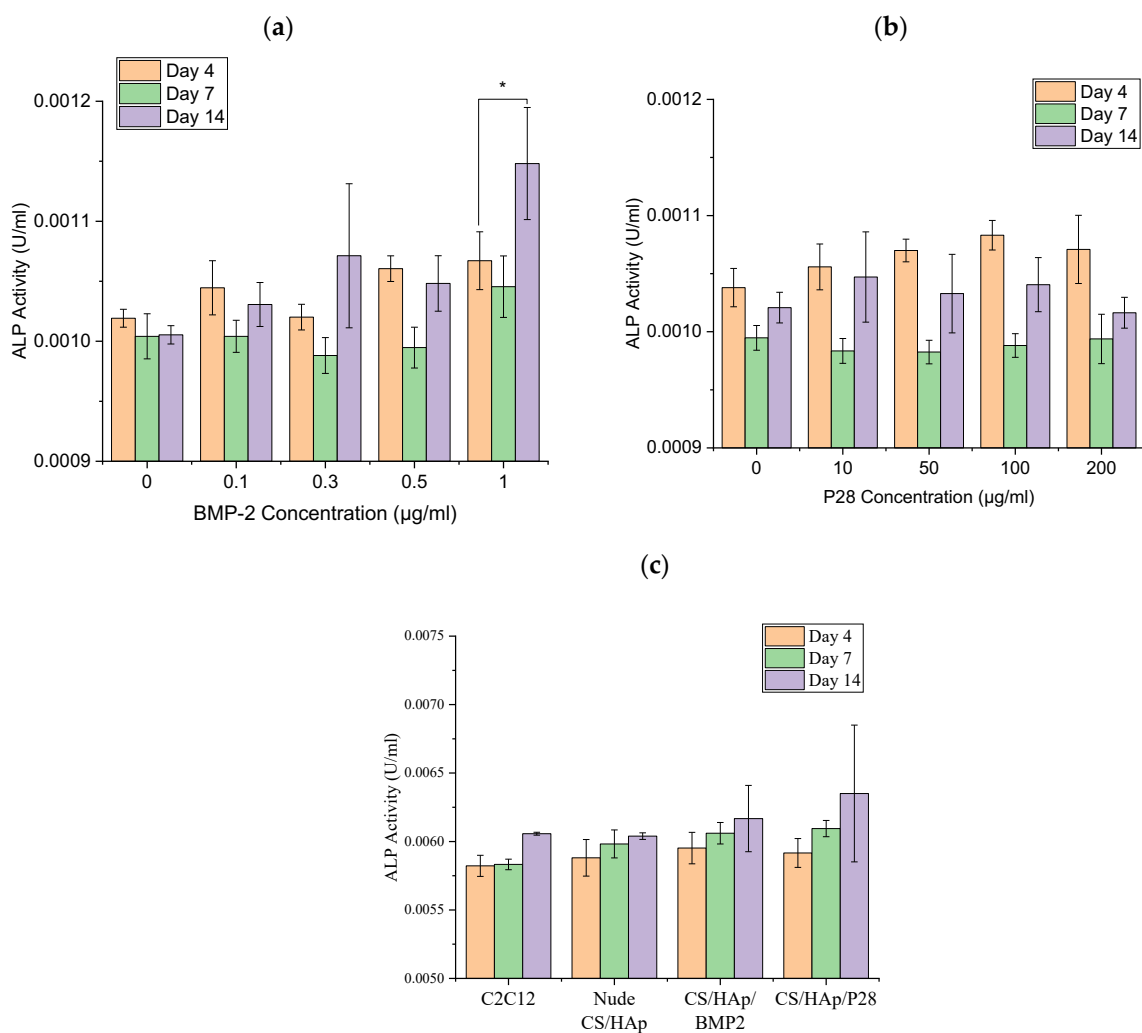


Figure 4.5 Alkaline phosphatase response of C2C12-treated with various concentrations of (a) BMP-2 and (b) P28 controls and (c) the CS/HAp scaffolds. An increased ALP response was observed in the culture with 1 µg/ml BMP-2 after 14 days, despite the high background control.

A high background was observed in the negative control, which was the untreated cells over the 14 days ($p > 0.05$). For each BMP-2 concentration, a reduction in ALP activity was observed from day 4 to day 7 before an upregulation of ALP expression from day 7 to day 14 for the treated C2C12 cultures. The BMP-2 standard with 1 µg/ml concentration presented the highest ALP activity compared to the other BMP-2 concentrations for the given culture time ($p < 0.05$). Generally, the ALP response in the C2C12 treated with BMP-2 in this work was lower than ALP expression from C2C12 cells reported by Katagiri et al. (Katagiri et al., 1994), where 0.6 U/ml alkaline phosphatase activity was recorded after six days of incubation. The reason for the lower-than-expected mineralisation data could be the method used to lyse the cells, which in this case was a mechanical disruption method using a vortex, which may have been inefficient compared to the pulsed sonicating device recommended by the kit supplier but was not available in our laboratory. Nevertheless, the increase in ALP expression indicates the inhibition of

the C2C12 myogenic cell lineage following the osteogenic treatments with BMP-2 (Hidaka et al., 2020).

Previously, researchers had studied the osteoinductivity of P28 peptide in the culture with MC3T3-E1 pre-osteoblasts phenotype (Sun et al., 2017; J. Zhou et al., 2020). To our knowledge, no study has investigated the application of P28 peptides in converting the differentiation pathway of C2C12 in bone healing treatments. Therefore, we used the same C2C12 culture system indicated for BMP-2 treatments, with cells cultured in various P28 peptide concentrations. Corresponding to the BMP-2 response, an initial reduction in the ALP activity was observed from day 4 to 7 before increasing on day 14. However, after 14 days of treatment, the ALP response remained lower than on day 4 in all P28 concentrations, although no significant difference was recorded ($p > 0.05$). The potential of several peptides derived from the similar knuckle epitope of BMP-2, such as P28, to induce calcification in the murine multipotent mesenchymal (C3H10T1/2) cell line and upregulation of ALP activity have been reported (Saito et al., 2003). P28 peptide scaffold's efficacy had also been investigated, where the positive ALP activity in the chitosan scaffold on the pre-osteoblast cell line, MC3T3-E1, was addressed (Cui et al., 2018). In addition, a recent study reported the use of another five peptides derived from BMP-2 knuckle epitope named P1 to P5 peptides to investigate the binding affinity of these peptides to the bone morphogenetic protein receptor (BMPRII) in the C2C12 cell line and deduced the P5 peptide to present the highest binding affinity to BMPRII and thus has the potential to promote osteogenesis (Gudivada et al., 2021). Therefore, the BMP-2-derived peptides, especially from the knuckle epitope of the protein structure, are indeed osteoinductive, thus reserving the P28 osteogenic potential to be further investigated.

ALP activity of C2C12 cells was also assessed in the presence of BMP-2 and P28-incorporated scaffolds (CS/HAp, CS/HAp/BMP-2 and CS/HAp/P28) to investigate whether the osteogenic factors remained bioactive following the crosslinking procedures employed in the preparation of the scaffold. A higher ALP response was recorded in the C2C12 culture with the CS/HAp, CS/HAp/BMP-2 and CS/HAp/P28 scaffolds compared to the culture with the growth factor standards presented previously. However, only day 7 of the culture showed a significant difference between the negative controls (C2C12 only and nude CS/HAp compared to CS/HAp/BMP-2 and CS/HAp/P28 ($p < 0.05$)), where an increased ALP activity was recorded for the osteogenic factors incorporated

scaffolds. In contrast, no significant difference was seen in the ALP activity in all samples on day 4 and day 14 of treatment. These results might be due to insufficient scaffold degradation or the small concentrations of both BMP-2 and P28 used in the scaffolds. However, the increase in ALP activity observed on day 7 illustrated the bioactivity of the growth factors following encapsulation. The ALP activity was lower than values reported in the literature following the incorporation of BMP-2 into scaffolds. However, in most, if not all cases, researchers utilised supplemented media, which was not used in this work. For example, Wu et al. (Y. Wu et al., 2015) utilised 50 µg/ml ascorbic acid and 10 mM β-glycerol phosphate in their C2C12 cultured with or without 100 ng/ml BMP2, where they observed an increased differentiation following the treatments. In addition, similar components were supplemented as calcification medium (10 mM β-glycerophosphate and 50 µM ascorbic acid) in C2C12 cultured with midazolam and rhBMP-2, where mineralised nodules were observed after 10 days of treatment (Hidaka et al., 2020). The supplemented media were postulated to increase the osteogenic induction further, thus enhancing ALP activity in the treatments containing the P28 standards and their associated scaffolds. The absence of these supplements in this current work might explain the lower ALP values recorded. However, the initial purpose of excluding the supplements was to eliminate any possible background responses and investigate the original osteoinductive response of our scaffold formulations without the external aid of an osteogenic medium.

A complementary investigation was attempted to validate the possible increased osteogenic response postulated earlier upon the change in the media composition. The FBS was decreased from 10% (growth medium (GM)) to 2% (differentiation medium (DM)) before treating the C2C12 cells with the scaffolds (Figure 4.6). The physical observations of the C2C12 culture in the different conditions showed the changes in the morphology of the cells after seven days in the culture using the DM and GM. It was observed that the myotubes were formed in the DM and GM culture without the scaffolds. When the scaffold was introduced, the structure of the cells changed with evidence of cuboidal structures observed in both media for all scaffold treatments, with the effect more pronounced in the GM cells (Metzger, 2016; Sondag et al., 2014).

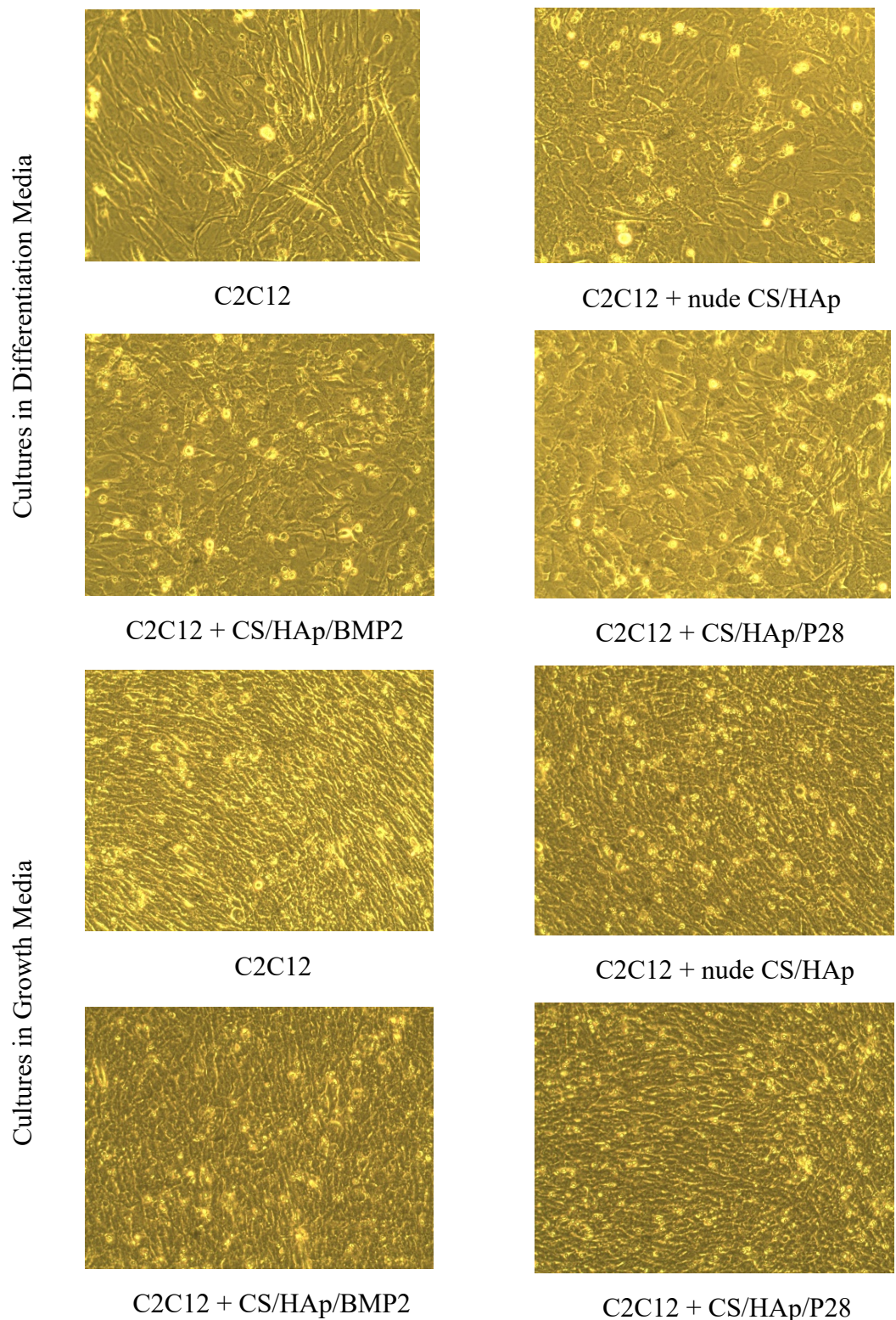


Figure 4.6 Morphological changes in C2C12 following cultured with the various scaffold formulations in differentiation media (magnification: 10×) and growth media (magnification: 4×). Cuboidal morphology can be observed in the culture with CS/HAp/BMP-2 and CS/HAp/P28 compared to the controls.

Studies have previously shown that C2C12 cells maintained their tubular shape without the treatment of growth factors, while the cell morphology changed in the presence of lower FBS content (DM) and osteogenic factor conditions (Katagiri et al., 1994). This

morphology change observed indicates a change in the cell phenotype in response to the growth factor-loaded scaffolds. These results highlight that cell culture media selection is vital in differentiation experiments as it has the possibility to affect cellular behaviour and cell expression (Kang et al., 2004).

4.3.5 C2C12 Mineralisation through Culture with P28 Peptide and BMP-2 Loaded Scaffolds Using Alizarin Red Staining

Alizarin red staining (ARS) was utilised to stain calcium deposits or mineralised nodules due to osteogenic differentiation of C2C12 subsequent to the treatment of various BMP-2 and P28 peptide concentrations for 7, 14, 21 and 28 days, followed by a destaining step using cetylpyridinium chloride (CPC). The induction from BMP-2 and P28 will shift the differentiation pathway of the myoblasts towards an osteoblastic phenotype instead of the normal myotube pathway, thus causing mineralisation (Akiyama et al., 1997; Gleeson et al., 2010; D. P. L. Lin et al., 2017; Rauch et al., 2002).

Positive ARS in C2C12 cultured with BMP-2 was observed, with an enhanced stain in the treatments with 0.5 and 1 µg/ml BMP-2 after four weeks (Figure 4.7a). In addition, there was an increased CPC response following the ARS in each of the BMP-2 concentrations over the four weeks of treatments ($p < 0.05$), where BMP-2 of 0.3 µg/ml gave the highest optical density of more than 0.5 after four weeks. Conversely, no significant difference was achieved for the negative control set over the four weeks ($p > 0.05$) (Figure 4.7b). The response of the BMP-2-treated cells was higher compared to the controls, thus indicating increased mineralisation following the induction of the growth factors up to the fourth week. Positive results were also previously obtained through a study with the treatment of rhBMP-2 and fibroblast growth factor-2 (FGF-2) in C2C12 culture, where the 4 µg/ml of rhBMP-2 and 2 ng/mL FGF-2 showed the highest level of mineralisation after four weeks. However, the cells marked with ARS were not de-stained with CPC for quantitative values, hence presenting only qualitative observation (Song et al., 2017).

Other interesting results were reported, testing the effects of rhBMP-2 in the calcification activity of C2C12 cultured with the osteogenic medium (Hidaka et al., 2020). However, no appearance of the calcium nodules stained by ARS was observed in culture using an osteogenic medium with the presence of 0.5 µg/ml rhBMP-2 after ten days, whereas in the current study, calcium nodules were observed as early as seven days in the same

concentration. This mineralisation shows that BMP-2 has the ability to shift the differentiation pathway of the C2C12, although the culture media used was not supplemented with any osteoinductive components such as the ascorbic acid and β -glycerophosphate that were used by the other studies (Gleeson et al., 2010; Hidaka et al., 2020; Ho et al., 2014; Y. Wu et al., 2015). Nevertheless, it was reported that the osteogenic medium would indeed enable the higher induction of mineral deposition of BMSCs in 14 days (Shalumon et al., 2016).

Subsequently, various P28 peptide concentrations were tested using ARS and CPC assay to assess the ability to induce C2C12 calcification. A positive ARS was visible from week two of the treatments and the staining intensity increased over the four weeks studied (Figure 4.7c). The CPC assay showed a significant difference in the staining intensity in each of the P28 concentrations over four weeks ($p < 0.05$) (Figure 4.7d). In addition, a significant difference was also obtained comparing the 0 and 10 $\mu\text{g/ml}$ P28 to 50, 100 and 200 $\mu\text{g/ml}$ P28 concentrations at week four ($p < 0.05$). This result indicated that P28 concentrations of 50 $\mu\text{g/ml}$ and above can induce calcification in the C2C12 culture. This work is in alignment with the literature where ARS was conducted on the MC3T3-E1 pre-osteoblasts cultured with P28-infused scaffolds, where cells cultured with P28 scaffolds showed an increase in mineralisation compared to a negative control scaffold (J. Zhou et al., 2020). In addition, P28 was found to possess osteoinductivity similar to its protein of origin, BMP-2, which was further validated *in vivo* through the implantation of silicone/hydroxyapatite scaffold with P28 peptide (Si/HAp/P28) in the rat calvarial defects (Cui et al., 2018).

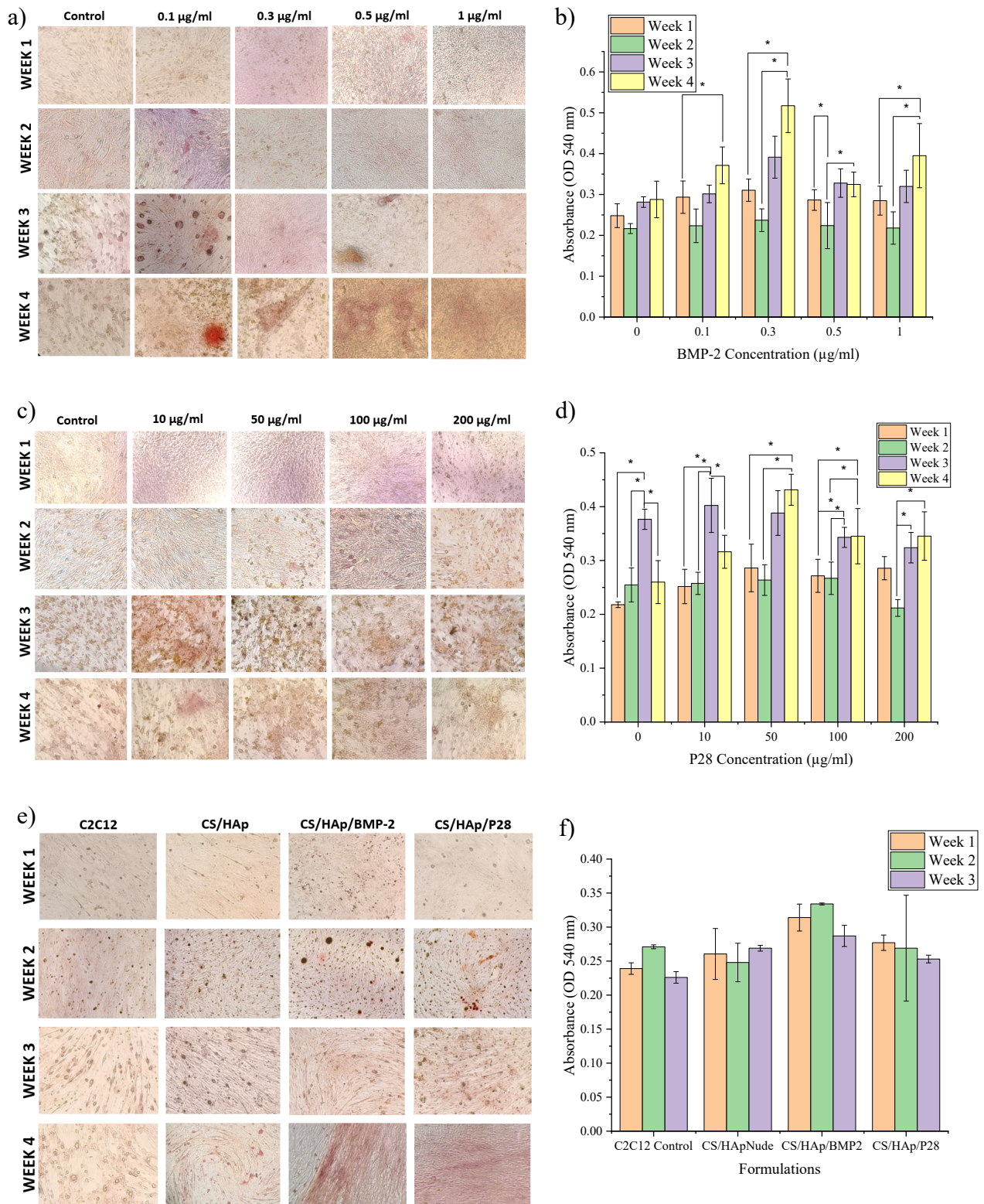


Figure 4.7 Alizarin red stained images and the destaining by CPC quantitation. (a) ARS of C2C12 treated with various concentrations of BMP-2. (b) CPC quantitation of the destained ARS of C2C12 treated with various concentrations of BMP-2. (c) ARS of C2C12 treated with various concentrations of P28. (d) CPC quantitation of the destained ARS of C2C12 treated with various concentrations of P28. (e) ARS of C2C12 treated with various CS/HAp scaffolds. (f) CPC quantitation of the destained ARS of C2C12 treated with various CS/HAp scaffolds. Positive ARS was observed in week 4 following the treatments with BMP-2 and P28 as well as CS/HAp/BMP-2, CS/HAp/P28 compared to the controls. (* $p < 0.05$).

Complications with the use of high doses of growth factors have been widely reported (Bouyer et al., 2016; Durham et al., 2020; Hettiaratchi et al., 2020; Kisiel, 2013; Lee et al., 2021; Mumcuoglu et al., 2018). As such, low-dose osteogenic factor treatments (0.1 µg BMP-2 or 25µg P28) were used for ARS, carried out in the presence of the CS/HAp scaffolds UV-grafted with either (CS/HAp, CS/HAp/BMP-2 and CS/HAp/P28) for four weeks. The treated cells were stained with ARS (Figure 4.7e), which was followed by de-staining using CPC (Figure 4.7f). However, CPC results could not be measured until week 3 due to the sterility of the scaffolds from the condensation that might cause contamination and leaving only one sample at week 4. It is suggestive to use sterile freshly made scaffolds to avoid possible contamination from the stored scaffolds.

Slightly positive ARS was observed in CS/HAp/BMP-2 and CS/HAp/P28 treatments in C2C12 compared to the cells without any scaffolds and the cells with nude CS/HAp. However, due to the low intensity of the ARS, the CPC assay shows no significant difference in all scaffold treatments. This low calcification might have been caused by the insufficient degradation of the scaffolds since the scaffolds were found to degrade after eight weeks, thus delaying the release of the growth factors in this mineralisation assay.

In addition, the low growth factor concentrations incorporated in the CS/HAp scaffolds might also have caused the low mineralisation seen in the cells. A previous study had reported that using 3 mg/ml P28 in the mineralised small intestinal submucosa (mSIS) scaffolds resulted in the highest mineralisations in the rat calvarial defects, compared to the negative control (Sun et al., 2018). However, the P28 incorporation method used in this study was the absorption method which is known to lead to weak binding with the scaffold and to a burst release of ca. 10% of the P28 loading (Sun et al., 2018). It is likely that the higher peptide concentrations used by Sun et al. led to a more rapid C2C12 response, thereby enhancing the cellular response.

4.3.6 Post-Operative Evaluations of the Animals

The post-surgery recovery of the animals was examined in terms of pain, lameness, inflammation and growth rate, where the body weight of rats was compared relative to the initial weight before implantation (Alghamdi et al., 2014; Luckanagul et al., 2016). In relation to the mean body weight curve per group, a slight decrease in body weight was noted just after the surgery (Figure 4.8). This bodyweight reduction could be explained

by the lameness development that might decrease the animal's appetite, thus reducing the animal's capacity to catch food (Brennan et al., 2009). The observed weight loss was similar to several studies reporting less than 10% weight loss post-operative, indicating a normal phenomenon (Baker, 2016; Brennan et al., 2009). However, no intervention was needed since the rats did not reach the maximum admissible weight loss ($\leq 20\%$) (Baker, 2016). In addition, it was observed that the mean body weight in all groups started to increase after day six, which was in line with the physiological increase seen with ageing, thus suggesting that neither the surgery nor the lameness affected animal metabolism (Z. Zhao et al., 2009).

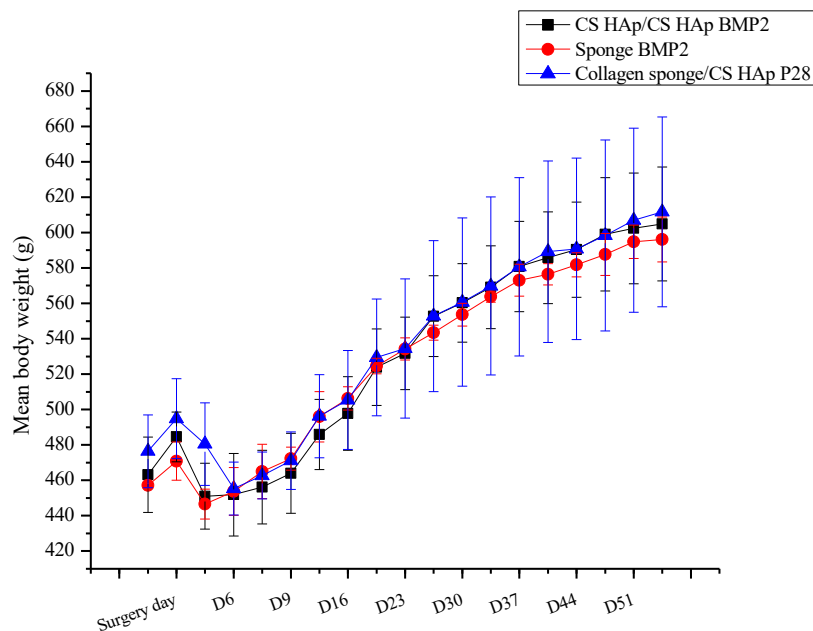


Figure 4.8 Mean body weight curve for each group.

4.3.7 Macroscopic Evaluation

Following euthanasia, the implanted femoral condyles were harvested, and local macroscopic evaluation was carried out. Traces of defects were still visible and appeared as small irregular bumps in condyles with the implanted CS/HAp scaffolds or collagen sponge alone (Figure 4.9). In contrast, they appeared as regular holes closed by transparent tissue in collagen sponge/rhBMP-2 condyles. The defects were visible in condyles implanted with CS/HAp scaffolds, whether the scaffold was conjugated with the growth factors or not, suggesting that the entry of the defect was not completely closed after two months of implantation. These visible defects might have been caused by the incomplete degradation of the chitosan-based scaffolds *in vivo*, although proven otherwise (X. Zhang et al., 2019).

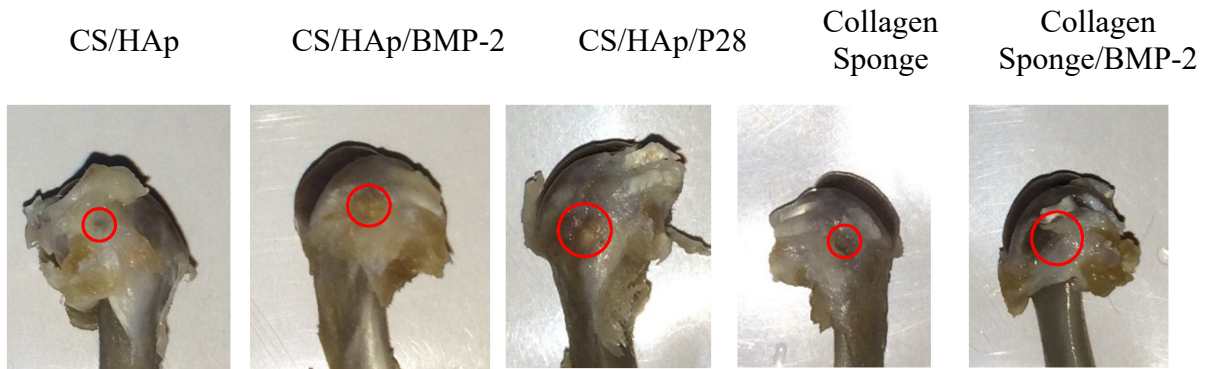


Figure 4.9 Defects visibility on the condyles after eight weeks (red circle). Traces of defects were still visible and appeared as small irregular bumps, especially in condyles with the implanted CS/HAp scaffolds.

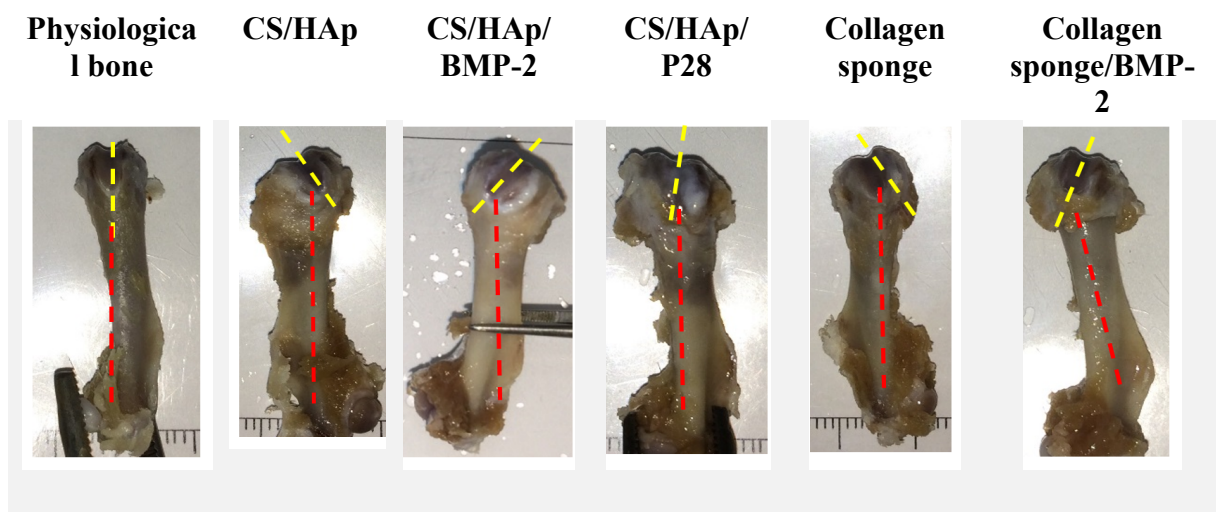


Figure 4.10 Representative images of twisted condyles comparisons between the implanted and physiological femoral condyle after eight weeks, showing that all groups experienced twisted condyle formation that might be caused by rotational instability from the defect induction and implantation. Annotations: Yellow broken lines=condyle axis; Red broken lines=femoral diaphysis axis

Observing the bone physiology, 71% of the femoral condyles in all types of implanted material were, surprisingly, twisted towards the defect side, compared to a normal femoral condyle (Figure 4.10). This bone torsion could have been caused by the presence of the scaffolds as foreign materials or the defect induction surgery causing a level of rotational instability upon ambulation from the press-fitted implant in the defects of the animals, which could not be confirmed due to the absence of an empty defect in this study (Mohiuddin et al., 2019). Since this study takes the collagen sponge/BMP-2 as the positive control while the nude CS/HAp scaffold is considered as the negative control, an empty defect should also be considered in the future. However, a similar phenomenon was also seen in a study regarding an osteoarthritic joint remodelling, where slight gross morphological changes and deformations, such as twisted shapes in the temporomandibular joint of Sprague Dawley rats, were observed post-development of

prosthetic unilateral anterior crossbite rodent model, which might have been caused by the modifications in deep zone cartilage (H. Y. Zhang et al., 2019; J. Zhang et al., 2018). Therefore, this contorted or twisted condyles observation following the implantation is worth to be investigated in the future since this phenomenon somehow might affect the healing capacity of the bone defects.

4.3.8 Micro-CT Evaluation of the Femoral Defects Treated with the Scaffolds

Micro-computed tomography (μ CT) scanning analyses were conducted on the implanted condyles following the harvest after eight weeks of implantation and the images were reconstructed to observe the new bone formation within the defects. In scaffold conditions (with or without BMP-2 or P28), the defect was mainly visible and delineated with bone tissue at the defect margin, while the entry of the defect remained empty. Femoral distortion was observed to be subsided to the side of the defect in all types of scaffolds, while no other bone lesions were observed (Figure 4.11). This architectural distortion observed in the remodelled bone could have been secondary to the various incidents of collapse, asymmetric growth and disturbed ossification process (Bejar et al., 2005).

In addition, mineralised areas inside the defect, and at the defect entrance, were observed. These mineralised areas may have corresponded to HAp residues (a mineralised cement) that could block the defect closure even after eight weeks. However, the mineralised areas may also have corresponded to newly formed bone islets, suggesting osteogenesis (X. Chen et al., 2016). Conversely, the defect was almost not visible in condyles implanted with the collagen sponge (with or without BMP-2). Only a few traces of defect margin were still observed while the defect entrance was already closed. Moreover, the collagen sponge was not visible anymore. It was previously reported that the collagen sponge could be entirely resorbed in 28 days, thus showing that the bone healing was almost ended (Lyles et al., 2015).

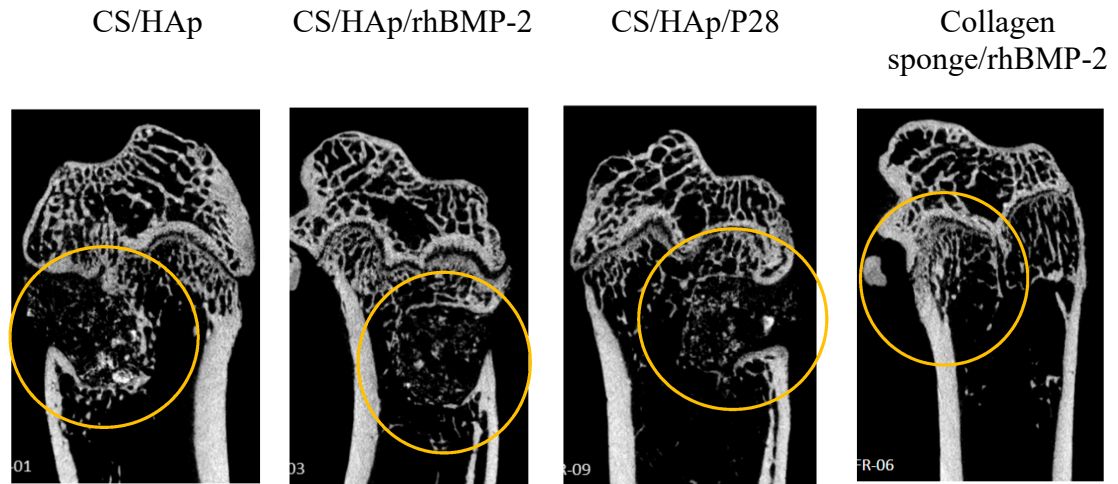


Figure 4.11 Representative coronal view images of the femoral condyle in CT scan per sample group after eight weeks of implantation. The condyle implanted with collagen sponge/rhBMP-2 is observed to reach the terminal healing process while traces of scaffolds were still present in CS/HAp scaffolds. However, CS/HAp/P28 gave better defect closure compared to CS/HAp and CS/HAp/rhBMP-2. (Annotation: Yellow circle= Implantation site)

4.3.8.1 Quantitative Analysis of Micro-Computed Tomography Scanning

The bone volume fraction (BV/TV) and bone mineral density (BMD) (Figure 4.12) were measured, including both the entire defect and its margin (ROI 4 mm). The hydroxyapatite might have caused a higher bone volume fraction (BV/TV) and bone mineral density (BMD) in the presence of a chitosan-based scaffold compared to the collagen sponge, with a significant difference between collagen sponge/rhBMP-2 and CS/HAp/BMP-2 ($p < 0.05$) (there was an increase of 22% for BV/TV and 38% for BMD).

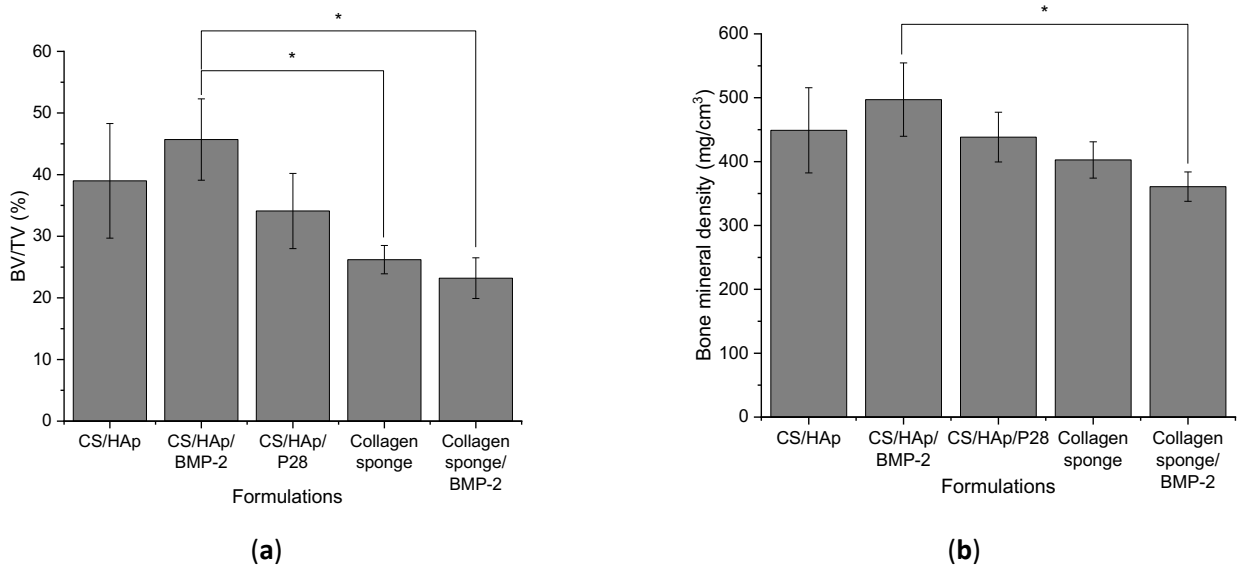


Figure 4.12 (a) Graph of mean volume fraction for each sample group in the entire defect and its margin after eight weeks (ROI 4 mm) (CS/HAp: $39 \pm 9.3\%$; CS/HAp/BMP-2: $45.7 \pm 6.6\%$; CS/HAp/P28: $34.1 \pm 6.1\%$; Collagen sponge: $26.2 \pm 2.3\%$; Collagen sponge/BMP-2: $23.2 \pm 3.3\%$). (b) Graph of mean bone mineral density per sample group in the entire defect and margin after eight weeks (ROI 4 mm) (CS/HAp: $449.06 \pm 66.69 \text{ mg/cm}^3$; CS/HAp/BMP-2: $497.03 \pm 57.45 \text{ mg/cm}^3$; CS/HAp/P28: $438.37 \pm 38.94 \text{ mg/cm}^3$; Collagen sponge: $402.6 \pm 28.45 \text{ mg/cm}^3$; Collagen sponge/BMP-2: $360.83 \pm 22.93 \text{ mg/cm}^3$). Significant difference was achieved in CS/HAp/rhBMP-2 treatments compared to the others. However, the values might be due to traces of HAp, which is a type of ceramic. (* $p < 0.05$).

Previously, the BV/TV values of the nude collagen sponge and collagen sponge soaked with a clinical dose of BMP-2 (5000 ng) were reported to be around only 4% and 9%, respectively (Durham et al., 2018). This value was much less than the values recorded in this work, where the newly formulated scaffolds with 100 ng BMP-2 yielded more than 40% BV/TV value, which was almost four times more than the reported BV/TV of collagen sponge/BMP-2. This result also validated the efficiency of the growth factor UV grafting method compared to the anionic binding method, where the latter might lead to a burst release phenomenon, thus resulting in a low yield of new bone formation (Oliveira et al., 2021). Furthermore, the report showed decreased BV/TV values in increasing BMP-2 concentrations, indicating decreased bone healing. However, an increased ectopic bone formation was yielded with increasing BMP-2 concentrations in the collagen sponge (Durham et al., 2018). Therefore, the low dose of BMP-2 and its peptide, P28, in the chitosan-based scaffold might be the better alternative for clinical use.

4.3.9 Histopathologic Analysis

A Hematoxylin-Eosin (HE) staining was carried out to perform a deep qualitative analysis of the tissues (Figure 4.13). In addition, ISO10993-6:2016 explains the possible assessment of local tissue changes post-implantation of biomedical devices, where the inflammatory response, tissue morphology, presence of fibrosis, necrosis, biomaterial residues, inflammation and bone formation are evaluated (Maglio et al., 2020).

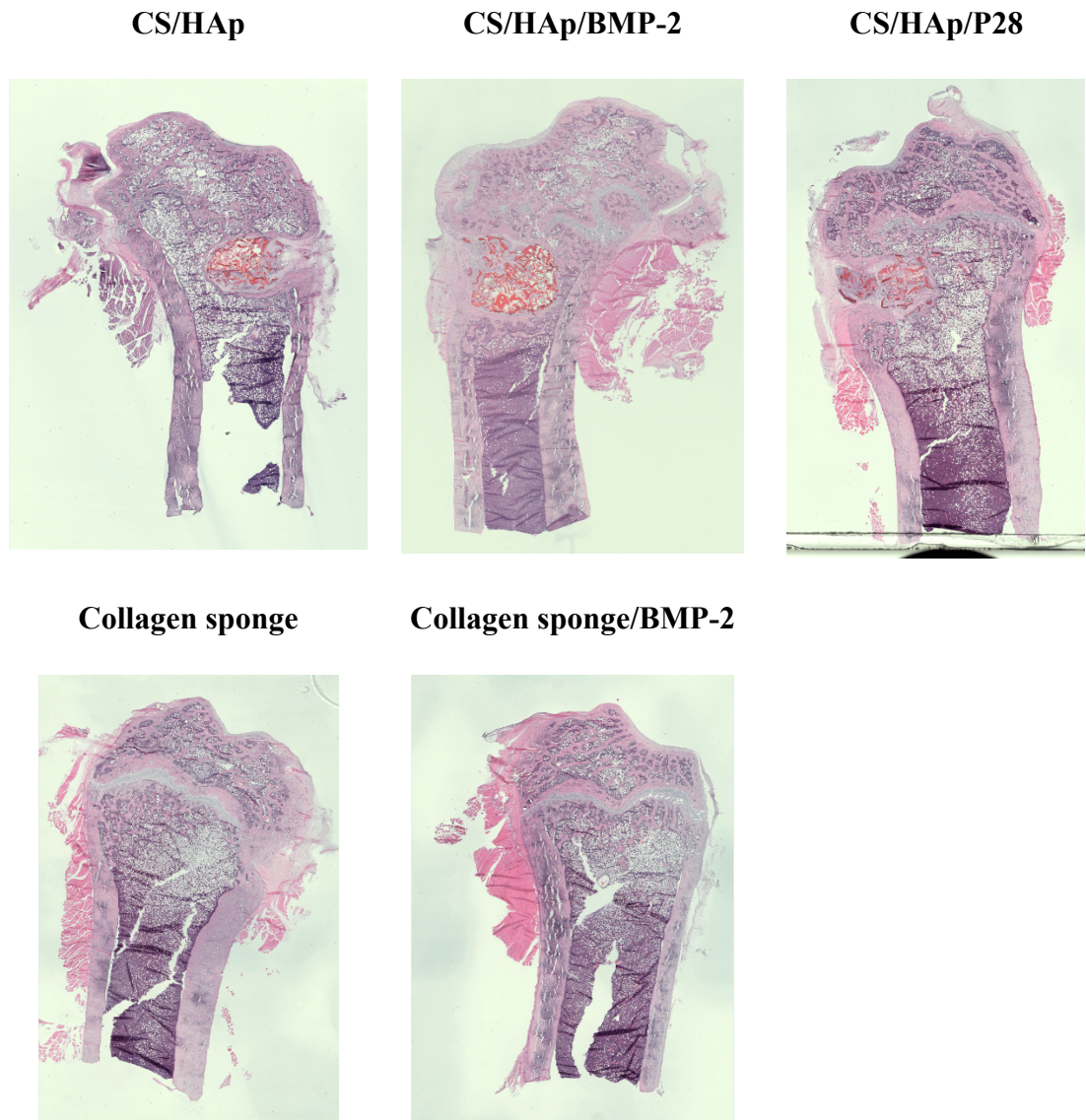


Figure 4.13 Representative images of condyles per sample group on H&E stained slides (x1 magnification).

4.3.9.1 Fibrosis

In the CS/HAp scaffold condition (Figure 4.14A), bone tissue seen at the defect margin and defect entry was still open with significant fibrosis due to periosteal activation (normal stage of the bone healing process). Eosinophilic homogenous and mineralised fragments were present in the defect as residues of the scaffold, thus showing poor bone formation (Ghiacci et al., 2016).

On the other hand, only traces of bone tissue at the defect margin and inside the defect were seen in sponge conditions (Figure 4.14B). The defect entrance was closed by lamellar cortical or spongy bone, and no fibrosis was highlighted, but physiologic bone marrow suggested that the terminal stage of the bone healing process was reached in bone

defects implanted with sponge material (Ansari, 2019). Moreover, there was no trace of collagen sponge, suggesting either substantial material leakage or strong resorption.

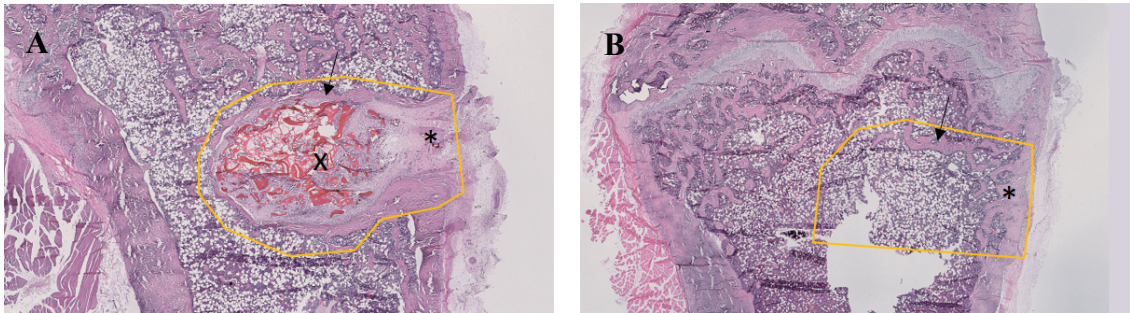


Figure 4.14 Representative images of the defect behaviour in scaffold and collagen sponge in H&E stained slides (x1.25 magnification). Annotations: A=CS/HAp; B=Collagen sponge; Yellow line=Defect boundaries; X=remaining material inside the defect; *= defect entry; arrow=bone tissue at the defect margin.

4.3.9.2 Biomaterial Residues

The non-degraded materials were observed in the condyle defects implanted with the chitosan-based scaffolds (Figure 4.15). Scaffold material corresponded to homogenous eosinophilic fragments, which may correspond to the chitosan part of the scaffold and lamellar mineralised fragments, which may correspond to the hydroxyapatite part of the scaffold. Although most material residues were seen in the defect, some leaked from the region (Figure 4.15B and C), which may explain the deformation of the defect and may block the defect closure.

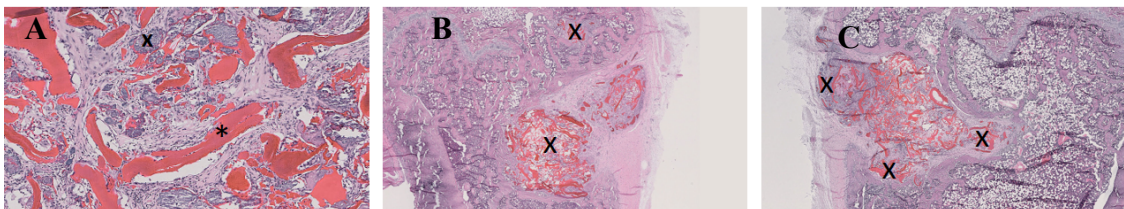


Figure 4.15 Remaining materials in scaffold-implanted condyles in the defect (A) leaked outside the defect (B&C) on H&E stained slides (x10 magnification for A and x1.25 magnification for B and C. Annotations: A= CS/HAp/BMP-2; B= CS/HAp; C= CS/HAp/BMP-2; x=mineralised acellular fragments; *=homogenous to lamellar eosinophilic fragment; X=leakage of materials.

The number of remaining materials in the defect was scored, and the mean score per material was calculated (Figure 4.16). The residual material was scored zero in the collagen sponge conditions, confirming the previous results, while the scaffold residue quantity in the defect was moderated with an almost similar quantity between CS/HAp, CS/HAp/rhBMP-2 and CS/HAp/P28, where a statistical difference was recorded between the scaffold and collagen sponge conditions ($p < 0.05$). The presence of residual scaffold suggests that this chitosan-based material was not completely degraded, while no

residuals of collagen sponge were found. This observation might be due to the fact that the collagen sponge can be resorbed in 28 days (Lyles et al., 2015).

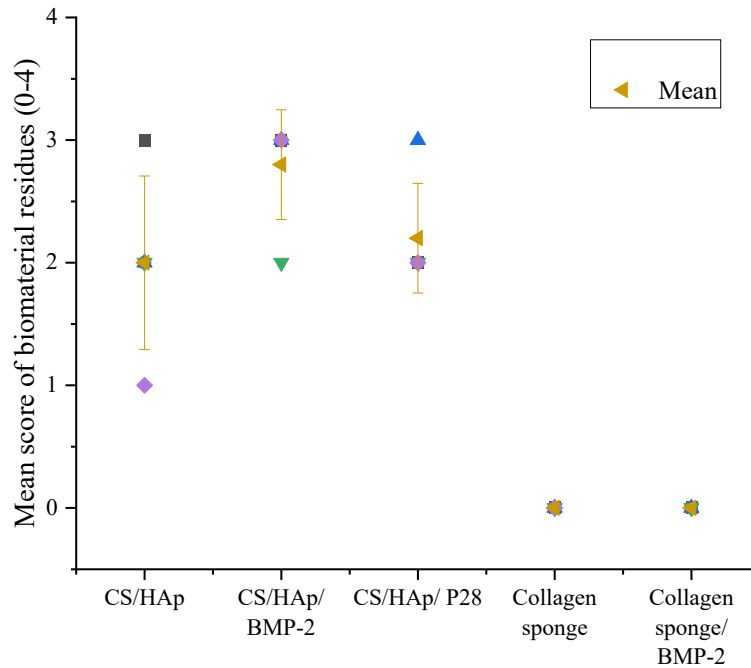


Figure 4.16 Graph of mean score of biomaterial residues per sample group.

4.3.9.3 Inflammation

Inflammation which is the initial response of bone formation and the natural healing variables and fibroplasia, which is a concentric deposition of collagen fibres (Bedeloğlu et al., 2017) were observed only in samples implanted with both nude and growth factor infused CS/HAp scaffolds (Figure 4.17). Since the inflammatory response occurs during the early stages of the bone healing process, the inflammation observed is connected to the bone healing process and the potent material degradation/resorption (Loi et al., 2016). Besides the inflammatory response, bone healing is accompanied by a considerable proliferation of fibroblasts leading to fibroplasia. These fibroblasts produce a semi-rigid soft callus, which can provide mechanical support to the defect and act as a template for the bony callus that will later supersede it (AffshanaM. & Saveethna, 2015).

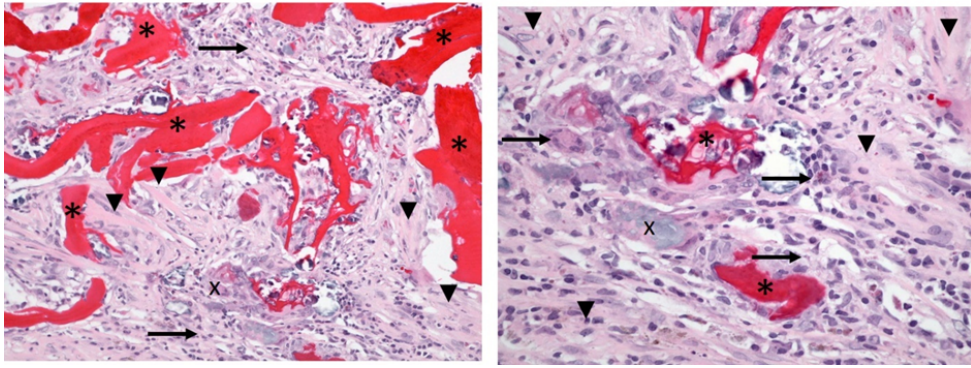


Figure 4.17 Representative images of inflammatory process and fibroplasia inside the defects in scaffold conditions in HES stained slides (x20 magnification on the left panel and x40 magnification on the right panel). Annotations: *=homogenous to lamellar eosinophilic fragments; X=mineralised acellular fragments; Arrows=immune cells; Arrow heads=deposition of collagen fibres.

There was no evidence of the inflammatory response and fibroplasia in the condyles implanted with a collagen sponge, which are usually observed in the first stages of the bone healing process (Figure 4.18a and b), suggesting that the healing process is completed. However, a slight increase in inflammation was observed in condyles implanted with chitosan scaffolds containing osteogenic factors compared to scaffold alone (an increase of 20 to 35%), suggesting an increased inflammatory response in any osteogenic factor's presence. Nevertheless, this inflammation remained mild and was not harmful. The scoring of fibroplasia was equivalent and mild in scaffold conditions confirming the early stages of the bone healing process in these conditions. In contrast, the score of inflammation and fibroplasia was at 0 in sponge conditions ($p < 0.05$), confirming the absence of an inflammatory response and that the healing process might have reached a later stage in these conditions (Ansari, 2019).

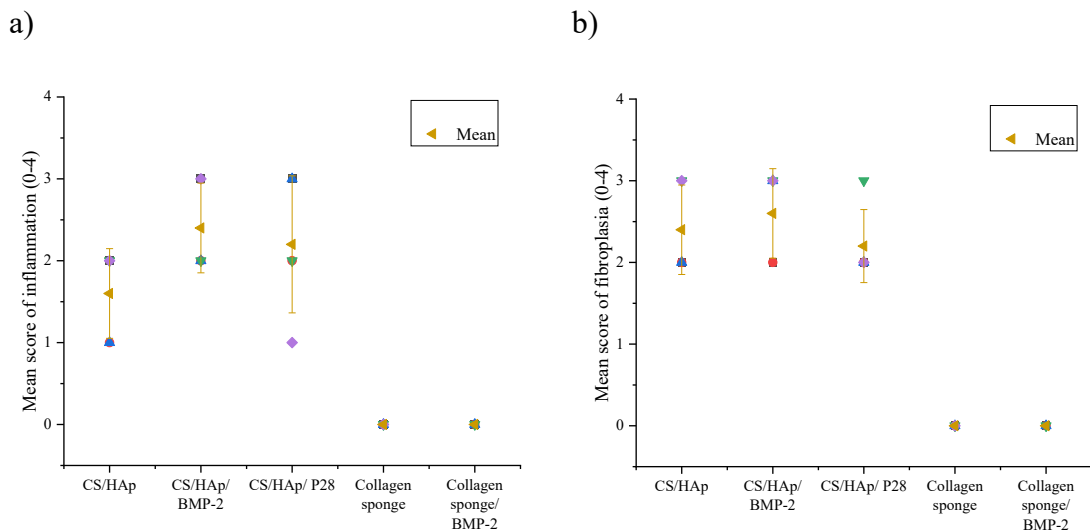


Figure 4.18 Graph of mean score of inflammation (a) and fibroplasia (b) per sample group

4.3.9.4 Necrosis

Necrosis was evaluated since it is connected to the toxicity of material that could induce necrosis in adjacent cells (Figure 4.19). Thermal osteonecrosis can also be caused by increased heat during the drilling of the defect using the metallic bur, resulting from the lack of irrigation given (X. Chen et al., 2015; Gao et al., 2018). Islets of necrosis were observed in some samples implanted with scaffold with or without the osteogenic factors (two condyles with CS/HAp scaffold, three condyles with CS/HAp/BMP-2 and two condyles with CS/HAp/P28) (Figure 4.20). However, no necrotic islets were highlighted in condyles implanted with collagen sponge, with or without rhBMP-2. Since not all of the condyles implanted with scaffolds presented necrotic foci ($p>0.05$), it is not confirmed that the scaffolds had contributed to potent toxicity. The necrosis might be due to an increased density of material locally that could block the oxygenation of the adjacent cells (Skuk et al., 2007).

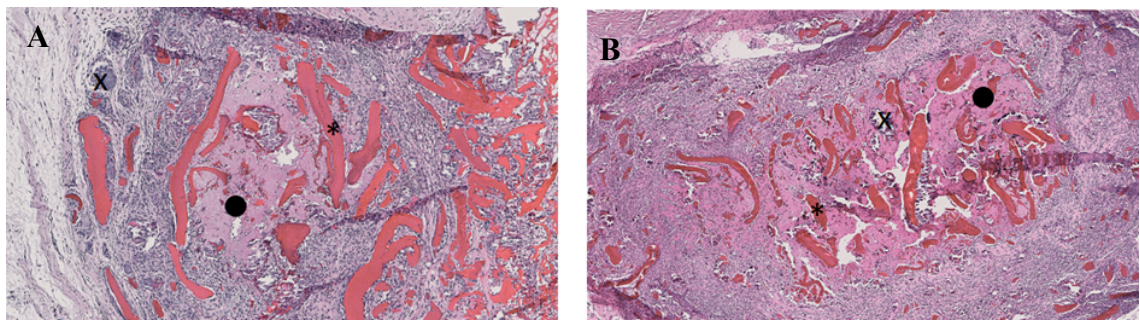


Figure 4.19 Representative images of necrotic areas in scaffold conditions on H&E stained slides (x5 magnification). Annotations: A=CS/HAp/rhBMP-2; B=CS/HAp *= homogenous to lamellar eosinophilic fragments; X= mineralised acellular fragments; •= necrotic areas

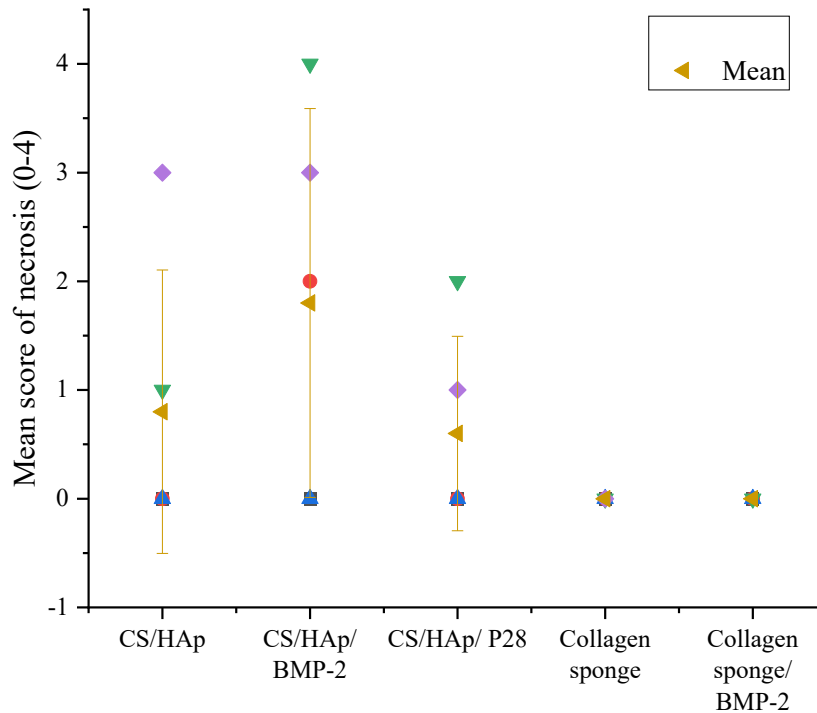


Figure 4.20 Graph of mean score of necrosis per sample group.

4.3.9.5 Bone Formation

Since fibrosis might act as a template for newly formed bone during the soft callus stage, the bone healing process continues with a primitive and relatively low mineral bone tissue known as woven bone (Maglio et al., 2020). This woven bone is deposited on fibrotic tissue, the late soft callus stage of the bone healing process. It is then replaced with poorly organised mineralised mature bone tissue, which is the early bony callus stage of bone healing and is subsequently degraded and replaced with regularly thick and well oriented mature bone in the late bony callus stage of bone healing (Ansari, 2019).

Well oriented mature bone was observed at the defect margin of chitosan scaffold conditions (Figure 4.21A), whereas foci of woven bone were seen surrounding the defect margin and inside the defect close to material fragments (Figure 4.21B). The presence of immature bone was associated with osteoblast lining in contact with woven bone leading to high osteoblastic activity. This observation suggests that the bone healing process reached late soft callus and early bony callus stages. This woven bone could provide extra mechanical support in this first stage of the mineralisation process with the aid of the scaffold (Loi et al., 2016).

Interestingly, in the presence of P28 in the chitosan composite scaffold, non-anastomosed mature bone lamellae were observed in three out of five samples (Figure 4.21C), suggesting that the P28 peptide had indeed aided in the upregulation of the osteoblast differentiation and led to the bone regeneration reaching the later stage of hard callus remodelled bone formation (Cui et al., 2016; J. Li & Stocum, 2014). In collagen sponge conditions (Figure 4.21D), mature lamellar bone was seen at the entrance and appeared as traces at the defect margin and inside the defect, indicating a successful osteogenic differentiation (Amini et al., 2012). Moreover, osteoblastic activity was almost absent, which might suggest that the hard callus stage of bone healing has been reached with the total degraded collagen sponge (Cui et al., 2016).

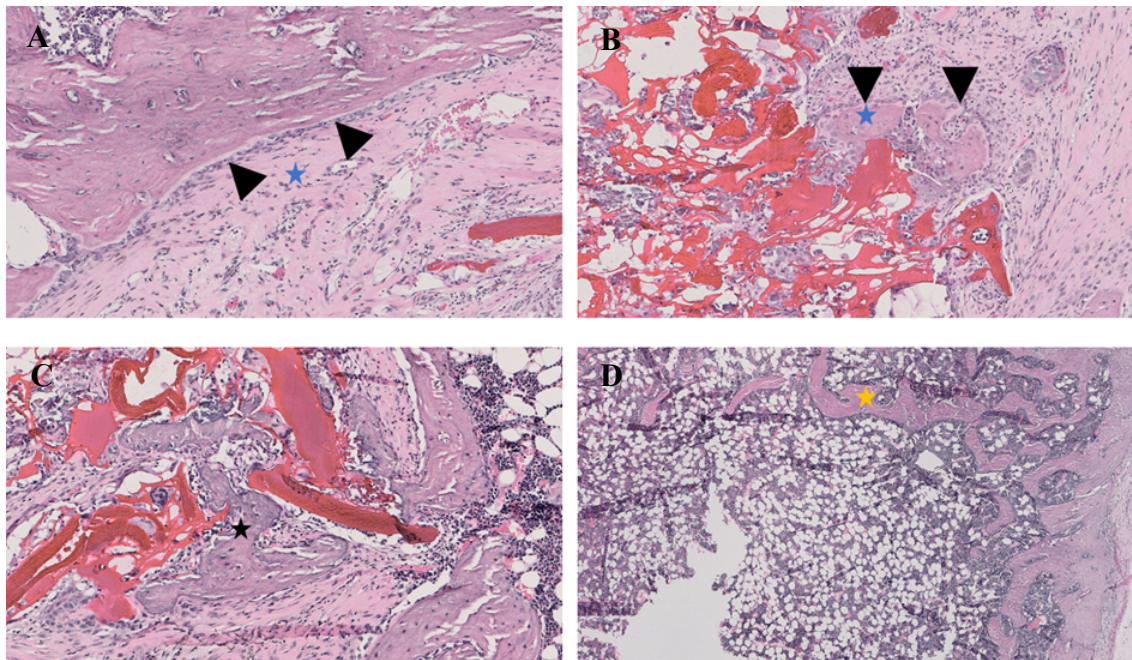


Figure 4.21 Representative images of newly formed bone at the defect margin (A&D) and inside the defect (B&C) on HES stained slides (x10 magnification for A-C, x2.5 magnification for D). Annotations: A&B= CS/HAp; C= CS/HAp/P28; D= Collagen sponge; Blue stars= woven bone; black star= small lamellae, disseminated not anastomosed; yellow star= mature lamellar bone; arrow heads= osteoblast lining.

The nature and quantity of new bone tissue were scored at the defect area. The scoring was denoted from 0 (woven bone) to 4 (mature bone tissue) for qualitative assessment and from 0 (absent) to 4 (large amount) for the quantity of new bone assessment. Generally, it was observed that the CS/HAp/P28 and CS/HAp/BMP-2 implanted defects achieved a significant difference in terms of qualitative bone formation ($p < 0.05$) (mean scores of 1.60 and 0.80, respectively) (Figure 4.22a). However, no significant difference was noted quantitatively in all implanted materials, although the nude CS/HAp scored the lowest mean compared to the CS/HAp/BMP-2 and CS/HAp/P28 (mean scores of 1.60,

2.40 and 2.20, respectively) (Figure 4.22b). Moreover, focal newly formed bone was also found inside the defect with the presence of the osteogenic factors. This result might support that this osteogenic factor can speed up bone healing than a scaffold without osteogenic factors (Huber et al., 2017). The BV/TV measurement on CT-scan images (decreased bone volume in sponge conditions compared to scaffold conditions) was because this scoring of bone quantity had taken both the mineralised and non-mineralised new bone tissues into account, while the CT-scan images only highlighted the mineralised bone.

Nevertheless, the scoring of bone quality was the highest in sponge conditions (Figure 4.22a) associated with the absence of osteoblastic activity (Figure 4.22c), thus supporting previous observations, where the healing process might have ended. Furthermore, most samples with low bone formation scores (bone quality and osteoblastic activity) have a high necrosis score, suggesting that necrosis may block bone formation. Therefore, these results show that in the presence of a scaffold, early stages in the bone healing process were reached with a slight increase in bone formation with the osteogenic factors, whereas in collagen sponge conditions, the terminal stage of the bone healing process was reached.

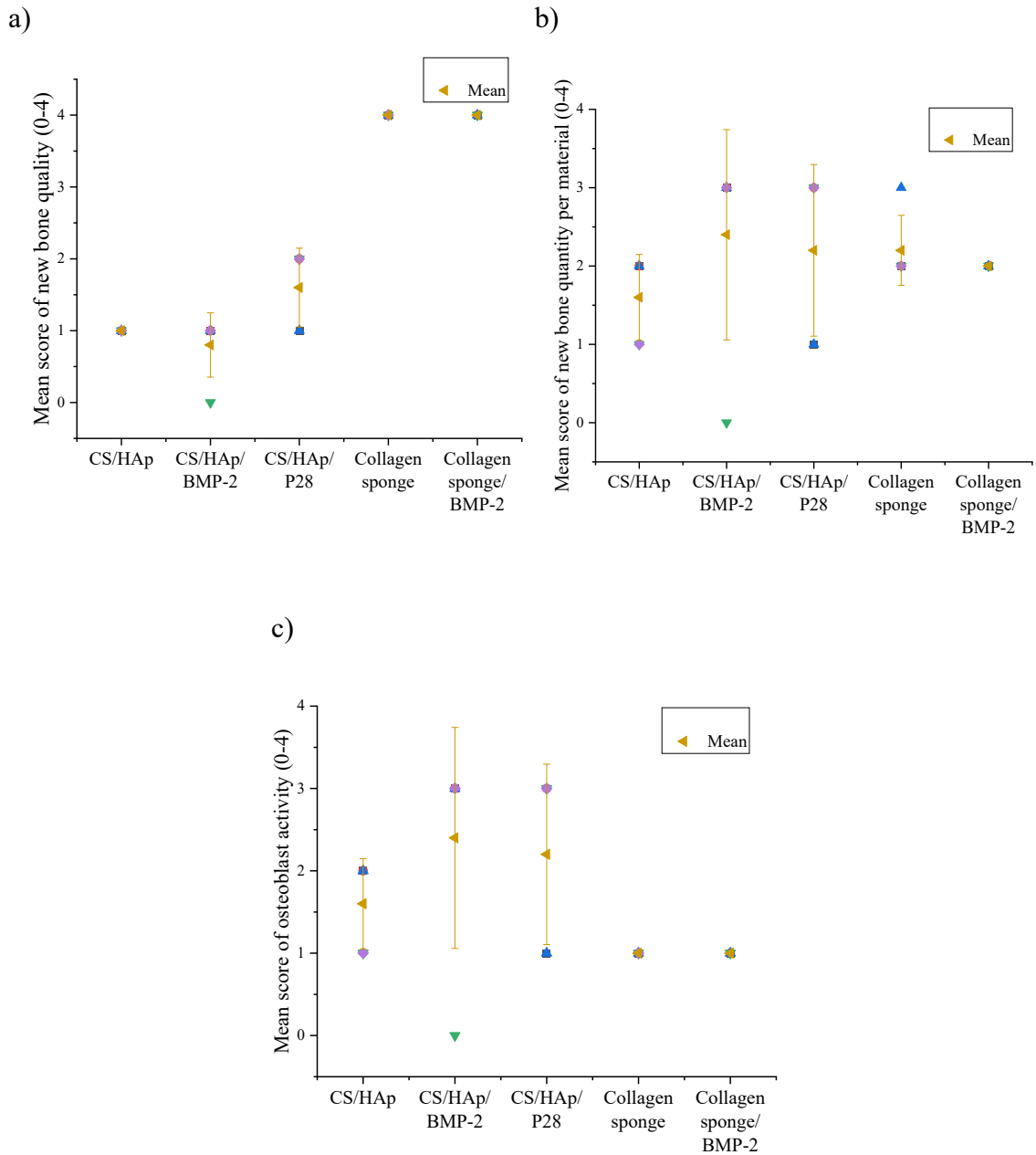


Figure 4.22 Graph of mean score of new trabecular bone quality (a), trabecular bone quantity (b) and osteoblast activity (c) per sample group.

4.3.10 Mineralised and Osteoid Tissue Evaluation through Von Kossa Staining

Mineralised and osteoid tissues were evaluated on Von Kossa stained slides (Figure 4.23) as it enabled a distinction between osteoid and mature mineralised bone matrix (Gruber & In, 2003). This staining confirmed ECM mineralisation that is detected through the presence of phosphate and seen as black mineralised thin layers (de Azevedo e Sousa Munhoz et al., 2020). Generally, homogenous mineralised tissue deposition was noted at the defect margin in scaffold conditions, and focal mineralised fragments were seen locally in the defect. These mineralised tissues were differentiated from focal mineralised

fragments in the defect, indicating newly formed bone and hydroxyapatite residues, respectively (Sulaiman et al., 2013).

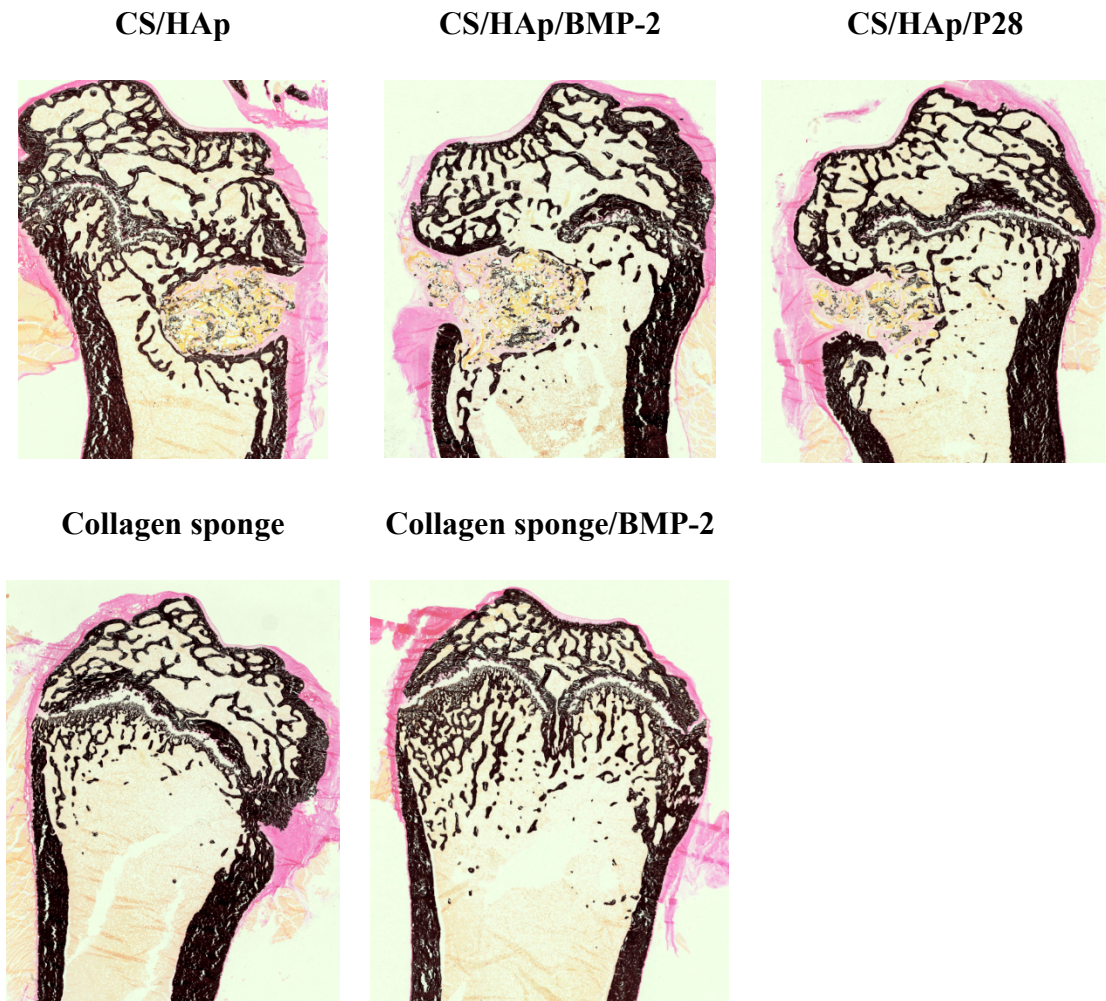


Figure 4.23 Overview of the implanted defects stained using Von Kossa staining (x1 magnification).

However, the intense calcium deposits observed in the defect region could also be explained by the implanted materials having the ability to promote bone mineralisation by mimicking the natural mineralisation profile of native bone, thus providing an appropriate microenvironment for bone cell division and differentiation as well as the structural support for vascular growth (de Azevedo e Sousa Munhoz et al., 2020). This observation is due to the osteoid presence (Figure 4.24), which will produce mineralised bone at the end of the bone formation process (McGregor et al., 2020). The defects implanted with chitosan based-scaffolds showed osteoid tissue along the mineralised bone at the defect margin, corresponding to the non-mineralised, organic portion of the bone matrix that forms by osteoblast before the maturation of bone tissue (Czekańska, 2014; McGregor et al., 2020).

In addition, focal homogenous mineralised tissue was also observed inside the defect. The presence of osteoid tissue matched the osteoblast lining, indicating that osteogenic differentiation had started. This result confirmed the high bone formation process along the defect margin and the newly formed bone inside the defect filled with the chitosan-based scaffolds (Roseti et al., 2017). In contrast, defects implanted with a collagen sponge showed homogenous mineralised tissue at the defect entrance and some traces of mineralised tissue at the defect margin and inside the defect. Only a few osteoid tissues were observed in sponge conditions and were mainly seen in bone tissue at the defect entrance, not inside the defect induced, confirming the low bone formation activity.

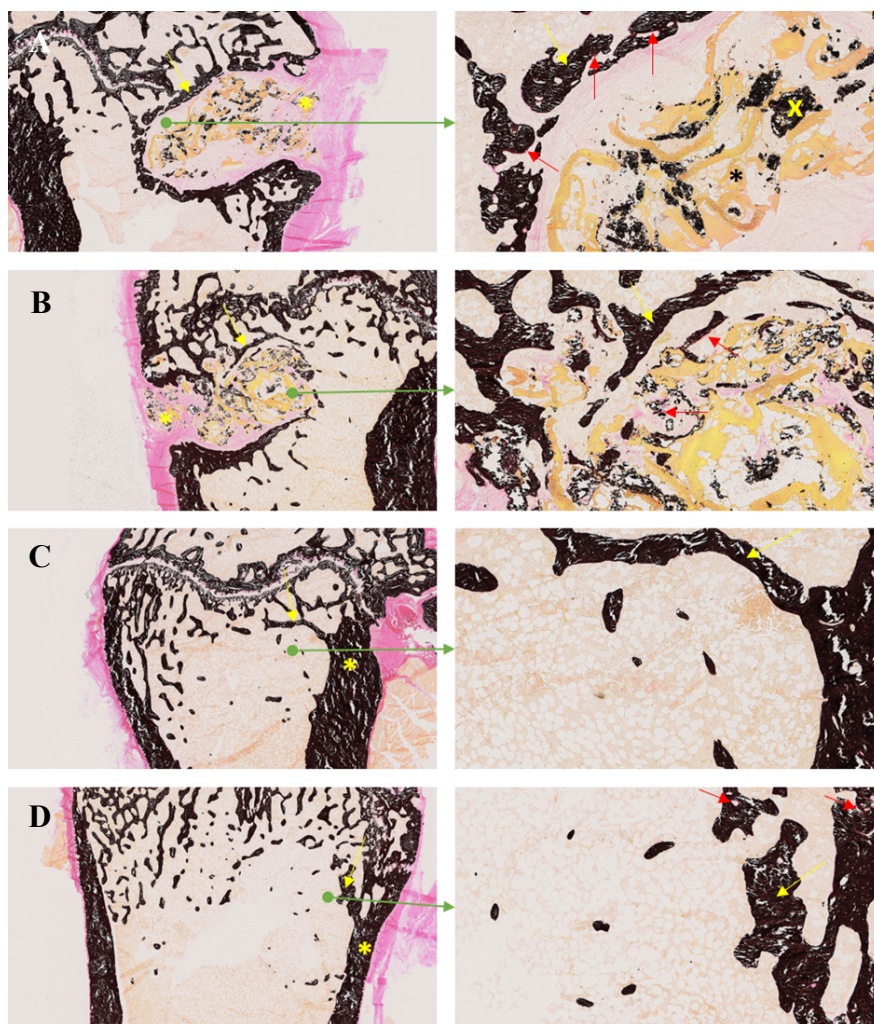


Figure 4.24 The representative images of mineralised tissue in the defect and margin in scaffold conditions (A&B) or sponge conditions (C&D). Von Kossa stained slides (x1.25 magnification on left panels, x5 magnification on right panels). Annotations: A= CS/HAp; B= CS/HAp/P28; C= Collagen sponge; D= Collagen sponge/rhBMP-2. Yellow arrows = bone tissue at defect margin; Red arrows = osteoid tissue; Yellow star = defect entrance; Black star = homogenous material fragments; Yellow cross = mineralised fragments.

The mineralised volume in the defect was observed to be equivalent in all sample groups ($p > 0.05$) (Figure 4.25a), which might be explained by the compensation of decreased

bone tissue in sponge conditions compared to scaffold conditions with bone formation at the defect entrance. Nonetheless, the values achieved (20-30%) are indeed around the same range as that was reported in a previous study, showing the similar mineralised bone volume in empty defects, demineralised bone (DBM) and DBM with BMP-2 treatments (Huber et al., 2017). However, DBM/BMP-2 showed a higher amount of bone tissue compared to the rest of the samples, thus validating the osteogenicity of the growth factor.

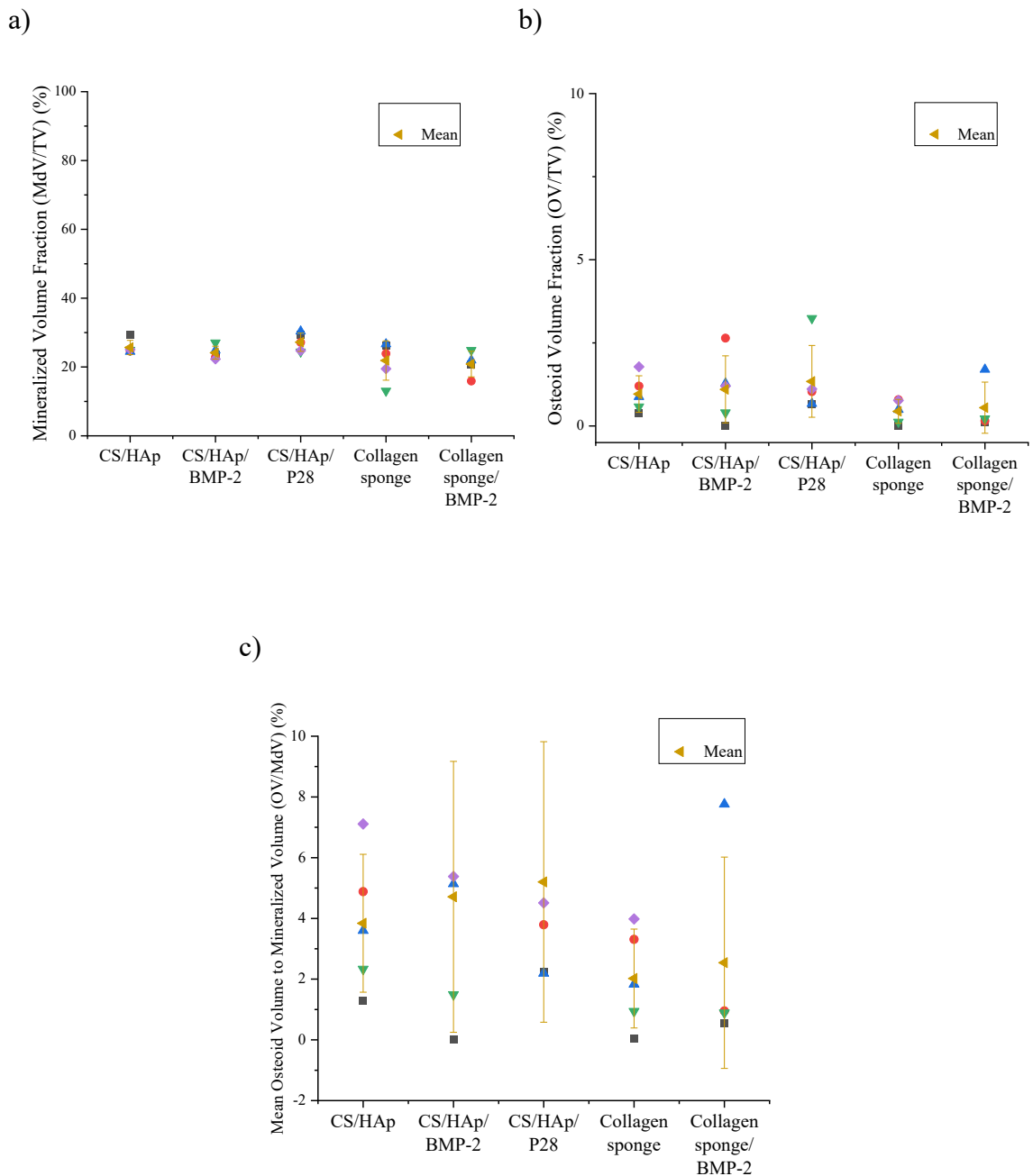


Figure 4.25 Graph of mean mineralised volume fraction (a), osteoid volume fraction (b) and mean osteoid volume to mineralised volume (c) per sample group.

Although CS/HAp/BMP-2 and CS/HAp/P28 recorded the highest osteoid volume ratio to the bone volume (OV/TV), thus proposing the increase in bone formation activity in scaffold conditions, the values in the defect were low in all sample groups ($p>0.05$) (Figure 4.25b). This result might suggest that bone formation might not be pathologic or in response to growth factors as the stimuli of bone regeneration (De Vlam et al., 2006).

Comparing the mean osteoid volume to the mineralised volume (OV/MdV) (Figure 4.25c), the defects implanted with chitosan-based scaffolds recorded a higher mean OV/MdV compared to the collagen sponge conditions, although no significant difference was recorded ($p>0.05$). Here, CS/HAp/P28 showed the highest mean value, with the lowest value observed in nude collagen sponge conditions. This result might support the osteoconductivity of the chitosan-based scaffold production of mineralisation in the newly synthesized ECM (osteoid) by osteoblast (Jahan et al., 2020; H. T. Liao et al., 2018)

4.3.11 Evaluation of the Presence of Osteoclast through Tartrate-Resistant Acid Phosphatase Staining

The identification and study of osteoclasts and osteoblasts are routinely carried out through enzyme histochemistry. The presence of osteoclasts, seen as a multinucleated cell (containing more than three nuclei) under the microscope (X. Chen et al., 2015), was evaluated using a lysosomal enzyme, tartrate-resistant acid phosphatase (TRAP) stained slides (Figure 4.26). TRAP is abundantly expressed in osteoclasts, so its localisation provides a sensitive method of osteoclast identification during osteoclastic resorption of new bone formed and replaced by mature bone, thus evaluating potent material resorption (Gruber & In, 2003; Harada et al., 2013).

Only a few osteoclasts were observed in all implanted materials leading to low osteoclast activity. In scaffold conditions (Figure 4.27 A-D), osteoclasts were present at the edge of newly-formed bone tissue inside the defect and the margin. Some osteoclasts were also observed at the edge of residual mineralised material. This result indicates that the implanted scaffolds somehow have the ability to recruit the TRAP-positive cells, which might be aided by the rough surface of the scaffolds that support cell attachment and proliferation (e Silva et al., 2021). Therefore, the newly formed bone that was slightly resorbed could suggest that the bony callus stage of the bone healing process was just initiated (X. Chen et al., 2015).

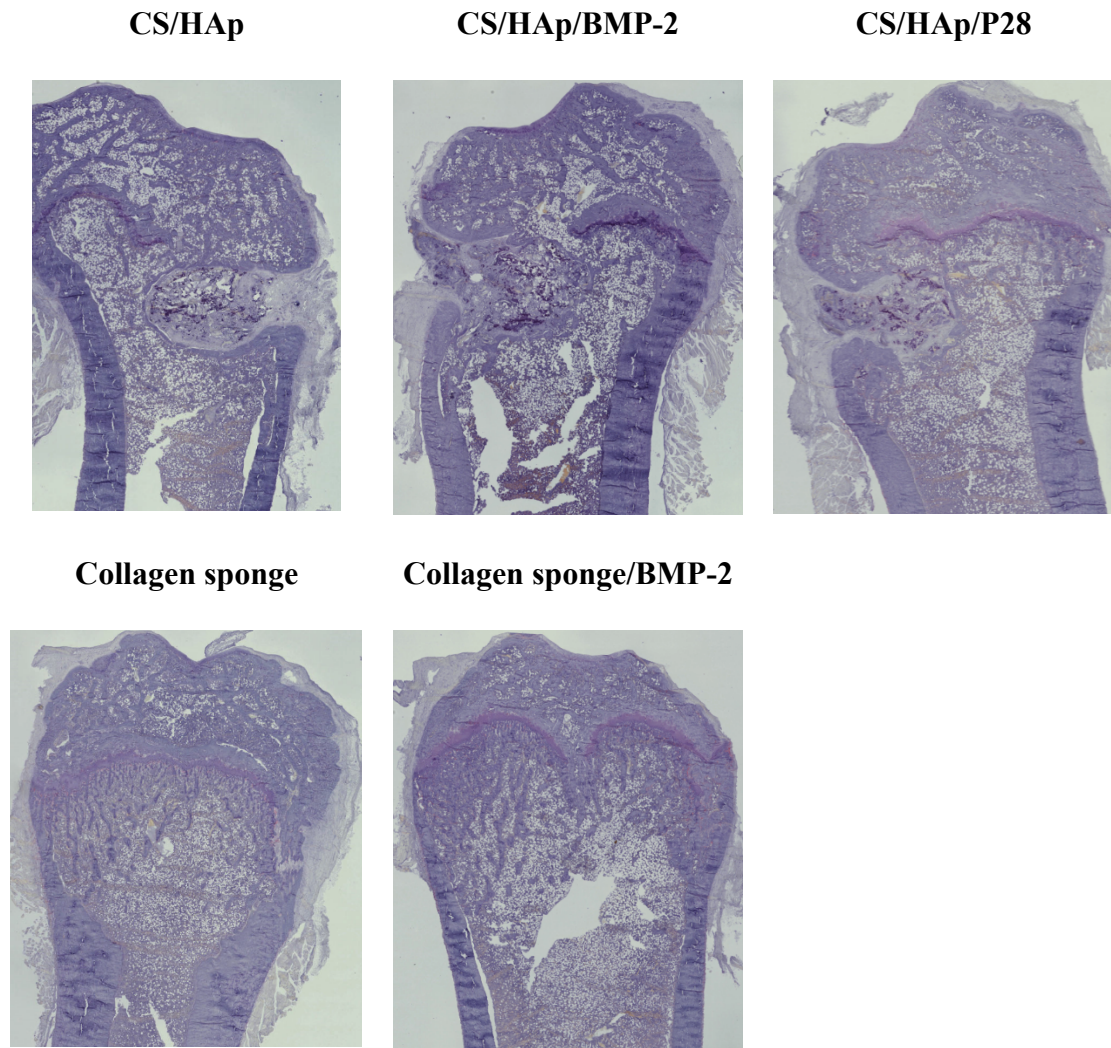


Figure 4.26 Overview of the implanted defects stained using TRAP staining (x1 magnification).

Conversely, lesser osteoclasts were seen in the defects implanted with a collagen sponge (Figure 4.27 E-F) compared to the scaffold conditions. Rare osteoclasts were observed mainly at the bone surface of the defect entrance. This result might suggest that the bone resorption and remodelling process have slowed down in the defects with the collagen sponge and reached the final stage of the bone healing process (Lidgren et al., 2015). This hypothesis is also in line with a study that achieved increasing TRAP-positive osteoclast in the first four weeks, and the osteoclast number was then decreased in week eight, indicating the inhibition of the bone resorption process (X. Chen et al., 2015).

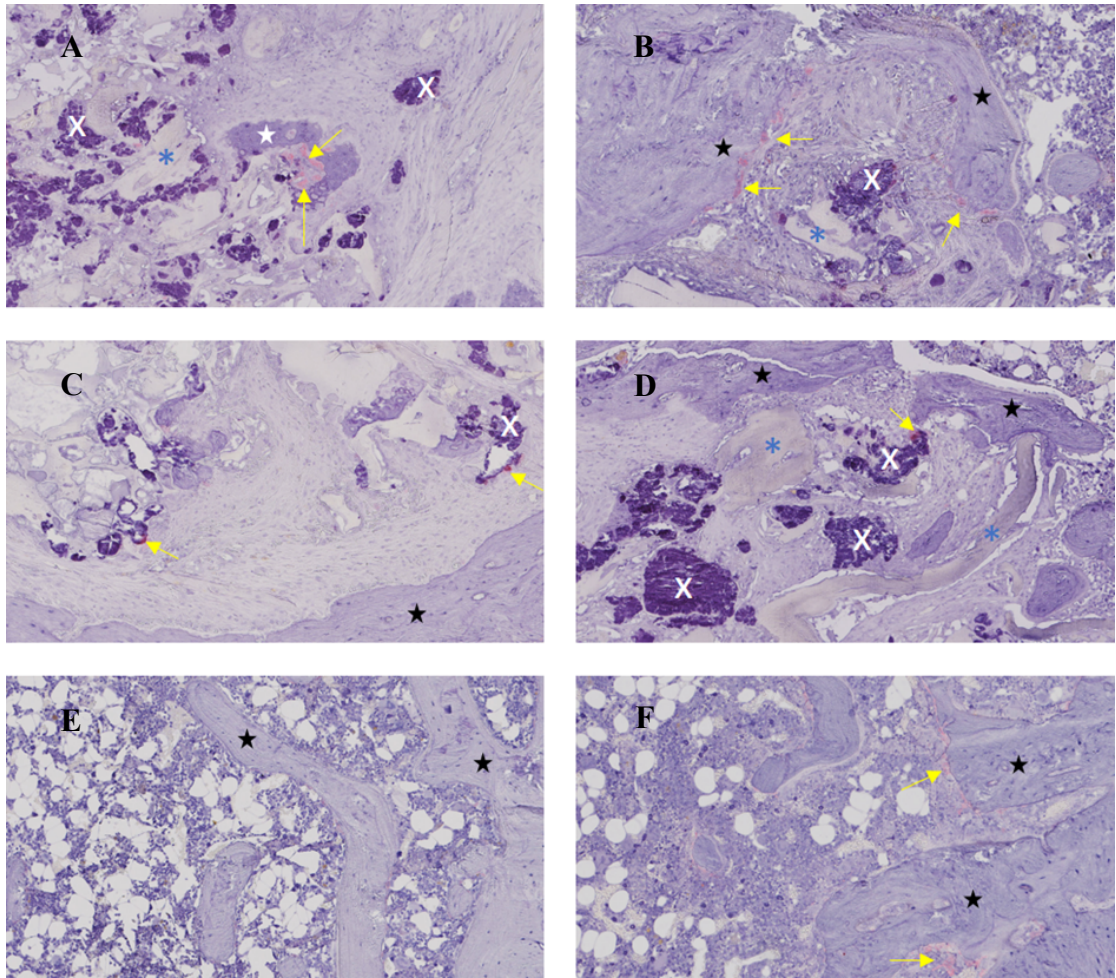


Figure 4.27 Representative images of TRAP-positive osteoclasts at defect level in scaffold conditions (A to D) and sponge conditions (E & F) on TRAP stained slides (x10 magnification). Annotations: A= CS/HAp; B&C= CS/HAp/P28; D= CS/HAp/rhBMP-2; E= Collagen sponge/rhBMP-2; F= Collagen sponge; Yellow arrow = TRAP positive osteoclasts; White cross = mineralised fragments; Blue stars = homogenous material fragments; White star = woven bone; Black stars = lamellar bone.

The mean osteoclast surface to the bone surface (OcS/BS) (Figure 4.28) explains the quantitative measurements of the TRAP-positive osteoclasts that play the role of bone resorption in the remodelling process. A lower mean of OcS/BS was detected in the defects implanted with collagen sponges compared to those implanted with chitosan-based scaffolds ($p < 0.05$). In addition, a similar OcS/BS response was observed in defects implanted with CS/HAp/BMP-2 and CS/HAp/P28, giving comparable osteoclast activation between these scaffolds (James et al., 2016), as well as the collagen sponge/BMP-2 that gave a slightly higher value of OcS/BS compared to the nude collagen sponge.

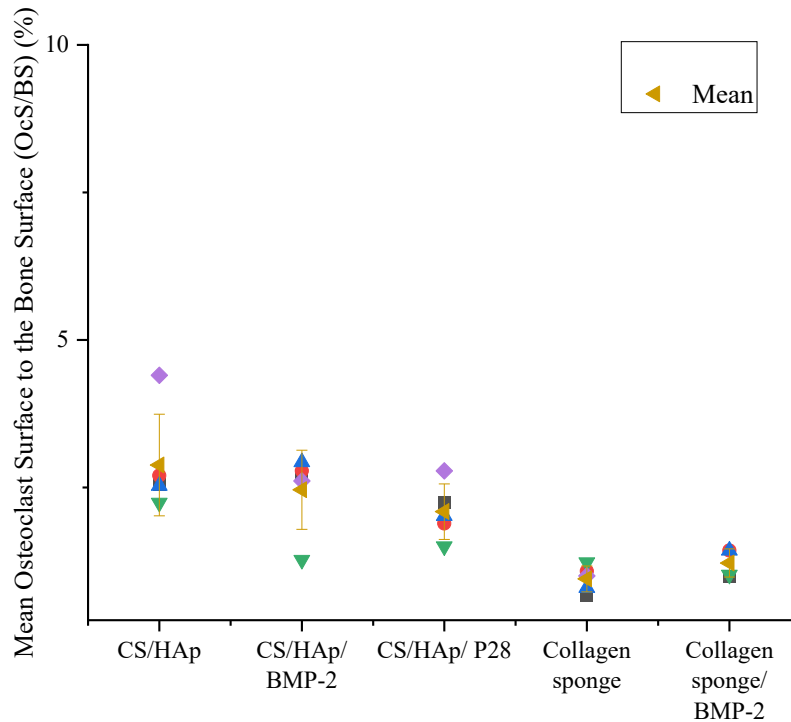


Figure 4.28 Graph of mean osteoclast surface to the bone surface per material.

4.3.12 Dynamic Bone Formation Analysis through Fluorescent Labelling

Fluorescent labelling was evaluated as the dynamic of bone formation that corresponds to mineralisation speed, time, location, as well as the direction of the mineralisation (Shanker, 2019; van Gaalen et al., 2010). The calcein green (CG) and xylenol orange (XO) fluorochromes injected *in vivo* ten and four days before sacrifice chelated the mineralised front during the bone mineralisation process by osteoblasts, which enables the evaluation of the dynamic of bone formation by measurements of fluorochromes labelling (Spicer et al., 2012). It was also documented that fluorochrome labelling was used to evaluate bone mineralisation rate, remodelling, and the signs of toxicity of the implants on bone *in vivo* (Alves et al., 2020).

Double labelling with CG and XO at the bone surface suggests that two mineralisation processes occurred on the day of the two injections. One labelling present suggests that only one mineralisation process occurred within six days. Two labels' appearance would indicate bony deposition and thus suggest that one bone remodelling cycle is completed (Shanker, 2019). Moreover, single labelling with only XO (the second injected fluorochrome) suggests that a bone remodelling cycle is ongoing, while in contrast, single

labelling with only CG (first injected fluorochrome) suggests that a bone remodelling is initiated but is not ended, leading to a longer bone remodelling cycle.

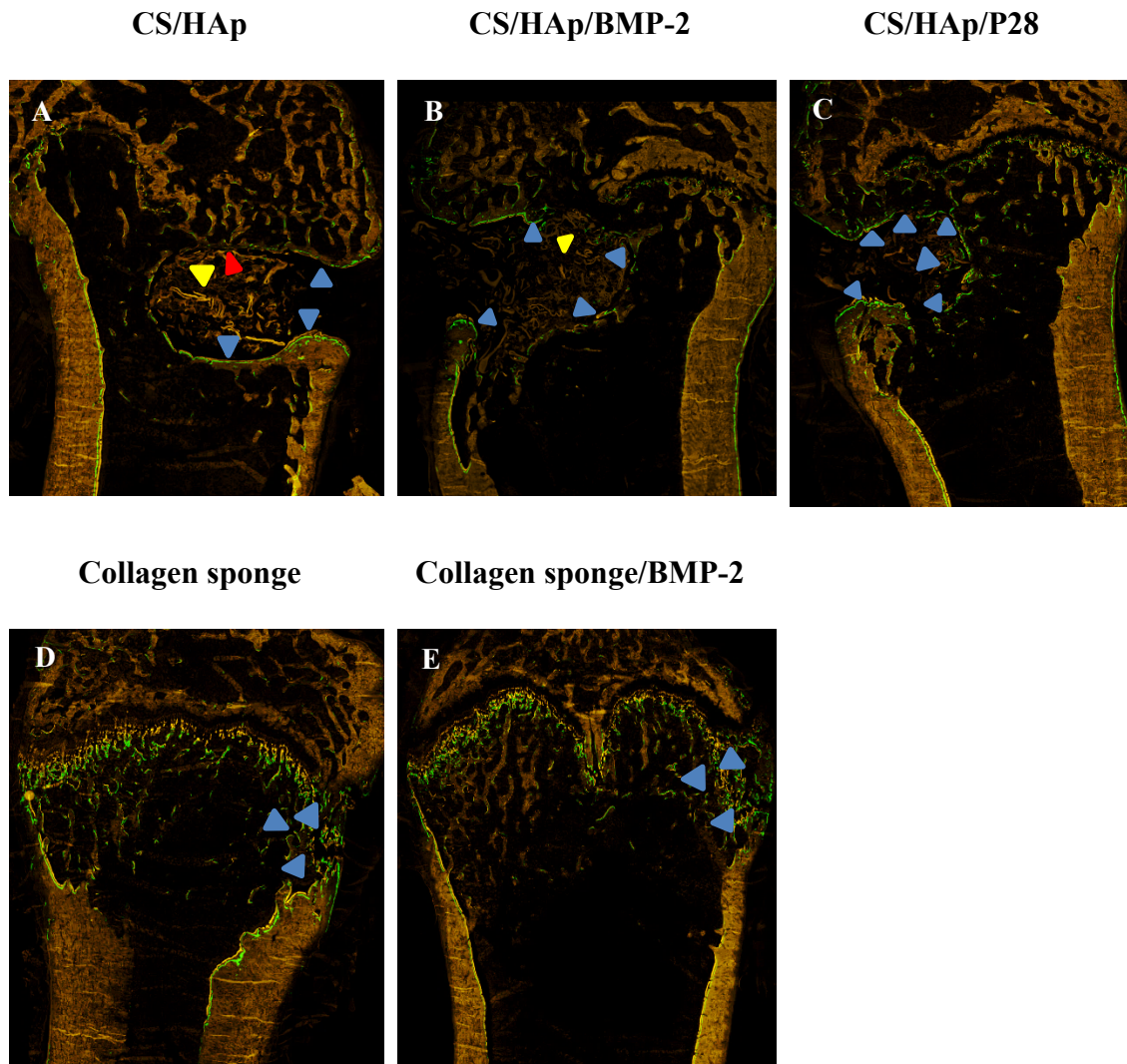


Figure 4.29 Representative images of the fluorochromes-labelled condyles viewed under a fluorescent microscope (x1.25 magnification). Annotations: Blue arrowheads = double labelling; Yellow arrowheads = single calcein green labelling, Red arrowheads = single xylene orange labelling.

The double labelling was mainly observed along the defect margin in chitosan scaffold-implanted samples (Figure 4.29), suggesting that the physiological bone remodelling cycle occurred at the defect margin (Erben, 2003). Rare double or single labelling was seen at the surface of mineralised tissue inside the defect leading to the mineralisation process, which occurred at the new-bone tissue or the residual material surface at that specified time point (Goldschlager et al., 2010; Shim, 2016). Therefore, the mineralisation was more or less faster inside the defect when present. Since the labelling (double and single) matched with osteoblast lining and osteoid tissue, the high bone formation activity in the scaffold conditions is validated. In collagen sponge conditions,

a few fluorochrome labelling were seen at the bone surface and corresponded only to double labelling suggesting physiological bone remodelling at the bone surface. Double labelling was mainly seen at the bone surface at the defect entrance and was co-localised with osteoid tissue leading to the residual bone formation process at the defect entrance (Xiao et al., 2011).

Fluorochrome labelling was utilised to evaluate time-dependent bone formation *in vivo* due to its calcium chelating properties that bind to extravascular-deposited calcium in tissues (Shanker, 2019). Therefore, the labels were assessed in terms of the mineral appositional rate (MAR), mineralised surface to bone surface (MS/BS), as well as bone formation rate to bone surface (BFR/BS), which is the enhanced qualitative analysis of bone formation *in vivo*.

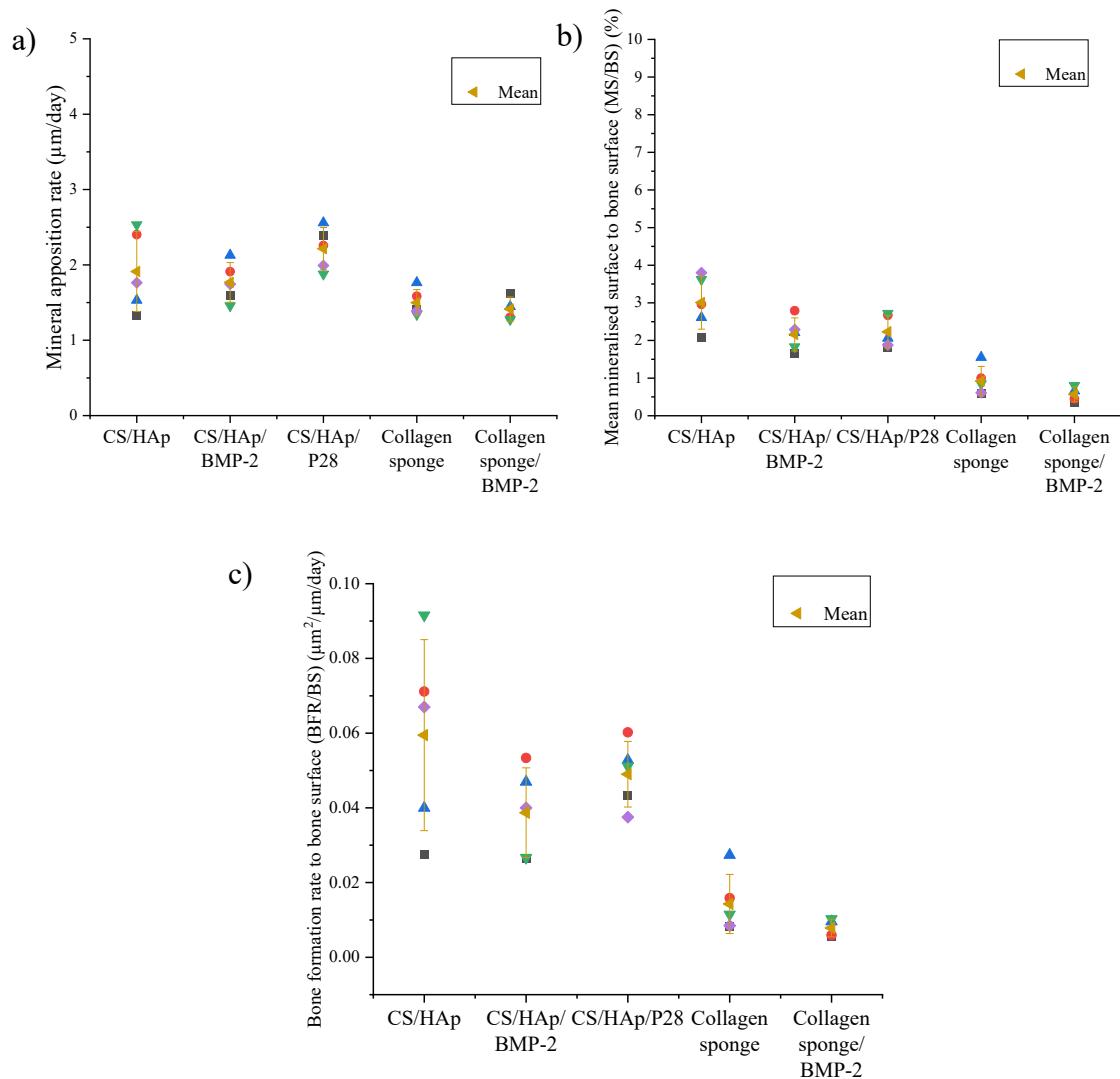


Figure 4.30 Graph of mean mineral apposition rate (a), mean mineralised surface to bone surface (b) and mean bone formation rate to bone surface (c) per sample group.

The final measurement was the calculation of BFR, which is the amount of newly mineralised bone formed in unit time per unit of the bone surface, by multiplying MAR and MS/BS. An increase in BFR was seen in scaffold implants compared to collagen sponges ($p < 0.05$) (Figure 4.30). This observation is in contrast with a report investigating BFR values in osteoporotic rats, where significantly decreased values of BFR were obtained (Bonucci & Ballanti, 2014). The same reduction of BFR values was also recorded in other diseased rats (colitis) (Porter et al., 2017), thus validating the high BFR values achieved in this work that utilised healthy rats.

In addition, no significant increase in dynamic of bone formation was highlighted in the presence of osteogenic factors compared to scaffold alone, which suggested that the increase of bone formation seen previously by histopathological analyses was faint and not strong enough to be seen by histomorphometric analyses. Eventually, these results suggest an increase of bone mineralisation in chitosan scaffold conditions compared to collagen sponge conditions due to an increase of mineralised surface but not mineralisation speed.

4.3.13 Overall Analysis

The overview of the Hematoxylin-Eosin (HE), Von Kossa (VK), Tartrate-Resistant Acid Phosphatase (TRAP), as well as calcein and xylenol fluorochrome labelling, is presented (Figure 4.31).

HE staining was carried out for a deep qualitative analysis of the tissues. In the defect implanted with nude CS/HAp, it can be observed that there was inflammation around the scaffold with some multinucleated giant cells, compared to the defects implanted with CS/HAp/BMP-2 and CS/HAp/P28, where there was more resorption observed, and the scaffold had broken down, despite the incomplete degradation. While this inflammation remained low, it was suggested that the CS/HAp scaffold was well tolerated and non-toxic. This result matched the absence of clinical signs during the *in vivo* phase. In addition, non-anastomosed mature bone lamellae were observed in CS/HAp/P28 scaffolds, suggesting that the P28 peptide can upregulate the osteoblast differentiation and lead to the bone regeneration towards the later stage of hard callus remodelled bone formation (J. Li & Stocum, 2014). This result was in line with previous work investigating P28 peptides in Si/HAp scaffold, where this peptide provided a significant new bone formation and increased osteoblastic activity compared with nude scaffolds and empty

defects (Cui et al., 2016). Therefore, it can be postulated that there was a sign of bone formation present that could lead to healing in the long run.

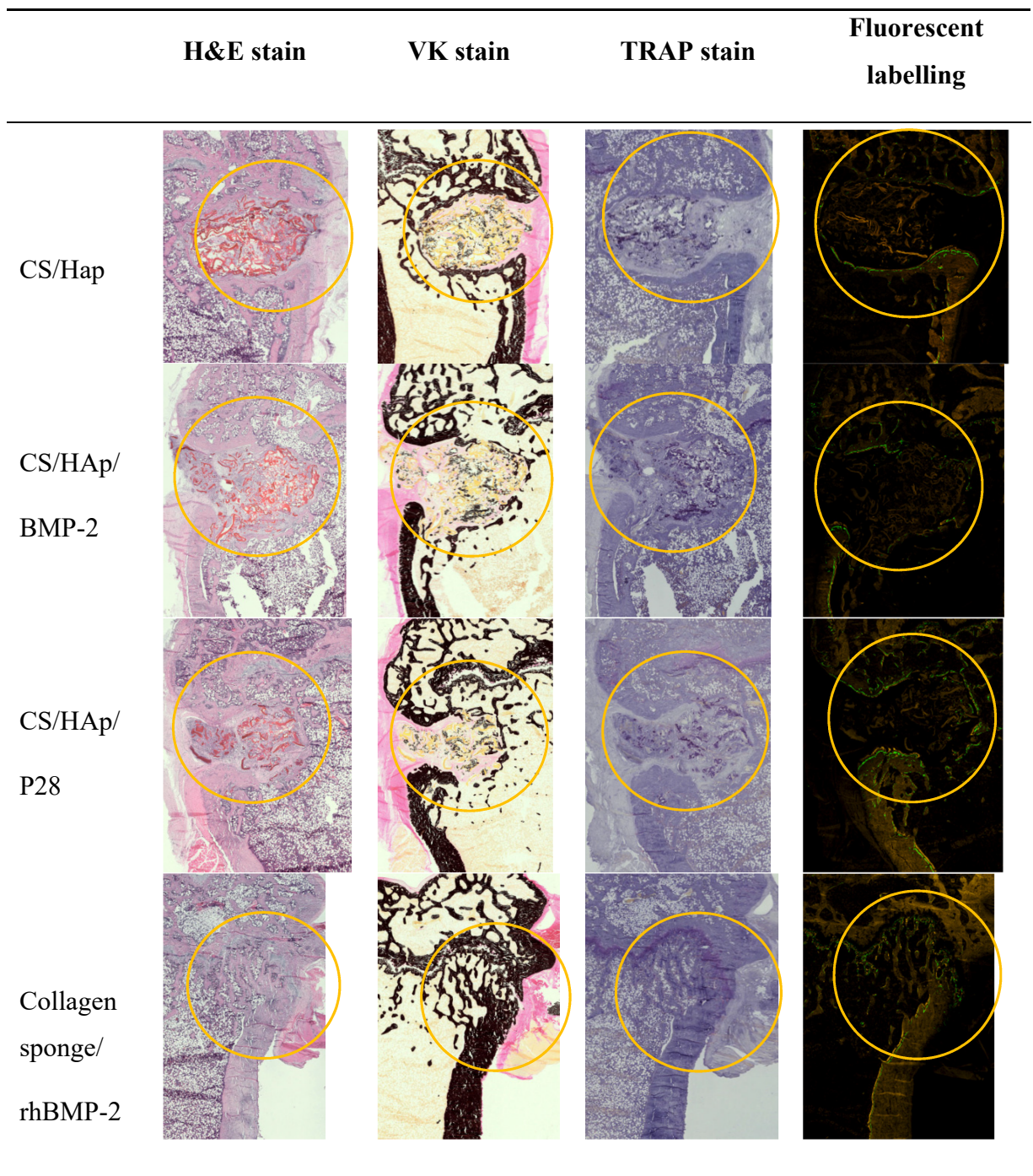


Figure 4.31 An overview of the HE, VK and TRAP staining as well as the calcein and xyleneol fluorescent labelling on the femoral condyles after eight weeks of healing. Observing the defect closure, the CS/HAp/P28 scaffolds presented better bone healing compared to CS/HAp and CS/HAp/rhBMP-2. (Annotation: Yellow circle= Implantation site)

Von Kossa staining was used to stain calcium black, thereby distinguishing between osteoid and mature mineralised bone matrix (de Azevedo e Sousa Munhoz et al., 2020; Gruber & In, 2003). Sections from the nude CS/HAp scaffold showed signs of

remodelling that occurred around the defect margin. Defects implanted with CS/HAp/P28 and CS/HAp/BMP-2 treatments resulted in bone islets been formed around the scaffold, and some calcium could be observed. However, this calcium could also have originated from the scaffold composite itself since hydroxyapatite is composed of calcium (Sulaiman et al., 2013). Subsequently, the defects implanted with both collagen sponges with and without BMP-2 seemed to be healed since the cortex was completely intact and the trabecular bone had remodelled that it was not distinguishable from the other side.

The presence of osteoclasts, seen as multinucleated cells under the microscope (X. Chen et al., 2015), was evaluated in TRAP-stained slides. Only a few osteoclasts were observed in all implanted materials. In scaffold conditions, osteoclasts were present at the edge of newly formed bone tissue inside the defect and the margin. Some osteoclasts were also observed at the edge of residual mineralised material. This result indicates that the implanted scaffolds can recruit TRAP-positive cells, which might be aided by the rough surface of the scaffolds that support cell attachment and proliferation (e Silva et al., 2021). Nevertheless, the observed osteoclastic activity could suggest that the bony callus stage of the bone healing process was just initiated (X. Chen et al., 2015). Conversely, fewer osteoclasts were seen in the defects implanted with a collagen sponge compared to the scaffold conditions, which was in line with observations from Von Kossa staining that indicated that healing and remodelling was near completion.

Finally, the fluorochrome labelling that was seen under fluorescent microscopy theoretically indicated the uptake of the labelling agent, thus showing that the bone healing process was ongoing during the injection days. Therefore, bone formation is still in progress, or remodelling could also occur. Since the labelling (double and single) matched with osteoblast lining and osteoid tissue, the high bone formation activity in the scaffold conditions is validated (Shim, 2016).

4.4 Summary

A bone-tissue-mimicking scaffold with osteoinductive growth factors is crucial to treat bone defects. This study presented that the CS/HAp scaffolds successfully crosslinked with either BMP-2 or its P28 via a UV crosslinking process. The release rate validated the ability of the scaffolds to degrade while releasing the therapeutic agents gradually until the scaffolds had lost the integrity after 12 weeks. Then, the ALP activity and ARS-CPC assay were evaluated to validate that our photo-crosslinking fabrication method did

not interfere with the functionality of the growth factors. It was recorded that the ALP activity of C2C12 had increased in both BMP-2 and P28 cultures, where 100 µg/ml P28 was comparable to 0.5 µg/ml BMP-2 after two weeks. The C2C12 cultured with CS/HAp/BMP-2 and CS/HAp/P28 scaffolds had also shown an increased ALP activity compared to the negative controls. ARS-CPC assay presented the highest optical density in 0.3 µg/ml BMP-2 and 50 µg/ml P28, while the highest intensity of ARS was observed in C2C12 cultured with CS/HAp/BMP-2 and CS/HAp/P28 scaffolds compared to the negative controls. The *in vivo* osteogenesis was investigated via rat femoral condyle defect model, where the new bone mineral density and the bone volume were found to increase in all CS/HAp scaffolds after eight weeks compared to the collagen sponges. The histological procedures showed a favourable bone regeneration efficacy through the CS/HAp/P28, thus showing the use of CS/HAp scaffolds with P28 as a promising osteoinductive scaffold for bone healing applications.

Hence, chitosan scaffold with P28 appears to be the alternative to its protein of origin, BMP-2, in bone tissue engineering for bone defect healing for its potent osteogenicity and biocompatibility, as well as its non-toxicity features following the implantation in the femoral condyles of the rats. However, due to the insufficient scaffold biodegradability *in vivo*, improved formulations should be considered to obtain a better degradation profile following implantation.

Following on from the osteogenic scaffolds' kinetic release, bioactivity assessment and the initial animal study in this chapter, the subsequent chapter will concentrate on the modifications of scaffolds' formulation to increase the biodegradability *in vivo* and its effect on bone healing.

Chapter 5

Chapter 5: Enhancement of Scaffold *in Vivo* Biodegradability for Bone Regeneration using P28 peptide Formulations

5.1 Abstract

The field of bone tissue engineering shows a great variety of bone graft substitute materials under development to date, with the aim to reconstruct new bone tissue while maintaining the characteristics close to the native bone. Currently, insufficient scaffold degradation remains the critical limitation for the success of tailoring the bone formation turnover rate. This study examines novel scaffold formulations to improve the degradation rate *in vivo*, utilising chitosan (CS), hydroxyapatite (HAp) and fluorapatite (FAp) at different ratios. Previously, the P28 peptide was reported to present similar, if not better performance in new bone production to its native protein, bone morphogenetic protein-2 (BMP-2), in promoting osteogenesis *in vivo*. Therefore, various P28 concentrations were incorporated into the CS/HAp/FAp scaffolds for implantation *in vivo*. HE staining shows minimal scaffold traces in most of the defects induced after eight weeks, showing the enhanced biodegradability of the scaffolds *in vivo*. The HE stain highlighted the thickened periosteum indicating a new bone formation in the scaffolds, where CS/HAp/FAp/P28 75 µg and CS/HAp/FAp/P28 150 µg showed the cortical and trabecular thickening. CS/HAp/FAp 1:1 P28 150 µg scaffolds showed a higher intensity of calcein green label with the absence of xylenol orange label which indicates mineralisation and remodelling was not ongoing four days prior to sacrifice. Conversely, double labelling was observed in the CS/HAp/FAp 1:1 P28 25 µg and CS/HAp/FAp/P28 75 µg, which indicates continued mineralisation at days ten and four prior to sacrifice. Based on the HE and fluorochrome label, CS/HAp/FAp 1:1 with P28 peptides presented a consistent positive osteoinduction following the implantation in the femoral condyle defects. These results show the ability of this tailored formulation to improve the scaffold degradation for bone regeneration and present a cost-effective alternative to BMP-2..

5.2 Introduction

Biodegradable scaffolds for bone tissue engineering are of great interest to researchers, due to their promising characteristics and performance to mimic the extracellular matrices in promoting natural bone healing (Dorati et al., 2017; Kaliva et al., 2020; Sanchez-Salvador et al., 2021). These engineered scaffolds are great alternatives to the natural-sourced treatments available such as bone grafts, despite their gold standard properties

due to the multiple surgical interventions required (autografts) as well as the existing risk of immune rejection (allografts) (Choy et al., 2021; e Silva et al., 2021; Fournet et al., 2019).

A common approach to the development of biodegradable scaffolds is to initially culture osteogenic cells containing growth factors on 3D scaffolds prior to implantation as suggested by the diamond concept, to simulate the physiological conditions (Andrzejowski & Giannoudis, 2019; Baruffaldi et al., 2021; Yamada et al., 2020). However, the additional cellular harvesting and culturing on the scaffolds prior to use are time consuming, thus leading the studies toward acellular osteoconductive and osteoinductive scaffolds with osteogenic growth factors (S. Jiang et al., 2021; L. Li, Lu, et al., 2019; S. J. Wang et al., 2019). The current study combines biology and engineering principles to develop viable substitutes to restore and maintain the function of human bone tissue. It was aimed to enhance the mechanical and biodegradable properties of bone scaffolds by modifying the crosslinking reaction to avoid the burst release of the growth factors. The fabricated biodegradable scaffold will release growth factors while degrading and then be secreted from the body naturally after it completes its function. Therefore, an ideal scaffold should be able to degrade in a gradational way for an expected period to be replaced by a newly formed bone tissue from the bonded cells, known as the osteotransduction process (Alves et al., 2020). This degradation will result in the breakdown of the scaffold and the resorption of the protein such as bone morphogenetic protein-2 (BMP-2) incorporated in the scaffold to the targeted location.

The current market leader for Food and Drug Administration (FDA)-approved growth factor delivery system is the recombinant human BMP-2 (rhBMP-2) known under the trade name INFUSE[®], with an absorbable collagen sponge carrier to be used as a bone graft substitute in treating open tibial fractures. This product is in line with another FDA-approved AUGMENT[®] by Wright Medical and i-Factor by Cerapedics (Arnold et al., 2021; Biswas et al., 2019; Govoni et al., 2021; James et al., 2016). However, this INFUSE[®] treatment has limited success in the treatment of non-union healing and this product is associated with several documented complications, such as ectopic calcification and bone formation as well as transient bioactivity, which is the off-target reaction (Briquez et al., 2021; Durham et al., 2018; Paxton et al., 2020). INFUSE[®] has

also faced an FDA warning following reports of severe dysphagia due to inflammation, as well as the increased loss of life.

An alternative to the use of BMP-2 is the use of the derived osteogenic peptides from BMP group proteins due to their small relative molecular weight, known physiological effect, flexibility to use, as well as lower cost demands (Meng et al., 2021). There are two sites of interest in the complex structure of BMP-2 dimer, known as wrist and knuckle epitope regions. Extensive reports were proposing the ability of peptides derived from this knuckle region to induce osteogenesis, thus enabling it to substitute the full-length of rhBMP-2 (Bain et al., 2015). Initially, a synthetic peptide, P4, synthesised from the knuckle epitope of BMP-2 (73-92), was reported to increase the alkaline phosphatase (ALP) and osteocalcin activity to the highest levels in the murine multipotent mesenchymal cell line (C3H10T1/2), compared to the other BMP-2 derived peptides (Ahn & Je, 2019; Saito et al., 2003). This BMP-2 knuckle epitope derived peptide (P4) has also shown to increase the osteopontin and mineral deposition in clonally derived murine mesenchymal stem cells (7F2) (Madl et al., 2014). Subsequently, another short BMP-2 related peptide called P24 with a molecular weight of 2630.88 g/mol was then synthesised (Niu et al., 2009). This peptide consists of chemically stable small molecules and a linear structure as a biological active site, and is believed to promote bone marrow stromal cell adhesion, enhance ectopic osteogenesis, and repair critical-sized rabbit bone defects (Y. Chen et al., 2017).

Following the P24 synthesis, Cui et al. (Cui et al., 2016) had improved the work mentioned above by synthesising a longer BMP-2 dimer-knuckle epitope derived peptide chain called P28 (S^[PO₄]DDDDDDDKIPKASSVPTELSAISTLYL) (Chao et al., 2021). This P28 indeed possess several significant properties compared to BMP-2 in terms of its smaller relative molecular weight and better chemical stability that can improve its biological effects. The most impressive feature of P28 in this bone tissue engineering field is its repetitive amino acid sequences with high bonding ability towards calcium phosphate materials. This feature can lead to an extended release with higher delivery specificity to the intended site, thus giving a promising outcome to be discovered in future bone substitutes research (Meng et al., 2021). Moreover, the biomimetic feature of peptides in retaining the osteogenic features of the larger proteins offers greater control over cellular interactions. The shorter chains of peptides are advantageous in overcoming

the steric effects, folding, immunogenicity and susceptibility to degradation problems of the larger proteins, thus leading to better signalling and binding domains availability for the required cellular interactions (Bullock et al., 2021).

To date, the scaffold degradation profile that outlines the scaffold's capability to release the growth factors in the time frame was still not successfully altered (Govoni et al., 2021). Hence, despite the great potential of the osteogenic peptide P28, there is a need to design a fully-functional carrier, to ensure it is retained in the defect until it has fulfilled its function. The performance of bone substitutes can be improved by tuning the scaffold composition and its fabrication method, as well as incorporating the growth factors. Also, the ability of the scaffolds to mitigate bacterial infections through the use of anti-infective biomaterial should also be examined.

This chapter employed the revised P28 delivery systems with a faster degradation than previous formulations presented in Chapter 4 by incorporating the combinations of hydroxyapatite and fluorapatite ceramics into the chitosan composite. In addition, the osteogenicity of different P28 concentrations was tested since our initial animal trial utilising 25 µg P28 showed a promising osteoinductivity. Therefore, an increased P28 content (75 and 150 µg) was tested in CS/HAp/FAp scaffolds in order to investigate the best osteogenicity effect on the rat femoral condyle defect model utilised in this work. This proposed model has also undergone a commercial feasibility review for an orthopaedic scaffold alternative to the existing options.

The animal handling and surgical procedure training was undergone in Animal Research and Service Centre, Universiti Sains Malaysia. The experiment protocol for this animal study was carried out with the ethical approval from the Institutional Animal Care and Use Committee (IACUC USM) with reference number: USM/IACUC/2020/(122)(1048). The overview of this second animal trial is presented in the chart (Figure 5.1).

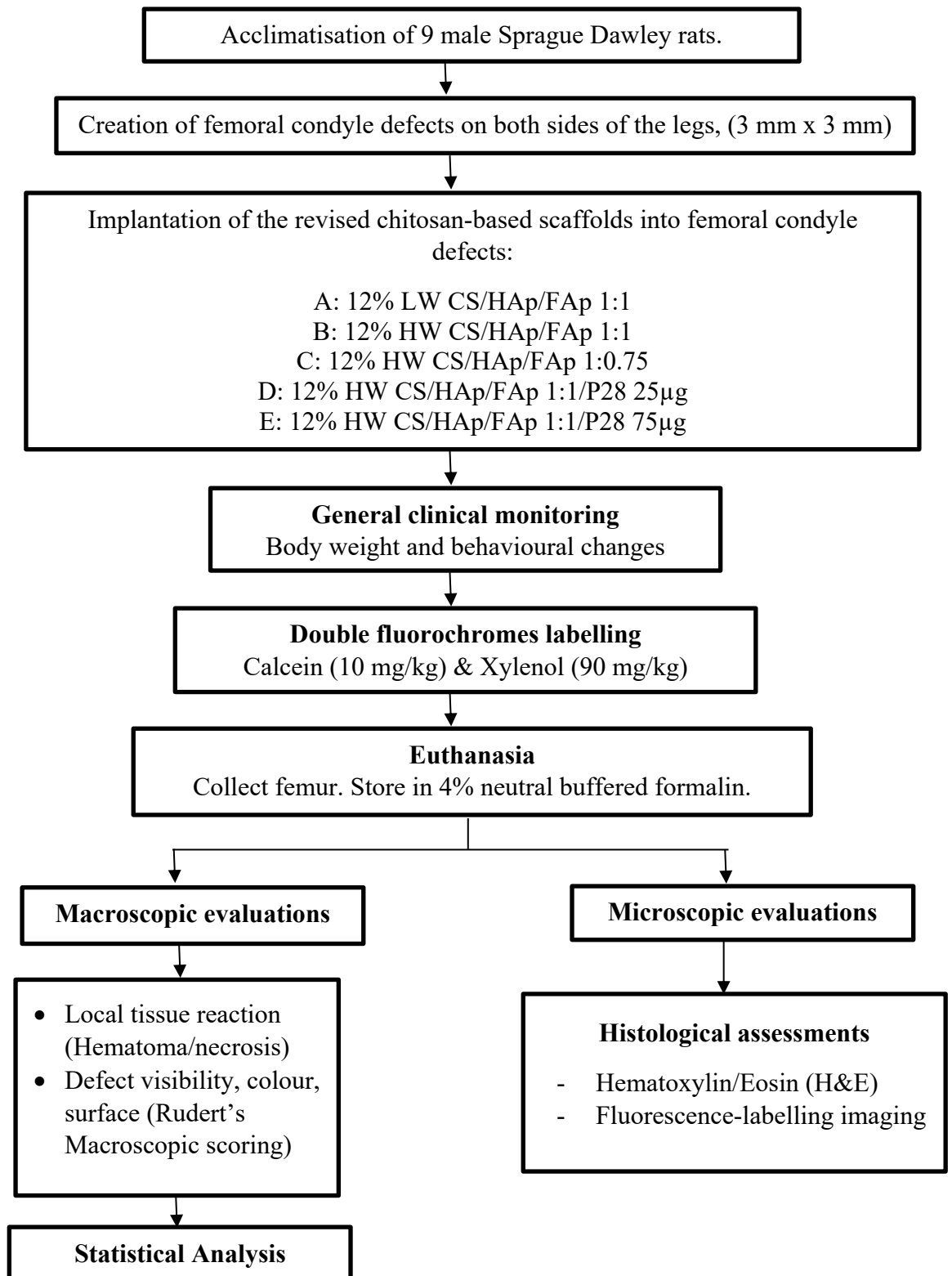


Figure 5.1 Summary of the second animal trial experiments.

5.3 Results and Discussion

5.3.1 Antimicrobial Functionality of UV-Crosslinked Chitosan Scaffolds with Fluorapatite Bioceramics

Resazurin antimicrobial test was performed prior to the *in vitro* bioactivity assessment to investigate the ability of the scaffolds to prevent any microbial growth in the cell culture. This test is essential to validate the optimum performance of the growth factors in promoting osteogenic differentiation of the C2C12 myoblast cell line.

The dye reduction of the treatments in the bacterial strains was observed (Figure 5.2a) and evaluated spectrometrically at 600 nm (n=3) (Figure 5.2b). The scaffold formulated with CS/FAp recorded the most potent antimicrobial activity compared to the other test groups in both *S.aureus* and *E.coli* ($p < 0.05$). This result would validate the antimicrobial properties of the fluorapatite bioceramic reported (Alhilou et al., 2016; Anastasiou et al., 2019). However, a study mentioned the need for doping silver ions with documented antibacterial properties to enhance the lower antibacterial properties of FAp compared to its original CaP form, HAp (Pajor et al., 2019). Another doping system of FAp with and without cerium ions (Ce^{3+}) gave a similar antibacterial behaviour compared to the lower activity following doping with strontium ions (Sr^{2+}) (Anastasiou et al., 2019).

On the other hand, the lower antimicrobial activity achieved in the rest of the formulations other than CS/FAp might also be caused by several factors, such as the possible insufficiency of scaffold sterilisation procedures and the condensation observed on the scaffolds. This hypothesis mentioned is due to the well-known antimicrobial properties of the chitosan itself and its ability to effectively exhibit the antibacterial activities of the pathogens (Y. Liao et al., 2020). In addition, CS/HAp combination was reported to inhibit the bacterial growth even better than CS alone in three antimicrobial tests conducted; the bacterial counting method, zone of inhibition test as well as the optical technique (B. Li, Xia, et al., 2019). Therefore, freshly prepared scaffolds are suggested to be used in any tests, especially involving bacteria and cells, to avoid the possible risks mentioned. In addition, it is suggestive to include the raw materials in the test to investigate the baseline of the antimicrobial capacity in comparison to the developed composites.

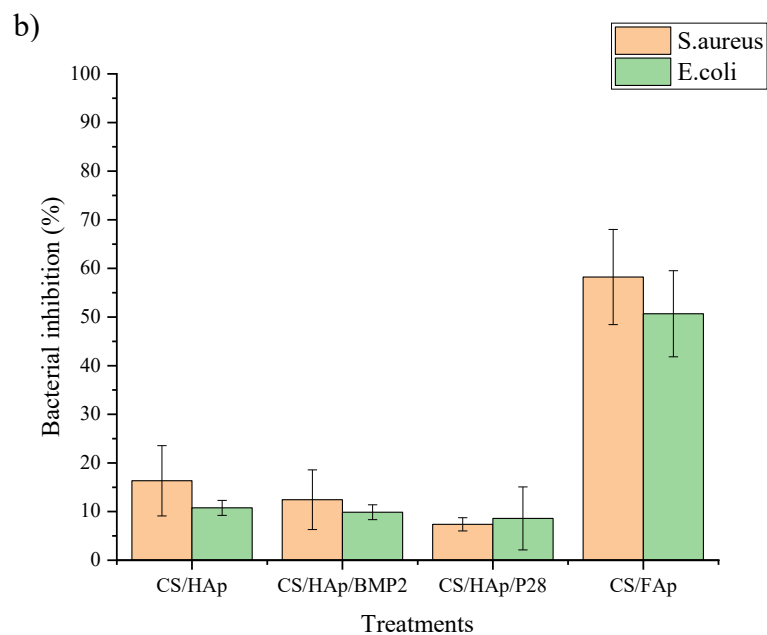
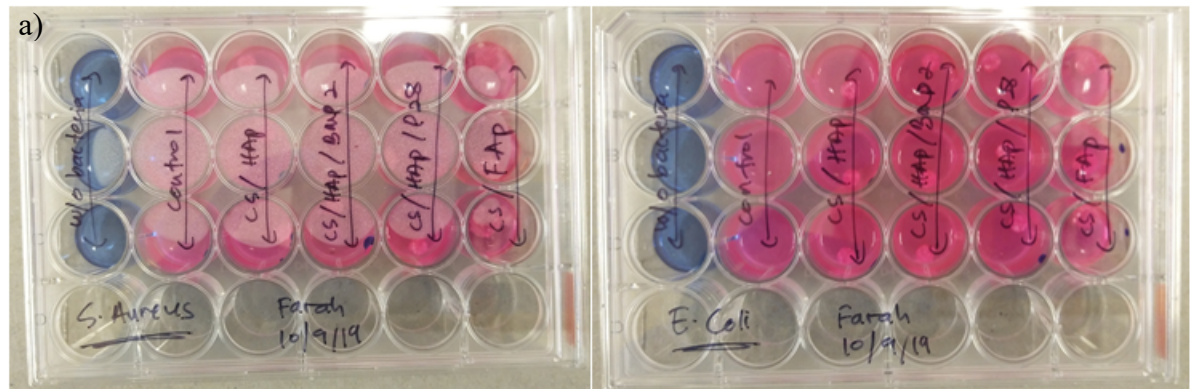


Figure 5.2 a) The resazurin blue dye reduction to pink colour was observed in the tests after 24 hours of incubation. Left panel= Treatments in *Staphylococcus aureus* (*S.aureus*). Right panel= Treatments in *Escherichia coli* (*E.coli*). b) The antimicrobial activity of the scaffold treatments in both *S.aureus* and *E.coli* strains, showing the highest bacterial inhibition in the CS/FAP treatments.

5.3.2 Post-operative Monitoring

The weights of the animals were monitored from the acclimatisation period until sacrifice (Figure 5.3). It was observed that the weight was increased during the acclimatisation period until the implantation day. Following implantation, the weight decreased for about a week, which is a sign of pain and discomfort in post-operative procedures and the effects of anaesthesia and analgesia that led to decreasing appetite or lameness (Talbot et al., 2020). In addition, several incidents of broken sutures had exposed the wound, increasing the risk of pain and infection to the wound, while the re-suturing procedures required anaesthesia and analgesia that will further cause the reduction of catching food. However, the weight loss threshold of a maximum of 20% was not reached (Helgers et al., 2020),

and the weight of all animals began to increase again after 7-10 days, indicating good tolerance of the selected model.

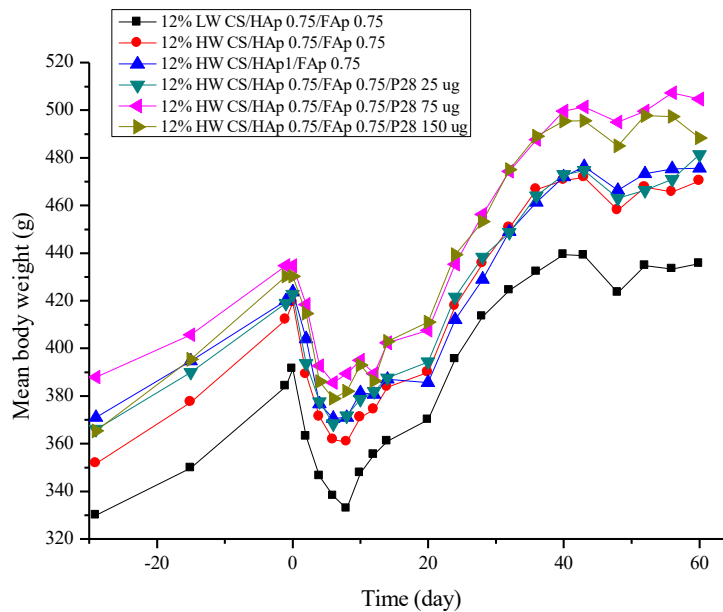


Figure 5.3 Post-operative weight monitoring of nine implanted Sprague Dawley rats.

5.3.3 Macroscopic Evaluation

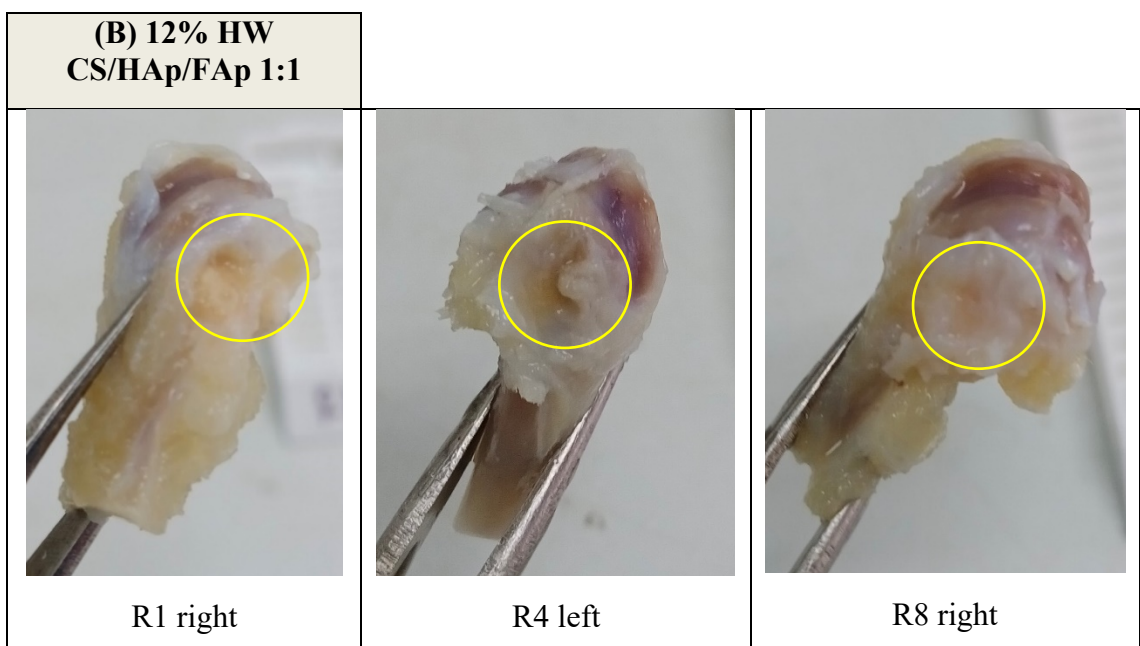
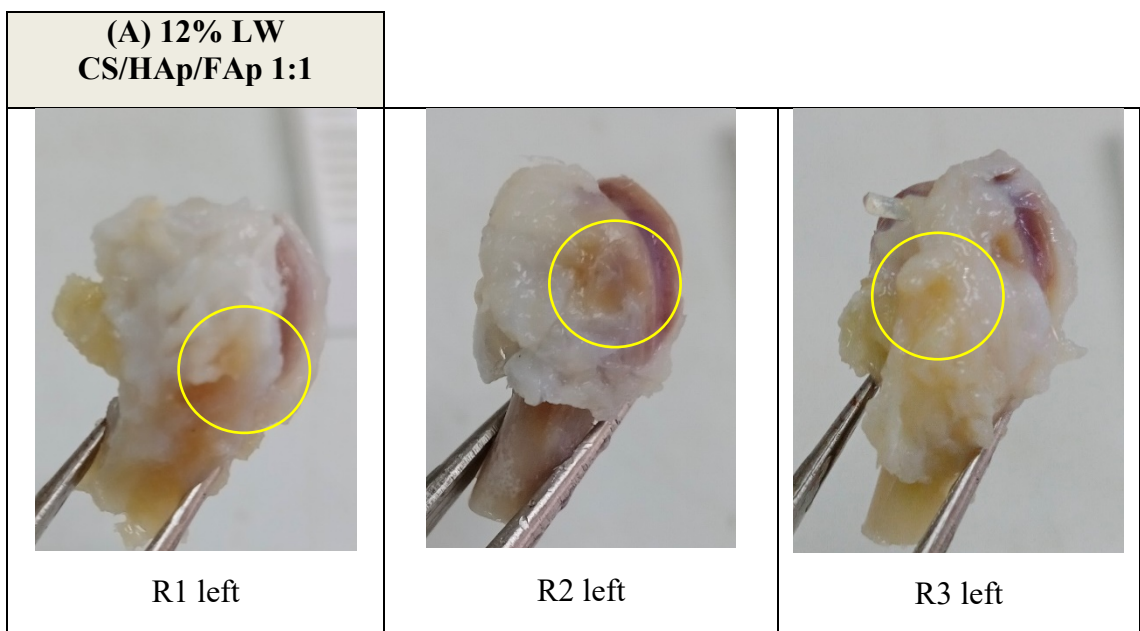
All femoral condyles with the implanted scaffolds from the six formulations (n=3) were harvested, and local macroscopic condition was evaluated using a modified scoring table from Rudert *et al.* (2005) (Figure 5.4). Scaffold-only controls (negative) and Infuse® (positive) were previously reported in Chapter 4. To avoid the unnecessary duplication of data and animals, these controls were not repeated in this work. While empty controls were not used, the 3mm defect in the rat femoral defect is not considered a critical size and as such is expected to heal.

	Samples																	
	R1L	R1R	R2L	R2R	R3L	R3R	R4L	R4R	R5L	R5R	R6L	R6R	R7L	R7R	R8L	R8R	R9L	R9R
Total score for each sample	5	3	5	5	3	3	6	3	5	3	7	3	5	3	7	6	3	6
Standard deviation	0.58	0	0.58	0.58	0	0	0	0	0.58	0	0.58	0	0.58	0	0.58	0	0	1

Figure 5.4 The macroscopic monitoring for the harvested condyles. Note: R1-R9 means Rat 1-9. R means right condyle and L means left condyle. The Kruskal-Wallis test showed $p > 0.05$ for the investigated criteria, possibly due to the small sample size used in this preliminary study.

Several remarks were observed macroscopically (Figure 5.5), where most defects were closed with a layer of transparent tissue. While new bone growth was seen around the defects in the presence of P28 (12% HW CS/HAp/FAp 1:1/P28 25µg), some of them

showed scaffold residues and more scaffold residues were seen in scaffolds formulated with higher HAp content (12% HW CS/HAp/FAp 1:0.75). In addition, there was a possibility of ectopic growth seen in scaffolds with the highest content of P28 (12% HW CS/HAp/FAp 1:1/P28 150 μ g). On the other hand, an incidence of drilling burr slippage off the site of interest had occurred on the right condyle of R6, producing a defect on the bone shaft instead of the condyle. Therefore, the result from this condyle was completely discounted. Altogether, the Kruskal-Wallis test showed $p > 0.05$ for the investigated criteria; however, the chi-square approximation from this test may not be accurate since the sample size was less than five.



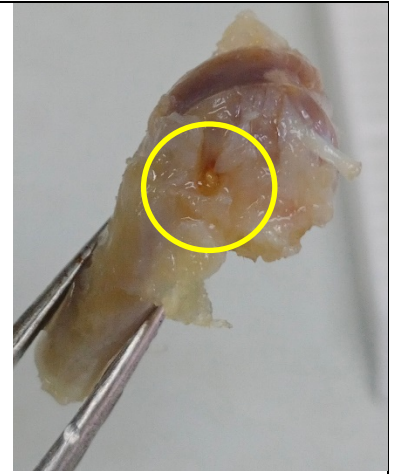
**(C) 12% HW
CS/HAp/FAp 1:0.75**



R2 right



R5 left



R7 right

**(D) 12% HW
CS/HAp/FAp 1:1/P28
25 μ g**



R3 right



R4 right



R6 left

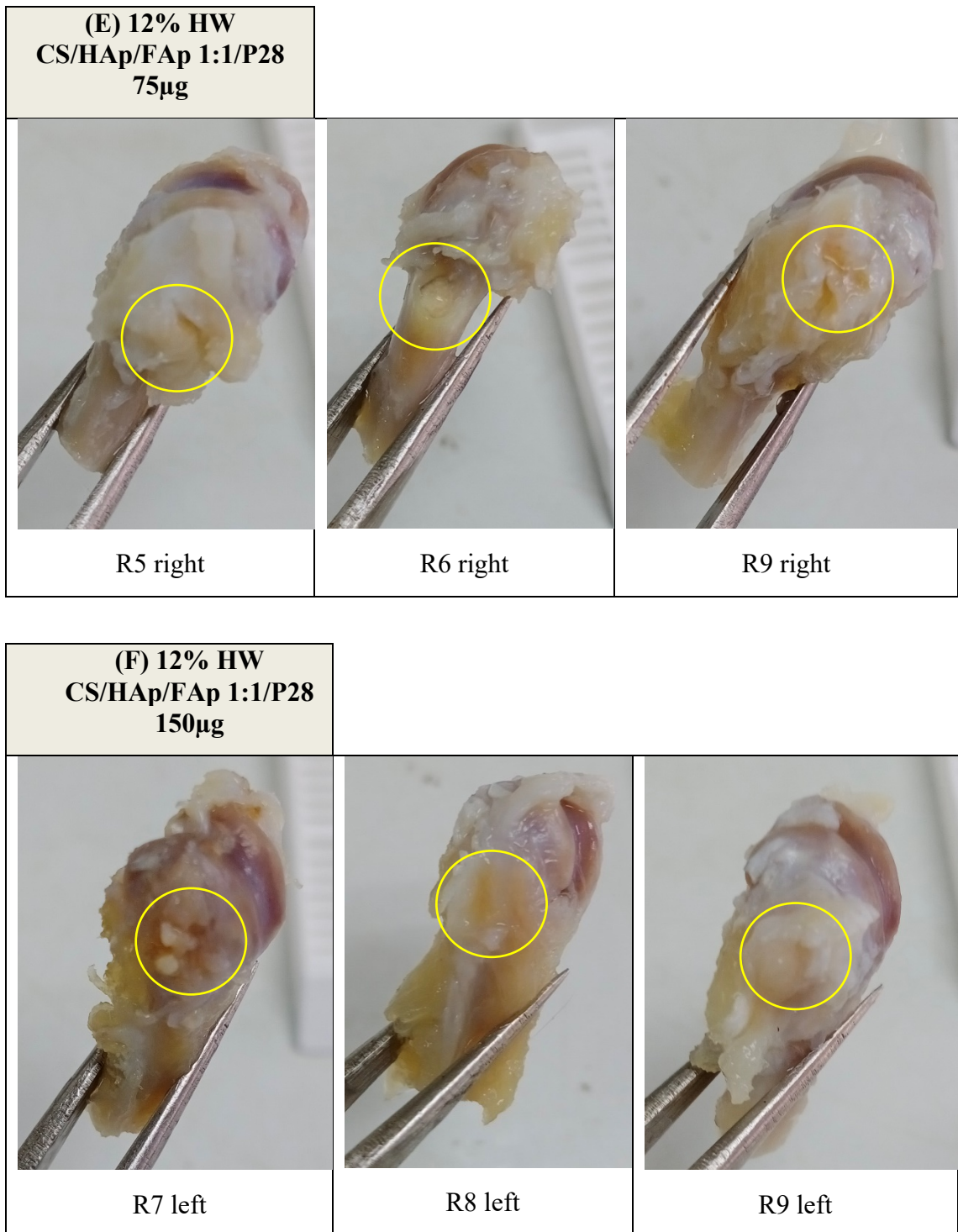


Figure 5.5 Macroscopic observations of the harvested condyles implanted with the developed bone regeneration scaffolds.

5.3.4 Histological Analysis using Hematoxylin-Eosin Staining

Histological analysis through HE staining was conducted in collaboration with a histopathologist to evaluate the performance of the implanted scaffolds and presented according to each formulation (Figure 5.6). Interestingly, the scaffold traces were observed to be minimal in most of the defects induced. This observation might validate

that the combination of HAp and FAp in the chitosan-based delivery system has escalated the biodegradability of the scaffolds *in vivo*, although it was reported that FAp alone possesses a lower solubility in biological fluids compared to HAp (Malysheva et al., 2021; Vidal et al., 2022). This behaviour observed is also in line with the biodegradability results reported previously in Chapter 3, where CS/FAp scaffold lost the integrity during handling as early as week two following submersion in simulated body fluid.

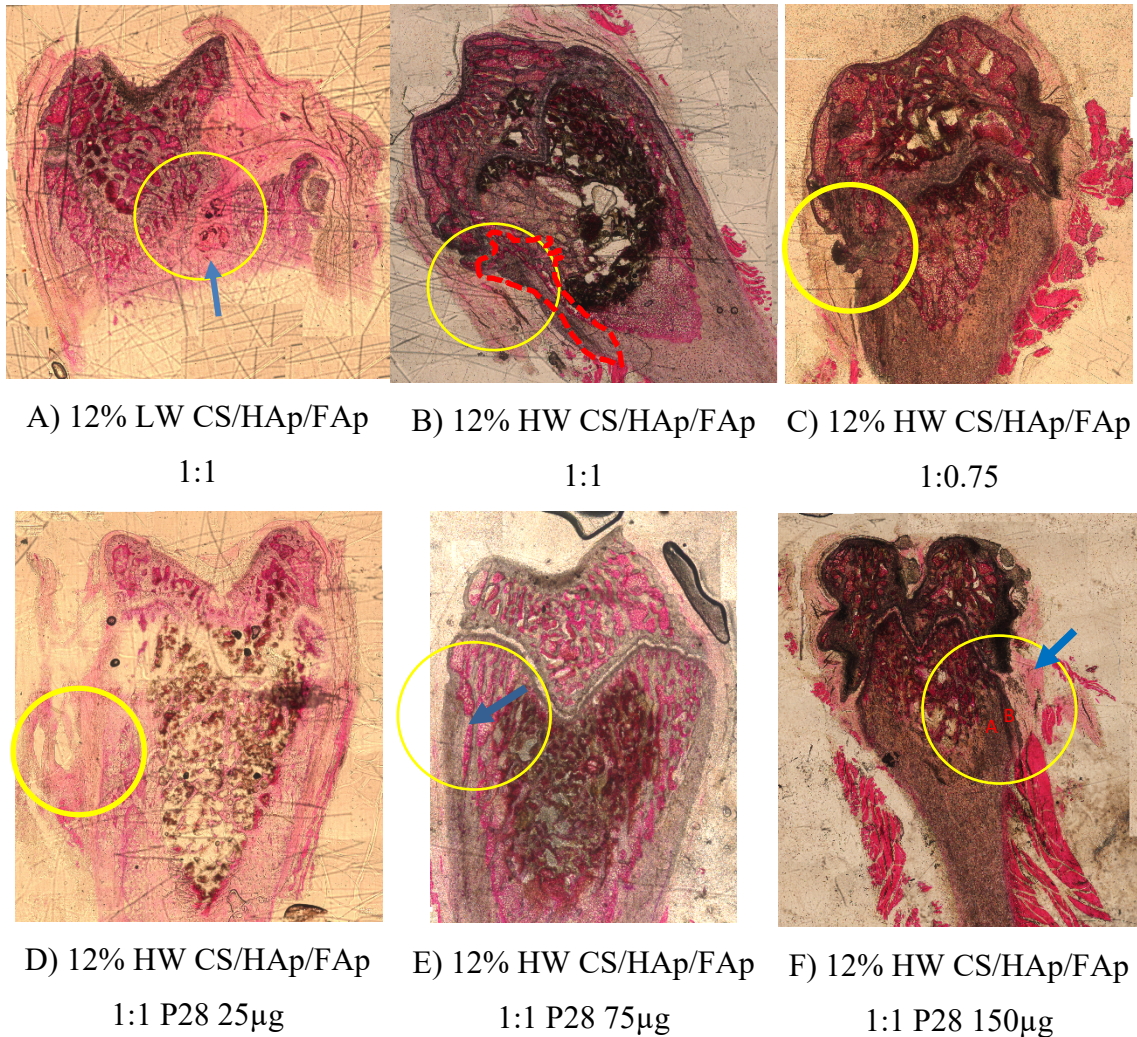


Figure 5.6 HE stained slides of the implanted condyle defects. Yellow circles highlight the site of implanted defects. Blue arrows represent the newly formed bone structure where the composite was implanted. Red coloured A,B shows the two different densities of the compact bone tissue.

From the review of the HE-stained sections, the projection of fibrous tissue containing central ossification separates the spongy bone tissue areas in the implanted defect region (Figure 5.6A). Cortical bone thickening was observed in the bone implanted with 12% HW CS/HAp/FAp 1:1 scaffold (Figure 5.6B), which could result from the osteointegration of the composite. Moreover, thickening of the periosteum near the defect

area with an external surface irregularity of the compact bone as well as osteointegration with the implant below the periosteum was observed for 12% HW CS/HAp/FAp 1:0.75 (Figure 5.6C). Similar periosteum thickening could also be seen in the defect implanted with 12% HW CS/HAp/FAp 1:1 P28 25 μ g (Figure 5.6D). On the other hand, the cortical and trabecular bone thickening (arrow) in the defect region of 12% HW CS/HAp/FAp 1:1/P28 75 μ g, might be due to osteointegration and induction from the implantation of the composite (Figure 5.6E). Compact bone tissue with two different densities (A,B) as well as the thickened periosteum (arrow) is present in the defects with 12% HW CS/HAp/FAp 1:1 P28 150 μ g, which might be derived from the osteoinductive activity of the composite with the highest peptide content (Figure 5.6F).

Enhanced bone formation resulting from the use of tissue engineering scaffolds incorporating P28 peptide has also been reported in the literature. In the initial studies reporting the use of P28, silicone/hydroxyapatite (Si/HAp) scaffold was loaded with P28 peptide and implanted in rat calvarial defects (Cui et al., 2016). The defects showed that the Si/HAp/P28 scaffold promoted bone recovery to a similar degree as the Si/HAp/rhBMP-2 scaffold. No new bone formation occurred in the empty defects (control) 6 weeks after surgery, although fibrous tissues were observed in the defect area, and the recovery did not improve even until 12 weeks post-implantation. Similarly in the later study by Chao et al. (Chao et al., 2021), the control in canine (dogs) defect model that was implanted with hydroxyapatite/ β -tricalcium phosphate/collagen (HAp/TCP/Col) scaffold alone revealed limited bone regeneration with noticeable HAp/TCP particles at four and eight weeks compared to the defects implanted with HAp/TCP/Col/P28, thus showing the positive bone regenerating capacity of this BMP-2 derived peptide.

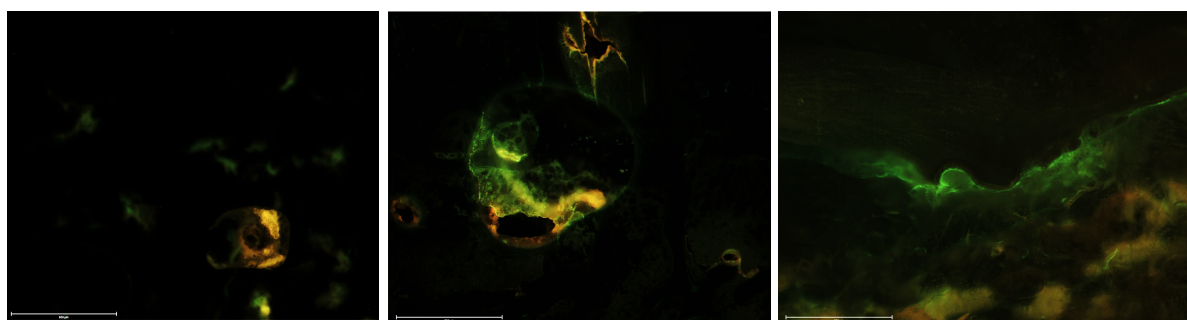
Earlier studies utilised a high concentration of P28 peptide in order to bind the peptide onto the scaffolds through the physisorb method to evaluate the osteogenic induction of bone defects in the presence of this P28 peptide (Meng et al., 2021; Sun et al., 2017; J. Zhou et al., 2020). However, no previous reports were found to investigate the efficacy of the P28 scaffolds in different mass content towards the osteogenic induction of bone defects using UV crosslinking in CS/HAp/FAp scaffolds. Therefore, the strongest new bone formation achieved with 150 μ g P28 in this work can be a potential reference for future work involving P28 peptides. This early histological evaluation of the P28 peptide's osteogenicity in an *in vivo* setting offers convincing proof of the compound's potential in

bone tissue engineering and regenerative medicine. The findings of this study indicate that P28 peptide may increase the quality of newly produced bone tissue and stimulate bone growth, but more studies are required to validate its efficacy and safety in people.

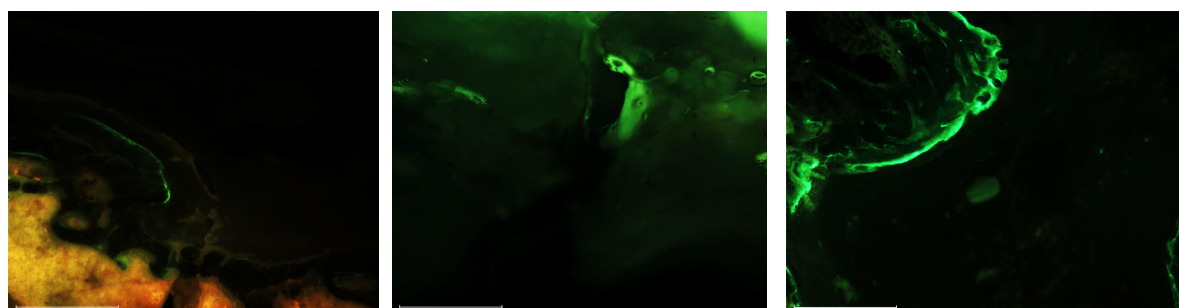
5.3.5 Fluorochrome Labelling Analyses

Fluorescent labelling was evaluated as the dynamic of bone formation that corresponds to mineralisation speed, time, location as well as the direction of the mineralisation (Shanker, 2019; van Gaalen et al., 2010). Calcein green (CG) and xylenol orange (XO) fluorochromes were injected *in vivo* ten and four days before sacrifice, respectively. The fluorochrome labels work by chelating the mineralised front during the bone mineralisation process at the time of injection, which enables the evaluation of the dynamic bone formation by measuring the distance between fluorochromes labels (Spicer et al., 2012). It has also been documented that fluorochrome labelling can be used to evaluate bone mineralisation rate, remodelling, and the signs of toxicity of the implants on bone *in vivo* (Alves et al., 2020).

From the analysis of fluorochrome labels (Figure 5.7), it was found that the presence of the XO label was observed in the condyle implanted with the 12% LW CS/HAp/FAp 1:1, indicating that mineralisation is still ongoing four days before sacrifice. However, the absence of CG may indicate that this mineralisation was in the form of remodelling bone formed earlier in the healing process. In contrast, the condyle implanted with 12% HW CS/HAp/FAp 1:1 showed the presence of double labelling, where a positive label was seen in both CG and XO. This double labelling indicated ongoing bony deposition on the injection days. In addition, a single CG label appeared in the condyle implanted with 12% HW CS/HAp/FAp 1:0.75 and 12% HW CS/HAp/FAp 1:1 P28 150µg indicating bone formation had occurred ten days prior to sacrifice. Since XO label is absence, it indicates that no bone formation occurred 4 days prior to sacrifice in this single condyle. This observation could indicate that bone remodelling had finished at that time prior to XO administration (Shanker, 2019). The samples with 12% HW CS/HAp/FAp 1:1 P28 25µg and 12% HW CS/HAp/FAp 1:1 P28 75µg shared a similar observation, where double labelling appeared in the condyles indicating the ongoing mineralisation at ten days and four days before sacrifice.



A) 12% LW CS/HAp/FAp B) 12% HW CS/HAp/FAp 1:1 C) 12% HW CS/HAp/FAp 1:0.75



D) 12% HW CS/HAp/FAp 1:1 P28 25µg E) 12% HW CS/HAp/FAp 1:1 P28 75µg F) 12% HW CS/HAp/FAp 1:1 P28 150µg

Figure 5.7 Fluorescent labelling imaging, observing the calcein green and xylanol orange labelling formed on the newly formed bone.

Fluorochrome labels, such as CG and XO, bind to mineralised tissues, including both newly formed bone and bone-like ceramics. These labels can provide information about the dynamic process of mineralisation, regardless whether it occurs in natural bone or synthetic ceramics, thus allowing for evaluation of the mineralisation process in both materials (Shih et al., 2017). However, the evaluations in this work were carried out considering the defect margin and not including the implanted composite scaffolds in order to distinguish between the two (Pautke et al., 2005, 2007, 2010; van Gaalen et al., 2010). Since the accuracy and interpretation of the results obtained using fluorochrome labels can be influenced by various factors, including the specific labelling technique and the interaction between the labels and the materials being studied (Zuncheddu et al., 2021), a quantitative assessment of fluorochrome labels is recommended in order to achieve a definite comparison between samples, evaluating the mineral apposition rate (MAR) and also bone formation rate (BFR). These measurements are proposed since the length of fluorescent labels and the distance between the labels are measurable parameters

which can be used to evaluate the new bone turnover (Dempster et al., 2014; Maglio et al., 2020). However, due to the small sample size and a lack of clear bone growth fronts in this work, these measurements were not possible.

5.4 Impact of Coronavirus Disease 2019 (COVID 19) Pandemic on the Studies

COVID 19 pandemic has caused a detrimental effect throughout the globe where hundreds of thousands of deaths were reported, economies were shut down, country borders were closed and thus causing chaos on an phenomenal scale that has tremendously affected the quality of life of everyone. Research field was not an exception, specifically to this project presented.

This project was about to begin during the emergence of COVID 19 in Wuhan, China. The experimental proposal was agreed with the field supervisors from Universiti Sains Malaysia (USM) in Kelantan, Malaysia and an ethical proposal was submitted to the Institutional Animal Care and Use Committee (IACUC USM). The ethics defence was a success, acquiring the ethical approval to conduct the planned animal studies. However, movement control order (MCO) was issued, causing a six months delay to the animal reception. The surgical procedures, post-operative monitoring and animal sacrifice procedures were managed to be completed despite the bottleneck situation. However, the real challenge was during the hard tissue processing and cutting procedures, where the instruments involved are due for maintenance and spare-parts replacement. Unfortunately, this issue took a very long time and complicated to resolve, that it was decided to send the samples to another university. Similarly, the MCO in Malaysia still left us in impediment, where a desperate measure was taken by sending the samples to a pathologist in The Federal Rural University of Pernambuco, Brazil. Due to the instruments' faulty and a long time gap to complete the processing procedures, the samples aged and thus causing a lower quality of histological results.

It is highly recommended that another animal study should be carried out to improve the current outcome and addressing the limitations encountered from this study. A more detailed suggestions will be discussed in the following chapter.

5.5 Summary

A preliminary *in vivo* trial was conducted bilaterally on nine male Sprague Dawley (SD) rats to evaluate the osteogenic potency of a CS/Hap/FAP scaffolds loaded with P28

peptide. In this study, our aim was to provide evidence for rationale of the effect of changing the ceramic content and changing the P28 concentration. As such this study was designed to narrow down the variables for future experiments (identifying the best ratio and the best concentration of P28). Post-mortem observations indicate that most defects were observed to be closed with a layer of transparent tissue, while new bone growth was seen around the defects in the presence of P28 (12% HW CS/HAp/FAp 1:1/P28 25µg). Also, there was a possibility of ectopic growth seen in scaffolds with the highest content of P28 (12% HW CS/HAp/FAp 1:1/P28 150µg).

For histological assessment, unstained sections were assessed for the presence of fluorochrome labels with HE staining used to assess the biological response to the scaffolds. The HE stain highlighted the thickened periosteum indicating a new bone formation in the scaffolds, where CS/HAp/FAp/P28 75 µg and CS/HAp/FAp/P28 150 µg showed the cortical and trabecular thickening as a result of implantation of composite in the region below the metaphysis. Subsequently, the CG and XO fluorochrome assessment indicated that CS/HAp/FAp 1:1 P28 150 µg scaffolds showed a high-intensity response to calcein green label, indicating mineralisation was ongoing 10 days prior to sacrifice. Similarly, the presence of double labelling which is indicative of ongoing mineralisation was observed at days 10 and four prior to sacrifice in the CS/HAp/FAp 1:1/P28 25 µg and CS/HAp/FAp/P28 75 µg. Based on the HE and fluorochrome label, CS/HAp/FAp 1:1 with P28 (especially in the 12% HW CS/HAp/FAp 1:1/P28 25 µg scaffold) showed some indications of new bone growth around the defects, but further investigation is needed to confirm the consistent positive osteoinductive effects following the implantation in the femoral condyle defects. Also, further investigation is required to rule out ectopic bone formation especially in the highest P28 content. While partial progress has been made on the technical milestones, significant further work is required to fully understand the therapeutic potential of this P28-loaded CS/HAp/FAp scaffold. Also, more study is required to find the ideal dose and delivery technique in order to guarantee the P28 peptide's safety and effectiveness in people.

Chapter 6

Chapter 6: Conclusions & Recommendations

6.1 Conclusions

The development of bone healing scaffolds possessing the key elements: biodegradable, osteoconductive, osteoinductive, and mechanically stable are currently the focal attention in bone tissue engineering research. However, there is a need to address the limitations of the current approach including the high burst release from uncontrolled scaffold degradation, the higher cost of therapeutic agents as well as the complex procedures of cell cultures prior to the scaffold implantation. The mitigation of bacterial infections are also crucial to produce a safe bone healing scaffolds following implantation. In order to address the aforementioned shortcomings, this study was aimed to develop a biodegradable, cell-free and osteoinductive scaffold with mechanical stability and antimicrobial features, producing a lower cost, off-the-shelf scaffolds with controllable release of the active agents.

Initially, the fabrication method of an osteoconductive bone regeneration scaffold was effectively modified using a tuneable UV crosslinking reaction incorporating several bioceramics and various photoinitiator contents into chitosan composite, providing a promising improved bone healing scaffold. The swelling test in acidic conditions presented a gel fraction of more than 50%, demonstrating efficient crosslinking was achieved. The FTIR showed the scaffold characteristics for both chitosan and ceramics following crosslinking, where a reduction in C=C peaks were recorded with decreasing BP content. Moreover, the surface morphology was confirmed through SEM-EDX analysis. The compression testing validated the mechanical performance of the scaffolds achieving 12-15 MPa, which was sustained to at least 10 MPa during degradation recorded over eight weeks in SBF. The scaffold mineralisation in SBF was monitored semi-quantitatively using SEM-EDX, where an increase of Ca/P ratio was recorded from week 1 to week 2 before gradually reduced from week 2 to week 8. Therefore, CS/HAp with 5 μ l of 0.1% w/v benzophenone scaffold formulation is proposed for future investigation as a biomimetic bone scaffold candidate since it was found to provide promising mechanical properties while degrading, in addition to favourable swelling and gel fraction characteristics.

Although the scaffold fabrication method presented is hypothesised to provide better control of the covalent grafting of active ingredient within the scaffold structure and its release *in vitro* and later *in vivo*, this chapter anticipates for several improvements. For instance, an extended analysis can be considered regarding the potential effect of altering the photoinitiator content in the other scaffold formulations including CS/TCP- α and CS/FAp mentioned in this body of work, since the change in the BP content was only investigated in CS/HAp. Additionally, a detailed study in terms of the effect of UV crosslinking and pulsed-UV sterilisation on the scaffold structure and the molecular activity of the osteogenic factors are suggested in order to avoid the consequences of reactive oxygen species upon implantation. Investigations using alternatives for sterilising the scaffolds could also be considered, such as the gamma ray, e-beam and supercritical fluid sterilisation, to ensure the sterilisation method does not adversely affect the scaffold structure and the osteogenicity of the incorporated protein and peptide.

Subsequently, the developed CS/HAp scaffolds were successfully crosslinked with either BMP-2 or P28 peptide under UV light. The release rate validated the ability of the scaffolds to degrade while releasing the osteogenic agents gradually in the desired 6-8 weeks' timeframe. Nevertheless, the main challenge involving the high affinity of protein and peptide towards the stainless-steel HPLC system has demanded a great deal of troubleshooting steps. Two different method was used in analysing the protein and peptide release rate; the MALDI-TOF and UV-Vis spectrometry but ultimately, it is crucial to extend this experiment using an inert or bioHPLC system to validate the release profile of the low concentration of osteogenic factors while avoiding the protein-surface interactions.

The ALP activity of C2C12 cultures had increased in both BMP-2 and P28 treatments, where 100 $\mu\text{g/ml}$ P28 was comparable to 0.5 $\mu\text{g/ml}$ BMP-2 after two weeks. The C2C12 cultured with CS/HAp/BMP-2 and CS/HAp/P28 scaffolds had also shown an increased ALP activity compared to the negative controls. ARS-CPC assay presented the highest optical density in 0.3 $\mu\text{g/ml}$ BMP-2 and 50 $\mu\text{g/ml}$ P28, while the highest intensity of ARS was observed in C2C12 cultured with CS/HAp/BMP-2 and CS/HAp/P28 scaffolds compared to the negative controls. However, a number of modifications can be considered for the cell culture experiments, including the osteogenic induction parameters to be applied and the method of harvesting the cell lysate in order to obtain a more

promising results. Two lysis methods were attempted in this work: the sonicating bath and vortex, substituting the unavailable pulse sonicating device suggested by the test kit supplier. From the experiments carried out, the sonicating bath method yielded even lower lysate and possessed the risk of protein degradation due to the change in water temperature, despite the temperature control using ice flakes. Therefore, it is best to follow the supplier recommendation which is the pulse sonicating device. Other options in testing the osteogenicity of the developed scaffolds can be considered, such as shifting to molecular biology investigations, specifically the nucleic acids-based techniques.

Subsequently, the *in vivo* osteogenesis was then investigated via a rat femoral condyle defect model, where the new bone mineral density and the bone volume were found to increase in all CS/HAp scaffolds after eight weeks compared to the collagen sponges. The histological procedures showed a favourable bone regeneration efficacy through the CS/HAp/P28, thus showing the use of CS/HAp scaffolds with P28 as a promising osteoinductive scaffold for bone healing applications. Hence, chitosan scaffold with P28 appears to be the alternative to its protein of origin, BMP-2, in bone tissue engineering for bone defect healing for its potent osteogenicity and biocompatibility, as well as its non-toxicity features following the implantation in the femoral condyles of the rats. However, due to the insufficient scaffold biodegradability *in vivo*, improved formulations should be considered to obtain a better degradation profile following implantation. Moreover, the rotational distortion causing the twisted condyles should also be further investigated in terms of the factors causing this phenomenon as well as the potential effect of this distortion on the bone healing.

Consequently, modifications in scaffold formulations were investigated in the current work, incorporating fluorapatite for its higher biodegradability achieved during the early development process of the scaffolds, although this high biodegradability result is in need of further explorations in terms of the interaction between chitosan and fluorapatite. However, the antimicrobial feature of these two materials are attractive. Antimicrobial Resazurin blue assay was carried out and the results show that the incorporation of fluorapatite into the chitosan composite formulation had provided the highest bacterial inhibition in both gram positive and negative bacteria. Therefore, in order to extend the investigations, additional test samples using the raw materials such as chitosan,

hydroxyapatite and fluorapatite alone as controls could provide a baseline antimicrobial properties of each materials in comparison to the developed scaffold composites.

Another preliminary *in vivo* trial was conducted for the implantation of CS/HAp/FAP scaffolds loaded with P28 peptide in the rat femoral condyle defect's model. This study aimed to provide evidence for rationale of the effect of changing the ceramic content and changing the P28 concentration to improve the *in vivo* biodegradability of the new scaffold formulations. A larger animal study was considered, however, due to the experimental nature of the work to respect the 3R principles of animal use (Replacement, Reduction and Refinement), a smaller preliminary study was carried out. As such this study was designed to narrow down the variables for future experiments (identifying the best CS, HAp and FAp ratio as well as the best concentration of P28).

Post-mortem observations indicate that most defects were observed to be closed with a layer of transparent tissue, while new bone growth was seen around the defects in the presence of P28 (12% HW CS/HAp/FAp 1:1/P28 25µg). Also, there was a possibility of ectopic growth seen in scaffolds with the highest content of P28 (12% HW CS/HAp/FAp 1:1/P28 150µg). The HE stain highlighted the thickened periosteum indicating a new bone formation in the scaffolds, where CS/HAp/FAp/P28 75 µg and CS/HAp/FAp/P28 150 µg showed the cortical and trabecular thickening as a result of implantation of composite in the region below the metaphysis. Subsequently, the CG and XO fluorochrome assessment indicated that CS/HAp/FAp 1:1 P28 150 µg scaffolds showed a high-intensity response to calcein green label, indicating mineralisation was ongoing 10 days prior to sacrifice. Similarly, the presence of double labelling which is indicative of ongoing mineralisation was observed at days 10 and four prior to sacrifice in the CS/HAp/FAp 1:1/P28 25 µg and CS/HAp/FAp/P28 75 µg. Based on the HE and fluorochrome label, CS/HAp/FAp 1:1 with P28 (especially in the 12% HW CS/HAp/FAp 1:1/P28 25 µg scaffold) showed some indications of new bone growth around the defects, but further investigations are needed to confirm the consistent positive osteoinductive effects following the implantation in the femoral condyle defects, and to rule out ectopic bone formation especially in the highest P28 content.

In conclusion, the research gaps mentioned in developing an off-the-shelf bone healing scaffold with controllable release of the active agents at a lower cost were successfully addressed in this study through the developed cell-free biodegradable scaffolds with

mechanical stability and antimicrobial feature. The key highlight of this study is the introduction of P28 peptide as the alternative to BMP-2, and its therapeutic effects in the improved bone scaffold formulations. While progresses have been made on the technical milestones, more studies are required to fully understand the therapeutic potential of this P28-loaded CS/HAp/FAp scaffold. Also, it is crucial to find the ideal dose and delivery technique in order to guarantee the P28 peptide's safety and effectiveness in people.

6.2 Future Work Recommendations

Several key points are recommended for future studies to address the limitations in the current research. Firstly in the scaffold development stage, the present scaffold formulations showed a relatively slow degradation profile, both *in vitro* and *in vivo*. However, the CS/FAp formulation showed an abrupt degradation from week 2 to week 4. Therefore, a more detailed investigations is needed to understand the reason behind this substantial degradation of CS/FAp. The chemistry in the material preparation (FAp) might also influence the reported behaviour in the SBF. It is also crucial to further tune the ratio between the polymer and bioceramics or introducing another material to speed up the degradation following the implantation. In addition, the effect of UV-crosslinking and pulsed-UV sterilisation method in the polymer structural changes and the osteogenicity of the protein and peptide should be further investigated. A reactive oxygen species (ROS) test which is crucial to avoid any adverse effects such as oxidative damage in the body following the implantation should be considered.

Subsequently, the current study has addressed its challenges in terms of utilising HPLC method for the protein and peptide release analyses due to the biomolecules' high affinity towards stainless steel hardware. Since the HPLC technique is pleasing for its low-cost and high sensitive feature in quantitating the protein and peptide at a low concentration, it is essential for the future study to develop a suitable method for osteogenic factor release analysis using an inert HPLC system in order to mitigate the aforementioned issues. A deeper understanding in terms of the chemistry of the biomolecules used in the study is also needed for an accurate and precise analyses. It was also realised that protein and peptides are biological components that can undergo non-specific reactions, including to the instruments' materials. Consequently, a collaboration with proteomics and biochemistry researchers is highly recommended since it was found very useful to understand the behaviour of the biomolecules.

Furthermore, the current work suggested the future experiments to use the freshly prepared and newly sterilised scaffolds in the *in vitro* cell culture as well as for the implantation stage to avoid any possibilities of the scaffolds being contaminated during storage. Therefore, it is also vital to find the best scaffold sterilisation method that can fully sterilise the scaffolds but does not compromising the bioactivity of the loaded osteogenic factors. A suitable storage method should also be further investigated to fulfil the intention of creating an off-the-shelf product. Additionally, this work outlines a preliminary investigation on the antimicrobial functionality of the composites, where chitosan was initially chosen for this reason. However, the antimicrobial capacity of this developed composite is not the main focus of this current work, hence it was not extensively investigated. Therefore, it is interesting to explore on this feature in the future work.

Although the experimental data achieved is useful to narrow down options regarding the use of P28, a larger animal studies is recommended to validate the research outcome from this pilot study. It is aware that P28 might not retain the original functionality of BMP-2, but P28 was found to remain osteogenic *in vitro* and *in vivo*. Therefore, it is still crucial to further optimising the concentration of P28 in the scaffolds to conclude the actual therapeutic dose of the osteogenic agents to ensure the safety and effectiveness of this product for the bone healing treatments in humans. In order to further benefit the animal trial conducted in the future, additional *ex vivo* tests are also suggested, namely the concentrations of the C-terminal peptide of type I collagen (CTX-1) as well as the nuclear factor of activated T-cells 1 (NFATc1) which are the bone resorption marker.

6.3 Invention Declaration

An invention declaration form was submitted, highlighting the osteogenicity of this developed device (RETAIN). Following the discussions with Synthes-DePuy, it was important that the final construct needed to have clean supply chains i.e. not based on BMP-2, since the researchers would have to purchase this product or they would have to set up and validate a costly system. Hence, P28 was selected as this peptide can be synthesised in a lab.

6.4 Commercial Feasibility Review for an Orthopaedic Scaffold

The scaffold developed in this thesis was sent to a commercial feasibility review for an orthopaedic scaffold conducted by KPMG Ireland. The review comprised of the technical and commercial assessment, as well as the future work suggested for this device to be able to be commercialised.

REFERENCES

- Abbasi, N., Hamlet, S., Love, R. M., & Nguyen, N. T. (2020). Porous scaffolds for bone regeneration. *Journal of Science: Advanced Materials and Devices*, 5(1), 1–9. <https://doi.org/10.1016/j.jsamd.2020.01.007>
- Abdallah, A. N., Shamaa, A. A., El-Tookhy, O. S., & Abd El-Mottaleb, E. M. (2016). Evaluation of low level laser-activated stromal vascular fraction as a single procedure for treatment of experimental chondral defects. *Asian Journal of Animal Sciences*, 10(1), 15–28. <https://doi.org/10.3923/ajas.2016.15.28>
- Abidin, I. Z., Rezoagli, E., Simonassi-Paiva, B., Fehrenbach, G. W., Masterson, K., Pogue, R., Cao, Z., Rowan, N., Murphy, E. J., & Major, I. (2020). A bilayer vaginal tablet for the localized delivery of disulfiram and 5-fluorouracil to the cervix. *Pharmaceutics*, 12(12), 1–21. <https://doi.org/10.3390/pharmaceutics12121185>
- AffshanaM., M., & Saveethna, J. (2015). Healing Mechanism in Bone Fracture. *Journal of Pharmaceutical Sciences and Research*, 7(7), 441–442.
- Ahn, C. B., & Je, J. Y. (2019). Bone health-promoting bioactive peptides. *Journal of Food Biochemistry*, 43(1). <https://doi.org/10.1111/jfbc.12529>
- Akiyama, S., Katagiri, T., Namiki, M., Yamaji, N., Yamamoto, N., Miyama, K., Shibuya, H., Ueno, N., Wozney, J. M., & Suda, T. (1997). Constitutively active BMP type I receptors transduce BMP-2 signals without the ligand in C2C12 myoblasts. *Experimental Cell Research*, 235(2), 362–369. <https://doi.org/10.1006/excr.1997.3680>
- Albulescu, R., Popa, A. C., Enciu, A. M., Albulescu, L., Dudau, M., Popescu, I. D., Mihai, S., Codrici, E., Pop, S., Lupu, A. R., Stan, G. E., Manda, G., & Tanase, C. (2019). Comprehensive in vitro testing of calcium phosphate-based bioceramics with orthopedic and dentistry applications. *Materials*, 12(22), 1–41. <https://doi.org/10.3390/ma12223704>
- Alghamdi, H. S., Van Den Beucken, J. J. J. P., & Jansen, J. A. (2014). Osteoporotic rat models for evaluation of osseointegration of bone implants. *Tissue Engineering - Part C: Methods*, 20(6), 493–505. <https://doi.org/10.1089/ten.tec.2013.0327>

- Alhazmi, A. S., Syame, S. M., Mohamed, W. S., & Hakim, A. S. (2022). Incorporation of Plant Extracted Hydroxyapatite and Chitosan Nanoparticles on the Surface of Orthodontic Micro-Implants: An In-Vitro Antibacterial Study. *Microorganisms*, *10*(3), 1–18. <https://doi.org/10.3390/microorganisms10030581>
- Alhilou, A., Do, T., Mizban, L., Clarkson, B. H., Wood, D. J., & Katsikogianni, M. G. (2016). Physicochemical and Antibacterial Characterization of a Novel Fluorapatite Coating. *ACS Omega*, *1*(2), 264–276. <https://doi.org/10.1021/acsomega.6b00080>
- Allushi, A., Kutahya, C., Aydogan, C., Kreutzer, J., Yilmaz, G., & Yagci, Y. (2017). Conventional Type II photoinitiators as activators for photoinduced metal-free atom transfer radical polymerization. *Polymer Chemistry*, *8*(12), 1972–1977. <https://doi.org/10.1039/c7py00114b>
- Alves, A., Wancket, L., & Metz, A. (2020). Current considerations in medical device pathology. In *Biocompatibility and Performance of Medical Devices* (Second Edn). Elsevier Ltd. <https://doi.org/10.1016/b978-0-08-102643-4.00020-3>
- Amariei, G., Kokol, V., Boltes, K., Letón, P., & Rosal, R. (2018). Incorporation of antimicrobial peptides on electrospun nanofibres for biomedical applications. *RSC Advances*, *8*(49), 28013–28023. <https://doi.org/10.1039/C8RA03861A>
- Amini, A. R., Laurencin, C. T., & Nukavarapu, S. P. (2012). Bone tissue engineering: Recent advances and challenges. *Critical Reviews in Biomedical Engineering*, *40*(5), 363–408. <https://doi.org/10.1615/CritRevBiomedEng.v40.i5.10>
- Anastasiou, A. D., Nerantzaki, M., Gounari, E., Duggal, M. S., Giannoudis, P. V., Jha, A., & Bikiaris, D. (2019). Antibacterial properties and regenerative potential of Sr²⁺ and Ce³⁺ doped fluorapatites; a potential solution for peri-implantitis. *Scientific Reports*, *9*(1), 1–11. <https://doi.org/10.1038/s41598-019-50916-4>
- Andrzejowski, P., & Giannoudis, P. V. (2019). The ‘diamond concept’ for long bone non-union management. *Journal of Orthopaedics and Traumatology*, *20*(1), 1–13. <https://doi.org/10.1186/s10195-019-0528-0>
- Anesi, A., Di Bartolomeo, M., Pellacani, A., Ferretti, M., Cavani, F., Salvatori, R., Nocini, R., Palumbo, C., & Chiarini, L. (2020). Bone Healing Evaluation

Following Different Osteotomic Techniques in Animal Models: A Suitable Method for Clinical Insights. *Applied Sciences*, 10(20), 1–28.
<https://doi.org/10.3390/app10207165>

Ansari, M. (2019). Bone tissue regeneration: biology, strategies and interface studies. *Progress in Biomaterials*, 8(4), 223–237. <https://doi.org/10.1007/s40204-019-00125-z>

Aranaz, I., Alcántara, A. R., Civera, M. C., Arias, C., Elorza, B., Caballero, A. H., & Acosta, N. (2021). Chitosan: An overview of its properties and applications. *Polymers*, 13(19). <https://doi.org/10.3390/polym13193256>

Arnold, P. M., Vaccaro, A. R., Sasso, R. C., Fehlings, M. G., & Kopjar, B. (2021). Six-year follow-up of i-FACTOR® peptide enhanced bone graft vs autograft in single level ACDF in a randomized single blinded FDA investigational device exemption study. *The Spine Journal*, 21(9), S203.
<https://doi.org/10.1016/j.spinee.2021.05.336>

Asplund, C. A. (2018a). *Midshaft femur fractures in adults*. UpToDate.

Asplund, C. A. (2018b). *Tibial shaft fractures in adults*. UpToDate.

Augat, P., Hollensteiner, M., & von Rüden, C. (2021). The role of mechanical stimulation in the enhancement of bone healing. *Injury*, 52, S78–S83.
<https://doi.org/10.1016/j.injury.2020.10.009>

Bachtiar, E. W., Amir, L. R., Suhardi, P., & Abas, B. (2016). Scaffold degradation during bone tissue reconstruction in *Macaca nemestrina* mandible. *Interventional Medicine and Applied Science*, 8(2), 77–81.
<https://doi.org/10.1556/1646.8.2016.2.5>

Bagheri, A., Fellows, C. M., & Boyer, C. (2021). Reversible Deactivation Radical Polymerization: From Polymer Network Synthesis to 3D Printing. *Advanced Science*, 8(5), 1–16. <https://doi.org/10.1002/advs.202003701>

Bahraminasab, M. (2020). Challenges on optimization of 3D-printed bone scaffolds. *BioMedical Engineering Online*, 19(1), 1–33. <https://doi.org/10.1186/s12938-020-00810-2>

Bai, X., Gao, M., Syed, S., Zhuang, J., Xu, X., & Zhang, X. Q. (2018). Bioactive

hydrogels for bone regeneration. *Bioactive Materials*, 3(4), 401–417.

<https://doi.org/10.1016/j.bioactmat.2018.05.006>

- Bain, J. L., Bonvallet, P. P., Abou-Arraj, R. V., Schupbach, P., Reddy, M. S., & Bellis, S. L. (2015). Enhancement of the Regenerative Potential of Anorganic Bovine Bone Graft Utilizing a Polyglutamate-Modified BMP2 Peptide with Improved Binding to Calcium-Containing Materials. *Tissue Engineering - Part A*, 21(17–18), 2426–2436. <https://doi.org/10.1089/ten.tea.2015.0160>
- Baker, E. A. (2016). *Enhancing Osseointegration of Orthopaedic Implants with Titania Nanotube Surfaces*. Michigan Technological University.
- Bandeira, M., Chee, B. S., Frassini, R., Nugent, M., Giovanela, M., Roesch-ely, M., Crespo, J. da S., & Devine, D. M. (2021). Antimicrobial paa/pah electrospun fiber containing green synthesized zinc oxide nanoparticles for wound healing. *Materials*, 14(11), 1–12. <https://doi.org/10.3390/ma14112889>
- Bandyopadhyay, A., Petersen, J., Fielding, G., Banerjee, S., & Bose, S. (2012). ZnO, SiO₂, and SrO doping in resorbable tricalcium phosphates: Influence on strength degradation, mechanical properties, and in vitro bone-cell material interactions. *Journal of Biomedical Materials Research Part B: Applied Biomaterials*, 100B(8), 2203–2212. <https://doi.org/10.1002/jbm.b.32789>
- Barcik, J., Ernst, M., Balligand, M., Dlaska, C. E., Drenchev, L., Zeiter, S., Epari, D. R., & Windolf, M. (2021). Short-term bone healing response to mechanical stimulation—a case series conducted on sheep. *Biomedicines*, 9(8), 1–11. <https://doi.org/10.3390/biomedicines9080988>
- Barroso, L. G. R., Azaman, F. A., Pogue, R., Devine, D., & Fournet, M. B. (2022). Monitoring In Vitro Extracellular Matrix Protein Conformations in the Presence of Biomimetic Bone-Regeneration Scaffolds Using Functionalized Gold-Edge-Coated Triangular Silver Nanoparticles. *Nanomaterials*, 13(57), 1–11.
- Baruffaldi, D., Palmara, G., Pirri, C., & Frascella, F. (2021). 3D Cell Culture: Recent Development in Materials with Tunable Stiffness. *ACS Applied Bio Materials*, 4(3), 2233–2250. <https://doi.org/10.1021/acsabm.0c01472>
- Becerra, J., Rodriguez, M., Leal, D., Noris-Suarez, K., & Gonzalez, G. (2022).

- Chitosan-collagen-hydroxyapatite membranes for tissue engineering. *Journal of Materials Science: Materials in Medicine*, 33(2), 1–16.
<https://doi.org/10.1007/s10856-022-06643-w>
- Bedeloğlu, E., Ersanlı, S., & Arisan, V. (2017). Vascular endothelial growth factor and biphasic calcium phosphate in the endosseous healing of femoral defects: An experimental rat study. *Journal of Dental Sciences*, 12(1), 7–13.
<https://doi.org/10.1016/j.jds.2016.04.005>
- Bejar, J., Peled, E., & Boss, J. H. (2005). Vasculature deprivation - Induced osteonecrosis of the rat femoral head as a model for therapeutic trials. *Theoretical Biology and Medical Modelling*, 2, 1–14. <https://doi.org/10.1186/1742-4682-2-24>
- Bergh, C., Wennergren, D., Möller, M., & Brisby, H. (2021). Fracture incidence in adults in relation to age and gender: A study of 27,169 fractures in the Swedish Fracture Register in a well-defined catchment area. *PLoS ONE*, 15(12 December), 1–18. <https://doi.org/10.1371/journal.pone.0244291>
- Bessa, P.C., Casal, M. and Reis, R. L. (2008). Bone morphogenetic proteins in tissue engineering: the road from laboratory to clinic, part II (BMP delivery). *Journal of Tissue Engineering and Regenerative Medicine*, 2(7), 81–96.
<https://doi.org/10.1002/term>
- Betsch, M., Schnependahl, J., Thuns, S., Hertel, M., Sager, M., Jungbluth, P., Hakimi, M., & Wild, M. (2013). Bone Marrow Aspiration Concentrate and Platelet Rich Plasma for Osteochondral Repair in a Porcine Osteochondral Defect Model. *PLoS ONE*, 8(8), 1–12. <https://doi.org/10.1371/journal.pone.0071602>
- Beyth, N., Farah, S., Domb, A. J., & Weiss, E. I. (2014). Antibacterial dental resin composites. *Reactive and Functional Polymers*, 75(1), 81–88.
<https://doi.org/10.1016/j.reactfunctpolym.2013.11.011>
- Bhushan, S., Singh, S., Maiti, T. K., Sharma, C., Dutt, D., Sharma, S., Li, C., & Tag Eldin, E. M. (2022). Scaffold Fabrication Techniques of Biomaterials for Bone Tissue Engineering: A Critical Review. *Bioengineering*, 9(12).
<https://doi.org/10.3390/bioengineering9120728>
- Biswas, D., Ray, L., & Halquist, M. (2019). Development and Validation of a Stability-

- Indicating Method for Bone Morphogenetic Protein-2. *Reviews in Separation Sciences*, 1(1), 3–16. <https://doi.org/10.17145/rss.19.002>
- Bjelić, D., & Finšgar, M. (2021). The role of growth factors in bioactive coatings. *Pharmaceutics*, 13(7), 1–30. <https://doi.org/10.3390/pharmaceutics13071083>
- Blackwood, K. A., Bock, N., Dargaville, T. R., & Ann Woodruff, M. (2012). Scaffolds for growth factor delivery as applied to bone tissue engineering. *International Journal of Polymer Science*, 2012, 1–25. <https://doi.org/10.1155/2012/174942>
- Blanchette, K. A., & Wenke, J. C. (2018). Current therapies in treatment and prevention of fracture wound biofilms: why a multifaceted approach is essential for resolving persistent infections. *Journal of Bone and Joint Infection*, 3(2), 50–67. <https://doi.org/10.7150/jbji.23423>
- Bonucci, E., & Ballanti, P. (2014). Osteoporosis—Bone Remodeling and Animal Models. *Toxicologic Pathology*, 42(6), 957–969. <https://doi.org/10.1177/0192623313512428>
- Borkowski, L., Przekora, A., Belcarz, A., Palka, K., Jojczuk, M., Lukasiewicz, P., Nogalski, A., & Ginalska, G. (2021). Highly porous fluorapatite/ β -1,3-glucan composite for bone tissue regeneration: Characterization and in vitro assessment of biomedical potential. *International Journal of Molecular Sciences*, 22(19), 1–18. <https://doi.org/10.3390/ijms221910414>
- Borkowski, L., Przekora, A., Belcarz, A., Palka, K., Jozefaciuk, G., Lübek, T., Jojczuk, M., Nogalski, A., & Ginalska, G. (2020). Fluorapatite ceramics for bone tissue regeneration: Synthesis, characterization and assessment of biomedical potential. *Materials Science and Engineering C*, 116(April), 1–10. <https://doi.org/10.1016/j.msec.2020.111211>
- Borok, M. J., Mademtoglou, D., & Relaix, F. (2020). Bu-M-P-ing iron: How BMP signaling regulates muscle growth and regeneration. *Journal of Developmental Biology*, 8(1), 1–14. <https://doi.org/10.3390/JDB8010004>
- Bouyer, M., Guillot, R., Lavaud, J., Plettinx, C., Olivier, C., Curry, V., Boutonnat, J., Coll, J. L., Peyrin, F., Jossierand, V., Bettega, G., & Picart, C. (2016). Surface delivery of tunable doses of BMP-2 from an adaptable polymeric scaffold induces

volumetric bone regeneration. *Biomaterials*, *104*, 168–181.

<https://doi.org/10.1016/j.biomaterials.2016.06.001>

Brennan, M. P., Sinusas, A. J., Horvath, T. L., Collins, J. G., & Harding, M. J. (2009). Correlation between body weight changes and postoperative pain in rats treated with meloxicam or buprenorphine. *Lab Animal*, *38*(3), 87–93.
<https://doi.org/10.1038/lab0309-87>

Briquez, P. S., Tsai, H. M., Watkins, E. A., & Hubbell, J. A. (2021). Engineered bridge protein with dual affinity for bone morphogenetic protein-2 and collagen enhances bone regeneration for spinal fusion. *Science Advances*, *7*(24).
<https://doi.org/10.1126/sciadv.abh4302>

Brun, P., Zamuner, A., Battocchio, C., Cassari, L., Todesco, M., Graziani, V., Iucci, G., Marsotto, M., Tortora, L., Secchi, V., & Dettin, M. (2021). Bio-functionalized chitosan for bone tissue engineering. *International Journal of Molecular Sciences*, *22*(11), 1–18. <https://doi.org/10.3390/ijms22115916>

Brydone, A. S., Meek, D., & MacLaine, S. (2010). Bone grafting, orthopaedic biomaterials, and the clinical need for bone engineering. *Proceedings of the Institution of Mechanical Engineers, Part H: Journal of Engineering in Medicine*, *224*(12), 1329–1343. <https://doi.org/10.1243/09544119JEIM770>

Bullock, G., Atkinson, J., Gentile, P., Hatton, P., & Miller, C. (2021). Osteogenic peptides and attachment methods determine tissue regeneration in modified bone graft substitutes. *Journal of Functional Biomaterials*, *12*(2), 1–24.
<https://doi.org/10.3390/jfb12020022>

Burger, E. H. (2004). *Resorbable Bone Cement Containing Active Agents* (Patent No. US 2004/0131678A1).

Burke, G., Cao, Z., Devine, D. M., & Major, I. (2019). Preparation of biodegradable polyethylene glycol dimethacrylate hydrogels via thiol-ene chemistry. *Polymers*, *11*(8), 1–18. <https://doi.org/10.3390/polym11081339>

Busch, A., Jäger, M., Mayer, C., & Sowislok, A. (2021). Functionalization of synthetic bone substitutes. *International Journal of Molecular Sciences*, *22*(9), 1–12.
<https://doi.org/10.3390/ijms22094412>

- Cai, Y., Tong, S., Zhang, R., Zhu, T., & Wang, X. (2018). In vitro evaluation of a bone morphogenetic protein-2 nanometer hydroxyapatite collagen scaffold for bone regeneration. In *Molecular Medicine Reports* (Vol. 17, Issue 4, pp. 5830–5836). <https://doi.org/10.3892/mmr.2018.8579>
- Calori, G. M., & Giannoudis, P. V. (2011). Enhancement of fracture healing with the diamond concept: The role of the biological chamber. *Injury*, *42*(11), 1191–1193. <https://doi.org/10.1016/j.injury.2011.04.016>
- Campillo, M., Lacharmoise, P. D., Reparaz, J. S., Goñi, A. R., & Valiente, M. (2010). On the assessment of hydroxyapatite fluoridation by means of Raman scattering. *Journal of Chemical Physics*, *132*(24), 2–6. <https://doi.org/10.1063/1.3428556>
- Canillas, M., De Lima, G. G., Rodríguez, M. A., Nugent, M. J. D., & Devine, D. M. (2016). Bioactive composites fabricated by freezing-thawing method for bone regeneration applications. *Journal of Polymer Science, Part B: Polymer Physics*, *54*(7), 761–773. <https://doi.org/10.1002/polb.23974>
- Cao, S., Han, J., Sharma, N., Msallem, B., Jeong, W., Son, J., Kunz, C., Kang, H. W., & Thieringer, F. M. (2020). In vitro mechanical and biological properties of 3D printed polymer composite and β -tricalcium phosphate scaffold on human dental pulp stem cells. *Materials*, *13*(14), 1–14. <https://doi.org/10.3390/ma13143057>
- Chang, F.-C., Tsao, C.-T., Lin, A., Zhang, M., Levensgood, S., & Zhang, M. (2016). PEG-Chitosan Hydrogel with Tunable Stiffness for Study of Drug Response of Breast Cancer Cells. *Polymers*, *8*(4), 1–13. <https://doi.org/10.3390/polym8040112>
- Chao, Y. L., Lin, L. D., Chang, H. H., & Wang, T. M. (2021). Preliminary evaluation of BMP-2-derived peptide in repairing a peri-implant critical size defect: A canine model. *Journal of the Formosan Medical Association*, *120*(5), 1212–1220. <https://doi.org/10.1016/j.jfma.2020.07.023>
- Chatzipetros, E., Christopoulos, P., Donta, C., Tosios, K. I., Tsi-Ambas, E., Tsiourvas, D., Kalogirou, E. M., & Tsiklakis, K. (2018). Application of nano-hydroxyapatite/chitosan scaffolds on rat calvarial critical-sized defects: A pilot study. *Medicina Oral Patologia Oral y Cirugia Bucal*, *23*(5), e625–e632. <https://doi.org/10.4317/medoral.22455>

- Chen, H., Sun, K., Tang, Z., Law, R. V., Mansfield, J. F., Czajka-Jakubowska, A., & Clarkson, B. H. (2006). Synthesis of fluorapatite nanorods and nanowires by direct precipitation from solution. *Crystal Growth and Design*, 6(6), 1504–1508. <https://doi.org/10.1021/cg0600086>
- Chen, J., Garcia, E. S., & Zimmerman, S. C. (2020). Intramolecularly Cross-Linked Polymers: From Structure to Function with Applications as Artificial Antibodies and Artificial Enzymes. *Accounts of Chemical Research*, 53(6), 1244–1256. <https://doi.org/10.1021/acs.accounts.0c00178>
- Chen, L., Liu, J., Guan, M., Zhou, T., Duan, X., & Xiang, Z. (2020). Growth factor and its polymer scaffold-based delivery system for cartilage tissue engineering. *International Journal of Nanomedicine*, 15, 6097–6111. <https://doi.org/10.2147/IJN.S249829>
- Chen, X., Zhao, Y., Geng, S., Miron, R. J., Zhang, Q., Wu, C., & Zhang, Y. (2015). In vivo experimental study on bone regeneration in critical bone defects using PIB nanogels/boron-containing mesoporous bioactive glass composite scaffold. *International Journal of Nanomedicine*, 10, 839–846. <https://doi.org/10.2147/IJN.S69001>
- Chen, X., Zhou, R., Chen, B., & Chen, J. (2016). Nanohydroxyapatite/cellulose nanocrystals/silk fibroin ternary scaffolds for rat calvarial defect regeneration. *RSC Advances*, 6(42), 35684–35691. <https://doi.org/10.1039/c6ra02038k>
- Chen, Y. (2018). *Development and in vitro evaluation of PLA/HNT based biodegradable composites for use in coronary stents* (Issue January).
- Chen, Y., Cavalcanti De Sá, M. J., Dalton, M., & Devine, D. M. (2019). Biodegradable medical implants. In G. Perale & J. Hilborn (Eds.), *Bioresorbable Polymers and their Biomedical Applications* (First, pp. 17–46). Woodhead Publishing Series in Biomaterials. <https://doi.org/10.1515/9783110640571-002>
- Chen, Y., Liu, X., Liu, R., Gong, Y., Wang, M., Huang, Q., Feng, Q., & Yu, B. (2017). Zero-order controlled release of BMP2-derived peptide P24 from the chitosan scaffold by chemical grafting modification technique for promotion of osteogenesis in vitro and enhancement of bone repair in vivo. *Theranostics*, 7(5), 1072–1087. <https://doi.org/10.7150/thno.18193>

- Chen, Y., Whetstone, H. C., Youn, A., Nadesan, P., Chow, E. C. Y., Lin, A. C., & Alman, B. A. (2007). β -Catenin signaling pathway is crucial for bone morphogenetic protein 2 to induce new bone formation. *Journal of Biological Chemistry*, 282(1), 526–533. <https://doi.org/10.1074/jbc.M602700200>
- Chitnis, A., Ray, B., Sparks, C., Grebenyuk, Y., Vanderkarr, M., & Holy, C. E. (2020). Long bone fractures: treatment patterns and factors contributing to use of intramedullary nailing. *Expert Review of Medical Devices*, 17(7), 731–738. <https://doi.org/10.1080/17434440.2020.1779055>
- Chiyindiko, E., & Conradie, J. (2021). An electrochemical and computational chemistry study of substituted benzophenones. *Electrochimica Acta*, 373, 137894. <https://doi.org/10.1016/j.electacta.2021.137894>
- Choi, G., & Cha, H. J. (2019). Recent advances in the development of nature-derived photocrosslinkable biomaterials for 3D printing in tissue engineering. *Biomaterials Research*, 23(1), 1–7. <https://doi.org/10.1186/s40824-019-0168-8>
- Choi, S. M., Chaudhry, P., Zo, S. M., & Han, S. S. (2018). Cutting-Edge Enabling Technologies for Regenerative Medicine. In *Cutting-Edge Enabling Technologies for Regenerative Medicine. Advances in Experimental Medicine and Biology*. (Vol. 1078). <https://doi.org/10.1007/978-981-13-0950-2>
- Choy, C. S., Lee, W. F., Lin, P. Y., Wu, Y. F., Huang, H. M., Teng, N. C., Pan, Y. H., Salamanca, E., & Chang, W. J. (2021). Surface Modified β -Tricalcium phosphate enhanced stem cell osteogenic differentiation in vitro and bone regeneration in vivo. *Scientific Reports*, 11(1), 1–14. <https://doi.org/10.1038/s41598-021-88402-5>
- Ciechacka, A. (2011). *Analysis and Characterisation of an Acylphosphine Oxide Photoinitiator*.
- Costa-Pinto, A. R., Lemos, A. L., Tavarina, F. K., & Pintado, M. (2021). Chitosan and hydroxyapatite based biomaterials to circumvent periprosthetic joint infections. *Materials*, 14(4), 1–20. <https://doi.org/10.3390/ma14040804>
- Cui, W., Liu, Q., Yang, L., Wang, K., Sun, T., Ji, Y., Liu, L., Yu, W., Qu, Y., Wang, J., Zhao, Z., Zhu, J., & Guo, X. (2018). Sustained Delivery of BMP-2-Related Peptide from the True Bone Ceramics/Hollow Mesoporous Silica Nanoparticles Scaffold

for Bone Tissue Regeneration. *ACS Biomaterials Science and Engineering*, 4(1), 211–221. <https://doi.org/10.1021/acsbiomaterials.7b00506>

Cui, W., Sun, G., Qu, Y., Xiong, Y., Sun, T., Ji, Y., Yang, L., Shao, Z., Ma, J., Zhang, S., & Guo, X. (2016). Repair of rat calvarial defects using Si-doped hydroxyapatite scaffolds loaded with a bone morphogenetic protein-2-related peptide. *Journal of Orthopaedic Research*, 34(11), 1874–1882. <https://doi.org/10.1002/jor.23208>

Czekańska, E. M. (2014). *In vitro cell and culture models for osteoblasts and their progenitors*. April.

Dai, Z., Ronholm, J., Tian, Y., Sethi, B., & Cao, X. (2016). Sterilization techniques for biodegradable scaffolds in tissue engineering applications. *Journal of Tissue Engineering*, 7, 204173141664881. <https://doi.org/10.1177/2041731416648810>

Davidenko, N., Bax, D. V., Schuster, C. F., Farndale, R. W., Hamaia, S. W., Best, S. M., & Cameron, R. E. (2016). Optimisation of UV irradiation as a binding site conserving method for crosslinking collagen-based scaffolds. *Journal of Materials Science: Materials in Medicine*, 27(1), 1–17. <https://doi.org/10.1007/s10856-015-5627-8>

de Azevedo e Sousa Munhoz, M., Pomini, K. T., de Guzzi Plepis, A. M., da Conceição Amaro Martins, V., Machado, E. G., de Moraes, R., Cunha, F. B., Santos, A. R., Cardoso, G. B. C., Duarte, M. A. H., Alcalde, M. P., Buchaim, D. V., Buchaim, R. L., & da Cunha, M. R. (2020). Elastin-derived scaffolding associated or not with bone morphogenetic protein (BMP) or hydroxyapatite (HA) in the repair process of metaphyseal bone defects. *PLoS ONE*, 15(4), 1–21. <https://doi.org/10.1371/journal.pone.0231112>

De Gorter, D. J. J., Van Dinther, M., & Ten Dijke, P. (2010). Measurement of constitutive activity of BMP type I receptors. In *Methods in Enzymology* (1st ed., Vol. 484, Issue C). Elsevier Inc. <https://doi.org/10.1016/B978-0-12-381298-8.00015-0>

De Mori, A., Hafidh, M., Mele, N., Yusuf, R., Cerri, G., Gavini, E., Tozzi, G., Barbu, E., Conconi, M., Draheim, R. R., & Roldo, M. (2019). Sustained release from injectable composite gels loaded with silver nanowires designed to combat bacterial resistance in bone regeneration applications. *Pharmaceutics*, 11(3), 1–19.

<https://doi.org/10.3390/pharmaceutics11030116>

- De Vlam, K., Lories, R. J. U., & Luyten, F. P. (2006). Mechanisms of pathologic new bone formation. *Current Rheumatology Reports*, 8(5), 332–337.
<https://doi.org/10.1007/s11926-006-0061-z>
- De Witte, T.-M., Fratila-Apachitei, L. E., Zadpoor, A. A., & Peppas, N. A. (2018). Bone tissue engineering via growth factor delivery: from scaffolds to complex matrices. *Regenerative Biomaterials*, June, 197–211.
<https://doi.org/10.1093/rb/rby013>
- De Witte, T. M., Wagner, A. M., Fratila-Apachitei, L. E., Zadpoor, A. A., & Peppas, N. A. (2020). Immobilization of nanocarriers within a porous chitosan scaffold for the sustained delivery of growth factors in bone tissue engineering applications. *Journal of Biomedical Materials Research - Part A*, 108(5), 1122–1135.
<https://doi.org/10.1002/jbm.a.36887>
- Dehghani, F., & Annabi, N. (2011). Engineering porous scaffolds using gas-based techniques. *Current Opinion in Biotechnology*, 22(5), 661–666.
<https://doi.org/10.1016/j.copbio.2011.04.005>
- Della Sala, F., Biondi, M., Guarnieri, D., Borzacchiello, A., Ambrosio, L., & Mayol, L. (2020). Mechanical behavior of bioactive poly(ethylene glycol) diacrylate matrices for biomedical application. *Journal of the Mechanical Behavior of Biomedical Materials*, 110(December 2019), 1–9.
<https://doi.org/10.1016/j.jmbbm.2020.103885>
- Dempster, D. W., Compston, J. E., Drezner, M. K., Kanis, F. H. G., John A Malluche, Ott, S., Malluche, H., M, P. J. M., Recker, R. R., & Parfitt, M. (2014). Histomorphometry Nomenclature: A 2012 Update of the Report of the ASBMR Histomorphometry Nomenclature David. *Journal of Bone and Mineral Research*, 28(1), 2–17. <https://doi.org/10.1002/jbmr.1805>.Standardized
- Devine, D. M., & Higginbotham, C. L. (2005). Synthesis and characterisation of chemically crosslinked N-vinyl pyrrolidinone (NVP) based hydrogels. *European Polymer Journal*, 41(6), 1272–1279.
<https://doi.org/10.1016/j.eurpolymj.2004.12.022>

- Devine, D. M., & Higginbotham, C. L. (2006). *Synthesis and Characterisation of Novel N-Vinyl Pyrrolidinone/Acrylic Acid Copolymers for Use in Biomedical Applications* (Issue August).
- Devine, D. M., Hooctor, E., Hayes, J. S., Sheehan, E., & Evans, C. H. (2017). Extended release of proteins following encapsulation in hydroxyapatite/chitosan composite scaffolds for bone tissue engineering applications. *Materials Science and Engineering C, November*, 1–9. <https://doi.org/10.1016/j.msec.2017.11.001>
- Dimitriou, R., Tsiridis, E., & Giannoudis, P. V. (2005). Current concepts of molecular aspects of bone healing. *Injury, 36*(12), 1392–1404. <https://doi.org/10.1016/j.injury.2005.07.019>
- Dittmer, K. E., & Firth, E. C. (2017). Mechanisms of bone response to injury. *Journal of Veterinary Diagnostic Investigation, 29*(4), 385–395. <https://doi.org/10.1177/1040638716679861>
- Dixon, D. T., & Gomillion, C. T. (2022). Conductive scaffolds for bone tissue engineering: Current state and future outlook. *Journal of Functional Biomaterials, 13*(1), 1–23. <https://doi.org/10.3390/jfb13010001>
- Dolan, J. W. (2008). System Suitability. *LC.GC Europe, 2–4*. <https://doi.org/10.1002/lcgc.200800004>
- Donnalaja, F., Jacchetti, E., Soncini, M., & Raimondi, M. T. (2020). Natural and synthetic polymers for bone scaffolds optimization. *Polymers, 12*(4), 1–27. <https://doi.org/10.3390/POLYM12040905>
- Dorati, R., DeTrizio, A., Modena, T., Conti, B., Benazzo, F., Gastaldi, G., & Genta, I. (2017). Biodegradable scaffolds for bone regeneration combined with drug-delivery systems in osteomyelitis therapy. *Pharmaceuticals, 10*(4), 1–21. <https://doi.org/10.3390/ph10040096>
- Draenert, F. G., Nonnenmacher, A. L., Kämmerer, P. W., Goldschmitt, J., & Wagner, W. (2013). BMP-2 and bFGF release and in vitro effect on human osteoblasts after adsorption to bone grafts and biomaterials. *Clinical Oral Implants Research, 24*(7), 750–757. <https://doi.org/10.1111/j.1600-0501.2012.02481.x>
- Durham, E. L., Howie, R. N., Hall, S., Larson, N., Oakes, B., Houck, R., Grey, Z.,

- Steed, M., Larue, A. C., Muise-Helmericks, R., & Cray, J. (2018). Optimizing bone wound healing using BMP2 with absorbable collagen sponge and Talymed nanofiber scaffold. *Journal of Translational Medicine*, *16*(1), 1–8.
<https://doi.org/10.1186/s12967-018-1697-y>
- Durham, E. L., Kishinchand, R., Grey, Z. J., & Cray, J. J. (2020). rhBMP2 alone does not induce macrophage polarization towards an increased inflammatory response. *Molecular Immunology*, *117*(October 2019), 94–100.
<https://doi.org/10.1016/j.molimm.2019.10.021>
- e Silva, E. P., Huang, B., Helachil, J. V., Nalesso, P. R. L., Bagne, L., de Oliveira, M. A., Albiazetti, G. C. C., Aldabahi, A., El-Newehy, M., Santamaria-Jr, M., Mendonça, F. A. S., Bártolo, P., & Caetano, G. F. (2021). In vivo study of conductive 3D printed PCL/MWCNTs scaffolds with electrical stimulation for bone tissue engineering. *Bio-Design and Manufacturing*, *4*(2), 190–202.
<https://doi.org/10.1007/s42242-020-00116-1>
- Einhorn, T. A., & Gerstenfeld, L. C. (2015). Fracture healing: Mechanisms and interventions. *Nature Reviews Rheumatology*, *11*(1), 45–54.
<https://doi.org/10.1038/nrrheum.2014.164>
- El-fiqi, A., Kim, J., Bang, S., El-fiqi, A., & Kim, H. (2013). Fabrication of nanofibrous macroporous scaffolds of poly (lactic acid) incorporating bioactive glass nanoparticles by camphene-assisted phase separation Fabrication of nano fi brous macroporous scaffolds of poly (lactic acid) incorporating bioactive g. *Materials Chemistry and Physics*, *143*(3), 1092–1101.
<https://doi.org/10.1016/j.matchemphys.2013.11.009>
- El Bialy, I., Jiskoot, W., & Reza Nejadnik, M. (2017). Formulation, Delivery and Stability of Bone Morphogenetic Proteins for Effective Bone Regeneration. *Pharmaceutical Research*, *34*(6), 1152–1170. <https://doi.org/10.1007/s11095-017-2147-x>
- Elakkiya, S., Ramesh, A. S., & Prabhu, K. (2017). Systematic analysis on the efficacy of bone enhancement methods used for success in dental implants. *The Journal of Indian Prosthodontic Society*, *19*(1), 219–225. <https://doi.org/10.4103/jips.jips>
- Erben, R. G. (2003). Bone-Labeling Techniques. In Y. H. An & K. L. Martin (Eds.),

Handbook of Histology Methods for Bone and Cartilage (1st ed., pp. 99–117). Humana Press, Totowa, NJ. https://doi.org/https://doi.org/10.1007/978-1-59259-417-7_5

Ercal, P., & Pekozer, G. G. (2020). A current overview of scaffold-based bone regeneration strategies with dental stem cells. *Advances in Experimental Medicine and Biology*, 1288, 61–85. https://doi.org/10.1007/5584_2020_505

European Collection of Authenticated Cell Cultures, E. (2019). *General Cell Collection_91031101 C2C12*. https://www.culturecollections.org.uk/products/celllines/generalcell/detail.jsp?refId=91031101&collection=ecacc_gc

Feng, P., Wei, P., Shuai, C., & Peng, S. (2014). Characterization of mechanical and biological properties of 3-D scaffolds reinforced with zinc oxide for bone tissue engineering. *PLoS ONE*, 9(1). <https://doi.org/10.1371/journal.pone.0087755>

Feng, T., Niu, J., Pi, B., Lu, Y., Wang, J., Zhang, W., Li, B., Yang, H., & Zhu, X. (2020). Osteogenesis enhancement of silk fibroin/ α -TCP cement by N-acetyl cysteine through Wnt/ β -catenin signaling pathway in vivo and vitro. *Journal of the Mechanical Behavior of Biomedical Materials*, 101(September 2018), 103451. <https://doi.org/10.1016/j.jmbbm.2019.103451>

Fern, H. W., & Salimi, M. N. (2021). Hydroxyapatite nanoparticles produced by direct precipitation method: Optimization and characterization studies. *AIP Conference Proceedings*, 2339(May), 1–9. <https://doi.org/10.1063/5.0044252>

Fernandez-Yague, M. A., Abbah, S. A., McNamara, L., Zeugolis, D. I., Pandit, A., & Biggs, M. J. (2015). Biomimetic approaches in bone tissue engineering: Integrating biological and physicommechanical strategies. *Advanced Drug Delivery Reviews*, 84, 1–29. <https://doi.org/10.1016/j.addr.2014.09.005>

Fernández, M. P. R., Gehrke, S. A., Martinez, C. P. A., Guirado, J. L. C., & de Aza, P. N. (2017). SEM-EDX study of the degradation process of two xenograft materials used in sinus lift procedures. *Materials*, 10(5), 1–19. <https://doi.org/10.3390/ma10050542>

Fields, K. B. (2018). *Overview of tibial fractures in adults Author: Karl B Fields*.

- Foster, A. L., Moriarty, T. F., Zalavras, C., Morgenstern, M., Jaiprakash, A., Crawford, R., Burch, M. A., Boot, W., Tetsworth, K., Miclau, T., Ochsner, P., Schuetz, M. A., Richards, R. G., & Metsemakers, W. J. (2021). The influence of biomechanical stability on bone healing and fracture-related infection: the legacy of Stephan Perren. *Injury*, *52*(1), 43–52. <https://doi.org/10.1016/j.injury.2020.06.044>
- Fourie, J., Taute, F., du Preez, L., & de Beer, D. (2022). Chitosan Composite Biomaterials for Bone Tissue Engineering—a Review. *Regenerative Engineering and Translational Medicine*, *8*(1), 1–21. <https://doi.org/10.1007/s40883-020-00187-7>
- Fournet, M. E. B., Alwani, F., Gunbay, S., Chen, Y. Y., & Devine, D. M. (2019). Orthopedic 3D Printing in Orthopedic Medicine. In D. M. Devine (Ed.), *Polymer-Based Additive Manufacturing: Biomedical Application* (pp. 121–142). Springer, Cham. https://doi.org/https://doi.org/10.1007/978-3-030-24532-0_6
- Fu, C., Yang, X., Tan, S., & Song, L. (2017). Enhancing Cell Proliferation and Osteogenic Differentiation of MC3T3-E1 Pre-osteoblasts by BMP-2 Delivery in Graphene Oxide-Incorporated PLGA/HA Biodegradable Microcarriers. *Scientific Reports*, *7*(1), 1–13. <https://doi.org/10.1038/s41598-017-12935-x>
- Fu, R., Feng, Y., Liu, Y., Willie, B. M., & Yang, H. (2022). The combined effects of dynamization time and degree on bone healing. *Journal of Orthopaedic Research*, *40*(3), 634–643. <https://doi.org/10.1002/jor.25060>
- Galindo, T. G. P., Chai, Y., & Tagaya, M. (2019). Hydroxyapatite nanoparticle coating on polymer for constructing effective biointeractive interfaces. *Journal of Nanomaterials*, *2019*. <https://doi.org/10.1155/2019/6495239>
- Gao, L., Goebel, L. K. H., Orth, P., Cucchiari, M., & Madry, H. (2018). Subchondral drilling for articular cartilage repair: A systematic review of translational research. *DMM Disease Models and Mechanisms*, *11*(6). <https://doi.org/10.1242/dmm.034280>
- Garcia, E. L., Attallah, O. A., Mojicevic, M., Devine, D. M., & Fournet, M. B. (2021). Antimicrobial active bioplastics using triangular silver nanoplate integrated polycaprolactone and polylactic acid films. *Materials*, *14*(5), 1–15. <https://doi.org/10.3390/ma14051132>

- Ghassemi, T., Shahroodi, A., Ebrahimzadeh, M. H., Mousavian, A., Movaffagh, J., & Moradi, A. (2018). Current concepts in scaffolding for bone tissue engineering. *Archives of Bone and Joint Surgery*, *6*(2), 90–99. <https://doi.org/10.22038/abjs.2018.26340.1713>
- Gherasim, O., Grumezescu, A. M., Grumezescu, V., Negut, I., Dumitrescu, M. F., Stan, M. S., Nica, I. C., Holban, A. M., Socol, G., & Andronescu, E. (2021). Bioactive coatings based on hydroxyapatite, kanamycin, and growth factor for biofilm modulation. *Antibiotics*, *10*(2), 1–19. <https://doi.org/10.3390/antibiotics10020160>
- Ghiacci, G., Graiani, G., Ravanetti, F., Lumetti, S., Manfredi, E., Galli, C., Cacchioli, A., Macaluso, G. M., & Sala, R. (2016). “Over-inlay” block graft and differential morphometry: A novel block graft model to study bone regeneration and host-to-graft interfaces in rats. *Journal of Periodontal and Implant Science*, *46*(4), 220–233. <https://doi.org/10.5051/jpis.2016.46.4.220>
- Ghiasi, M. S., Chen, J., Vaziri, A., Rodriguez, E. K., & Nazarian, A. (2017). Bone fracture healing in mechanobiological modeling: A review of principles and methods. *Bone Reports*, *6*, 87–100. <https://doi.org/10.1016/j.bonr.2017.03.002>
- Gimble, J. M., Morgan, C., Kelly, K., Wu, X., Dandapani, V., Wang, C. -S, & Rosen, V. (1995). Bone morphogenetic proteins inhibit adipocyte differentiation by bone marrow stromal cells. *Journal of Cellular Biochemistry*, *58*(3), 393–402. <https://doi.org/10.1002/jcb.240580312>
- Glatt, V., Evans, C. H., & Tetsworth, K. (2021). Reverse dynamisation: A modern perspective on stephan perren’s strain theory. *European Cells and Materials*, *41*, 668–679. <https://doi.org/10.22203/eCM.v041a43>
- Gleeson, J. P., Plunkett, N. A., & O’Brien, F. J. (2010). Addition of hydroxyapatite improves stiffness, interconnectivity and osteogenic potential of a highly porous collagen-based scaffold for bone tissue regeneration. *European Cells and Materials*, *20*(July), 218–230. <https://doi.org/10.22203/eCM.v020a18>
- Goharian, A. (2019). Fundamentals in Loosening and Osseointegration of Orthopedic Implants. In *Osseointegration of Orthopaedic Implants* (pp. 1–26). Elsevier Inc. <https://doi.org/10.1016/b978-0-12-813384-2.00001-1>

- Goldschlager, T., Abdelkader, A., Kerr, J., Boundy, I., & Jenkin, G. (2010). Undecalcified bone preparation for histology, histomorphometry and fluorochrome analysis. *Journal of Visualized Experiments*, 35, 1–3. <https://doi.org/10.3791/1707>
- Govoni, M., Vivarelli, L., Mazzotta, A., Stagni, C., Maso, A., & Dallari, D. (2021). Commercial bone grafts claimed as an alternative to autografts: Current trends for clinical applications in orthopaedics. *Materials*, 14(12), 1–19. <https://doi.org/10.3390/ma14123290>
- Grabska-Zielińska, S., Sionkowska, A., Reczyńska, K., & Pamuła, E. (2020). Physico-chemical characterization and biological tests of collagen/silk fibroin/chitosan scaffolds cross-linked by dialdehyde starch. *Polymers*, 12(2), 1–13. <https://doi.org/10.3390/polym12020372>
- Granke, M., Does, M. D., & Nyman, J. S. (2015). The Role of Water Compartments in the Material Properties of Cortical Bone. *Calcified Tissue International*, 97(3), 292–307. <https://doi.org/10.1007/s00223-015-9977-5>
- Greenwald, A. S., Boden, S. D., Barrack, R. L., Bostrom, M. P. G., Goldberg, V. M., Yazemski, M. J., & Heim, C. S. (2010). The Evolving Role of Bone-Graft Substitutes. *American Academy of Orthopaedic Surgeons*, 83, 98–103.
- Gruber, H. E., & In, J. A. (2003). Basic Staining and Histochemical Techniques and Immunohistochemical Localizations Using Bone Sections. In Y. H. An & K. L. Martin (Eds.), *Handbook of Histology Methods for Bone and Cartilage* (1st ed., pp. 281–286). Humana Press, Totowa, NJ. https://doi.org/https://doi.org/10.1007/978-1-59259-417-7_21
- Gudivada, V. N., Huang, C. J., Luo, Y. H., & Dong, G. C. (2021). A cyclic bmp-2 peptide upregulates bmp-2 protein-induced cell signaling in myogenic cells. *Polymers*, 13(15), 1–11. <https://doi.org/10.3390/polym13152549>
- Guler, E., Baripoglu, Y. E., Alenezi, H., Arikan, A., Babazade, R., Unal, S., Duruksu, G., Alfares, F. S., Yazir, Y., Oktar, F. N., Gunduz, O., Edirisinghe, M., & Cam, M. E. (2021). Vitamin D3/vitamin K2/magnesium-loaded polylactic acid/tricalcium phosphate/polycaprolactone composite nanofibers demonstrated osteoinductive effect by increasing Runx2 via Wnt/ β -catenin pathway. *International Journal of Biological Macromolecules*, 190(August), 244–258.

<https://doi.org/10.1016/j.ijbiomac.2021.08.196>

Guo, T., Li, Y., Cao, G., Zhang, Z., Chang, S., Czajka-Jakubowska, A., Nör, J. E., Clarkson, B. H., & Liu, J. (2014). Fluorapatite-modified scaffold on dental pulp stem cell mineralization. *Journal of Dental Research*, *93*(12), 1290–1295.

<https://doi.org/10.1177/0022034514547914>

Halloran, D., Vratsha, V., Durbano, H. W., & Nohe, A. (2020). Bone morphogenetic protein-2 conjugated to quantum dot@s is biologically functional. *Nanomaterials*, *10*(6), 1–13. <https://doi.org/10.3390/nano10061208>

Hamilton, P. T., Jansen, M. S., Ganesan, S., Benson, R. E., Hyde-DeRuyscher, R., Beyer, W. F., Gile, J. C., Nair, S. A., Hodges, J. A., & Grøn, H. (2013). Improved Bone Morphogenetic Protein-2 Retention in an Injectable Collagen Matrix Using Bifunctional Peptides. *PLoS ONE*, *8*(8), 1–10.

<https://doi.org/10.1371/journal.pone.0070715>

Hao, Z., Li, H., Wang, Y., Hu, Y., Chen, T., Zhang, S., Guo, X., Cai, L., & Li, J. (2022). Supramolecular Peptide Nanofiber Hydrogels for Bone Tissue Engineering: From Multihierarchical Fabrications to Comprehensive Applications. *Advanced Science*, *9*(11), 1–36. <https://doi.org/10.1002/advs.202103820>

Harada, K., Itoh, H., Kawazoe, Y., Miyazaki, S., Doi, K., Kubo, T., Akagawa, Y., & Shiba, T. (2013). Polyphosphate-mediated inhibition of tartrate-resistant acid phosphatase and suppression of bone resorption of osteoclasts. *PLoS ONE*, *8*(11), 1–6. <https://doi.org/10.1371/journal.pone.0078612>

Harugade, A., Sherje, A. P., & Pethe, A. (2023). Chitosan : A review on properties , biological activities and recent progress in biomedical applications. *Reactive and Functional Polymers*, *191*(May 2022), 105634.

<https://doi.org/10.1016/j.reactfunctpolym.2023.105634>

Hasirci, V., Huri, P. Y., Tanir, T. E., Eke, G., & Hasirci, N. (2017). Polymer fundamentals: Polymer synthesis. In *Comprehensive Biomaterials II* (Vol. 1, Issue June 2016, pp. 478–506). <https://doi.org/10.1016/B978-0-12-803581-8.10208-5>

Haubruck, P., Kammerer, A., Korff, S., Apitz, P., Xiao, K., Bichler, A., Biglari, B., Zimmermann, G., Daniel, V., Schmidmaier, G., & Moghaddam, A. (2016). The

treatment of nonunions with application of BMP-7 increases the expression pattern for angiogenic and inflammable cytokines: A matched pair analysis. *Journal of Inflammation Research*, 9, 155–165. <https://doi.org/10.2147/JIR.S110621>

He, Y., Jin, Y., Wang, X., Yao, S., Li, Y., Wu, Q., Ma, G., Cui, F., & Liu, H. (2018). An Antimicrobial Peptide-Loaded Gelatin/Chitosan Nanofibrous Membrane Fabricated by Sequential Layer-by-Layer Electrospinning and Electrospraying Techniques. *Nanomaterials (Basel)*, 8(5), 1–13. <https://doi.org/10.3390/nano8050327>

Helgers, S. O. A., Talbot, S. R., Riedesel, A. K., Wassermann, L., Wu, Z., Krauss, J. K., Häger, C., Bleich, A., & Schwabe, K. (2020). Body weight algorithm predicts humane endpoint in an intracranial rat glioma model. *Scientific Reports*, 10(1), 1–10. <https://doi.org/10.1038/s41598-020-65783-7>

Henkel, J. (2017). *Bone Tissue Engineering in Two Preclinical Ovine Animal Models*. Queensland University of Technology.

Hernandez, E., Robles-Vazquez, O., Orozco-Avila, I., & Sánchez-Díaz, J. (2016). An Overview of Mechanical Tests for Polymeric Biomaterial Scaffolds Used in Tissue Engineering. *Journal of Research Updates in Polymer Science*, 4(4), 168–178. <https://doi.org/10.6000/1929-5995.2015.04.04.1>

Hettiaratchi, M. H., Krishnan, L., Rouse, T., Chou, C., McDevitt, T. C., & Guldberg, R. E. (2020). Heparin-mediated delivery of bone morphogenetic protein-2 improves spatial localization of bone regeneration. *Science Advances*, 6(1), 1–12. <https://doi.org/10.1126/sciadv.aay1240>

Hidaka, Y., Chiba-ohkuma, R., Karakida, T., & Onuma, K. (2020). Combined Effect of Midazolam and Bone Morphogenetic Protein-2 for Differentiation Induction from C2C12 Myoblast Cells to Osteoblasts. *Pharmaceutics*, 12(218), 1–18. <https://doi.org/doi:10.3390/pharmaceutics12030218>

Higgins, A., Glover, M., & Yang, Y. (2014). EXOGEN Ultrasound Bone Healing System for Long Bone Fractures with Non-Union or Delayed Healing : A NICE Medical Technology Guidance. *Appl Health Econ Health Policy*, 12, 477–484. <https://doi.org/10.1007/s40258-014-0117-6>

- Hirenkumar, M., & Steven, S. (2012). Poly Lactic-co-Glycolic Acid (PLGA) as Biodegradable Controlled Drug Delivery Carrier. *Polymers*, 3(3), 1–19. <https://doi.org/10.3390/polym3031377>.Poly
- Ho, M. H., Liao, M. H., Lin, Y. L., Lai, C. H., Lin, P. I., & Chen, R. M. (2014). Improving effects of chitosan nanofiber scaffolds on osteoblast proliferation and maturation. *International Journal of Nanomedicine*, 9, 4293–4304. <https://doi.org/10.2147/IJN.S68012>
- Homayoni, H., Ravandi, S. A. H., & Valizadeh, M. (2009). Electrospinning of chitosan nanofibers: Processing optimization. *Carbohydrate Polymers*, 77(3), 656–661. <https://doi.org/10.1016/j.carbpol.2009.02.008>
- Honda, T., Yamamoto, H., Ishii, A., & Inui, M. (2010). PDZRN3 Negatively Regulates BMP-2–induced Osteoblast Differentiation through Inhibition of Wnt Signaling. *Molecular Biology of the Cell*, 21, 3269–3277. <https://doi.org/10.1091/mbc.E10>
- Howe, A. S. (2018). *General principles of fracture management: Early and late complications*.
- Huang, T. L., Li, Y. H., & Chen, Y. C. (2020). Benzophenone derivatives as novel organosoluble visible light Type II photoinitiators for UV and LED photoinitiating systems. *Journal of Polymer Science*, 58(20), 2914–2925. <https://doi.org/10.1002/pol.20200437>
- Huber, E., Pobloth, A. M., Bormann, N., Kolarczik, N., Schmidt-Bleek, K., Schell, H., Schwabe, P., Duda, G. N., & Wildemann, B. (2017). Demineralized bone matrix as a carrier for bone morphogenetic protein-2: Burst release combined with long-Term binding and osteoinductive activity evaluated in vitro and in vivo. *Tissue Engineering - Part A*, 23(23–24), 1321–1330. <https://doi.org/10.1089/ten.tea.2017.0005>
- Iga, C., Pawel, S., Marcin, L., & Justyna, K. L. (2020). Polyurethane composite scaffolds modified with the mixture of gelatin and hydroxyapatite characterized by improved calcium deposition. *Polymers*, 12(2), 1–18. <https://doi.org/10.3390/polym12020410>
- Islam, M. M., Shahruzzaman, M., Biswas, S., Nurus Sakib, M., & Rashid, T. U. (2020).

Chitosan based bioactive materials in tissue engineering applications-A review. *Bioactive Materials*, 5(1), 164–183.

<https://doi.org/10.1016/j.bioactmat.2020.01.012>

Jahan, K., Manickam, G., Tabrizian, M., & Murshed, M. (2020). In vitro and in vivo investigation of osteogenic properties of self-contained phosphate-releasing injectable purine-crosslinked chitosan-hydroxyapatite constructs. *Scientific Reports*, 10(1), 1–17. <https://doi.org/10.1038/s41598-020-67886-7>

James, A. W., LaChaud, G., Shen, J., Asatrian, G., Nguyen, V., Zhang, X., Ting, K., & Soo, C. (2016). A Review of the Clinical Side Effects of Bone Morphogenetic Protein-2. *Tissue Engineering - Part B: Reviews*, 22(4), 284–297. <https://doi.org/10.1089/ten.teb.2015.0357>

Jenis, L. G. (2016). *Bone grafts in Spine Surgery*. OrthoInfo.

<https://orthoinfo.aaos.org/en/treatment/bone-grafts-in-spine-surgery/>

Jhala, D., Rather, H. A., & Vasita, R. (2020). Extracellular matrix mimicking polycaprolactone-chitosan nanofibers promote stemness maintenance of mesenchymal stem cells via spheroid formation. *Biomedical Materials (Bristol)*, 15(3), 1–16. <https://doi.org/10.1088/1748-605X/ab772e>

Jiang, S., Wang, M., & He, J. (2021). A review of biomimetic scaffolds for bone regeneration: Toward a cell-free strategy. *Bioengineering & Translational Medicine*, 6, 1–36. <https://doi.org/https://doi.org/10.1002/btm2.10206>

Jiang, Y.-H., Lou, Y.-Y., Li, T.-H., Liu, B.-Z., Chen, K., Zhang, D., & Li, T. (2022). Cross-linking methods of type I collagen-based scaffolds for cartilage tissue engineering. *American Journal of Translational Research*, 14(2), 1146–1159. <http://www.ncbi.nlm.nih.gov/pubmed/35273719><http://www.pubmedcentral.nih.gov/articlerender.fcgi?artid=PMC8902548>

Jiao, C., Xie, D., He, Z., Liang, H., Shen, L., Yang, Y., Tian, Z., Wu, G., & Wang, C. (2022). Additive manufacturing of Bio-inspired ceramic bone Scaffolds: Structural Design, mechanical properties and biocompatibility. *Materials and Design*, 217, 110610. <https://doi.org/10.1016/j.matdes.2022.110610>

Jin, H., Zhuo, Y., Sun, Y., Fu, H., & Han, Z. (2019). Microstructure design and

degradation performance in vitro of three-dimensional printed bioscaffold for bone tissue engineering. *Advances in Mechanical Engineering*, 11(10), 1–10.

<https://doi.org/10.1177/1687814019883784>

Julia E. Samorezov, & Alsberg, E. (2016). Spatial regulation of controlled bioactive factor delivery for bone tissue engineering. *Advanced Drug Delivery Reviews*, 84, 45–67. <https://doi.org/10.1016/j.addr.2014.11.018>.Spatial

Junka, R., & Yu, X. (2020). Polymeric nanofibrous scaffolds laden with cell-derived extracellular matrix for bone regeneration. *Materials Science and Engineering C*, 113(November 2019), 110981. <https://doi.org/10.1016/j.msec.2020.110981>

Kaliva, M., Georgopoulou, A., Dragatogiannis, D. A., Charitidis, C. A., Chatzinikolaidou, M., & Vamvakaki, M. (2020). Biodegradable Chitosan-graft-Poly(L-lactide) Copolymers For Bone Tissue Engineering. *Polymers*, 12(316), 1–19.

Kamoun, E. A., El-Betany, A., Menzel, H., & Chen, X. (2018). Influence of photoinitiator concentration and irradiation time on the crosslinking performance of visible-light activated pullulan-HEMA hydrogels. *International Journal of Biological Macromolecules*, 120, 1884–1892. <https://doi.org/10.1016/j.ijbiomac.2018.10.011>

Kang, Q., Sun, M. H., Cheng, H., Peng, Y., Montag, A. G., Deyrup, A. T., Jiang, W., Luu, H. H., Luo, J., Szatkowski, J. P., Vanichakarn, P., Park, J. Y., Li, Y., Haydon, R. C., & He, T. C. (2004). Characterization of the distinct orthotopic bone-forming activity of 14 BMPs using recombinant adenovirus-mediated gene delivery. *Gene Therapy*, 11(17), 1312–1320. <https://doi.org/10.1038/sj.gt.3302298>

Kapadnis, G., Dey, A., Dandekar, P., & Jain, R. (2019). Effect of degree of deacetylation on solubility of low-molecular-weight chitosan produced via enzymatic breakdown of chitosan. *Polymer International*, 68(6), 1054–1063. <https://doi.org/10.1002/pi.5795>

Kargozar, S., Mozafari, M., Hamzehlou, S., & Milan, P. B. (2019). Bone Tissue Engineering Using Human Cells : A Comprehensive Review on Recent Trends , Current Prospects , and Recommendations. *Applied Sciences*, 9(174), 1–49. <https://doi.org/10.3390/app9010174>

- Kasgoz, H., & Heydarova, S. (2011). Styrene-PEG (600) DMA crosslinked polymers for absorption of oil derivatives. *Journal of Macromolecular Science, Part A: Pure and Applied Chemistry*, 48(7), 556–561.
<https://doi.org/10.1080/10601325.2011.579818>
- Katagiri, T., Yamaguchi, A., Komaki, M., Abe, E., Takahashi, N., Ikeda, T., Rosen, V., Wozney, J. M., Fujisawa-Sehara, A., & Suda, T. (1994). Bone morphogenetic protein-2 converts the differentiation pathway of C2C12 myoblasts into the osteoblast lineage. *Journal of Cell Biology*, 127(6 I), 1755–1766.
<https://doi.org/10.1083/jcb.127.6.1755>
- Kelly, F. (2019). *Evaluation of modified flow-through pulsed UV technology for bacterial inactivation with comparison to a standard continuous-flow low pressure UV system*. National University of Ireland Galway.
- Khalifeh, J. M., Zohny, Z., MacEwan, M., Stephen, M., Johnston, W., Gamble, P., Zeng, Y., Yan, Y., & Ray, W. Z. (2018). Electrical Stimulation and Bone Healing: A Review of Current Technology and Clinical Applications. *IEEE Reviews in Biomedical Engineering*, 11(c), 217–232.
<https://doi.org/10.1109/RBME.2018.2799189>
- Khouri, J., Penlidis, A., & Moresoli, C. (2019). Viscoelastic properties of crosslinked chitosan films. *Processes*, 7(3), 1–18. <https://doi.org/10.3390/pr7030157>
- Killion, J. A., Geever, L. M., Devine, D. M., Farrell, H., & Higginbotham, C. L. (2014). Compressive strength and bioactivity properties of photopolymerizable hybrid composite hydrogels for bone tissue engineering. *International Journal of Polymeric Materials and Polymeric Biomaterials*, 63(13), 641–650.
<https://doi.org/10.1080/00914037.2013.854238>
- Killion, J. A., Geever, L. M., Devine, D. M., Kennedy, J. E., & Higginbotham, C. L. (2011). Mechanical properties and thermal behaviour of PEGDMA hydrogels for potential bone regeneration application. *Journal of the Mechanical Behavior of Biomedical Materials*, 4(7), 1219–1227.
<https://doi.org/10.1016/j.jmbbm.2011.04.004>
- Kim, H. J., Czech, Z., Bartkowiak, M., Shim, G. S., Kabatc, J., & Licbarski, A. (2022). Study of UV-initiated polymerization and UV crosslinking of acrylic monomers

mixture for the production of solvent-free pressure-sensitive adhesive films.

Polymer Testing, 105, 107424.

<https://doi.org/10.1016/j.polymertesting.2021.107424>

Kim, T., See, C. W., Li, X., & Zhu, D. (2020). Orthopedic implants and devices for bone fractures and defects: Past, present and perspective. *Engineered Regeneration*, 1(May), 6–18. <https://doi.org/10.1016/j.engreg.2020.05.003>

Kimoto, K., Okudera, T., Okudera, H., Nordquist, W. D., & Krutchkoff, D. J. (2011). Part I: crystalline fluorapatite-coated hydroxyapatite, physical properties. *The Journal of Oral Implantology*, 37(1), 27–33. <https://doi.org/10.1563/AAID-JOI-D-09-00118.1>

Kisiel, M. (2013). Bone Enhancement with BMP-2 for Safe Clinical Translation. In *Science and Technology*. Uppsala University.

Kizuki, T., Matsushita, T., & Kokubo, T. (2015). Apatite-forming PEEK with TiO₂ surface layer coating. *Journal of Materials Science: Materials in Medicine*, 26(41), 1–9. <https://doi.org/10.1007/s10856-014-5359-1>

Klein, A., Baranowski, A., Ritz, U., Mack, C., Götz, H., Langendorf, E., Al-Nawas, B., Drees, P., Rommens, P. M., & Hofmann, A. (2019). Effect of bone sialoprotein coating on progression of bone formation in a femoral defect model in rats. *European Journal of Trauma and Emergency Surgery*, 46, 277–286. <https://doi.org/10.1007/s00068-019-01159-5>

Kokubo, T., & Takadama, H. (2006). How useful is SBF in predicting in vivo bone bioactivity? *Biomaterials*, 27(15), 2907–2915. <https://doi.org/10.1016/j.biomaterials.2006.01.017>

Kowalska, A., Sokolowski, J., & Bociong, K. (2021). The photoinitiators used in resin based dental composite—a review and future perspectives. *Polymers*, 13(3), 1–17. <https://doi.org/10.3390/polym13030470>

Kulshrestha, S., Khan, S., Hasan, S., Khan, M. E., Misba, L., & Khan, A. U. (2016). Calcium fluoride nanoparticles induced suppression of *Streptococcus mutans* biofilm: an in vitro and in vivo approach. *Applied Microbiology and Biotechnology*, 100(4), 1901–1914. <https://doi.org/10.1007/s00253-015-7154-4>

- Kumar, a A., Karthick, K., & Arumugam, K. P. (2011). Properties of Biodegradable Polymers and Degradation for Sustainable Development. *International Journal of Chemical Engineering and Applications*, 2(3), 164–167.
<https://doi.org/10.7763/IJCEA.2011.V2.95>
- Kumar, A., & Kumar, A. (2017). Chitosan as a biomedical material: Properties and applications. In *Biopolymers: Structure, Performance and Applications* (Issue June 2017, pp. 139–154).
- Kurniati, M., Nuraini, I., & Winarti, C. (2021). Investigation of Swelling Ratio and Textures Analysis of Acrylamide-Nanocellulose Corncobs Hydrogel. *Journal of Physics: Conference Series*, 1805(1), 1–7. <https://doi.org/10.1088/1742-6596/1805/1/012036>
- Kus-Liskiewicz, M., Rzeszutko, J., Bobitski, Y., Barylyak, A., Nechyporenko, G., Zinchenko, V., & Zebrowski, J. (2019). Alternative approach for fighting bacteria and fungi: Use of modified fluorapatite. *Journal of Biomedical Nanotechnology*, 15(4), 848–855. <https://doi.org/10.1166/jbn.2019.2725>
- Lan Levengood, S., & Zhang, M. (2015). Chitosan-based scaffolds for bone tissue engineering. *J Mater Chem B Mater Biol Med.*, 2(21), 3161–3184.
<https://doi.org/10.1039/C4TB00027G>.Chitosan-based
- Lavanya, K., Chandran, S. V., Balagangadharan, K., & Selvamurugan, N. (2020). Temperature- and pH-responsive chitosan-based injectable hydrogels for bone tissue engineering. *Materials Science and Engineering C*, 111(January), 1–12.
<https://doi.org/10.1016/j.msec.2020.110862>
- Lee, D., Wufuer, M., Kim, I., Choi, T. H., Kim, B. J., Jung, H. G., Jeon, B., Lee, G., Jeon, O. H., Chang, H., & Yoon, D. S. (2021). Sequential dual-drug delivery of BMP-2 and alendronate from hydroxyapatite-collagen scaffolds for enhanced bone regeneration. *Scientific Reports*, 11(1), 1–10. <https://doi.org/10.1038/s41598-020-80608-3>
- Li, B., Wang, J., Moustafa, M. E., & Yang, H. (2019). Ecofriendly Method to Dissolve Chitosan in Plain Water. *ACS Biomaterials Science and Engineering*, 5(12), 6355–6360. <https://doi.org/10.1021/acsbmaterials.9b00695>

- Li, B., Xia, X., Guo, M., Jiang, Y., Li, Y., Zhang, Z., Liu, S., Li, H., Liang, C., & Wang, H. (2019). Biological and antibacterial properties of the micro-nanostructured hydroxyapatite/chitosan coating on titanium. *Scientific Reports*, 9(1), 1–10. <https://doi.org/10.1038/s41598-019-49941-0>
- Li, J., & Stocum, D. L. (2014). Fracture Healing. In D. B. Burr & M. R. Allen (Eds.), *Basic and Applied Bone Biology* (pp. 205–223). Elsevier Science Publishing Co. Inc. <https://doi.org/10.1016/B978-0-12-416015-6.00010-1>
- Li, L., Lu, H., Zhao, Y., Luo, J., Yang, L., Liu, W., & He, Q. (2019). Functionalized cell-free scaffolds for bone defect repair inspired by self-healing of bone fractures: A review and new perspectives. *Materials Science and Engineering C*, 98(January), 1241–1251. <https://doi.org/10.1016/j.msec.2019.01.075>
- Li, N., Wu, G., Yao, H., Tang, R., Gu, X., & Tu, C. (2019). Size effect of nano-hydroxyapatite on proliferation of odontoblast-like MDPC-23 cells. *Dental Materials Journal*, 38(4), 534–539. <https://doi.org/10.4012/dmj.2018-155>
- Li, X., Sun, Q., Li, Q., Kawazoe, N., & Chen, G. (2018). Functional hydrogels with tunable structures and properties for tissue engineering applications. *Frontiers in Chemistry*, 6(OCT), 1–20. <https://doi.org/10.3389/fchem.2018.00499>
- Li, Y., Chen, S. K., Li, L., Qin, L., Wang, X. L., & Lai, Y. X. (2015). Bone defect animal models for testing efficacy of bone substitute biomaterials. *Journal of Orthopaedic Translation*, 3(3), 95–104. <https://doi.org/10.1016/j.jot.2015.05.002>
- Liao, C., Chen, C., Chen, J., Chiang, S., Lin, Y., & Chang, K. (2001). *Fabrication of porous biodegradable polymer scaffolds using a solvent merging / particulate leaching method*. <https://doi.org/10.1002/jbm.10030>
- Liao, H. T., Tsai, M. J., Brahmayya, M., & Chen, J. P. (2018). Bone Regeneration Using Adipose-Derived Stem Cells in Injectable Thermo-Gelling Hydrogel Scaffold Containing Platelet-Rich Plasma and Biphasic Calcium Phosphate. *International Journal of Molecular Sciences*, 19(9), 1–18. <https://doi.org/10.3390/ijms19092537>
- Liao, Y., Li, H., Shu, R., Chen, H., Zhao, L., Song, Z., & Zhou, W. (2020). Mesoporous Hydroxyapatite/Chitosan Loaded With Recombinant-Human Amelogenin Could

Enhance Antibacterial Effect and Promote Periodontal Regeneration. *Frontiers in Cellular and Infection Microbiology*, 10(April), 1–14.

<https://doi.org/10.3389/fcimb.2020.00180>

Lidgren, L., Tägil, M., Raina, D. B., Mishra, R., Pelkonen, M., Kumar, A., Raina, D. B., Pelkonen, M., Lidgren, L., Tägil, M., & Kumar, A. (2015). Study of in Vitro and in Vivo Bone Formation in Composite Cryogels and the Influence of Electrical Stimulation. *International Journal of Biological Sciences*, 11(11), 1325–1336.
<https://doi.org/10.7150/ijbs.13139>

Ligon, S. C., Liska, R., Stampfl, J., Gurr, M., & Mulhaupt, R. (2017). Polymers for 3D Printing and Customized Additive Manufacturing. *Chemical Reviews*, 117, 10212–10290. <https://doi.org/10.1021/acs.chemrev.7b00074>

Lim, K. T., Patel, D. K., Choung, H. W., Seonwoo, H., Kim, J., & Chung, J. H. (2019). Evaluation of Bone Regeneration Potential of Long-Term Soaked Natural Hydroxyapatite. *ACS Applied Bio Materials*, 2(12), 5535–5543.
<https://doi.org/10.1021/acsabm.9b00345>

Lin, C. Y., & Kang, J. H. (2021). Mechanical properties of compact bone defined by the stress-strain curve measured using uniaxial tensile test: A concise review and practical guide. *Materials*, 14(15), 1–16. <https://doi.org/10.3390/ma14154224>

Lin, D. P. L., Carnagarin, R., Dharmarajan, A., & Dass, C. R. (2017). Transdifferentiation of myoblasts into osteoblasts – possible use for bone therapy. *Journal of Pharmacy and Pharmacology*, 69(12), 1661–1671.
<https://doi.org/10.1111/jphp.12790>

Lin, H., Tang, Y., Lozito, T. P., Oyster, N., Wang, B., & Tuan, R. S. (2019). Efficient in vivo bone formation by BMP-2 engineered human mesenchymal stem cells encapsulated in a projection stereolithographically fabricated hydrogel scaffold. *Stem Cell Research and Therapy*, 10(1), 1–13. <https://doi.org/10.1186/s13287-019-1350-6>

Liu, C. G., Zeng, Y. T., Kankala, R. K., Zhang, S. S., Chen, A. Z., & Wang, S. Bin. (2018). Characterization and preliminary biological evaluation of 3D-printed porous scaffolds for engineering bone tissues. *Materials*, 11(10).
<https://doi.org/10.3390/ma11101832>

- Liu, X., Chen, Y., Huang, Q., He, W., Feng, Q., & Yu, B. (2014). A novel thermo-sensitive hydrogel based on thiolated chitosan/ hydroxyapatite/beta-glycerophosphate. *Carbohydrate Polymers*, *110*, 62–69.
<https://doi.org/10.1016/j.carbpol.2014.03.065>
- Loi, F., Córdova, L. A., Pajarinen, J., Lin, T.-H., Yao, Z., & Goodman, S. B. (2016). Inflammation, Fracture and Bone Repair. *Bone*, *86*, 119–130.
<https://doi.org/10.1016/j.bone.2016.02.020>
- López-Lacomba, J. L., García-Cantalejo, J. M., Casado, J. V. S., Abarrategi, A., Magaña, V. C., & Ramos, V. (2006). Use of rhBMP-2 Activated Chitosan Films To Improve Osseointegration. *Biomacromolecules*, *7*(3), 792–798.
<https://doi.org/10.1021/bm050859e>
- Lu, H., Liu, Y., Guo, J., Wu, H., Wang, J., & Wu, G. (2016). Biomaterials with antibacterial and osteoinductive properties to repair infected bone defects. *International Journal of Molecular Sciences*, *17*(3), 1–18.
<https://doi.org/10.3390/ijms17030334>
- Luckanagul, J. A., Metavarayuth, K., Feng, S., Maneesaay, P., Clark, A. Y., Yang, X., García, A. J., & Wang, Q. (2016). Tobacco Mosaic Virus Functionalized Alginate Hydrogel Scaffolds for Bone Regeneration in Rats with Cranial Defect. *ACS Biomaterials Science and Engineering*, *2*(4), 606–615.
<https://doi.org/10.1021/acsbiomaterials.5b00561>
- Lv, S. H. (2016). High-performance superplasticizer based on chitosan. In *Biopolymers and Biotech Admixtures for Eco-Efficient Construction Materials* (pp. 131–150).
<https://doi.org/10.1016/B978-0-08-100214-8.00007-5>
- Lyles, M. B., Hu, J. C., Varanasi, V. G., Hollinger, J. O., & Athanasiou, K. A. (2015). Bone tissue engineering. In *Regenerative Engineering of Musculoskeletal Tissues and Interfaces*. <https://doi.org/10.1016/B978-1-78242-301-0.00005-7>
- Ma, G. (2019). Three common preparation methods of hydroxyapatite. *IOP Conference Series: Materials Science and Engineering*, *688*(3), 1–12.
<https://doi.org/10.1088/1757-899X/688/3/033057>
- Maachou, H., Bal, K. E., Bal, Y., Chagnes, A., Cote, G., & Alliouche, D. (2008).

- Characterization and in vitro bioactivity of chitosan/hydroxyapatite composite membrane prepared by freeze-gelation method. *Trends in Biomaterials and Artificial Organs*, 22(1), 15–24. <https://doi.org/10.1016/j.bbrc.2006.02.100>
- Maciejewska, M., Rogulska, M., Józwicki, M., & Głodowska, N. (2021). Synthesis and characterization of porous copolymers of 2-hydroxyethyl methacrylate with ethylene glycol dimethacrylate. *Polymers for Advanced Technologies*, 32(6), 2566–2575. <https://doi.org/10.1002/pat.5288>
- Madl, C. M., Mehta, M., Duda, G. N., Heilshorn, S. C., & Mooney, D. J. (2014). Presentation of BMP-2 Mimicking Peptides in 3D Hydrogels Directs Cell Fate Commitment in Osteoblasts and Mesenchymal Stem Cells. *Biomacromolecules*, 15(2), 445–455. <https://doi.org/10.1021/bm401726u.Presentation>
- Maglio, M., Salamanna, F., Brogini, S., Borsari, V., Pagani, S., Nicoli Aldini, N., Giavaresi, G., & Fini, M. (2020). Histological, Histomorphometrical, and Biomechanical Studies of Bone-Implanted Medical Devices: Hard Resin Embedding. *BioMed Research International*, 2020, 1–13. <https://doi.org/10.1155/2020/1804630>
- Mahmood, S. K., Razak, I. S. A., Ghaji, M. S., Yusof, L. M., Mahmood, Z. K., Rameli, M. A. B. P., & Zakaria, Z. A. B. (2017). In vivo evaluation of a novel nanocomposite porous 3D scaffold in a rabbit model: Histological analysis. *International Journal of Nanomedicine*, 12, 8587–8598. <https://doi.org/10.2147/IJN.S145663>
- Maji, K., Dasgupta, S., Pramanik, K., & Bissoyi, A. (2016). Preparation and Evaluation of Gelatin-Chitosan-Nanobioglass 3D Porous Scaffold for Bone Tissue Engineering. *International Journal of Biomaterials*, 2016, 1–14. <https://doi.org/10.1155/2016/9825659>
- Malysheva, K., Kwaśniak, K., Gnilitskyi, I., Barylyak, A., Zinchenko, V., Fahmi, A., Korchynskyi, O., & Bobitski, Y. (2021). Functionalization of polycaprolactone electrospun osteoplastic scaffolds with fluorapatite and hydroxyapatite nanoparticles: Biocompatibility comparison of human versus mouse mesenchymal stem cells. *Materials*, 14(6). <https://doi.org/10.3390/ma14061333>
- Manolagas, S. C., Drezner, M. K., & Mulder, J. E. (2018). Normal skeletal development

and regulation of bone formation and resorption. *UpToDate*, 17–19.

Marongiu, G., Dolci, A., Verona, M., & Capone, A. (2020). The biology and treatment of acute long-bones diaphyseal fractures: Overview of the current options for bone healing enhancement. *Bone Reports*, *12*(January), 100249.

<https://doi.org/10.1016/j.bonr.2020.100249>

Marques, C., Som, C., Schmutz, M., Borges, O., & Borchard, G. (2020). How the Lack of Chitosan Characterization Precludes Implementation of the Safe-by-Design Concept. *Frontiers in Bioengineering and Biotechnology*, *8*(March), 1–12.

<https://doi.org/10.3389/fbioe.2020.00165>

Marsell, R., & Einhorn, T. A. (2012). THE BIOLOGY OF FRACTURE HEALING. *Injury*, *42*(6), 551–555. <https://doi.org/10.1016/j.injury.2011.03.031>. THE

Maruyama, M., Rhee, C., Utsunomiya, T., Zhang, N., Ueno, M., Yao, Z., & Goodman, S. B. (2020). Modulation of the Inflammatory Response and Bone Healing.

Frontiers in Endocrinology, *11*(June), 1–14.

<https://doi.org/10.3389/fendo.2020.00386>

Masters, K. S. (2011). Covalent Growth Factor Immobilization Strategies for Tissue Repair and Regeneration. *Macromolecular Bioscience*, *11*(9), 1149–1163.

<https://doi.org/10.1002/mabi.201000505>

Mazalan, E., Chaudhary, K., Haider, Z., Abd Hadi, S. F., & Ali, J. (2018).

Determination of calcium to phosphate elemental ratio in natural hydroxyapatite using LIBS. *Journal of Physics: Conference Series*, *1027*(1), 1–8.

<https://doi.org/10.1088/1742-6596/1027/1/012013>

McGregor, N., Poulton, I., Walker, E., & Sims, N. (2020). Testing Bone Formation Induction by Calvarial Injection Assay in vivo. *Bio-Protocol*, *10*(6), 1–12.

<https://doi.org/10.21769/bioprotoc.3560>

Meeremans, M., Van Damme, L., De Spiegelaere, W., Van Vlierberghe, S., & De Schauwer, C. (2021). Equine tenocyte seeding on gelatin hydrogels improves elongated morphology. *Polymers*, *13*(5), 1–16.

<https://doi.org/10.3390/polym13050747>

Meng, C., Su, W., Liu, M., Yao, S., Ding, Q., Yu, K., Xiong, Z., Chen, K., Guo, X., Bo,

- L., & Sun, T. (2021). Controlled delivery of bone morphogenic protein-2-related peptide from mineralised extracellular matrix-based scaffold induces bone regeneration. *Materials Science and Engineering: C*, *126*, 1–11.
<https://doi.org/10.1016/j.msec.2021.112182>
- Metzger. (2016). *Tunable and cell-responsive 3D poly(ethylene glycol) microenvironments for the development of tissue models* [University of Zurich].
<https://doi.org/10.5167/uzh-134629>
- Miculescu, F., Luță, C., Constantinescu, A. E., Maidaniuc, A., Mocanu, A. C., Miculescu, M., Voicu, Ștefan I., & Ciocan, L. T. (2020). Considerations and Influencing Parameters in EDS Microanalysis of Biogenic Hydroxyapatite. *Journal of Functional Biomaterials*, *11*(4), 1–10. <https://doi.org/10.3390/jfb11040082>
- Mills, L. A., & Simpson, A. H. R. W. (2013). The relative incidence of fracture non-union in the Scottish population (5.17 million): A 5-year epidemiological study. *BMJ Open*, *3*(2), 1–6. <https://doi.org/10.1136/bmjopen-2012-002276>
- Mohan, N., Montazer, Z., Sharma, P. K., & Levin, D. B. (2020). Microbial and Enzymatic Degradation of Synthetic Plastics. *Frontiers in Microbiology*, *11*(November). <https://doi.org/10.3389/fmicb.2020.580709>
- Mohiuddin, O. A., Campbell, B., Poche, J. N., Ma, M., Rogers, E., Gaupp, D., Harrison, M. A. A., Bunnell, B. A., Hayes, D. J., & Gimble, J. M. (2019). Decellularized Adipose Tissue Hydrogel Promotes Bone Regeneration in Critical-Sized Mouse Femoral Defect Model. *Frontiers in Bioengineering and Biotechnology*, *7*(September), 1–15. <https://doi.org/10.3389/fbioe.2019.00211>
- Moreno, D., Vargas, F., Ruiz, J., & López, M. E. (2020). Solid-state synthesis of alpha tricalcium phosphate for cements used in biomedical applications. *Boletín de La Sociedad Española de Cerámica y Vidrio*, *59*(5), 193–200.
<https://doi.org/10.1016/j.bsecv.2019.11.004>
- Mumcuoglu, D., Fahmy-Garcia, S., Ridwan, Y., Nickel, J., Farrell, E., Kluijtmans, S. G. J. M., & van Osch, G. J. V. M. (2018). Injectable BMP-2 delivery system based on collagen-derived microspheres and alginate induced bone formation in a time-and dose-dependent manner. *European Cells and Materials*, *35*, 242–254.
<https://doi.org/10.22203/eCM.v035a17>

- Muñoz-Bonilla, A., & Fernández-García, M. (2012). Polymeric materials with antimicrobial activity. *Progress in Polymer Science (Oxford)*, 37(2), 281–339. <https://doi.org/10.1016/j.progpolymsci.2011.08.005>
- Mututuvvari, T. M., Harkins, A. L., & Tran, C. D. (2013). Facile synthesis, characterization, and antimicrobial activity of cellulose-chitosan-hydroxyapatite composite material: A potential material for bone tissue engineering. *Journal of Biomedical Materials Research - Part A*, 101(11), 3266–3277. <https://doi.org/10.1002/jbm.a.34636>
- Nair, A. K., Gautieri, A., Chang, S. W., & Buehler, M. J. (2013). Molecular mechanics of mineralized collagen fibrils in bone. *Nature Communications*, 4, 1724–1729. <https://doi.org/10.1038/ncomms2720>
- Nandra, R., Grover, L., & Porter, K. (2016). Fracture non-union epidemiology and treatment. *Trauma*, 18(1), 3–11. <https://doi.org/10.1177/1460408615591625>
- Nazeer, M. A., Yilgör, E., & Yilgör, I. (2017). Intercalated chitosan/hydroxyapatite nanocomposites: Promising materials for bone tissue engineering applications. *Carbohydrate Polymers*, 175, 38–46. <https://doi.org/10.1016/j.carbpol.2017.07.054>
- Ng, J., Spiller, K., Bernhard, J., & Vunjak-Novakovic, G. (2017). Biomimetic Approaches for Bone Tissue Engineering. *Tissue Engineering - Part B: Reviews*, 23(5), 480–493. <https://doi.org/10.1089/ten.teb.2016.0289>
- Nga, N. K., Thanh Tam, L. T., Ha, N. T., Hung Viet, P., & Huy, T. Q. (2020). Enhanced biomineralization and protein adsorption capacity of 3D chitosan/hydroxyapatite biomimetic scaffolds applied for bone-tissue engineering. *RSC Advances*, 10(70), 43045–43057. <https://doi.org/10.1039/d0ra09432c>
- Nicholson, J. A., Makaram, N., Simpson, A. H. R. W., & Keating, J. F. (2021). Fracture nonunion in long bones: A literature review of risk factors and surgical management. *Injury*, 52, S3–S11. <https://doi.org/10.1016/j.injury.2020.11.029>
- Nicolas, J., Magli, S., Rabbachin, L., Sampaolesi, S., Nicotra, F., & Russo, L. (2020). 3D Extracellular Matrix Mimics: Fundamental Concepts and Role of Materials Chemistry to Influence Stem Cell Fate. *Biomacromolecules*, 21(6), 1968–1994. <https://doi.org/10.1021/acs.biomac.0c00045>

- Nikonenko, N. A., Buslov, D. K., Sushko, N. I., & Zhabankov, R. G. (2000). Investigation of stretching vibrations of glycosidic linkages in disaccharides and polysaccharides with use of IR spectra deconvolution. *Biopolymers - Biospectroscopy Section*, 57(4), 257–262. [https://doi.org/10.1002/1097-0282\(2000\)57:4<257::AID-BIP7>3.0.CO;2-3](https://doi.org/10.1002/1097-0282(2000)57:4<257::AID-BIP7>3.0.CO;2-3)
- Niu, X., Feng, Q., Wang, M., Guo, X., & Zheng, Q. (2009). Porous nano-HA/collagen/PLLA scaffold containing chitosan microspheres for controlled delivery of synthetic peptide derived from BMP-2. *Journal of Controlled Release*, 134(2), 111–117. <https://doi.org/10.1016/j.jconrel.2008.11.020>
- Nokoorani, Y. D., Shamloo, A., Bahadoran, M., & Moravvej, H. (2021). Fabrication and characterization of scaffolds containing different amounts of allantoin for skin tissue engineering. *Scientific Reports*, 11(1), 1–20. <https://doi.org/10.1038/s41598-021-95763-4>
- Nordquist, W. D., Okudera, H., Kitamura, Y., Kimoto, K., Okudera, T., & Krutchkoff, D. J. (2011). Part II: crystalline fluorapatite-coated hydroxyapatite implant material: a dog study with histologic comparison of osteogenesis seen with FA-coated HA grafting material versus HA controls: potential bacteriostatic effect of fluoridated HA. *The Journal of Oral Implantology*, 37(1), 35–42. <https://doi.org/10.1563/AAID-JOI-D-10-00164>
- Ogose, A., Hotta, T., Kawashima, H., Kondo, N., Gu, W., Kamura, T., & Endo, N. (2005). Comparison of hydroxyapatite and beta tricalcium phosphate as bone substitutes after excision of bone tumors. *Journal of Biomedical Materials Research - Part B Applied Biomaterials*, 72(1), 94–101. <https://doi.org/10.1002/jbm.b.30136>
- Oliveira, É. R., Nie, L., Podstawczyk, D., Allahbakhsh, A., Ratnayake, J., Brasil, D. L., & Shavandi, A. (2021). Advances in growth factor delivery for bone tissue engineering. *International Journal of Molecular Sciences*, 22(2), 1–33. <https://doi.org/10.3390/ijms22020903>
- Osuchukwu, O. A., Salihi, A., Abdullahi, I., Abdulkareem, B., & Nwannenna, C. S. (2021). Synthesis techniques, characterization and mechanical properties of natural derived hydroxyapatite scaffolds for bone implants: a review. *SN Applied Sciences*,

3(10), 1–23. <https://doi.org/10.1007/s42452-021-04795-y>

- Oustadi, F., Imani, R., Haghbin Nazarpak, M., & Sharifi, A. M. (2020). Genipin-crosslinked gelatin hydrogel incorporated with PLLA-nanocylinders as a bone scaffold: Synthesis, characterization, and mechanical properties evaluation. *Polymers for Advanced Technologies*, 31(8), 1783–1792. <https://doi.org/10.1002/pat.4905>
- Pajor, K., Pajchel, L., & Kolmas, J. (2019). Hydroxyapatite and fluorapatite in conservative dentistry and oral implantology-a review. *Materials*, 12(7). <https://doi.org/10.3390/ma12172683>
- Park, S. Y. Y., Marsh, K. S. S., & Rhim, J. . W. (2002). Characteristics of Different Molecular Weight Chitosan Films Affected by the Type of Organic Solvents. *JOURNAL OF FOOD SCIENCE—Vol*, 67(Hon 1997), 16–19. <https://doi.org/10.1111/j.1365-2621.2002.tb11382.x>
- Patel, P. P., Buckley, C., Taylor, B. L., Sahyoun, C. C., Patel, S. D., Mont, A. J., Mai, L., Patel, S., & Freeman, J. W. (2019). Mechanical and biological evaluation of a hydroxyapatite-reinforced scaffold for bone regeneration. *Journal of Biomedical Materials Research - Part A*, 107(4), 732–741. <https://doi.org/10.1002/jbm.a.36588>
- Pautke, C., Tischer, T., Vogt, S., Haczek, C., Deppe, H., Neff, A., Horch, H. H., Schieker, M., & Kolk, A. (2007). New advances in fluorochrome sequential labelling of teeth using seven different fluorochromes and spectral image analysis. *Journal of Anatomy*, 210(1), 117–121. <https://doi.org/10.1111/j.1469-7580.2006.00660.x>
- Pautke, C., Vogt, S., Kreutzer, K., Haczek, C., Wexel, G., Kolk, A., Imhoff, A. B., Zitzelsberger, H., Milz, S., & Tischer, T. (2010). Characterization of eight different tetracyclines: Advances in fluorescence bone labeling. *Journal of Anatomy*, 217(1), 76–82. <https://doi.org/10.1111/j.1469-7580.2010.01237.x>
- Pautke, C., Vogt, S., Tischer, T., Wexel, G., Deppe, H., Milz, S., Schieker, M., & Kolk, A. (2005). Polychrome labeling of bone with seven different fluorochromes: Enhancing fluorochrome discrimination by spectral image analysis. *Bone*, 37(4), 441–445. <https://doi.org/10.1016/j.bone.2005.05.008>

- Paxton, N. C., Wong, C. S., Desselle, M. R., Allenby, M. C., & Woodruff, M. A. (2020). Bone morphogenetic protein–assisted bone regeneration and applications in biofabrication. In N. E. Vrana, H. Knopf-Marques, & J. Barthes (Eds.), *Biomaterials for Organ and Tissue Regeneration: New Technologies and Future Prospects*. Woodhead Publishing Series in Biomaterials. <https://doi.org/10.1016/B978-0-08-102906-0.00016-7>
- Perren, S. M. (2002). Evolution of the internal fixation of long bone fractures. *Journal of Bone and Joint Surgery - Series B*, *84*(8), 1093–1110. <https://doi.org/10.1302/0301-620X.84B8.13752>
- Polo-Corrales, L. ; Latorre-Esteves, M. ; Ramirez-Vick, J. (2013). Scaffold Design for Bone Regeneration. *Journal of Nanoscience and Nanotechnology*, *31*(9), 1713–1723. <https://doi.org/10.1109/TMI.2012.2196707>.Separate
- Porter, A., Irwin, R., Miller, J., Horan, D. J., Robling, A. G., & McCabe, L. R. (2017). Quick and inexpensive paraffin-embedding method for dynamic bone formation analyses. *Scientific Reports*, *7*(January), 1–7. <https://doi.org/10.1038/srep42505>
- Pountos, I., Panteli, M., Lampropoulos, A., Jones, E., Calori, G. M., & Giannoudis, P. V. (2016). The role of peptides in bone healing and regeneration: A systematic review. *BMC Medicine*, *14*(1), 1–15. <https://doi.org/10.1186/s12916-016-0646-y>
- Prasadh, S., & Wong, R. C. W. (2018). Unraveling the mechanical strength of biomaterials used as a bone scaffold in oral and maxillofacial defects. *Oral Science International*, *15*(2), 48–55. [https://doi.org/10.1016/S1348-8643\(18\)30005-3](https://doi.org/10.1016/S1348-8643(18)30005-3)
- Predoi, D., Iconaru, S. L., Predoi, M. V., Stan, G. E., & Buton, N. (2019). Synthesis, characterization, and antimicrobial activity of magnesium-doped hydroxyapatite suspensions. *Nanomaterials*, *9*(9), 1–20. <https://doi.org/10.3390/nano9091295>
- Qin, X. H., Ovsianikov, A., Stampfl, J., & Liska, R. (2014). Additive manufacturing of photosensitive Hydrogels for tissue engineering applications. *BioNanoMaterials*, *15*(3–4), 49–70. <https://doi.org/10.1515/bnm-2014-0008>
- Qiu, Y. (2008). *Chitosan Derivatives For Tissue Engineering*. August, 1–226.
- Queiroz, M. F., Melo, K. R. T., Sabry, D. A., Sasaki, G. L., & Rocha, H. A. O. (2015). Does the use of chitosan contribute to oxalate kidney stone formation? *Marine*

Drugs, 13(1), 141–158. <https://doi.org/10.3390/md13010141>

- Rademakers, T., Horvath, J. M., van Blitterswijk, C. A., & LaPointe, V. L. S. (2019). Oxygen and nutrient delivery in tissue engineering: Approaches to graft vascularization. *Journal of Tissue Engineering and Regenerative Medicine*, 13(10), 1815–1829. <https://doi.org/10.1002/term.2932>
- Radzak, N. A., Murali, M. R., & Kamarul, T. (2021). Assessing the potential of bone marrow concentrate for cartilage repair and regeneration in animal models: A systemic review. *Sains Malaysiana*, 50(6), 1727–1744. <https://doi.org/10.17576/jsm-2021-5006-19>
- Raftery, R., O'Brien, F. J., & Cryan, S. A. (2013). Chitosan for gene delivery and orthopedic tissue engineering applications. *Molecules*, 18(5), 5611–5647. <https://doi.org/10.3390/molecules18055611>
- Rameshbabu, N., Sampath Kumar, T. S., & Prasad Rao, K. (2006). Synthesis of nanocrystalline fluorinated hydroxyapatite by microwave processing and its in vitro dissolution study. *Bulletin of Materials Science*, 29(6), 611–615. <https://doi.org/10.1007/s12034-006-0012-3>
- Ratnayake, J. T., Ross, E. D., Dias, G. J., Shanafelt, K. M., Taylor, S. S., Gould, M. L., Guan, G., & Cathro, P. R. (2020). Preparation, characterisation and in-vitro biocompatibility study of a bone graft developed from waste bovine teeth for bone regeneration. *Materials Today Communications*, 22(November 2019), 1–10. <https://doi.org/10.1016/j.mtcomm.2019.100732>
- Rauch, C., Brunet, A., Deleule, J., Farge, E., Rauch, C., Brunet, A., Deleule, J., Farge, E., Brunet, A., & Deleule, J. (2002). C2C12 myoblast/osteoblast transdifferentiation steps enhanced by epigenetic inhibition of BMP2 endocytosis C2C12 myoblast/osteoblast transdifferentiation steps enhanced by epigenetic inhibition of BMP2 endocytosis. *American Journal of Physiological Cell Physiology*, 283(July 2002), 235–243. <https://doi.org/https://doi.org/10.1152/ajpcell.00234.2001>
- Redondo, F. L., Giaroli, M. C., Ciolino, A. E., & Ninago, M. D. (2022). Preparation of porous poly(Lactic acid)/tricalcium phosphate composite scaffolds for tissue engineering. *Biointerface Research in Applied Chemistry*, 12(4), 5610–5624.

<https://doi.org/10.33263/BRIAC124.56105624>

- Reves, B. T., Jennings, J. A., Bumgardner, J. D., & Haggard, W. O. (2011). Osteoinductivity assessment of BMP-2 loaded composite chitosan-nano-hydroxyapatite scaffolds in a rat muscle pouch. *Materials*, *4*(8), 1360–1374. <https://doi.org/10.3390/ma4081360>
- Rey, C., Combes, C. G., Drouet, C., & Sfihi, H. (2008). Fluoride-Based Bioceramics. In *Fluorine and Health*. <https://doi.org/10.1016/B978-0-444-53086-8.00006-0>
- Riga, E. K., Saar, J. S., Erath, R., Hechenbichler, M., & Lienkamp, K. (2017). On the limits of benzophenone as cross-linker for surface-attached polymer hydrogels. *Polymers*, *9*(12), 1–14. <https://doi.org/10.3390/polym9120686>
- Rinaudo, M. (2006). Chitin and chitosan: Properties and applications. *Progress in Polymer Science (Oxford)*, *31*(7), 603–632. <https://doi.org/10.1016/j.progpolymsci.2006.06.001>
- Roohani-Esfahani, S. I., Newman, P., & Zreiqat, H. (2016). Design and Fabrication of 3D printed Scaffolds with a Mechanical Strength Comparable to Cortical Bone to Repair Large Bone Defects. *Scientific Reports*, *6*(October 2015), 1–8. <https://doi.org/10.1038/srep19468>
- Rosenberg, M., Shilo, D., Galperin, L., Capucha, T., Tarabieh, K., Rachmiel, A., & Segal, E. (2019). Bone morphogenic protein 2-loaded porous silicon carriers for osteoinductive implants. *Pharmaceutics*, *11*(11), 4–6. <https://doi.org/10.3390/pharmaceutics11110602>
- Roseti, L., Parisi, V., Petretta, M., Cavallo, C., Desando, G., Bartolotti, I., & Grigolo, B. (2017). Scaffolds for Bone Tissue Engineering: State of the art and new perspectives. *Materials Science and Engineering C*, *78*, 1246–1262. <https://doi.org/10.1016/j.msec.2017.05.017>
- Ross, A., Sauce-Guevara, M. A., Alarcon, E. I., & Mendez-Rojas, M. A. (2022). Peptide Biomaterials for Tissue Regeneration. *Frontiers in Bioengineering and Biotechnology*, *10*(August), 1–16. <https://doi.org/10.3389/fbioe.2022.893936>
- Rudert, M., Wilms, U., Hoberg, M., & Wirth, C. J. (2005). Cell-based treatment of osteochondral defects in the rabbit knee with natural and synthetic matrices:

cellular seeding determines the outcome. *Archives of Orthopaedic and Trauma Surgery*, 125(9), 598–608. <https://doi.org/10.1007/s00402-005-0008-2>

Rupp, M., Biehl, C., Budak, M., Thormann, U., Heiss, C., & Alt, V. (2018). Diaphyseal long bone nonunions — types, aetiology, economics, and treatment recommendations. *International Orthopaedics*, 42(2), 247–258. <https://doi.org/10.1007/s00264-017-3734-5>

Rusu, A. G., Chiriac, A. P., Nita, L. E., Mititelu-Tartau, L., Tudorachi, N., Ghilan, A., & Rusu, D. (2019). Multifunctional BSA Scaffolds Prepared with a Novel Combination of UV-Crosslinking Systems. *Macromolecular Chemistry and Physics*, 220(24), 1–12. <https://doi.org/10.1002/macp.201900378>

Ruvinov, E., Tavor Re'em, T., Witte, F., & Cohen, S. (2019). Articular cartilage regeneration using acellular bioactive affinity-binding alginate hydrogel: A 6-month study in a mini-pig model of osteochondral defects. *Journal of Orthopaedic Translation*, 16, 40–52. <https://doi.org/10.1016/j.jot.2018.08.003>

Ryan, E., & Yin, S. (2022). Compressive strength of β -TCP scaffolds fabricated via lithography-based manufacturing for bone tissue engineering. *Ceramics International*, 48(11), 15516–15524. <https://doi.org/10.1016/j.ceramint.2022.02.085>

Sahu, K. K., & Modi, Y. K. (2021). Investigation on dimensional accuracy, compressive strength and measured porosity of additively manufactured calcium sulphate porous bone scaffolds. *Materials Technology*, 36(8), 492–503. <https://doi.org/10.1080/10667857.2020.1774728>

Saito, A., Suzuki, Y., Ogata, S. I., Ohtsuki, C., & Tanihara, M. (2003). Activation of osteo-progenitor cells by a novel synthetic peptide derived from the bone morphogenetic protein-2 knuckle epitope. *Biochimica et Biophysica Acta - Proteins and Proteomics*, 1651(1–2), 60–67. [https://doi.org/10.1016/S1570-9639\(03\)00235-8](https://doi.org/10.1016/S1570-9639(03)00235-8)

Salamanca, E., Tsao, T. C., Hseuh, H. W., Wu, Y. F., Choy, C. S., Lin, C. K., Pan, Y. H., Teng, N. C., Huang, M. C., Lin, S. M., & Chang, W. J. (2021). Fabrication of Poly(lactic Acid)/ β -Tricalcium Phosphate FDM 3D Printing Fiber to Enhance Osteoblastic-Like Cell Performance. *Frontiers in Materials*, 8(May), 1–10.

<https://doi.org/10.3389/fmats.2021.683706>

Sanchez-Salvador, J. L., Balea, A., Monte, M. C., Negro, C., & Blanco, A. (2021). Chitosan grafted/cross-linked with biodegradable polymers: A review.

International Journal of Biological Macromolecules, 178, 325–343.

<https://doi.org/10.1016/j.ijbiomac.2021.02.200>

Saravanan, S., Nethala, S., Pattnaik, S., Tripathi, A., Moorthi, A., & Selvamurugan, N. (2011). Preparation, characterization and antimicrobial activity of a bio-composite scaffold containing chitosan/nano-hydroxyapatite/nano-silver for bone tissue engineering.

International Journal of Biological Macromolecules, 49(2), 188–193.

<https://doi.org/10.1016/j.ijbiomac.2011.04.010>

Schmidt, A. H. (2021). Autologous bone graft: Is it still the gold standard? *Injury*, 52,

S18–S22. <https://doi.org/10.1016/j.injury.2021.01.043>

Seyedmajidi, S., Rajabnia, R., & Seyedmajidi, M. (2018). Evaluation of antibacterial properties of hydroxyapatite/bioactive glass and fluorapatite/bioactive glass nanocomposite foams as a cellular scaffold of bone tissue.

Journal of Laboratory Physicians, 10(03), 265–270. https://doi.org/10.4103/jlp.jlp_167_17

Seyedmajidi, S., & Seyedmajidi, M. (2022). Fluorapatite: A Review of Synthesis, Properties and Medical Applications vs Hydroxyapatite. *Iranian Journal of Materials Science and Engineering*, 19(2), 1–20.

<https://doi.org/10.22068/ijmse.2430>

Shalumon, K. T., Sheu, C., Fong, Y. T., Liao, H. T., & Chen, J. P. (2016). Microsphere-based hierarchically juxtapositioned biphasic scaffolds prepared from poly(lactic-co-glycolic acid) and nanohydroxyapatite for osteochondral tissue engineering.

Polymers, 8(12), 1–29. <https://doi.org/10.3390/polym8120429>

Shanker, M. D. (2019). *Utilisation of injectable fluorochromes for quantification of bone growth in a sheep tibial*. Queensland University of Technology.

Sheikh, Z., Javaid, M. A., Hamdan, N., & Hashmi, R. (2015). Bone regeneration using bone morphogenetic proteins and various biomaterial carriers. *Materials*, 8(4),

1778–1816. <https://doi.org/10.3390/ma8041778>

Shemshad, S., Kamali, S., Khavandi, A., & Azari, S. (2019). Synthesis, characterization

and in-vitro behavior of natural chitosan-hydroxyapatite-diopside nanocomposite scaffold for bone tissue engineering. *International Journal of Polymeric Materials and Polymeric Biomaterials*, 68(9), 516–526.

<https://doi.org/10.1080/00914037.2018.1466138>

Shih, Y.-R., Padke, A., Yamaguchi, T., Kang, H., Inoue, N., Masuda, K., & Varghese, S. (2017). Synthetic bone mimetic matrix-mediated in situ bone tissue formation through host cell recruitment. *Acta Biomaterialia*, 19, 1–9.

<https://doi.org/10.1016/j.actbio.2015.03.017>

Shim, M.-J. (2016). Bone Changes in Femoral Bone of Mice Using Calcein Labeling. *Korean Journal of Clinical Laboratory Science*, 48(2), 114–117.

<https://doi.org/10.15324/kjcls.2016.48.2.114>

Sinusaite, L., Antuzevics, A., Popov, A. I., Rogulis, U., Misevicius, M., Katelnikovas, A., Kareiva, A., & Zarkov, A. (2021). Synthesis and luminescent properties of Mn-doped alpha-tricalcium phosphate. *Ceramics International*, 47(4), 1–6.

<https://doi.org/10.1016/j.ceramint.2020.10.114>

Skuk, D., Paradis, M., Goulet, M., & Tremblay, J. P. (2007). Ischemic central necrosis in pockets of transplanted myoblasts in nonhuman primates: Implications for cell-transplantation strategies. *Transplantation*, 84(10), 1307–1315.

<https://doi.org/10.1097/01.tp.0000288322.94252.22>

Solomon, L., Warwick, D. J., & Nayagam, S. (2005). Fractures and Joint Injury. In *Apley's Concise System of Orthopaedics and Fractures* (3rd Revise, pp. 266–280). Hodder Education.

Sommer, U., Laurich, S., Azevedo, L. De, Vieho, K., Wenisch, S., Thormann, U., Alt, V., Heiss, C., & Schnettler, R. (2020). In Vitro and In Vivo Biocompatibility Studies of a Cast and Coated Titanium Alloy. *Molecules*, 25(3399), 1–23.

<https://doi.org/https://doi.org/10.3390/molecules25153399>

Sondag, G. R., Salihoglu, S., Lababidi, S. L., Crowder, D. C., Moussa, F. M., Abdelmagid, S. M., & Safadi, F. F. (2014). Osteoactivin induces transdifferentiation of C2C12 myoblasts into osteoblasts. *Journal of Cellular Physiology*, 229(7), 955–966. <https://doi.org/10.1002/jcp.24512>

- Song, R., Wang, D., Zeng, R., & Wang, J. (2017). Synergistic effects of fibroblast growth factor-2 and bone morphogenetic protein-2 on bone induction. *Molecular Medicine Reports*, *16*(4), 4483–4492. <https://doi.org/10.3892/mmr.2017.7183>
- Sparks, D. S., Saifzadeh, S., Savi, F. M., Dlaska, C. E., Berner, A., Henkel, J., Reichert, J. C., Wullschleger, M., Ren, J., Cipitria, A., McGovern, J. A., Steck, R., Wagels, M., Woodruff, M. A., Schuetz, M. A., & Hutmacher, D. W. (2020). A preclinical large-animal model for the assessment of critical-size load-bearing bone defect reconstruction. *Nature Protocols*, *15*(3), 877–924. <https://doi.org/10.1038/s41596-019-0271-2>
- Spicer, P. P., Kretlow, J. D., Young, S., Jansen, J. A., Kasper, F. K., & Mikos, A. G. (2012). Evaluation of bone regeneration using the rat critical size calvarial defect. *Nature Protocols*, *7*(10), 1918–1929. <https://doi.org/10.1038/nprot.2012.113>
- Suamte, L., Tirkey, A., & Babu, P. J. (2023). Design of 3D smart scaffolds using natural, synthetic and hybrid derived polymers for skin regenerative applications. *Smart Materials in Medicine*, *4*(June 2022), 243–256. <https://doi.org/10.1016/j.smaim.2022.09.005>
- Sukpaita, T., Chirachanchai, S., Suwattanachai, P., Everts, V., Pimkhaokham, A., & Ampornaramveth, R. S. (2019). In vivo bone regeneration induced by a Scaffold of chitosan/dicarboxylic acid seeded with human periodontal ligament cells. *International Journal of Molecular Sciences*, *20*(19), 1–11. <https://doi.org/10.3390/ijms20194883>
- Sulaiman, S. Bin, Keong, T. K., Cheng, C. H., Saim, A. Bin, & Hj Idrus, R. B. (2013). Tricalcium phosphate/hydroxyapatite (TCP-HA) bone scaffold as potential candidate for the formation of tissue engineered bone. *Indian Journal of Medical Research*, *137*(6), 1093–1101.
- Suliman, S., Xing, Z., Wu, X., Xue, Y., Pedersen, T. O., Sun, Y., Døskeland, A. P., Nickel, J., Waag, T., Lygre, H., Finne-Wistrand, A., Steinmüller-Nethl, D., Krueger, A., & Mustafa, K. (2015). Release and bioactivity of bone morphogenetic protein-2 are affected by scaffold binding techniques in vitro and in vivo. *Journal of Controlled Release*, *197*, 148–157. <https://doi.org/10.1016/j.jconrel.2014.11.003>
- Sultankulov, B., Berillo, D., Sultankulova, K., Tokay, T., & Saparov, A. (2019).

Progress in the development of chitosan-based biomaterials for tissue engineering and regenerative medicine. *Biomolecules*, 9(9).

<https://doi.org/10.3390/biom9090470>

Sun, T., Liu, M., Yao, S., Ji, Y., Shi, L., Tang, K., Xiong, Z., Yang, F., Chen, K., & Guo, X. (2018). Guided osteoporotic bone regeneration with composite scaffolds of mineralized ECM/heparin membrane loaded with BMP2-related peptide.

International Journal of Nanomedicine, 13, 791–804.

<https://doi.org/10.2147/IJN.S152698>

Sun, T., Qu, Y., Cui, W., Yang, L., Ji, Y., Yu, W., Navinduth, R., Shao, Z., Yang, H., & Guo, X. (2017). Evaluation of osteogenic inductivity of a novel BMP2-mimicking peptide P28 and P28-containing bone composite. *Journal of Biomedical Materials Research Part A*, 106(1), 210–220.

<https://doi.org/10.1002/jbm.a.36228>

Surowiec, R. K., Allen, M. R., & Wallace, J. M. (2022). Bone hydration: How we can evaluate it, what can it tell us, and is it an effective therapeutic target? *Bone Reports*, 16(December 2021), 1–19.

<https://doi.org/10.1016/j.bonr.2021.101161>

Svedbom, A., Hernlund, E., Ivergård, M., Compston, J., Cooper, C., Stenmark, J., McCloskey, E. V., Jönsson, B., & Kanis, J. A. (2013). Osteoporosis in the European Union: A compendium of country-specific reports.

Archives of Osteoporosis, 8(1–2). <https://doi.org/10.1007/s11657-013-0137-0>

Svystonyuk, D. A., Mewhort, H. E. M., & Fedak, P. W. M. (2018). Using Acellular Bioactive Extracellular Matrix Scaffolds to Enhance Endogenous Cardiac Repair. *Frontiers in Cardiovascular Medicine*, 5(April), 1–8.

<https://doi.org/10.3389/fcvm.2018.00035>

Szurkowska, K., Szeleszczuk, Ł., & Kolmas, J. (2020). Effects of synthesis conditions on the formation of si-substituted alpha tricalcium phosphates. *International Journal of Molecular Sciences*, 21(23), 1–12.

<https://doi.org/10.3390/ijms21239164>

Taktak, R., Elghazel, A., Bouaziz, J., Charfi, S., & Keskes, H. (2018). Tricalcium phosphate-Fluorapatite as bone tissue engineering: Evaluation of bioactivity and biocompatibility. *Materials Science and Engineering C*, 86(November), 121–128.

<https://doi.org/10.1016/j.msec.2017.11.011>

- Talbot, S. R., Biernot, S., Bleich, A., van Dijk, R. M., Ernst, L., Häger, C., Helgers, S. O. A., Koegel, B., Koska, I., Kuhla, A., Miljanovic, N., Müller-Graff, F. T., Schwabe, K., Tolba, R., Vollmar, B., Weegh, N., Wölk, T., Wolf, F., Wree, A., ... Zechner, D. (2020). Defining body-weight reduction as a humane endpoint: a critical appraisal. *Laboratory Animals*, *54*(1), 99–110.
<https://doi.org/10.1177/0023677219883319>
- Tao, L., Zhonglong, L., Ming, X., Zezheng, Y., Zhiyuan, L., Xiaojun, Z., & Jinwu, W. (2017). In vitro and in vivo studies of a gelatin/carboxymethyl chitosan/LAPONITE® composite scaffold for bone tissue engineering. *RSC Advances*, *7*(85), 54100–54110. <https://doi.org/10.1039/c7ra06913h>
- Taraballi, F., Bauza, G., McCulloch, P., Harris, J., & Tasciotti, E. (2017). Concise Review : Biomimetic Functionalization of Biomaterials to Stimulate the Endogenous Healing Process of Cartilage and Bone Tissue. *Tissue Engineering and Regenerative Medicine*, *6*, 2186–2196. <https://doi.org/10.1002/sctm.17-0181>
- Taschner, R., Gauss, P., Knaack, P., & Liska, R. (2019). Biocompatible Photoinitiators Based on Poly- α -ketoesters. *Journal of Polymer Science*, *58*, 242–253.
- Thaitalay, P., Srakaew, N. L. O., & Rattanachan, S. T. (2018). Comparison among alpha-tricalcium phosphate synthesized by solid state reaction and wet chemical reaction for calcium phosphate cements. *Chiang Mai Journal of Science*, *45*(5), 2123–2131.
- Thomas, J. D., & Kehoe, J. L. (2022). Bone Nonunion. In *StatPearls Publishing LLC*.
<http://www.ncbi.nlm.nih.gov/pubmed/32119272>
- Thomas, M. V., & Puleo, D. A. (2011). Infection, inflammation, and bone regeneration: A paradoxical relationship. *Journal of Dental Research*, *90*(9), 1052–1061.
<https://doi.org/10.1177/0022034510393967>
- Thompson, C. L., Fu, S., Knight, M. M., & Thorpe, S. D. (2020). Mechanical Stimulation: A Crucial Element of Organ-on-Chip Models. *Frontiers in Bioengineering and Biotechnology*, *8*(December), 1–18.
<https://doi.org/10.3389/fbioe.2020.602646>
- Tian, R., Zheng, F., Zhao, W., Zhang, Y., Yuan, J., Zhang, B., & Li, L. (2020).

Prevalence and influencing factors of nonunion in patients with tibial fracture: Systematic review and meta-analysis. *Journal of Orthopaedic Surgery and Research*, 15(1), 1–16. <https://doi.org/10.1186/s13018-020-01904-2>

Tosun, H. B., Gürger, M., Gümüştas, S. A., Uludag, A., Üçer, Ö., Serbest, S., & Çelik, S. (2017). The effect of sodium hyaluronate–chondroitin sulfate combined solution on cartilage formation in osteochondral defects of the rabbit knee: An experimental study. *Therapeutics and Clinical Risk Management*, 13, 523–532. <https://doi.org/10.2147/TCRM.S133635>

Tsiklin, I. L., Shabunin, A. V., Kolsanov, A. V., & Volova, L. T. (2022). In Vivo Bone Tissue Engineering Strategies: Advances and Prospects. *Polymers*, 14(15). <https://doi.org/10.3390/polym14153222>

Tucker, N. J., Mauffrey, C., & Parry, J. A. (2021). Are pre- and postoperative true translational and angular displacement predictive of nonunion after intramedullary nail fixation of tibial shaft fractures? *European Journal of Orthopaedic Surgery and Traumatology*, 0123456789. <https://doi.org/10.1007/s00590-021-03154-2>

Turnbull, G., Clarke, J., Picard, F., Riches, P., Jia, L., Han, F., Li, B., & Shu, W. (2017). 3D bioactive composite scaffolds for bone tissue engineering. *Bioactive Materials*, 3, 278–314. <https://doi.org/10.1016/j.bioactmat.2017.10.001>

Van den Driessche, F., Rigole, P., Brackman, G., & Coenye, T. (2014). Optimization of resazurin-based viability staining for quantification of microbial biofilms. *Journal of Microbiological Methods*, 98(1), 31–34. <https://doi.org/10.1016/j.mimet.2013.12.011>

van Gaalen, S. M., Kruyt, M. C., Geuze, R. E., de Bruijn, J. D., Alblas, J., & Dhert, W. J. A. (2010). Use of fluorochrome labels in in vivo bone tissue engineering research. *Tissue Engineering. Part B, Reviews*, 16(2), 209–217. <https://doi.org/10.1089/ten.teb.2009.0503>

Venkatesan, J., & Kim, S. K. (2010). Chitosan composites for bone tissue engineering - An overview. *Marine Drugs*, 8(8), 2252–2266. <https://doi.org/10.3390/md8082252>

Verma, G. (2017). Photoreduction of Benzophenone in Green Chemistry Using an Alternate Solvent Ethyl Alcohol. *Chemical Sciences Journal*, 08(03), 10–12.

<https://doi.org/10.4172/2150-3494.1000165>

- Vidal, C., Alves, P., Alves, M. M., Carmezim, M. J., Fernandes, M. H., Grenho, L., Inácio, P. L., Ferreira, F. B., Santos, T. G., & Santos, C. (2022). Fabrication of a biodegradable and cytocompatible magnesium/nanohydroxyapatite/fluorapatite composite by upward friction stir processing for biomedical applications. *Journal of the Mechanical Behavior of Biomedical Materials*, 129(February), 1–39. <https://doi.org/10.1016/j.jmbbm.2022.105137>
- Vroman, I., & Tighzert, L. (2009). Biodegradable polymers. *Materials*, 2(2), 307–344. <https://doi.org/10.3390/ma2020307>
- Walsh, M. E., Ferris, H., Coughlan, T., Hurson, C., Ahern, E., Sorensen, J., & Brent, L. (2021). Trends in hip fracture care in the Republic of Ireland from 2013 to 2018: results from the Irish Hip Fracture Database. *Osteoporosis International*, 32(4), 727–736. <https://doi.org/10.1007/s00198-020-05636-1>
- Wang, C., Huang, W., Zhou, Y., He, L., He, Z., Chen, Z., He, X., Tian, S., Liao, J., Lu, B., Wei, Y., & Wang, M. (2020). 3D printing of bone tissue engineering scaffolds. *Bioactive Materials*, 5(1), 82–91. <https://doi.org/10.1016/j.bioactmat.2020.01.004>
- Wang, C., Liu, Y., Fan, Y., & Li, X. (2017). The use of bioactive peptides to modify materials for bone tissue repair. *Regenerative Biomaterials*, 4(3), 191–206. <https://doi.org/10.1093/rb/rbx011>
- Wang, L., He, S., Wu, X., Liang, S., Mu, Z., & Wei, J. (2014). Polyetheretherketone/nano- fluorohydroxyapatite composite with antimicrobial activity and osseointegration properties. *Biomaterials*, 1–18. <https://doi.org/10.1016/j.biomaterials.2014.04.085>
- Wang, S. J., Jiang, D., Zhang, Z. Z., Chen, Y. R., Yang, Z. D., Zhang, J. Y., Shi, J., Wang, X., & Yu, J. K. (2019). Biomimetic Nanosilica–Collagen Scaffolds for In Situ Bone Regeneration: Toward a Cell-Free, One-Step Surgery. *Advanced Materials*, 31(49), 1–10. <https://doi.org/10.1002/adma.201904341>
- Wang, W., Xue, C., & Mao, X. (2020). Chitosan: Structural modification, biological activity and application. *International Journal of Biological Macromolecules*, 164, 4532–4546. <https://doi.org/10.1016/j.ijbiomac.2020.09.042>

- Wang, W., & Yeung, K. W. K. K. (2017). Bone grafts and biomaterials substitutes for bone defect repair: A review. *Bioactive Materials*, 2(4), 224–247. <https://doi.org/10.1016/j.bioactmat.2017.05.007>
- Wang, Z., Wang, Z., Lu, W. W., Zhen, W., Yang, D., & Peng, S. (2017). Novel biomaterial strategies for controlled growth factor delivery for biomedical applications. *NPG Asia Materials*, 9(10), e435-17. <https://doi.org/10.1038/am.2017.179>
- Wei, S., Ma, J. X., Xu, L., Gu, X. S., & Ma, X. L. (2020). Biodegradable materials for bone defect repair. *Military Medical Research*, 7(1), 1–25. <https://doi.org/10.1186/s40779-020-00280-6>
- Wigmosta, T. B., Popat, K. C., & Kipper, M. J. (2021). Bone morphogenetic protein-2 delivery from polyelectrolyte multilayers enhances osteogenic activity on nanostructured titania. *Journal of Biomedical Materials Research - Part A*, 109(7), 1173–1182. <https://doi.org/10.1002/jbm.a.37109>
- Wildemann, B., Ignatius, A., Leung, F., Taitsman, L. A., Smith, R. M., Pesántez, R., Stoddart, M. J., Richards, R. G., & Jupiter, J. B. (2021). Non-union bone fractures. *Nature Reviews Disease Primers*, 7(1). <https://doi.org/10.1038/s41572-021-00289-8>
- Wong, K. C. (2016). *3D-printed patient-specific applications in orthopedics*. 57–66.
- Wozney, J. M., Rosen, V., Celeste, A. J., Mitsock, L. M., Whitters, M. J., Kriz, R. W., Hewick, R. M., & Wang, E. A. (1989). Novel regulators of bone formation: Molecular clones and activities. *Obstetrical and Gynecological Survey*, 44(5), 387–388. <https://doi.org/10.1097/00006254-198905000-00028>
- Wu, A. M., Bisignano, C., James, S. L., Abady, G. G., Abedi, A., Abu-Gharbieh, E., Alhassan, R. K., Alipour, V., Arabloo, J., Asaad, M., Asmare, W. N., Awedew, A. F., Banach, M., Banerjee, S. K., Bijani, A., Birhanu, T. T. M., Bolla, S. R., Cámara, L. A., Chang, J. C., ... Vos, T. (2021). Global, regional, and national burden of bone fractures in 204 countries and territories, 1990–2019: a systematic analysis from the Global Burden of Disease Study 2019. *The Lancet Healthy Longevity*, 2(9), e580–e592. [https://doi.org/10.1016/S2666-7568\(21\)00172-0](https://doi.org/10.1016/S2666-7568(21)00172-0)

- Wu, J., Zheng, K., Huang, X., Liu, J., Liu, H., Boccaccini, A. R., Wan, Y., Guo, X., & Shao, Z. (2019). Thermally triggered injectable chitosan/silk fibroin/bioactive glass nanoparticle hydrogels for in-situ bone formation in rat calvarial bone defects. *Acta Biomaterialia*, *91*, 60–71. <https://doi.org/10.1016/j.actbio.2019.04.023>
- Wu, M., Wu, P., Xiao, L., Zhao, Y., Yan, F., Liu, X., Xie, Y., Zhang, C., Chen, Y., & Cai, L. (2020). Biomimetic mineralization of novel hydroxyethyl cellulose/soy protein isolate scaffolds promote bone regeneration in vitro and in vivo. *International Journal of Biological Macromolecules*, *162*, 1627–1641. <https://doi.org/10.1016/j.ijbiomac.2020.08.029>
- Wu, Y., Jia, G., Chi, H., Jiao, Z., & Sun, Y. (2020). Integrated In Silico-In Vitro Identification and Optimization of Bone Morphogenic Protein-2 Armpit Epitope as Its Antagonist Binding Site. *Protein Journal*, *39*(6), 703–710. <https://doi.org/10.1007/s10930-020-09937-6>
- Wu, Y., Zhou, J., Li, Y., Zhou, Y., Cui, Y., Yang, G., & Hong, Y. (2015). Rap1A regulates osteoblastic differentiation via the ERK and p38 mediated signaling. *PLoS ONE*, *10*(11), 1–13. <https://doi.org/10.1371/journal.pone.0143777>
- Xiao, C., Zhou, H., Liu, G., Zhang, P., Fu, Y., Gu, P., Hou, H., Tang, T., & Fan, X. (2011). Bone marrow stromal cells with a combined expression of BMP-2 and VEGF-165 enhanced bone regeneration. *Biomedical Materials*, *6*(1), 1–9. <https://doi.org/10.1088/1748-6041/6/1/015013>
- Xiong, Z., Sun, T., Qu, Y., Yang, L., Zhou, J., Chen, K., Yao, S., Shao, Z., Guo, X., Cui, W., & Teng, Y. (2020). Sustained delivery of PIGF-2123-144-fused BMP2-related peptide P28 from small intestinal submucosa/polylactic acid scaffold material for bone tissue regeneration. *RSC Advances*, *10*(12), 7289–7300. <https://doi.org/10.1039/c9ra07868a>
- Xu, Z., Omar, A. M., & Bartolo, P. (2021). Experimental and numerical simulations of 3d-printed polycaprolactone scaffolds for bone tissue engineering applications. *Materials*, *14*(13). <https://doi.org/10.3390/ma14133546>
- Yadav, L. R., Chandran, S. V., Lavanya, K., & Selvamurugan, N. (2021). Chitosan-based 3D-printed scaffolds for bone tissue engineering. *International Journal of Biological Macromolecules*, *183*(June), 1925–1938.

<https://doi.org/10.1016/j.ijbiomac.2021.05.215>

- Yamada, Y., Yoshida, C., Hamada, K., Kikkawa, Y., & Nomizu, M. (2020). Development of Three-Dimensional Cell Culture Scaffolds Using Laminin Peptide-Conjugated Agarose Microgels. *Biomacromolecules*, *21*(9), 3765–3771. <https://doi.org/10.1021/acs.biomac.0c00871>
- Yang, F., Wang, J., Hou, J., Guo, H., & Liu, C. (2013). Bone regeneration using cell-mediated responsive degradable PEG-based scaffolds incorporating with rhBMP-2. *Biomaterials*, *34*(5), 1514–1528. <https://doi.org/10.1016/j.biomaterials.2012.10.058>
- Yang, N., Zhong, Q., Zhou, Y., Kundu, S. C., Yao, J., & Cai, Y. (2016). Controlled degradation pattern of hydroxyapatite/calcium carbonate composite microspheres. *Microscopy Research and Technique*, *79*(6), 518–524. <https://doi.org/10.1002/jemt.22661>
- Yi, H., Ur Rehman, F., Zhao, C., Liu, B., & He, N. (2016). Recent advances in nano scaffolds for bone repair. *Bone Research*, *4*(June). <https://doi.org/10.1038/boneres.2016.50>
- Yun, Y. P., Lee, S. Y., Kim, H. J., Song, J. J., & Kim, S. E. (2013). Improvement of osteoblast functions by sustained release of bone morphogenetic protein-2 (BMP-2) from heparin-coated chitosan scaffold. *Tissue Engineering and Regenerative Medicine*, *10*(4), 183–191. <https://doi.org/10.1007/s13770-013-0389-1>
- Zhang, F., & King, M. W. (2020). Biodegradable Polymers as the Pivotal Player in the Design of Tissue Engineering Scaffolds. *Advanced Healthcare Materials*, *9*(13), 1–22. <https://doi.org/10.1002/adhm.201901358>
- Zhang, H., Migneco, F., Lin, C. Y., & Hollister, S. J. (2010). Chemically-conjugated bone morphogenetic protein-2 on three-dimensional polycaprolactone scaffolds stimulates osteogenic activity in bone marrow stromal cells. *Tissue Engineering - Part A*, *16*(11), 3441–3448. <https://doi.org/10.1089/ten.tea.2010.0132>
- Zhang, H. Y., Liu, Q., Liu, J. Q., Wang, J., Yang, H. X., Xu, X. J., Xie, M. J., Liu, X. D., Yu, S. Bin, Zhang, M., Lu, L., Zhang, J., & Wang, M. Q. (2019). Molecular changes in peripheral blood involving osteoarthritic joint remodelling. *Journal of*

Oral Rehabilitation, 46(9), 820–827. <https://doi.org/10.1111/joor.12810>

- Zhang, J., Liao, L., Zhu, J., Wan, X., Xie, M., Zhang, H., Zhang, M., Lu, L., Yang, H., Jing, D., Liu, X., Yu, S., Lu, X. L., Chen, C., Shan, Z., & Wang, M. (2018). Osteochondral Interface Stiffening in Mandibular Condylar Osteoarthritis. *Journal of Dental Research*, 97(5), 563–570. <https://doi.org/10.1177/0022034517748562>
- Zhang, Q., Wang, W., Schmelzer, E., Gerlach, J., Liu, C., & Nettleship, I. (2021). The degradation behavior of calcium-rich hydroxyapatite foams in vitro. *Journal of Biomedical Materials Research - Part A*, 109(6), 859–868. <https://doi.org/10.1002/jbm.a.37077>
- Zhang, X., Chang, W., Lee, P., Wang, Y., Yang, M., Li, J., Kumbar, S. G., & Yu, X. (2014). Polymer-ceramic spiral structured scaffolds for bone tissue engineering: Effect of hydroxyapatite composition on human fetal osteoblasts. *PLoS ONE*, 9(1), 2–11. <https://doi.org/10.1371/journal.pone.0085871>
- Zhang, X., Chen, Y., Han, J., Mo, J., Dong, P., Zhuo, Y., & Feng, Y. (2019). Biocompatible silk fibroin/carboxymethyl chitosan/strontium substituted hydroxyapatite/cellulose nanocrystal composite scaffolds for bone tissue engineering. *International Journal of Biological Macromolecules*, 136, 1247–1257. <https://doi.org/10.1016/j.ijbiomac.2019.06.172>
- Zhang, X. Y., Fang, G., & Zhou, J. (2017). Additively manufactured scaffolds for bone tissue engineering and the prediction of their mechanical behavior: A review. *Materials*, 10(1). <https://doi.org/10.3390/ma10010050>
- Zhang, Y., Wang, Y., Shi, B., & Cheng, X. (2007). A platelet-derived growth factor releasing chitosan/coral composite scaffold for periodontal tissue engineering. *Biomaterials*, 28(8), 1515–1522. <https://doi.org/10.1016/j.biomaterials.2006.11.040>
- Zhang, Y., Wu, D., Zhao, X., Pakvasa, M., Tucker, A. B., Luo, H., Qin, K. H., Hu, D. A., Wang, E. J., Li, A. J., Zhang, M., Mao, Y., Sabharwal, M., He, F., Niu, C., Wang, H., Huang, L., Shi, D., Liu, Q., ... El Dafrawy, M. (2020). Stem Cell-Friendly Scaffold Biomaterials: Applications for Bone Tissue Engineering and Regenerative Medicine. *Frontiers in Bioengineering and Biotechnology*, 8(December), 1–18. <https://doi.org/10.3389/fbioe.2020.598607>

- Zhao, G., Zhang, L., Che, L., Li, H., Liu, Y., & Fang, J. (2021). Revisiting bone morphogenetic protein-2 knuckle epitope and redesigning the epitope-derived peptides. *Journal of Peptide Science*, 27(6), 1–11. <https://doi.org/10.1002/psc.3309>
- Zhao, Z., Yang, D., Ma, X., Zhao, H., Nie, C., & Si, Z. (2009). Successful repair of a critical-sized bone defect in the rat femur with a newly developed external fixator. *Tohoku Journal of Experimental Medicine*, 219(2), 115–120. <https://doi.org/10.1620/tjem.219.115>
- Zheng, X., Yin, Y., Jiang, W., Xing, L., & Pu, J. (2015). Low-mass chitosan. *BioResources*, 10(2), 2338–2349.
- Zhong, L., Chen, J., Ma, Z., Feng, H., Chen, S., Cai, H., Xue, Y., Pei, X., Wang, J., & Wan, Q. (2020). 3D printing of metal-organic framework incorporated porous scaffolds to promote osteogenic differentiation and bone regeneration. *Nanoscale*, 12(48), 24437–24449. <https://doi.org/10.1039/d0nr06297a>
- Zhou, J., Xiong, Z., Liu, M., Yang, L., Yao, S., Chen, K., Yu, K., Qu, Y., Sun, T., & Guo, X. (2020). Creation of bony microenvironment with extracellular matrix doped-bioactive ceramics to enhance osteoblast behavior and delivery of aspartic acid-modified bmp-2 peptides. *International Journal of Nanomedicine*, 15, 8465–8478. <https://doi.org/10.2147/IJN.S272571>
- Zhou, K., Azaman, F. A., Cao, Z., Fournet, M. B., & Devine, D. M. (2023). Bone Tissue Engineering Scaffold Optimisation through Modification of Chitosan / Ceramic Composition. *Micromol*, 3, 326–342.
- Zuncheddu, D., Della Bella, E., Schwab, A., Petta, D., Rocchitta, G., Generelli, S., Kurth, F., Parrilli, A., Verrier, S., Rau, J. V., Fosca, M., Maioli, M., Serra, P. A., Alini, M., Redl, H., Grad, S., & Basoli, V. (2021). Quality control methods in musculoskeletal tissue engineering: from imaging to biosensors. *Bone Research*, 9(1). <https://doi.org/10.1038/s41413-021-00167-9>
- Zustiak, S. P., Wei, Y., & Leach, J. B. (2013). Protein–Hydrogel Interactions in Tissue Engineering: Mechanisms and Applications. *Tissue Engineering Part B: Reviews*, 19(2), 160–171. <https://doi.org/10.1089/ten.teb.2012.0458>

RESEARCH PARTICIPATIONS

1) Institute of Technology (IT) Sligo Lean Six Sigma Massive Online Open Course (MOOC) 2019

Starting October 14, 2019, a MOOC organized by IT Sligo was enrolled. This course was established for six weeks and officially ended on December 19, 2019. Lean Six Sigma is a process of improvement approach for organisations that wish to attain world-class performance in quality and customer satisfaction by increasing productivity, efficiency and eliminating 'waste' in the process, which does not add any value to the product or services. The students who enrolled on this course and achieved more than 50% of the overall weekly quizzes are awarded a Certificate of Accomplishment (Appendix 3).

2) Animal Ethics Defence, Universiti Sains Malaysia (USM)

Before the animal research in USM, a proposal was defended to the Institutional Animal Care and Use Committee (IACUC USM) for animal ethics approval. The defence was carried out on February 4, 2020, and the ethics of the proposal was approved on March 2, 2020, with approval number: USM/IACUC/2020/(122)/(1048). The animal ethics approval letter is attached as Appendix 4.

8) Laboratory Animal Training Programme (Rat - Exclusive Package)

This animal training was completed on October 2, 2020, at Animal Research and Service Centre (ARASC) Universiti Sains Malaysia. ARASC Veterinary Officers trained me on the animal handling and restraining method, blood collection, subcutaneous, intramuscular and intraperitoneal injection and also cardiac puncture. The most important part was the surgical training on performing the femoral condyle defect creation and suturing techniques. A Certificate of Participation was awarded following the completion of the animal training (Appendix 5).

10) USM Online Certificate Course in Laboratory Techniques for Molecular Biology & Biomaterial Development, Series 1: Fundamental Techniques in Cell Culture

I had participated in Series 1 of an online course organized by the School of Dental Sciences, Universiti Sains Malaysia on the Laboratory Techniques for Molecular Biology

& Biomaterial Development (Appendix 6), which is the Fundamental Techniques in Cell Culture that was held on April 7, 14, 21 and 28, 2021. This series covered the fundamental techniques in cell culture, which consists of the principles and applications of cell culture technologies, isolation and selection of cell culture dimension, fundamental understanding of cell growth, and the 3D cell culture techniques. The certificate of completion was received after passing the test regarding the Fundamental Techniques in Cell Culture and is attached in Appendix 7.

11) USM Online Certificate Course in Laboratory Techniques for Molecular Biology & Biomaterial Development, Series 2: Cell Viability and Cell Toxicity Assay

After completing the Series 1 of the Online Course, the second series continued with Cell Viability and Cell Cytotoxicity, organized on May 5, 9 25th and June 2nd 2021. This series covered the methods for cell viability, the principle of cytotoxicity assay, choosing the best cytotoxicity test, and cytotoxicity analysis. The certificate of completion was received after passing the test regarding the Cell Viability and Cell Cytotoxicity (Appendix 8).

12) USM Online Certificate Course in Laboratory Techniques for Molecular Biology & Biomaterial Development, Series 3: Techniques in Molecular Biology

The third series of this course, organized on June 10, 17, 24 and 28th 2021, covered the extraction of nucleic acids, conventional PCR, electrophoresis, and western blotting, which are crucial and common in molecular biology. The certificate of completion was received after passing the test regarding the *Techniques in Molecular Biology* (Appendix 9).

13) USM Online Certificate Course in Laboratory Techniques for Molecular Biology & Biomaterial Development, Series 4: Electron Microscopy

The fourth series was organised on July 7, 14, 22 and 28th 2021, where it covered electron microscopy in terms of Structural biology and biophysical analysis in EM, Resolution & revolution in cryo-EM: principals and applications, Immunogold in TEM: principals and applications and also 3D nano-structural visualization via TEM. The certificate of completion was received after passing the test regarding electron microscopy (Appendix 10).

14) USM Online Certificate Course in Laboratory Techniques for Molecular Biology & Biomaterial Development, Series 5: Advanced Technique & Development in Biomaterials Characterizations and Applications

This final series of the course was organised on August 4, 11, 18 and 25, 2021, covering the topics on the principles and techniques in biomaterials characterisations, application of mass spectrometry, biomechanics and biosensors development for medical applications and also the advances and future of biomaterial innovations. The certificate of completion was received after passing the test regarding these topics (Appendix 11).

15) USM Webinar on Animal Care & Management for Pre-Clinical Study

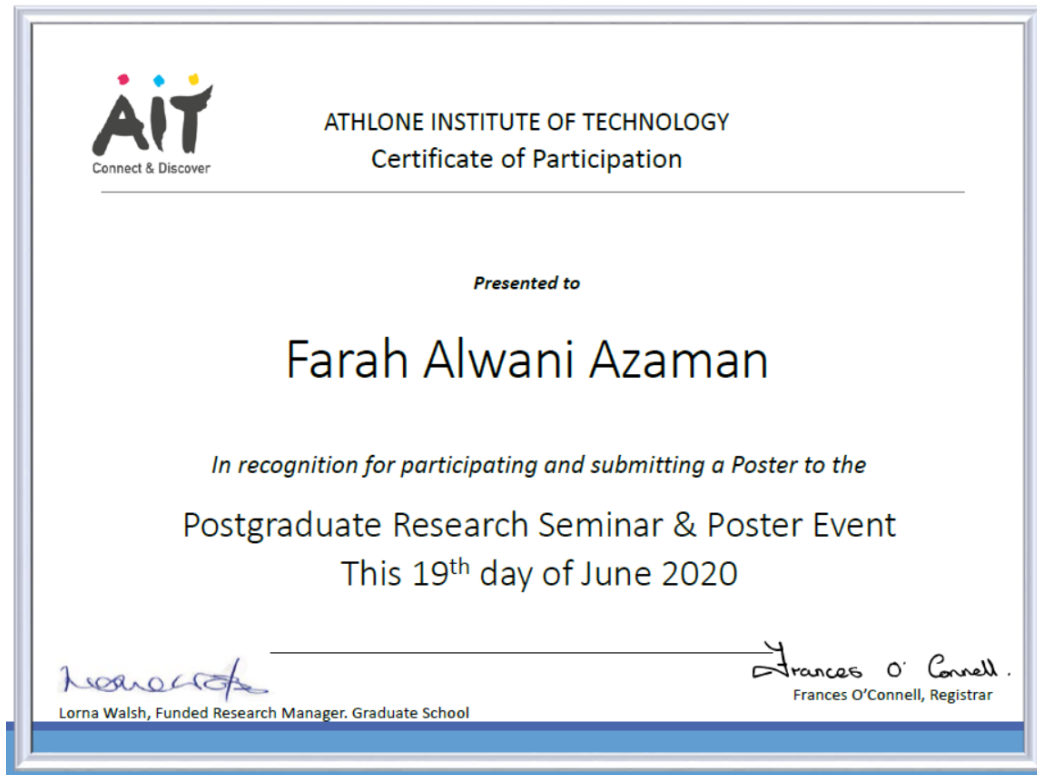
A webinar regarding animal care & management for the pre-clinical study was organised by USM Animal Research and Service Centre (ARASC) on July 14th 2021, via Cisco Webex. This webinar covered the facilities available in ARASC USM Kubang Kerian and ARASC USM Penang and the Advanced Medical and Dental Institute (AMDI). Then the webinar moved to the care management of rodents such as mice and rats and large animals such as rabbits and sheep. The certificate of attendance is attached as Appendix 12.

TRAININGS

- 1) Research Hub Induction
 - Health and safety induction
- 2) Research and Professional Development Plan Module
- 3) Research Communication Module
- 4) Intellectual Property Training Module
- 5) EPIGEUM Concise Research Integrity Online Course System
- 6) Data Handling and Statistical Analysis Module
- 7) Academic Writing Skills Training
- 8) Technical and Instrumentation Training
 - Fourier-Transform Infrared Spectroscopy (FTIR)
 - Compression test
 - Freeze-drying method
 - Differential Scanning Calorimetry (DSC)
 - UV-Visible Spectroscopy
 - High-Performance Liquid Chromatography (HPLC)
 - Cell work
 - Microbiology work
 - Hard tissue processing and cutting
 - Histological staining
 - Matrix-Assisted Laser Desorption Ionisation-Time of Flight (MALDI-TOF)
- 9) Introduction to Lean Sigma Quality (MOOC IT Sligo)
- 10) Animal Ethics Defence and Approval (IACUC USM)
- 11) Animal Handling and Restraining Training

APPENDICES

Appendix 1: Certificate of Participation in AIT Postgraduate Research Seminar & Poster Event 2020



Appendix 2: Materials Info 2021 Conference Certificate



Appendix 3: Institute of Technology Sligo MOOC Lean Six Sigma 2019



Appendix 4: Animal Ethics Approval



02nd March 2020

Prof. Dr. Suzina Sheikh Ab Hamid
Tissue Bank
School of Medical Sciences
Universiti Sains Malaysia
16150 Kubang Kerian
Kelantan

Dear Prof. Dr.,

Animal Ethics Approval

Project title (1048): Animal Trial for Bone Regeneration and Antimicrobial Assessment of Chitosan Based Biomimetic Anti-Infective Scaffold

The USM Institutional Animal Care and Use Committee (USM IACUC) has approved the above research project.

No. of Animal Ethics Approval: USM/IACUC/2020/(122)(1048)

Title : Animal Trial for Bone Regeneration and Antimicrobial Assessment of Chitosan Based Biomimetic Anti-Infective Scaffold

Source of Animals : Animal Research and Service Centre (ARASC), USM Health Campus

Location of Animals : Animal Research and Service Centre (ARASC), USM Health Campus

Duration : 02nd March 2020 – 02nd March 2021

Number of Samples : 50 Sprague Dawley Rats (Male)

Name of Principal Investigator : Prof. Dr. Suzina Sheikh Ab Hamid

Name of Co-Investigator : Dr. Declan Devine
: Dr. Margaret Brennan Fournet
: Dr. Muhamad Syahrul Fitri Zawawi
: Ms. Farah Alwani Azaman

(Please notify USM IACUC if there are additional staff/students who will be involved in animal handling for this project)

Jawatankuasa Penjagaan dan Penggunaan Haiwan Institusi USM
USM Institutional Animal Care and Use Committee (USM IACUC)

JKPPH USM



Appendix 5: Animal Handling and Training Certificate



Certificate of Participation

This is to certify that

FARAH ALWANI BT. AZAMAN

(940713-13-6080)

has attended

Laboratory Animal Training Programme

(Rat – Exclusive Package)

on

October 2, 2020

at

Animal Research And Service Centre (ARASC)

Organized by

Animal Research and Service Centre (ARASC)

Health Campus

Universiti Sains Malaysia


Dr. Nur Izni Mohd Zaharri
Coordinator
Animal Research and Service Centre
Health Campus
Universiti Sains Malaysia

Assoc. Prof. Dr. Badrul Hisham
Yahaya
Director
Animal Research and Service Centre
Universiti Sains Malaysia

Appendix 6: Online Certificate Course in Laboratory Techniques for Molecular Biology & Biomaterial Development

2021 Webinar Series

Online Certificate Course in Laboratory Techniques for Molecular Biology & Biomaterial Development




UNIVERSITI SAINS MALAYSIA APEX™
School of Dental Sciences

Series 1	Series 2	Series 3	Series 4	Series 5
(7, 14, 21 & 28 April)	(5, 19, 25 May & 2 June)	(10, 17, 24 June & 1 July)	(7, 14, 21 & 28 July)	(4, 11, 18 & 25 August)
Fundamental Techniques in Cell Culture	In-vitro Cell Viability & Cytotoxicity Assay	Techniques in Molecular Biology	Electron Microscopy Series - A Small World Shows Us the Unseen	Advanced Technique in Biomaterials Development and Applications
<p>Topics Covered:</p> <ol style="list-style-type: none"> 1. Principles and applications of cell culture techniques 2. Isolation and selection of cell culture dimension 3. Fundamental understanding on cell growth 4. All about 3D cell culture and large-scale expansion 	<p>Topics Covered:</p> <ol style="list-style-type: none"> 1. Methods for cell viability 2. Principle of cytotoxicity assay 3. Cytotoxicity tests: Which one is for you? 4. Cytotoxicity analysis 	<p>Topics Covered:</p> <ol style="list-style-type: none"> 1. Extraction of nucleic acids 2. Conventional PCR 3. Electrophoresis 4. Western blotting 	<p>Topics Covered:</p> <ol style="list-style-type: none"> 1. Resolution revolution in cryo-EM: Principles and applications 2. Immunogold in TEM: Principles and applications 3. Structural biology and biophysical analysis in EM 4. 3D nano-structural visualization via TEM 	<p>Topics Covered:</p> <ol style="list-style-type: none"> 1. Principles and techniques in biomaterials characterisation 2. Applications of Mass Spectrometry 3. Biomechanics and biosensors development for medical applications 4. Advances and future of biomaterials innovation


Fee:	Number of Series	1	2 Series	3 Series	4 Series	5 Series
Price		RM 70 / USD 20	RM 120 / USD 30	RM 180 / USD 45	RM 240 / USD 60	RM 300 / USD 75

For registration and payment please go to this link:
shorturl.at/opqBC



Organise by:
Basic Sciences and Oral Biology Unit,
School of Dental Sciences, Universiti Sains Malaysia

Co-Organisers:



Appendix 7: Certificate of Completion of Series 1: Fundamental Techniques in Cell Culture



Online Certificate Course in Laboratory Techniques for Molecular Biology & Biomaterial Development

CERTIFICATE OF COMPLETION

This certifies that

Farah Alwani Binti Azaman

has successfully completed the course

Series 1: Fundamental Techniques in Cell Culture

on

7, 14, 21 & 28 April 2021

organised by

School of Dental Sciences, Universiti Sains Malaysia



Assoc. Prof. Dr. Mohd Fadhli Khamis
Dean
School of Dental Sciences
Universiti Sains Malaysia



Dr. Norhayati Yusop
Head of Project
Series 1: Fundamental Techniques in Cell Culture
School of Dental Sciences
Universiti Sains Malaysia

Appendix 8: Certificate of Completion of Series 2: Cell Viability and Cell Toxicity Assay



Appendix 9: Certificate of Completion of Series 3: Techniques in Molecular Biology



Appendix 10: Certificate of Completion of Series 4: Electron Microscopy



Appendix 11: Certificate of Completion of Series 5: Advanced Technique & Development in Biomaterials Characterizations and Applications



Appendix 12: Certificate of Attendance: Webinar on Animal Care & Management for Pre-Clinical Study



CERTIFICATE OF ATTENDANCE

this certificate is presented to

Farah Alwani Binti Azaman

940713-13-6080

For attending the webinar

ANIMAL CARE & MANAGEMENT FOR PRE-CLINICAL STUDY

On July 14, 2021



Assoc. Professor Dr. Badrul Hisham Yahaya
Director

MAVMACPD-2021-118(1POINT)